Charles University in Prague
Faculty of Mathematics and Physics

DOCTORAL THESIS

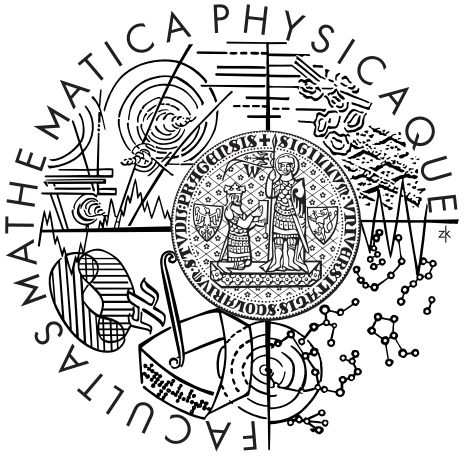

Mgr. Alena Habartová

Investigation of monomolecular organic layers and their interaction with atmospheric oxidants and polutants

Institute of Organic Chemistry and Biochemistry
Academy of Sciences of the Czech Republic

Advisor: prof. Mgr. Pavel Jungwirth, DSc.

Study programme: Physics

Specialization: Biophysics, Chemical and Macromolecular Physics

Prague 2015

Jsem vděčná své zesnulé školitelce Martině Roeselové, za její rozhodnutí umožnit mi se stát znovu studentkou. Obdivovala jsem ji, že dokázala spojit vědeckou práci a zároveň vybudovat velkou a šťastnou rodinu. Otevřela mi říši divů. Děkuji Pavlovi Jungwirthovi, že bez váhání převzal roli mého školitele. Díky němu a skvělé skupině lidí, které kolem sebe soustředil, jsem se hodně naučila. Honzovi a Lukaszovi děkuji za poskytnuté scripty a cenné rady. Jsem vdečná především Janě, Evě, Ivanovi, Mortezovi, Pepovi, Štěpánovi a Ondrovi za ochotnou pomoc a přátelství.

Svým nejbližším vděčím za pevné zázemí. Poděkování patří mé mamince, která je mi po celou dobu velkou oporou a vzorem. Svému muži Davidovi děkuji za stálou podporu a lásku. Díky Šimi, Ruti, Joni a Dani za vaši odolnost a inspiraci!

Martině a tátovi.

I declare that I carried out this doctoral thesis independently, and only with the cited sources, literature and other professional sources.

I understand that my work relates to the rights and obligations under the Act No. 121/2000 Coll., the Copyright Act, as amended, in particular the fact that the Charles University in Prague has the right to conclude a license agreement on the use of this work as a school work pursuant to Section 60 paragraph 1 of the Copyright Act.

In Prague, 30.6.2015 signature of the author

Název práce: Výzkum monomolekulárních organických vrstev a jejich interakce s atmosferickými oxidanty a polutanty

Autor: Mgr. Alena Habartová

Ústav: Ústav organické chemie a biochemie, Akademie věd České republiky

Vedoucí disertační práce: prof. Mgr. Pavel Jungwirth, DSc.

Abstrakt: Pomocí simulací klasické molekulové dynamiky jsme studovali interakce Langmuirových monovrstev kyseliny palmitové a haloalkanů, jako látek znečišťujících ovzduší a jako modelových systémů přirozeně se vyskytujících v atmosféricky relevantních makroskopických vodních systémech a aerosolech. Zkoumali jsme rozdělení, orientaci, solvataci, jakož i strukturu a morfologii jednotlivých složek a jejich směsi na rozhraní voda/vzduch při různých teplotách, abychom ověřili náš výpočetní model a doplnili experimentální data detaily na molekulové úrovni. Ukázali jsme, že halogenuhlovodíkové molekuly adsorbované na amorfních ledových nanočásticích při 100 K zůstávají převážně izolované a netvoří agregáty, na rozdíl od jejich shlukování na kryogenních argonových nanočásticích. Dokumentujeme, že chloro-, bromo- a jodoalkany s krátkými alkylovými řetězci (C1 až C5) preferují vnější oblast rozhraní voda/vzduch. Jejich průměrné rezidenční doby se pohybují v rozmezí stovek ps až několika ns při teplotě 300 K a závisejí na délce alkylového řetězce a povaze halogenu. Vypočtená molekulová orientace se mění z většinou dehydratovaného halogenu, který je vystaven vzduchu (pro halomethany) na částečně hydratovaný halogenový atom (pro halopentany). Dále ukazujeme, že více-substituované chloro- a bromomethany se snadno adsorbují na vodu nebo na krystalický led. Na základě výpočtů volné energie odhadujeme, že koncentrace více-substituovaných chloro- a bromometanů na vodním povrchu může být v závislosti na konkrétní molekule až o 4 řády vyšší vzhledem k jejich koncentraci v plynné fázi. K ověření našeho modelu palmitové kyseliny jsme zkoumali její monovrstvy na vodním povrchu a porovnali vypočtené strukturální parametry jako funkce povrchové hustoty filmu s experimentálními daty. Ukázali jsme, že neporušená monovrstva palmitové kyseliny zabraňuje přechodu molekul chlorometanu přes rozhraní voda/vzduch. Nakonec jsme studovali smíšené monovrstvy palmitové kyseliny s 1-bromoalkany o různé délce řetězce (C5, C10, a C16). Pozorovali jsme, že molekuly bromohexadekanu byly začleněny do monovrstvy palmitové kyseliny, zatímco bromoalkany s kratšími alkylovými řetězci nevytvořily stabilní smíšené monovrstvy. Vypočítané strukturální parametry jako funkce složení a povrchové hustoty poskytují nanoskopické detaily týkající se struktury a dynamiky smíšených monovrstev a doplňují experimentální výsledky získané našimi spolupracovníky. Naše výsledky mají významné důsledky pro (foto)chemické procesy na aerosolech s organickou povrchovou vrstvou v troposférických a stratosférických vrstvách.

Klíčová slova: molekulární dynamika, Langmuirovy monovrstvy, palmitová kyselina, haloalkany, solvatace, rozdělení na rozhraní

Title: Investigation of monomolecular organic layers and their interaction with atmospheric oxidants and polutants

Author: Mgr. Alena Habartová

Institute: Institute of Organic Chemistry and Biochemistry, Academy of Sciences of the Czech Republic

Advisor: prof. Mgr. Pavel Jungwirth, DSc.

Abstract: Using classical molecular dynamics simulations, we studied interactions between Langmuir monolayers of palmitic acid (PA) and haloalkanes as serious atmospheric pollutants, to model naturally occurring and atmospherically relevant complex surfaces of extended water bodies and aqueous aerosols. We investigated partitioning, orientation, solvation, as well as structure and morphology of the individual components and their mixture at water/vapor interfaces at different temperatures in order to validate our computational model and complement experimental data with molecular-level details. First, we have shown that halocarbon molecules adsorbed on amorphous ice nanoparticles at 100 K remain mostly isolated and do not form aggregates, in contrast to their clustering on cryogenic argon nanoparticles. Next, we report that chloro-, bromo-, and iodoalkanes with short alkyl chains (up to C5) exhibit high preference for the outermost region of the water/vapor interface. Their average residence times of several hundreds of ps to several ns at 300 K depend on the alkyl chain length and the nature of the halide atom. The calculated molecular orientation changes from a mostly dehydrated halide atom exposed to the vapor for halomethanes to a partially hydrated halide atom for halopentanes. In the next step, we show that multi-substituted chloro- and bromomethanes are readily adsorbed on water or crystalline ice surfaces. Based on free energy calculations we estimated that the concentration of multi-substituted chloro- and bromomethanes at the aqueous surface may be up to 4 orders higher relative to their concentration in the gas phase, depending on the particular species. Further, we investigated the PA monolayer at the water surface comparing calculated structural parameters as a function of film surface density with experimental data to validate our model. We have shown that the intact PA monolayer prevents mass transfer of chloromethanes across the water/vapor interfaces. Finally, we studied mixed PA monolayers with 1-bromoalkanes of different chain length (C5, C10, and C16). We observed that bromohexadecanes were incorporated into the PA monolayer, while bromoalkanes with shorter alkyl chains failed to form a stable mixed monolayer. Calculated structural properties as functions of composition and film surface density provided nanoscopic details about the organization and dynamics of mixed monolayers and supplemented experimental results from our collaborating group.Our results have important implications for (photo)chemical processes at the organic-coated aerosols in tropospheric and stratospheric regions.

Keywords: molecular dynamics, Langmuir monolayer, palmitic acid, haloalkanes, aqueous solvation, interfacial partitioning

Contents

Introduction

Water surfaces play an important role in many processes related to life on Earth. Surfaces of oceans, fresh water bodies, as well as tiny water droplets dispersed in air (aerosols) are coated by organic films of various chemical components originating from the decomposition of animal and plant cells and from ubiquitous pollution [1]. Presence of the organic films on water surfaces may have an effect on water evaporation or condensation, absorption or scattering of radiation, and catalyzing or suppressing chemical reactions with important consequences regarding the climate [2, 3, 4]. Atmospherically most relevant pollutants are halomethanes and haloethanes [5, 6, 7], uptake of which at the surface of aerosols may affect complex chemical processes involved in ozone destruction by reactive chlorine, bromine, and iodine radicals [8].

Organic molecules that accumulate on the water surfaces are called surfactants. These molecules possess both a water-attracting (hydrophilic) headgroup and a water-repelling (hydrophobic) tail resulting in their amphiphilic behaviour; hydrophilic heads keep them in the aqueous bulk while hydrophobic tails restrain these substances from dissolving. Typical surfactants are fatty acids and lipids. Surfactants lower the surface tension of water and tend to self-arrange into insoluble structures, such as micelles or films. A one-molecule thick surfactant layer spread on an aqueous surface is called a Langmuir monolayer in honour of Irving Langmuir, who pioneered monolayer studies for which he was awarded the Nobel Prize in 1932 [9]. Langmuir monolayers are utilized as experimental models for naturally occurring complex surfaces of water bodies, aqueous aerosols, or even pulmonary surfactants and tear films in the eyes [10, 11, 12].

Our environment is polluted by an enormous number of organic compounds. Prevalent pollutants in waste water, ground water, and in the atmosphere are halogenated organic compounds emitted from both natural and antropogenic sources [5]. The major natural source of the halogenated compounds are macroalgae in oceans, salt marshes, oxidative degradation of organic matter in soil, volcanic gases, and biomass burning [7, 13, 14, 15, 16]. In addition, the halogenated organics are produced by chemical industry and are used as organic solvents, pesticides, herbicides, fumigants, fire retardants, and anesthetics [17].

Processes on water surfaces can be investigated by chemical and physical experimentation, and by computational modeling. A special device called Langmuir trough was designed, in which organic Langmuir monolayers are formed under controlled conditions to study their physical and chemical properties using experimental methods, such as X-ray diffraction, infrared reflexion-absorption spectroscopy, vibrational sum frequency generation, or Brewster angle microscopy. The computational modeling was pioneered, among others, by Martin Karplus, Michael Levitt, and Arieh Warshel awarded the Nobel Prize in 2013. Today, classical molecular dynamics (MD) simulations provide a powerful tool for looking into the structure and dynamics of organic films at a molecular resolution. In the computational studies phospholipid monolayers have been often used as proxies for biological systems [18, 19, 20, 21]. Fatty acid monolayers received considerably less attention [22, 23, 24], although saturated fatty acids, specifically myristic (C14), palmitic (C16), and stearic (C18) acid, have been found

in aerosols released from ocean surface [25, 26, 27]. Measurements suggest that surfaces of aerosols are diverse in chemical composition and morphology, and therefore, mixed organic monolayer are more appropriate models [28]. However, a systematic MD study of multi-component Langmuir monolayers is missing.

An objective of the present thesis was to model interactions between haloalkanes and palmitic acid monolayers by means of classical MD. Palmitic acid (PA) was chosen because it is the most abundant saturated fatty acid in marine aerosols [1], while the haloalkanes consisting of one or more halogen atoms (Cl, Br, I) and 1-16 carbons were selected as the most relevant atmospheric pollutants.

First, to ensure that our model describes the haloalkane–water interactions correctly, I investigated their behavior without the presence of the organic monolayer. We aimed at understanding the factors affecting surface reactivity of haloalkanes; such as the residence time, partitioning, orientation, and solvation. I tuned interaction parameters (i.e., the force field) available for haloalkanes and water by comparing the calculated properties (such as the solvation free energy) to experimental data (Henry's law constants).

Next, I verified our model of the palmitic acid monolayer. I resumed the simulations previously performed in our lab [29] and tested additional force fields. I compared structural parameters (density profiles, film thickness, chain tilt angle, and alkyl chain order parameter) obtained under different compression states to published experimental data [30, 31].

Finally, I proceeded to a more complex system – the water/vapor interface covered by two-component monolayers composed of palmitic acid and long chain 1-bromoalkanes. Incorporation of haloalkanes into fatty acid monolayers has recently been studied in experiment [32]. Our MD simulations help to explain the experimental results providing molecular level details about the organization (morphology), stability, and dynamics.

The thesis is organized as follows. The background of MD simulations and experimental methods important for our topic are described in Chapter 1. Results and discussion concerning the behavior of haloalkanes on the water/vapor interface, of the palmitic acid monolayers, and of the mixed monolayers are presented in Chapters 2-4, respectively. Our principal findings are summarized in Conclusions. Two published and two submitted original papers supporting the thesis are presented in the Attachment.

1. Methods

This chapter provides a brief background of MD simulations and also several experimental methods, results of which were used for our calculations. An experiment and a computer simulation became complementary tools of scientific investigation. Usually a theoretical hypothesis is followed by an experiment. We start with an experiment performed by our colaborators that gave us an impuls to carry out MD simulations to provide a deeper insight into their experimental results.

1.1 Molecular beam experiment

Molecular beams are utilized for investigations of collision dynamics, scattering, sticking, or desorption at the detailed molecular level. In atmospheric chemistry and physics, large water clusters $(H_2O)_N$, $\bar{N} = 10^2$–10^3 (amorphous ice nanoparticles) can mimic ice particles in polar stratospheric clouds. Doping these ice nanoparticles with other molecules in the laboratory experiment allows to investigate the molecular photochemistry relevant to the analogous processes occurring in the atmosphere [33]. Molecular beam experiments are performed in a complex experimental device Fig. 1.1. Water nanoparticles of distinct sizes and velocities created by supersonic expansion pass through a skimmer and enter a scattering chamber (SC) with gas-phase molecules under controlled pressure. By collisions these molecules stick to the nanoparticles. The direction and velocity of the resulting nanoparticles (with adsorbed guest molecules) are measured in a chopper chamber (CC). Assuming that all adsorbed gas molecules transformed their linear momenta on the nanoparticle, then from the velocity difference we can gain the number of picked up guest molecules. Subsequently the nanoparticles fly into a photodissociation chamber (PDC), where they are fragmented and the fragments are analysed in a mass spectroscopy chamber (MSC) by a quadrupole mass spectrometer (QMS). The mass spectrometry data yield information about sizes and compositions of these photofragments.

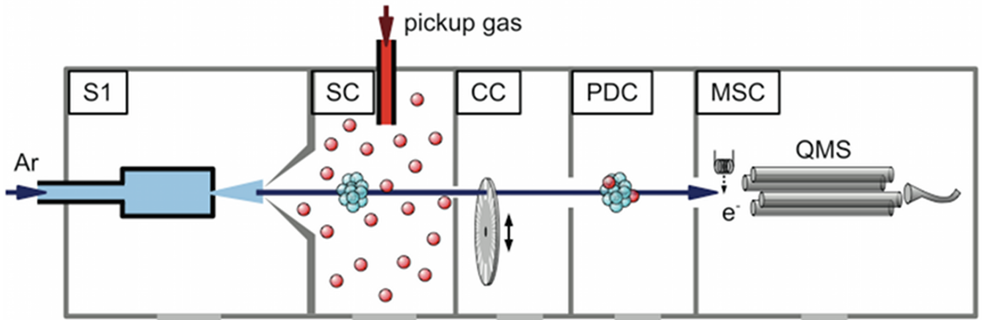

Figure 1.1: *Schematic picture of the molecular beam experiment modified from [34].*

1.2 Experimental investigation of the palmitic acid monolayer

Monolayers of organic amphiphilic molecules (lipids, or fatty acids) play an important role as the component of pulmonary surfactant, mammalian hair and fibres and ocean, fresh water and air droplets surfaces. Organic surfactant films decrease surface tension of water and influence significantly other factors such as water evaporation/uptake, mass transfer across the interface, and optical properties.

Palmitic acid, $H_{31}C_{15}COOH$ (PA), depicted in Fig. 1.2, is the most common saturated fatty acid found in animals, plants, and microorganisms [35]. As its name indicates, it is a major component of the oil from palm trees, but can also be found in meat, cheese, butter, and dairy products. Excess carbohydrates in the body are converted to palmitic acid. Palmitic acid is the first fatty acid produced during fatty acid synthesis and the precursor to longer fatty acids. As a consequence, upon cell decomposition, PA is found on surfaces of water bodies, and therefore, also on marine aerosols [25].

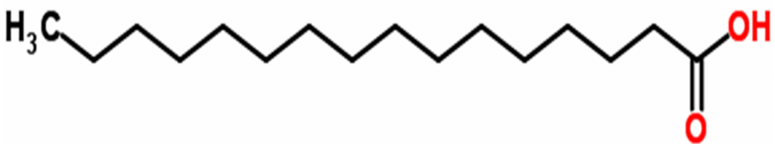

Figure 1.2: *Schematic representation of a palmitic acid molecule, $C_{16}H_{33}COOH$*

Langmuir trough experiment

A Langmuir trough Fig. 1.3 is an experimental device designed to form and study Langmuir monolayers on the surface of a liquid subphase (usually water). Surface of the trough covered by surface active molecules can be compressed/expanded by movable barriers resulting in a varying surface density of surfactants, expressed as a mean area per molecule, A_M. Surface tension of the interface is measured by the Wilhelmy balance. An useful concept is the surface pressure π, which is defined as the difference of surface tension of pure water γ_0 and surface tension of water with the surfactant γ_s.

$$\pi = \gamma_0 - \gamma_s$$

As a consequence of surfactants lowering the surface tension of water, $\pi \geq 0$. The curve that describes the dependence of surface pressure with respect to the area per molecule is called the surface pressure-area (π-A) isotherm. An experimental isotherm for palmitic acid is shown in Fig. 1.3.

When A_M is high (i.e., surface density of the monolayer is low) the surfactant molecules interact with each other only negligibly. The monolayer is referred to as a 2D-gas. When the film is compressed, the molecules form a 2D-liquid phase. Upon further compression the monolayer undergoes another phase transition to form a solid phase characterized by high ordering of the molecules. The phase transition is seen as the change of the isotherm's slope at 25 Å^2. The so called

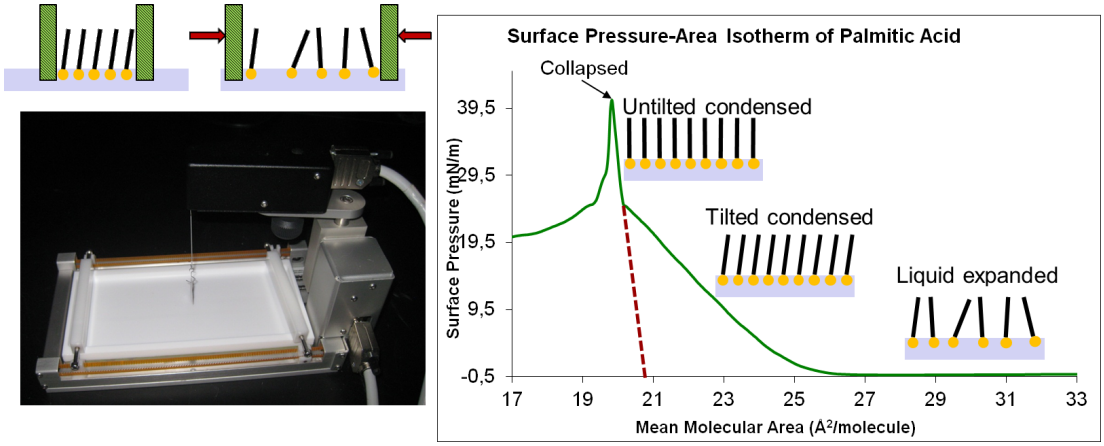

Figure 1.3: *Left: Langmuir trough. Right: Experimental π-A isotherm of the palmitic acid monolayer at 295 K. Courtesy of R. Sierra-Hernandez.*

"lift-off" indicates the tilted condense phase. For palmitic acid another phase transition occurs at 20 Å^2. This value of A_M, when alkyl chains become untilted, is characteristic for every fatty acid species and is called the "molecular print". Upon continuing compression at a certain threshold the monolayer collapses, as expressed in a sharp decrease of the surface pressure at 18 Å^2.

The Langmuir trough can be combined with other experimental techniques, such as grazing incidence synchrotron X-ray diffraction (GID), infrared reflexion absorption spectroscopy (IRRAS), vibrational sum frequency generation (VSFG), and Brewster angle microscopy (BAM). These surface sensitive methods provide structural information of interfacial molecules, such as their texture, orientation, alkyl chain order parameter and tilt angle, or chemical composition of the surfactant layer. A detailed description of these methods is given in the literature [30, 36, 37, 38].

1.3 Molecular dynamics simulations

Classical molecular dynamics (MD) simulations are computer simulations of motions of interacting particles (atoms and molecules), based on numerical solution of Newton's equations of motion. There is a vast literature about MD simulations [39, 40, 41, 42, 43, 44] and readily available MD software packages. Basically, to start a MD simulation we need 4 ingredients:

1. A model for the interaction between system components (atoms, molecules, surfaces, ...) called the force field.

2. An integrator, i.e. a computational algorithm which propagates particle positions and velocities from time t to t + δt.

3. A definition of a particular statistical ensemble, where thermodynamic quantities like volume, temperature or the number of particles are controlled.

4. Initial condition of system consisting of N particles with starting coordinates $\vec{r}_i$ and velocities $\vec{v}_i$

Classical MD simulations rely on the Born-Oppenheimer approximation, that separates motion of "heavy" nuclei and "light" electrons. The nuclei move on the potential energy surface given by other nuclei and a stationary distribution of electrons, which follow the motion of nuclei infinitely fast. Atoms are described as "soft" spheres with point charges in their centers moving according to the Newton laws under the interaction potential. The exact interaction potential is impossible to construct for a large system. Usually the interaction potential is approximated by an analytic form consisting of several terms:

$$\begin{aligned} V = &\sum_b k_b(r - r_0)^2 + \sum_a k_a(\theta - \theta_0)^2 + \sum_{d,n} k_{dn}[\cos(n\phi - \phi_0)] \\ &+ \frac{1}{2}\sum_{i,j} 4\epsilon_{ij}\left[\left(\frac{\sigma_{ij}}{r_{ij}}\right)^{12} - \left(\frac{\sigma_{ij}}{r_{ij}}\right)^{6}\right] + \frac{1}{2}\sum_{i,j}\frac{1}{4\pi\epsilon_0}\frac{q_i q_j}{r_{ij}}. \end{aligned} \tag{1.1}$$

The first term represents the harmonic potential of all chemical bonds between two connected atoms vibrating around an optimal bond length r_0 with k_b being the force constant determining the rigidity of the bond. The second harmonic term is used for valence angle vibrations (θ_0 being the equilibrium angle between three bonded atoms, and k_a standing for the force constant). The third, periodic term models the potential of different molecular conformations; the dihedral (torsion) angle potential of four connected atoms A, B, C, and D in the molecule is approximated by first n terms of series, where ϕ_0 is an equilibrium angle between planes ABC ans BCD, and k_{nd} is the force constant. On the next line of Eq. 1.1, the first intermolecular term represents the van der Waals interaction (using the empirical Lennard-Jones potential), where ϵ_{ij} and σ_{ij} are defined for interacting atoms i, j. Finally, the last term is given by the Coulomb law for the electrostatic interaction between two point charges q_i, q_j at a distance r_{ij}. Sometimes, an explicite treatment of the polarization interaction is added.

Assuming we know the potential energy V of the system of N particles, we can calculate the force $\vec{f}$ acting on them as

$$f_{ij}(t) = -\frac{\partial V}{\partial r_{ij}(t)} \qquad i = 1, 2...N; \quad j = x, y, z \tag{1.2}$$

By a numerical integration we get a new particle position $\vec{r}$ and a velocity $\vec{v}$ in time t+δt knowing the particle position, velocity and force in time t

$$\vec{r}(t + \delta t) = \vec{r}(t) + \vec{v}(t)\delta t + \frac{1}{2}\frac{\vec{f}(t)}{m}(\delta t)^2 \tag{1.3}$$

It is a finite difference scheme which moves trajectories discretely in time. The time step δt has to be carefully chosen to guarantee stability of the integrator (no drift in the system's energy). Due to the discretization and integration numerical errors accumulate. Several integrator method were developed to symetrize the integrator in time and enhance its precision, such as the Verlet or the "leap-frog" algorithms [45, 46].

In order to calculate thermodynamical properties it is important that the trajectory samples correctly the whole phase space and the investigated system obeys the ergodic theorem. Then the time average of any thermodynamic quantity over the trajectory equals to the average over the statistical ensemble. We

have to stress that results of MD simulations are only correct with respect to the interaction model which enters into the simulation and they have to be tested against theoretical predictions and experimental findings.

Our results were obtained using GROMACS [47] and AMBER [48] software packages. We used all atom interaction parameters derived from experimental measurements, the so called empirical all atom force fields, that were implemented in MD packages. Mainly, we utilized the general Amber force field (GAFF) [49] or Optimalized Parameters for Liquid Simulations (OPLS) [50]; some atomic charges were calculated by Gaussian 09 [51] and refined by RESP method [52]. For molecular topologies and force fields used in particular simulations we refer to our publications attached to the thesis.

We integrated equations of motion using the leap-frog algorithm with the time step 1–2 fs depending on the investigated system. Our simulations consisted of up to $\sim 10^4$ atoms and were run for $\sim$100 ns. This number of particles is still not sufficient to study directly the liquid phase. In order to remove surface effects, the system was replicated in all three dimensions employing the periodic boundary conditions. To save computer time during evaluation of forces according to Eq. 1.2 the short-range non-bonded interactions were truncated to zero beyond the cut-off distance of 10 Å, and long-range electrostatic interactions were accounted for by the particle mesh Ewald method [53, 54]. Bonds were constrained using the SHAKE or LINCS algorithms [55, 56]

Mostly, we performed MD simulations of systems at constant temperature and volume or pressure (NVT or NpT ensembles), where temperature and pressure were controlled by additional algorithms [57, 58, 59, 60, 61] Generalization of starting conditions of particular systems prior the MD run will be described together with results in following chapters. Positions of all atoms during the production MD were stored in regular intervals ($\sim$1 ps) for further analysis and visualized using the VMD software [62]. Graphical outputs were displayed by the Grace [63] or Matlab [64] programs.

Analytical tools

We performed the analysis of converged trajectory and energy data using the Gromacs analytical tools (`g_energy`, `g_density`, `g_rdf`, `g_order`, `g_wham`, etc.) and home made scripts to obtain quantities that could be compared to experimental results.

Structural information

The basic structural informations can be derived from the **density profile**, i.e. a calculated density distribution of specified atoms along a defined direction within the simulation box (usually the z-axis given by the normal of the water/vapor interface).

A useful structural concept is the **radial distribution function** $g_{AB}(r)$, which is the normalized probability density of finding a particle of type B at the distance r from the reference particle of type A

$$g_{AB}(r) = \frac{\langle \rho_B(r) \rangle}{\langle \rho_B \rangle_{local}} = \frac{1}{\langle \rho_B \rangle_{local}} \frac{1}{N_A} \sum_A \sum_B \frac{\delta(r - r_{AB})}{4\pi r^2} \tag{1.4}$$

with $\langle \rho_B(r) \rangle$ being the particle density of type B at a distance r around particles A, and $\langle \rho_B \rangle_{local}$ the mean particle density of type B averaged over all spheres around particles A with radius r_{max} (at most the half of the simulation box length). The radial distribution function can be deduced experimentally from diffraction studies.

Spatial distribution function $g(\vec{r}) = g(r, \varphi, \theta)$ determines the 3D density distribution of specified particle around the reference molecule. We calculated solvation of haloalkane molecules on the water interface. To construct the spatial density maps, all coordinates saved in a trajectory frame were transformed into a coordinate system having the halide atom X as the origin, the x-axis coinciding with the X–C1 bond, the X, C1, and one of the adjacent H atoms defining the xy-plane (with the z-axis perpendicular to it). The spatial coordinates of all water oxygen atoms were then recorded with respect to this molecule-fixed coordinate system. In this way, positions of water molecules around the haloalkane were obtained regardless of the instantaneous orientation of the haloalkane relative to the water surface.

Ordering of alkyl chains is characterized by the **order parameter** S. Generally, this quantity is a tensor $S_{\alpha\beta}$

$$S_{\alpha\beta} = \frac{1}{2}\langle 3\cos\theta_\alpha \cos\theta_\beta - \delta_{\alpha\beta} \rangle \tag{1.5}$$

where α,β= x, y, z directions and θ_α is the angle between the α^{th} molecular axis and the interface normal (z-axis). Since we investigate monolayers deposited on the water/vapor interface, these systems possess symetry with respect to the rotation around the z-axis. The diagonal element S_{zz} is related to the experimentally relevant deuterium order parameter S_{CD} as

$$S_{CD} = -\frac{1}{2} S_{zz} \tag{1.6}$$

and according to Eq. 1.5

$$S_{zz} = S_z = \frac{1}{2}\langle 3\cos\theta_z^2 - 1 \rangle \tag{1.7}$$

The order parameter S_z is calculated separately for every carbon atom along the alkyl chain (Fig. 1.4).

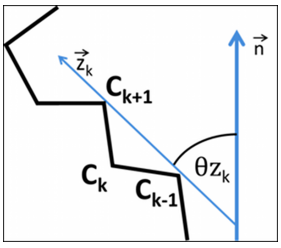

Figure 1.4: *Calculation of the order parameter S_z for a particular alkyl chain carbon C_k, where θ_{zk} is the angle between monolayer normal $\vec{n}$ and the molecular axis defined by two adjacent carbons $\vec{z}_k$.*

Free energy calculation

A measure of stability of a system (assuming the canonical ensemble) is the Gibbs free energy G. To understand the change of the system structure we need to know the difference in free energy ΔG related to this change. For example, we want to know the free energy of solvation ΔG_s, which is the free energy difference connected with the transition from the air to the bulk liquid water for a studied molecule. Our aim is to calculate a free energy profile along the appropriate reaction coordinate (i.e., the direction perpendicular to the water interface, z-coordinate). To sample directly the configuration space to get the free energy profile is usually not feasible and more sophisticated techniques have to be employed. We used the umbrella sampling method [65], which introduces biasing potentials of harmonic shape to restrict the movement of the particle of interest in particular configurations. The scheme of the protocol depicted in Fig. 1.5 consists of three steps. First, we draw the particle along the reaction coordinate to create starting positions ~1Å apart for a series of independent MD simulations. The particle is then held in a particular window by a biasing harmonic potential. The obtained biased probability distributions of positions from each window have to be processed by the weighted histogram analysis method (WHAM) [66] to subtract the bias and join them together to get the full probability distribution.

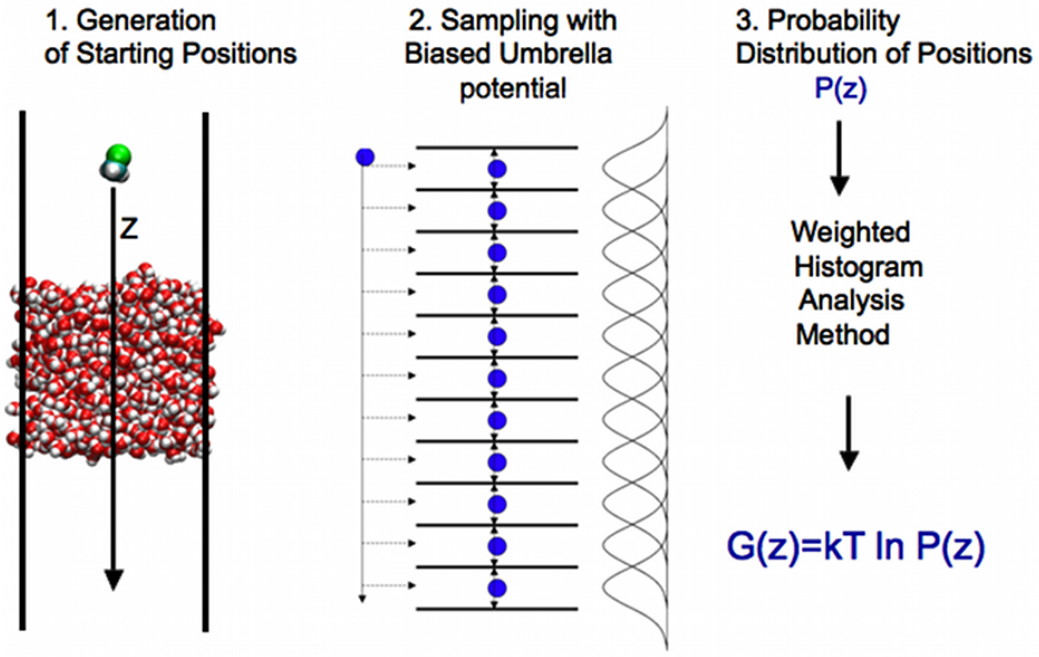

Figure 1.5: *Scheme of the free energy profile calculation using the umbrella sampling method*

2. Interactions of halocarbons with the water surface

This chapter presents our results of MD simulations carried out to investigate the interaction of small halogenated molecules of atmospheric relevance with water or ice surface.

2.1 Pick-up of halocarbons on ice nanoparticles

Our collaborators carried out molecular beam experiments to study the pick-up process of chlorinated molecules on amorphous ice nanoparticles with mean size of $\bar{N}$= 430 molecules at 100 K. The experiment probed different types of molecules from simple hydrochloric acid HCl to more complex chloromethane CH_3Cl and longer chain chloropropane C_3H_7Cl molecules, and also to aromatic species represented by chlorobenzene C_6H_5Cl. As a control to CH_3Cl and C_6H_5Cl molecules, methane CH_4 and benzene C_6H_6 were investigated, too.

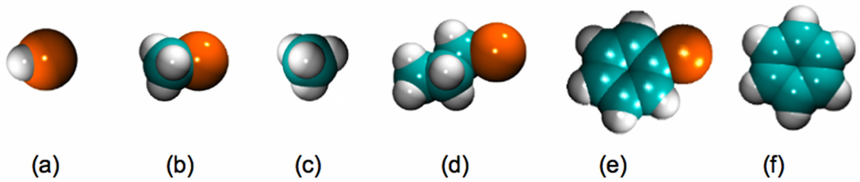

Figure 2.1: *Set of studied guest molecules: (a) HCl, (b) chloromethane CH_3Cl, (c) methane CH_4, (d) chloropropane C_3H_7Cl, (e) chlorobenzene C_6H_5Cl, and (f) benzene C_6H_6. Color coding: chlorine in orange, carbon in cyan and hydrogen in white.*

Experimental results are summarized in Tab. 2.1. The mass spectra provided evidence for only individual isolated molecules present on $(H_2O)_N$. For comparison, the beam of argon nanoparticles with a mean size of $\bar{N}$= 330 atoms at 37 K was exposed to the same set of molecules under same pressure conditions. The mass spectra measured after their uptake on Ar_N showed aggregation to clusters of different sizes. The largest clusters were observed for HCl, with m_{max} up to 11, for benzene this number was 9, and maximum cluster sizes of 7 molecules were detected for three other molecules CH_3Cl, C_3H_7Cl, and C_6H_5Cl. In contrast, CH_4 clusters beyond 3 molecules were not detected.

MD systems, initial conditions, and simulation runs. The aim of our MD simulations was to mimic the adsorption of the experimentally studied chlorinated molecules on water and argon nanoparticles. Spherical clusters consisting of 300 H_2O molecules or Ar atoms were carved out from previously simulated liquid water ($T \approx 300$ K) or liquid argon ($T \approx 80$ K) systems. Each cluster was then placed in the center of a cubic simulation cell with the edge dimension of 80 Å (the diameters of the water and argon clusters were about 30 Å). To equilibrate the clusters to the target temperature of 100 K (for water) and 37 K (for argon) corresponding to the experimental conditions, 50ns NVT simulations

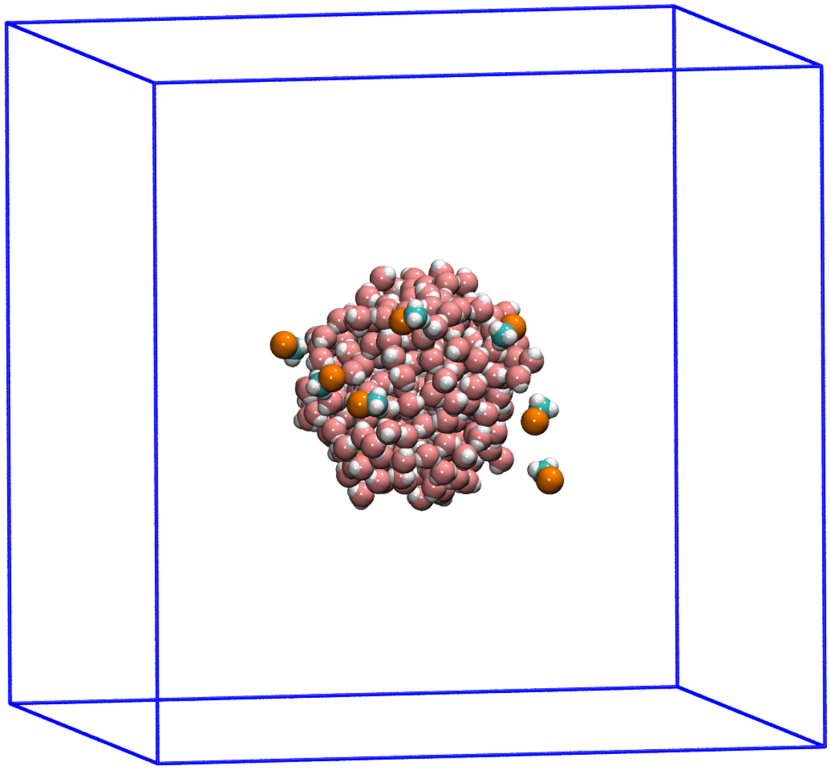

Figure 2.2: *Starting geometry of a roughly spherical cluster consisting of 300 H_2O molecules with 12 chloromethane molecules, placed in the center of a cubic simulation box with dimension of 80 Å. Color coding: chlorine in orange, carbon in cyan, oxygen in pink, and hydrogen in white.*

were performed. Subsequently, 12 identical molecules from the above list of studied pick-up species were added into the simulation cell (Fig. 2.2). The molecules were initially placed pseudo-randomly around the cluster at a distance of several Å from the cluster surface. The entire system was again shortly equilibrated ($\approx$ 10 ps) at the respective experimental temperature. During that period, most of the molecules landed on the cluster surface, and the resulting configurations of the water/argon clusters with 12 adsorbed molecules were used as initial conditions for the subsequent production runs. The systems were propagated for 50 ns simulation at the above given experimental temperatures to sample structural characteristics of the water or argon clusters with 12 molecules adsorbed on their surface. For each combination of a cluster and the pick-up species, 5 different initial configurations of molecules around the clusters were created and propagated independently.

Results from MD simulations are shown in Fig. 2.3. Each panel shows the last snapshot of the respective 50ns simulation. The averaged cluster size m_{cal} is listed in Tab. 2.1. Simulations show mostly individual guest molecules on the $(H_2O)_{300}$ surface. The interaction of molecular dipoles of adsorbed molecules with polar water molecules lowers mobility of the adsorbed molecules. The picked-up molecules thus generally remain at the position of the first contact with the $(H_2O)_{300}$ surface, but reorient with respect of the nearby H_2O molecules. The chlorine atom of the chlorine containing molecules is preferentially oriented to the vapor phase. Only chloropropane seems to be able to form small clusters (dimers and a trimer) at the timescale of the simulations. Small molecules such as HCl

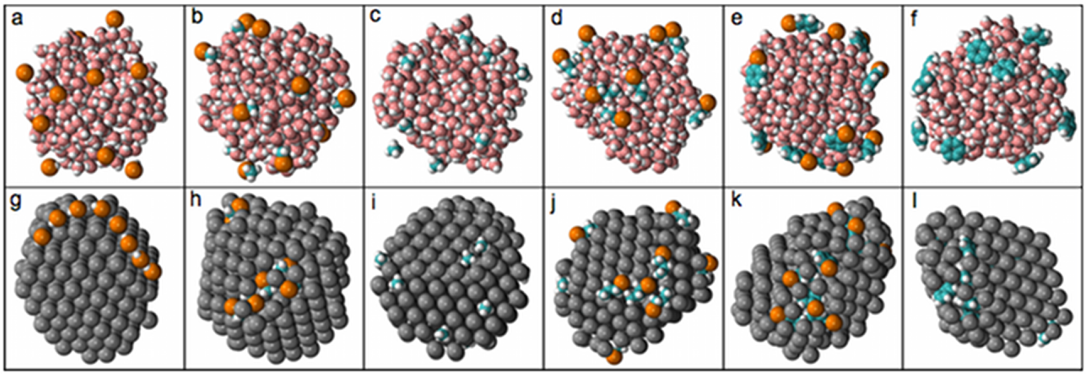

Figure 2.3: *The last snapshot of the 50 ns MD simulation of amorphous ice (the upper row) or argon (the bottom row, in grey) nanoparticles and 12 adsorbed guest molecules (in columns): (a,g) HCl, (b,h) chloromethane, (c,i) methane, (d,j) chloropropane, (e,k) chlorobenzene, and (f,l) benzene. Color coding: chlorine in orange, carbon in cyan, hydrogen in white, oxygen in pink, and argon in gray.*

and methane are able to desorb from the surface. Here, we have to stress that the present classical MD simulations do not allow for possible ionic dissociation of the HCl molecules on water.

In contrast to the simulation on the water particles, all studied molecules formed clusters on argon. We observed the largest clusters formed of HCl molecules (from 8 up to all 12 present molecules), while chloromethane, chloropropane, chlorobenzene, and benzene aggregated to a comparable extent forming mainly pentamers. The weakest coagulation was present for methane, clustering to dimers. Presence of a molecular dipole due to the chlorine atom (and similarly the presence of the aromatic benzene ring) influences both coagulation and orientation of the molecules. The calculated dipole moments of the studied species are 1.5 D (HCl), 2.1 D (chloromethane), 2.5 D (chloropropane), 2.1 D (chlorobenzene), and zero for methane and benzene. Molecular dipoles tend to orient with respect of each other resulting in creation of oriented dimers, trimers, etc. This

Table 2.1: *The maximum cluster fragment size observed in the mass spectra m_{max} and the mean number of adsorbed molecules m_p at the pressure p, and the averaged cluster size from MD simulations m_{cal}. The m_p value for methane on ice nanoparticles(*) is likely to be overestimated, and for benzene and chlorobenzene(**) on both argon and ice to have lower confidence level*

	p	Ar_N			$(H_2O)_N$		
M	10^{-4} mbar	m_p	m_{max}	m_{cal}	m_p	m_{max}	m_{cal}
HCl	3.0	17(3)	11(2)	8(3)	17(3)	1	1(0)
CH_4	3.3	22(2)	3(1)	2(1)	18(4)*	1	1(0)
CH_3Cl	1.7	10(3)	7(2)	5(1)	4(2)	1	2(1)
C_3H_7Cl	0.9	7(1)	7(2)	4(1)	3(1)	1	3(1)
C_6H_6	0.9	4(2)**	9(1)	5(1)	1(1)**	1	2(1)
C_6H_5Cl	0.7	3(2)**	7(1)	5(1)	1(1)**	1	2(1)

is the reason of efficient coagulation of chloromethane in comparison to methane which lacks a molecular dipole. Also, the presence of a chlorine atom poining to the vapor possibly prevents chlorobenzene from submerging deeper in the argon cluster. Interestingly, benzene even without a molecular dipole coagulates in the same extent as chlorobenzene, which is due to the π-stacking interaction of benzene rings. The shape of molecular clusters depends on the character of the interactions between the picked-up molecules. Also, weak dispersion forces acting among argon atoms do not restrain chloromethanes, chlorobenzenes or benzenes from embedding in the argon nanoparticle.

Our calculations confirmed the experimentally observed trends in aggregation of guest molecules on water and argon nanoparticles. The simulated results of the average maximal cluster sizes are in a good agreement with the respective measured values m_{max}. We have to mention, nevertheless, that our calculations catch the process of adsorption of guest molecules at a nanosecond time scale, while experimentally the process lasts for miliseconds.

2.2 Haloalkanes on the water surface

MD systems, initial conditions and simulation run. The simulated system consisted of 1 up to 20 identical haloalkanes molecules and 863 water molecules forming a liquid slab in the center of the simulation box, with two water/vapor interfaces (Fig. 2.4). The box was elongated along the z-axis with the dimensions of 30 Å, 30 Å, and 100 Å. Simulations were performed at 300 K for up to 50 ns.

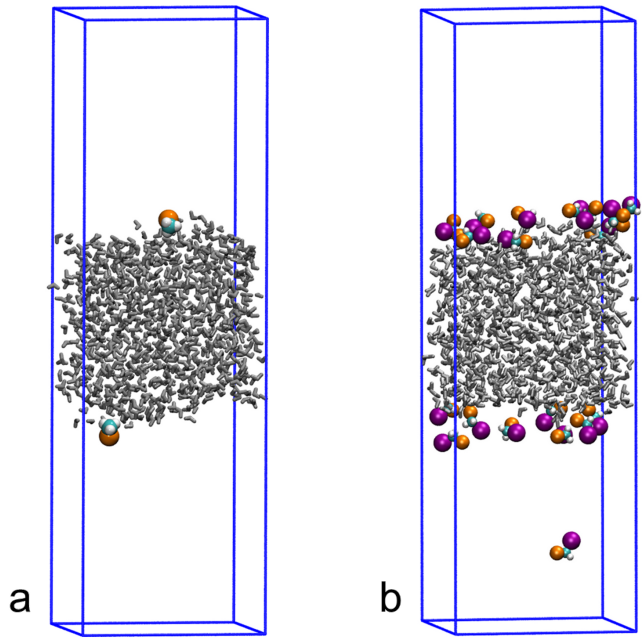

Figure 2.4: *Two examples of the simulated systems consisting of a water slab (gray color) in the center of the box, and (a) 2 chloromethane or (b) 20 chloroiodomethane molecules. A rectangular parallelepiped simulation box with x-, y-, and z-dimension of 30 Å, 30 Å, and 100 Å, was employed.*

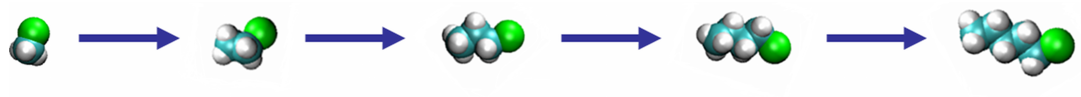

Figure 2.5: *Set of studied mono-substituted haloalkanes. Color coding: C in cyan, H in white and Cl, Br or I in green.*

2.2.1 Residence times, orientation and solvation

We performed a systematic study of mono-substituted haloalkanes, $C_nH_{2n}X$, where $n = 1 - 5$ and X = Cl, Br, or I (Fig. 2.5), at the water surface.

Typical trajectories of two haloalkane molecules interacting with the water slab are shown in Fig. 2.6, where the z-coordinate of the chlorine atom of chloromethane and chloropropane molecules is plotted versus time. Haloalkanes interact weekly with the water surface and undergo frequent desorption into the gas phase. While halomethanes and, to a lesser extent, also haloethanes occasionally immerse into the bulk water, no such events were observed for longer alkyl chain species in the course of 20 ns simulations.

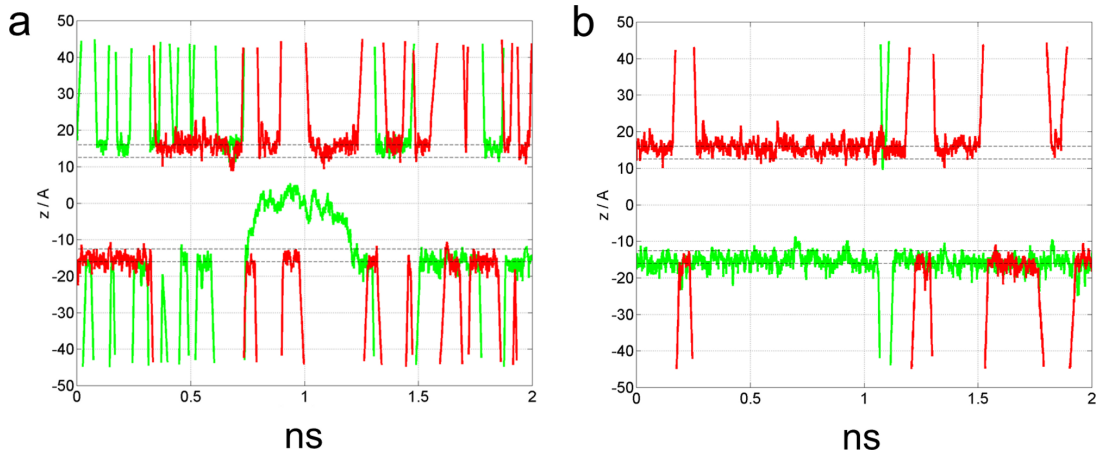

Figure 2.6: *Trajectories of (a) two chloromethanes and (b) two chlorobutane molecules interacting with the water slab are shown as the time dependent positions of the molecules along the interface normal using 2 ns of simulation data. In both panels, the trajectory of one molecule is depicted in red and the other one in green. Two water/vapor interfaces, defined as the regions between 90 % to 10 % of bulk water density value, are indicated by two pairs of dashed horizontal lines; z=0 corresponds to the middle of the slab.*

Calculated average residence times on the water surface (with 95% confidence intervals in brackets) increase from 140 (120-160) ps for CH_3Cl to 540 (440-690) ps for C_3H_7Cl, and 1010 (680-1920) ps for $C_5H_{11}Cl$. A similar trend was observed also for bromoalkanes and iodoalkanes. For the same chain length, the average residence times increase from chloride to bromide, and to iodide. For example, the following average residence times were obtained: 160 (140-180) ps for CH_3Br, and 180 (160-210) ps for CH_3I.

Density profiles of individual atoms averaged over the two equivalent surfaces for chloromethane, chloroethane, and chloropropane are shown on Fig. 2.7. Density profiles for all studied haloalkane species indicate their preference to reside

at the water/vapor interface, as their concentration is significantly enhanced in the interfacial region compared to the vapor, as well as to the bulk liquid phase.

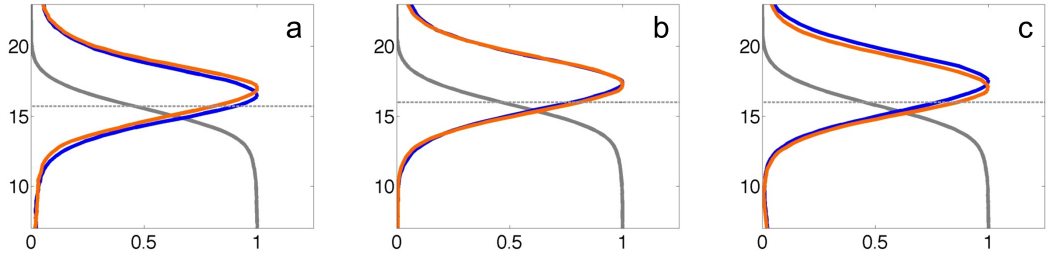

Figure 2.7: *Density profiles of (a) chloromethane, (b) chloroethane, and (c) chloropropane along the z-coordinate normal to the interface (z=0 is the center of the water slab). Density of water (grey) gradually decreases over the water/vapor interfacial region from its constant bulk liquid value to zero in the vapor phase. The dashed line represents the Gibbs dividing surface. The (normalized) density of the alkyl chloride molecules is represented by the density profiles of the last carbon (blue) of the alkyl chain (the methyl carbon) and of the chlorine atom (orange).*

In order to obtain a more complete picture of interfacial behavior of haloalkanes we were interested in their orientation and detailed solvation when adsorbed on the water surface.

The orientational profiles of chloroalkanes are plotted in Fig. 2.8 as a distribution $\mathrm{P}(\cos\theta)$, where the angle θ is between the interface normal (z-axis) and the molecular vector $\mathrm{X} \rightarrow \mathrm{C(H_3)}$ pointing from the halogen atom X (=Cl, Br, or I) to the carbon atom of the terminal methyl group.

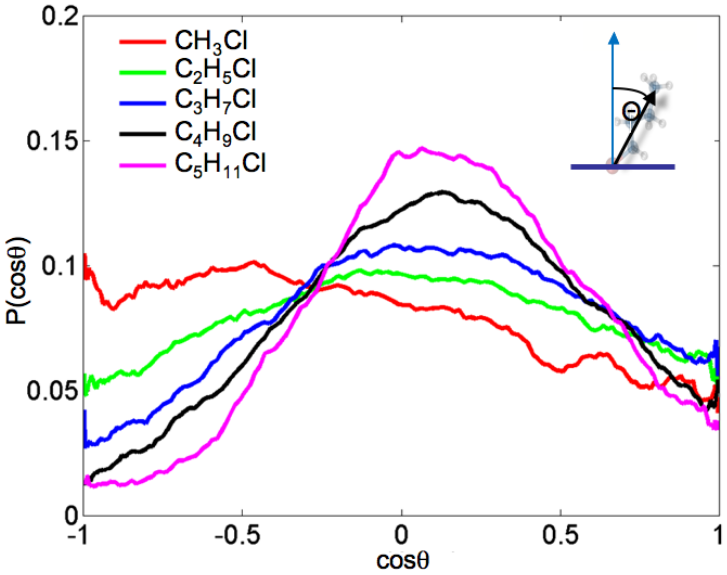

Figure 2.8: *Orientational distributions of chloroalkanes at the water/air interface. Molecular vector $X \rightarrow C(H_3)$, pointing from the halogen atom X (=Cl, Br, or I) to the carbon atom of the terminal methyl group, and interface normal (z-axis) define angle θ.*

According to this definition, $\cos\theta = 0$ indicates that the molecular vector is parallel with the surface, while $\cos\theta = 1$ corresponds to the molecular vector oriented perpendicular to the surface with the halogen atom pointing toward

water. The results show that the chloromethane orientations with the chlorine atom pointing to water are the least probable, whereas orientations parallel to the interface and, in particular, tilted orientations with the methyl group pointing toward the water phase are preferred. The maximum around $\cos\theta = -0.5$ corresponds to a tilt angle of 120° between the chloromethane molecular vector and the surface normal. Nevertheless, the orientational distribution is broad and relatively flat, indicating that the chloromethane molecules adsorbed at the water surface are rotationally highly mobile. With increasing length of the haloalkane molecule, the distributions become less broad, and the maxima shift systematically toward higher $\cos\theta$ values corresponding to parallel alignment of the molecules with the water/vapor interface. The maxima for chloropentane are found at $\cos\theta = 0.15$, indicating tilted orientation with the hydrocarbon chain pointing on average slightly away from water at an angle of 10° between the molecular vector and water surface. Bromo- and iodoalkanes follow the same trends as described above for the chlorinated species.

Fig. 2.9 shows spatial distributions of water oxygen atoms around the surface-adsorbed haloalkanes, averaged over 20 ns. Additionally, one randomly selected conformation is shown for each species. The plotted distributions represent the density isovalue corresponding to 1.5 times the density of bulk water.

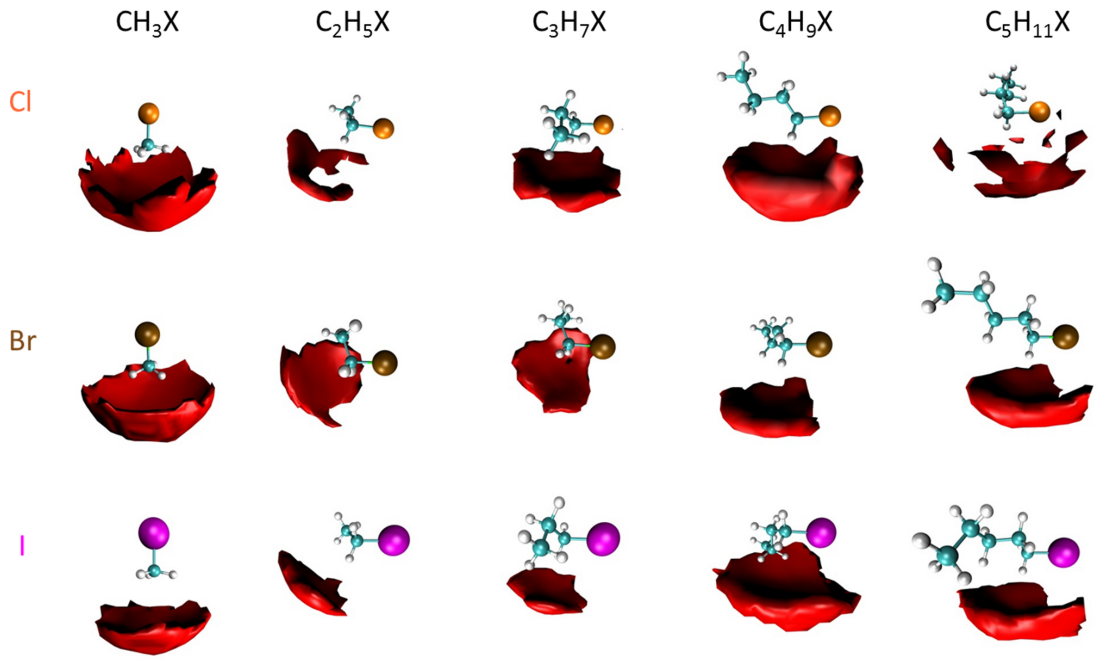

Figure 2.9: *Spatial density distributions of water around haloalkane molecules as obtained by averaging over 20 ns MD simulations. Colour coding: carbon in cyan, hydrogen in light gray, chlorine in orange, bromine in brown, and iodine in purple. The spatial distributions are plotted for the isodensity value of water oxygen (red) corresponding to 1.5 times the density of bulk water.*

The spatial plots show that halomethanes have an incomplete solvation shell centered on the methyl end of the molecule, leaving the halogen atom dehydrated. For the rest of the species, the maximum hydration is localized around the α-CH_2 group next to the halogen, in accord with the results of ab initio calculations for chloropentane [67]. However, there are important differences with regard to the

hydration of the halogen atom. While in haloethanes the C–X bond still essentially points away from water, the increasing length and, hence, hydrophobicity of the alkyl chain results in a gradual re-orientation of the C–X bond relative to the hydration shell. Consequently, haloethanes and, to a large degree, also halopropanes have the halogen atom fairly exposed, whereas in halobutanes and halopentanes the halogen becomes partially hydrated.

2.2.2 Free energy profile

We calculated free energy profiles across the water/vapor interface for halomethanes with up to 3 chlorine or bromine atoms: CH_3Cl, CH_2Cl_2, $CHCl_3$, CH_3Br, CH_2Br_2, and $CHBr_3$ (Fig.2.10).

Figure 2.10: *Set of studied halomethanes (carbon in cyan, hydrogen in white, chlorine or bromine in green).*

A schematic free energy profile of a haloalkane molecule is depicted in Fig. 2.11. As the molecule moves from the gas phase to the bulk liquid water, its free energy reaches minimum at the water/vapor interface. ΔG_s represents the free energy of the transition from the vapor to the bulk liquid water, and ΔG_{sl} is the free energy of the transition from the water surface into the bulk. As ΔG_s can be calculated from the experimentally measured Henry's law constant k_H [68], we aimed to reproduce this value in simulations. We succeeded to target experimental values of ΔG_s (within a $\pm$ 2 kJ/mol error) by scaling up partial atomic charges by a factor of 1.7–1.9 depending of the particular halomethane molecule (Tab. 2.2). Such a tuning of the force field helped to improve the molecular model of halomethanes in terms of their solvation for further studies. The results, plotted in Fig. 2.12 (left panel), reveal that the calculated free energy profiles of all the above halomethanes exhibit minima in the interfacial region corresponding to ΔG_{sl} of 11–15 kJ/mol (Tab. 2.2). We note that ΔG_{sl} is experimentally very hard to access.

From the free energy profiles $\Delta G(z)$ the corresponding relative concentration profiles $c_{rel}(z)$ of the halomethanes can be evaluated as seen in Fig. 2.12 (right panel). Upon setting the reference point into the gas phase (concentration c_g), we get

$$c_{rel}(z) = \frac{c(z)}{c_g} = exp(-\frac{\Delta G(z) - \Delta G_s}{RT}) \tag{2.1}$$

Results of averaged $c_{rel}(z)$ across the water/vapor interface (defined by z-coordinate between 90% and 10% water bulk density) are summarized in Tab. 2.2. As all halomethanes have a pronounced free energy minimum at the water/-vapor interface, they exhibit enhanced interfacial concentration by 2–4 orders of magnitude relative to the gas phase, depending on a particular species. This may have important implications for heterogeneous (photo)chemical processes involving haloalkanes on aqueous aerosols.

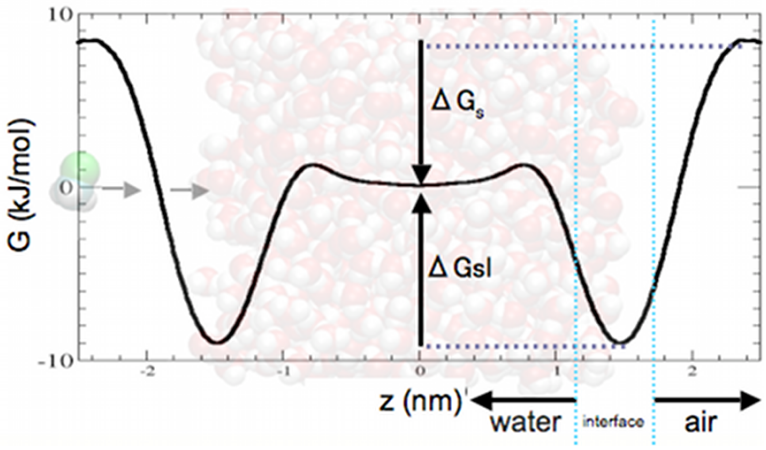

Figure 2.11: *Schematic free energy profile of a halomethane molecule across a liquid water slab. The z-coordinate direction normal to the water/vapor interface; z=0 corresponds to the center of the water slab.*

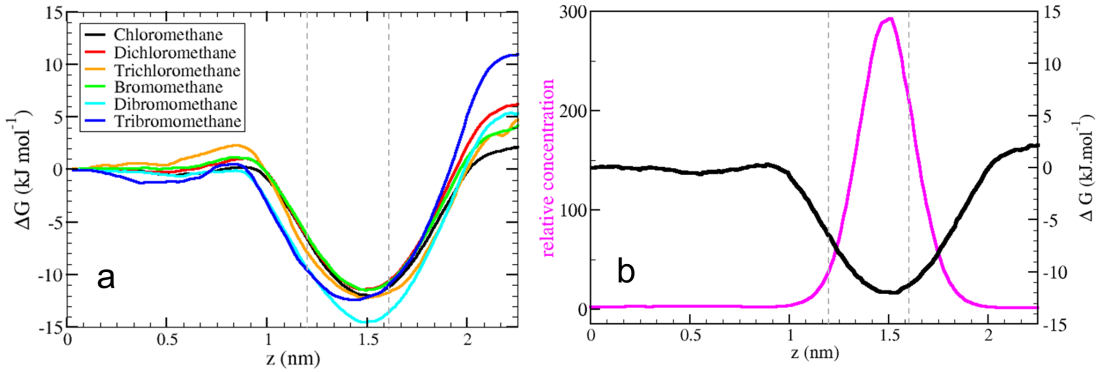

Figure 2.12: *(a) The calculated free energy profiles for a halomethane across a liquid water slab. The z-coordinate is parallel with the normal to the water/vapor interface; $z = 0$ represents the center of the water slab. (b) The corresponding concentration $c_{rel}(z)$ for chloromethane.*

Table 2.2: *Experimental Henry's law constants k_H, solvation free energies calculated from k_H, ΔG_s^H, and computed from MD simulations, ΔG_s, along with interfacial free energies, ΔG_{sl}, and relative concentrations c_{rel} at the water/vapor interface with respect to the gas phase for the set of investigated halomethanes.*

Molecule	k_H	ΔG_s^H	ΔG_s	ΔG_{sl}	c_{rel}			
	M/atm	kJ/mol	kJ/mol	kJ/mol	gas	bulk	surf_{max}	surf_{mean}
CH_3Cl	0.10	−2.2	−2	12	1	2	300	200
CH_2Cl_2	0.40	−5.6	−6	11	1	9	900	600
$CHCl_3$	0.25	−4.5	−4	12	1	6	800	500
CH_3Br	0.16	−3.4	−4	11	1	4	400	300
CH_2Br_2	1.10	−8.1	−6	15	1	26	8700	5600
$CHBr_3$	1.90	−9.5	−11	12	1	45	6500	5100

2.3 Halomethanes on the ice surface

We performed MD simulation of adsorption of halomethanes on the ice surface using a hexagonal (I_h) ice slab with the basal (0001) facet exposed to the vapor phase. We then studied the same set of halomethane molecules with an improved force field (scaled up charges). The ice sample, consisting of 1344 water molecules, was located in the middle of the simulation cell with x-, y-, and z-dimensions of 27 Å, 31 Å, and 160 Å, respectively. The thickness of the slab was ≈47 Å, corresponding to 14 ice crystal layers. Two halomethane molecules were added to the simulation cell, one to each ice surface. The system was propagated for 40 ns in a NVT simulation at $T = 235$ K to sample structural and dynamical characteristics of halomethanes adsorbed at the ice surface. The melting point of the employed water model is $T_m = 250$ K and thus, temperature of simulations was just 15 K below it.

Once halomethanes adsorb on the ice surface, they diffuse on the most outer disordered layer (quasi-liquid layer) which is formed on the crystaline ice slab. Only rare desorptions of admolecules from the ice/vapor surface were observed in the course of 40 ns long simulations. The typical configurations and the corresponding density profiles are shown in Fig. 2.13.

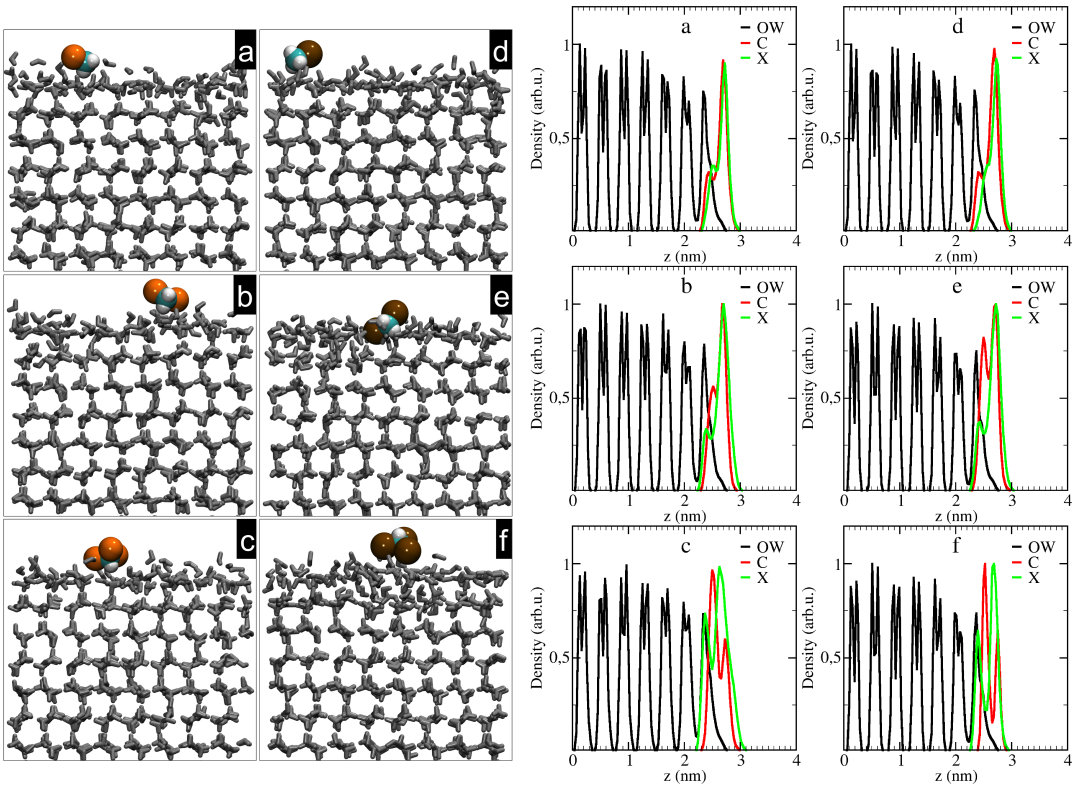

Figure 2.13: *Left: Snapshots of halomethanes on the ice surface. Right: Corresponding density profiles for (a, d) CH_3X, (b, e) CH_2X_2, and (c, f) CHX_3 species (X=Cl or Br).*

Orientational distributions $P(\cos\theta)$ for all halomethanes are presented in Fig 2.14. Again, θ is the angle between the interfacial normal and the molecular vector, exact definition of which varies with different halomethane species.

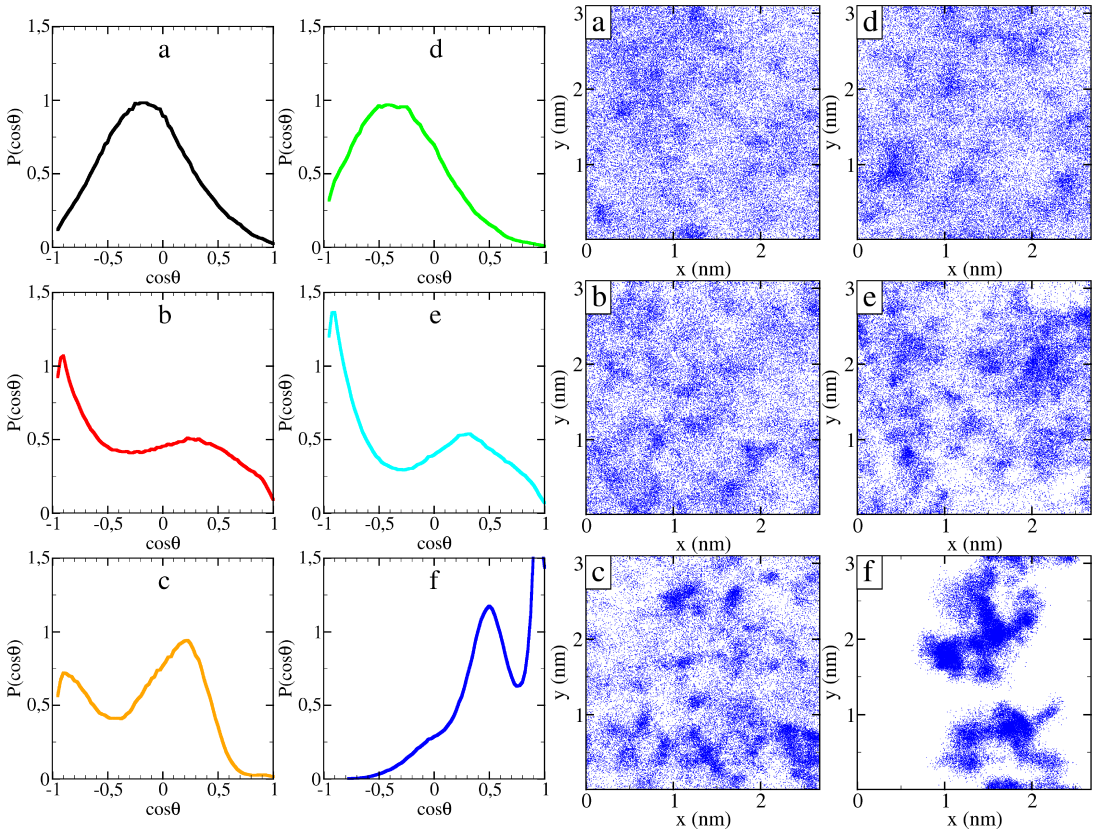

Figure 2.14: *Left: Orientation of halomethanes on the ice surface. The angle θ is defined between the interface normal (z-axis) and the molecular vector. (a,d) For the CH_3X molecules (X=Cl or Br), the molecular vector is defined as C→ X. (b, e) For the CH_2X_2 species, the molecular vector is taken as one C→H. (c, f) For the CHX_3 species, the molecular vector points from C→ H. Right: Positions (x- and y-coordinates of the C atom) on the ice surface visited by halomethanes: (a), (b), and (c) are chloro-, dichloro, and trichloromethanes, respectively; (d), (e), and (f) are bromo-, dibromo, and tribromomethanes, respectively.*

For CH_3X (X=Cl, Br) the molecular vector points from the halide atom towards the carbon, X→C. The distributions of orientations are rather broad with maxima around 101° and 113° with respect to the surface normal for CH_3Cl and CH_3Br, respectively. This finding indicates, that both halomethanes are rotationally mobile; chloromethane is preferentially adsorbed nearly parallel to the surface, while bromomethane is more tilted with bromine pointing to the vapor phase. In the case of CH_2X_2 the orientation is defined by the molecular vector X→H. For the analysis we took into account only one of the two (equivalent) hydrogen atoms. As a result of this definition, the orientational distributions obtained for both dichloro- and dibromomethane exhibit two peaks corresponding to the two possible orientations of the C-H bonds. The maximum is related to configurations where one C-H axis is directed toward the surface tilted by around 155° with respect to the surface normal and the second one is directed toward the gas phase (tilted by 72° from the surface normal).

Finally, the molecular vector for the trihalomethanes points from the carbon to the hydrogen atom C→ H. The orientational distribution of trichloromethane (Fig. 2.14 c) is characterized by a broad peak centered around $\theta = 72°$ and by

the second less intense broad peak for θ close to 180°, corresponding to the H atom pointing toward the ice surface and chlorines directed toward the vapor phase. The orientation of $CHBr_3$ (Fig. 2.14 f), exhibits a bimodal distribution with the broad peak centered also around $\theta = 72°$ and the second intense peak for θ close to 0°. This indicates a preferential orientation with the hydrogen atom pointing toward the gas phase, while the three bromine atoms are oriented to the ice surface. The orientation of the tribromomethane thus differs from that of its chlorinated analog.

In conclusion, we find the orientation for halomethanes on ice rather similar to their orientation on liquid water [69]. For CH_2Cl_2 and CH_2Br_2, some additional preferential orientations are pronounced on ice as a result of a more structured ice surface compared to the surface of a liquid.

The mobility of halomethane species on the ice surface is presented in Fig. 2.14 (right panel). The plotted distributions of the x- and y-coordinates of the C atom indicate that all halomethanes, except of tribromometanes, diffuse freely within the simulation box on the quasi liquid layer on the ice surface. The mobility of tribromomethane is clearly limited suggesting its stronger adsorption on the ice surface.

The orientational and mobility features obtained from our calculations indicate that, depending on the particular halomethane, some halogen atoms may be strongly bound to the surface layer while other atoms may point more freely toward the gas phase. To quantify this results we calculated the averaged interaction (short-range Lennard-Jones and Coulomb terms) energy between the halomethane species and water. The results summarized in Tab. 2.3 show that the interaction energy increases with the number of halogen atoms and, in particular, multi-substituted bromomethanes are bound to water more than chloromethanes. The present comparison agrees with the experimental results [70].

The differences in the nature of the adsorption may be important regarding the photodissociation of these species at the ice surface and the ability of the halogen atoms to be released in the gas phase or trapped at the surface.

Table 2.3: *Averaged interaction energies between halomethanes and ice with standard deviations (SD)*

Molecule	interaction energy (SD) kJ/mol
CH_3Cl	−22 (6)
CH_2Cl_2	−30 (8)
$CHCl_3$	−36 (8)
CH_3Br	−22 (8)
CH_2Br_2	−40 (12)
$CHBr_3$	−70 (15)

3. Palmitic acid monolayer

MD simulations of fatty acid monolayers at water surface are not numerous. There is a previous work investigating the effect of methylation of a arachidic acid (C20) monolayer on molecule packing using the united-atom force field (GROMOS) [71]. Another study focused on the collapse of the same monolayer described by the all-atom force field (CHARMM) [18]. The first simulation of a PA monolayer studying incorporation of a lung surfactant protein used the united-atom force field (Lipid) [23]. Only recently, the all-atom force field (Lipid 11) was used to study effects of surface pressure on properties of a PA monolayer [24]. The results of MD simulations can differ significantly depending on the force field used, therefore benchmarking of the model is very important. An investigation of structural properties of the PA monolayer under compression similar to that created in the experimental Langmuir trough setup started in our group several years ago using all-atom OPLS force field with calculated partial charges (RESP) and was performed at biologically relevant temperature of 37°C (310 K) [29]. I resumed that work evaluating the performance of additional force fields to compare calculated structural properties of the PA monolayer with experimental data at room temperature of 20°C (293 K). In our study, the PA molecules are assumed to be neutral since SFG spectra measurements have shown that the PA head groups at $pH = 6$ are mostly protonated [72].

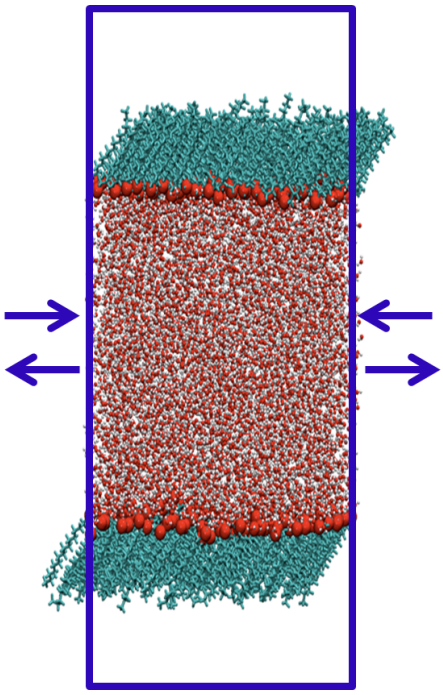

Table 3.1: *Box dimensions and the corresponding surface area, A_M, pertinet to the simulations.*

x	y [nm]	z	A_M [nm^2]
4.7	4.7	30	0.19
4.8	4.8	30	0.20
5.0	5.0	30	0.22
5.2	5.2	30	0.23
5.4	5.4	25	0.25
5.6	5.6	25	0.27
5.8	5.8	25	0.29
6.0	6.0	25	0.31
6.2	6.2	25	0.33
6.4	6.4	25	0.35

Figure 3.1: *Simulated system consisting of a water slab in the center of the box and PA molecules forming a monolayer (cyan) on each of two water surfaces. Initial simulation box with x-, y-, and z-dimension of 5.4 nm, 5.4 nm, and 25 nm, was laterally compressed or expanded to generate systems with different PA monolayer densities.*

MD systems, initial conditions, and simulation runs. The simulated systems consisted of 232 palmitic acid molecules and 6770 water molecules

forming a slab of a liquid in the central part of the simulation box with two water interfaces each of them covered by 116 PA molecules forming a monolayer perpendicular to the z axis. The initial x, y and z-dimensions of the prismatic simulation box were set to 5.4, 5.4 and 25 nm, to achieve the initial surface area per molecule A_M of 0.25 nm^2. In order to achieve different surface densities, the initial simulation box was laterally compressed/expanded in 1 Å steps and multiple systems were generated. The setup of the system can be seen in Fig. 3. In Tab. 3.1 actual simulation box dimensions and area per one PA molecule are listed. We run NVT simulations at $T = 293$ K. The starting configuration for each simulation was equilibrated for 10 ns, followed by a 90 ns production run.

3.1 Force field testing

To reproduce experimental properties of the PA monolayer at water/vapor interface, we employed the SPC/E water model and three different force fields for palmitic acid. For the PA molecule we proposed all-atom force fields composed of the OPLS Lennard-Jones interaction parameters and different partial atomic charges (Tab. 3.2). The force field A adopted the partial atomic charges used for long-chain alcohols [73], the force field B employed ab-initio calculated atomic charges (RESP), and the force field C used the atomic charges from phospholipid chains [74].

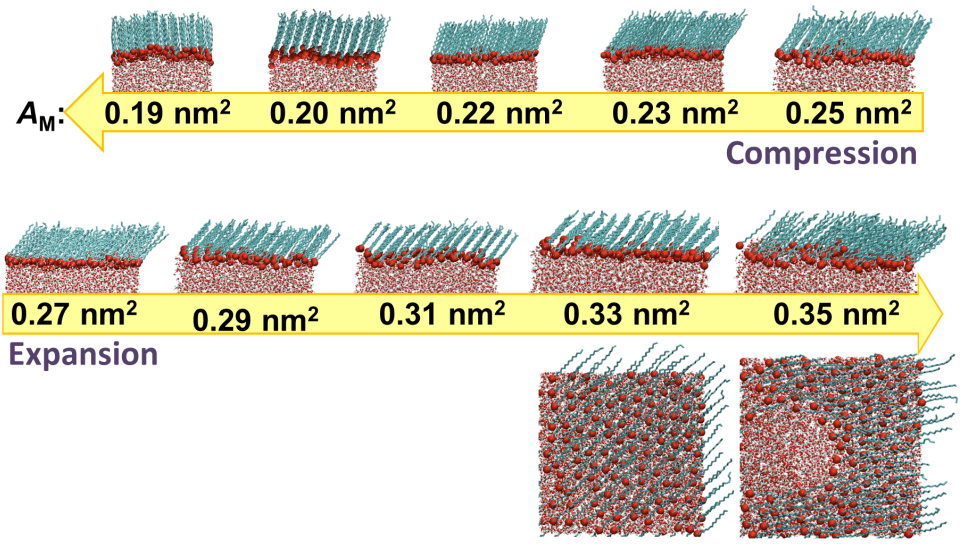

Figure 3.2: *Side views on the final PA monolayer states for several box sizes with the corresponding A_M. Top views along the z-axis for the two largest box sizes show a pore within the PA monolayer. The alkyl chain is rendered in cyan and COOH groups are depicted as red beads.*

The final configurations of the system are shown in Fig. 3.2. In the most compressed state, palmitic acid molecules are packed tightly and their alkyl chains are almost vertical. The water/monolayer interface is rippled, indicating a system near the collaps limit. When the surface area per PA molecule is increased, the

Table 3.2: *Tested force fields for the PA molecule: Lennard-Jones (L-J) parameters combined with different partial atomic charges. LA stands for long-chain alcohol, while PL means phospholipid. RESP* charges were modified to ensure electroneutrality of the COOH group.*

	A	B	C
L-J	OPLS	OPLS	OPLS
charges (chain)	LA	RESP	PL
charges (COOH)	OPLS	RESP	RESP*
-CH_3:C	−0.18	−0.05	−0.48
H	0.06	0.01	0.16
-CH_2:C	−0.12	−0.03 to 0.02	−0.24
H	0.06	−0.10—0.04	0.12
-COOH:C	0.52	0.73	0.75
O1	−0.44	−0.59	−0.57
O2	−0.53	−0.67	−0.65
H	0.45	0.46	0.47

water interface flattens, PA molecules chains tilt increases, and the thickness of the monolayers decreases. At the packing of $A_M = 0.35\ nm^2$, the water surface is no more completely covered by PA molecules and pores within the monolayers are created.

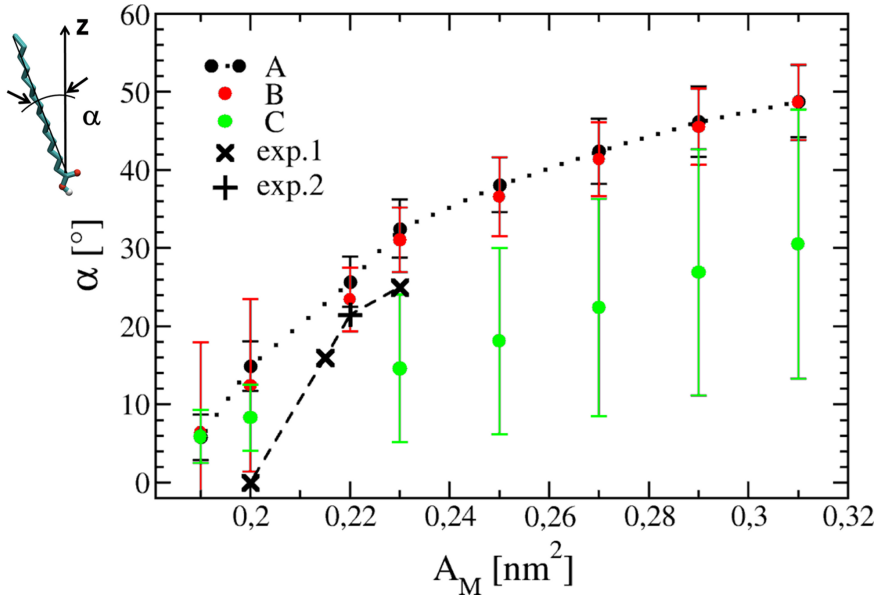

Figure 3.3: *Average chain tilt angle with respect to the surface normal as a function of A_M. Experimental values (x) from [30], and (+) from [31].*

We computed the chain tilt angle α, which is the angle between the molecular vector C1 → C16 and the normal to the water interface (z-axis). Results of the mean tilt angle (averaged over the trajectory and all molecules) as the function of A_M are plotted in Fig. 3.3. We took advantage of experimental values of the α

angle obtained for several surface pressure by [30, 31] and plotted them against the respective A_M using the experimental π-A isotherm [32] for comparison. The α values for both force fields A and B are close to each other and follow a similar trend as experimental values, while the force field C is hard to evaluate due to large error bars.

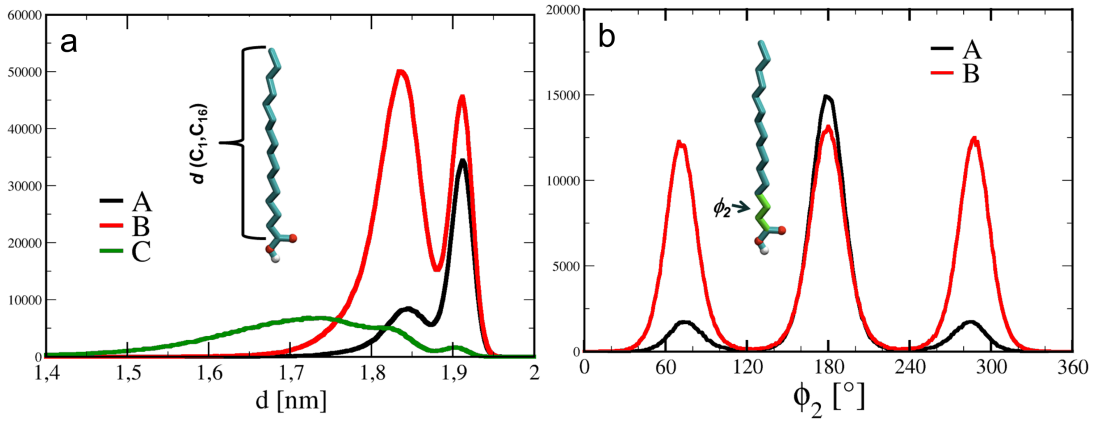

Figure 3.4: *a) Chain length distribution and b) C1-C2-C3-C4 dihedral angle distribution for* $A_M = 0.23\ nm^2$.

The calculated chain length distribution, where the chain length is the distance between the C1 and C16 atoms, has a bimodal character for all surface densities examined for the force field A and B (Fig. 3.4a). In contrast, force field C yields a disordered monolayer with a very broad chain length distribution, which fails to describe structural properties of the PA monolayer.

According to the preceding work [29] we attributed the phenomenon of the bimodal chain length distribution to the C1-C2-C3-C4 dihedral angle distribution (Fig. 3.4b). For the force field B we see almost equally pronounced trans (dihedral angle of 180°) and gauche conformations (dihedral angle of 60° or 300°). Experimental results derived from the sum-frequency generation spectra show presence of two conformations, however, the gauche population is negligible [72]. The force field A produced with a strong preference the trans conformation of the head groups. Therefore, we conclude that the force field A is more suitable for modeling of the PA monolayer and will be used for the next investigation of the structure and dynamics of PA monolayer at water/vapor interface.

3.2 Structural parameters

We have seen on Fig. 3.2 that with decreasing surface area the chain tilt decreases, and as a consequence, the thickness of the monolayers increases. To evaluate the PA monolayer thickness we calculated density profiles along the z-axis for several surfactant packing. The density profiles of water, the headgroup C1 atom and tail groups are shown in Fig 3.5. The Gibbs dividing surfaces are used to set $z = 0$. The density profiles associated with carbon chains are affected by changes of the surface area A_M and we extracted the thickness of the PA film as the full width of half maximum (FWHM) of both C1 atom and the tail groups. Obtained data are plotted in Fig. 3.5 and fitted by a function $f(x) = \frac{1}{2.4x}$. We

have found a good agreement with both an experimental measurement [31] and a recent MD study [24].

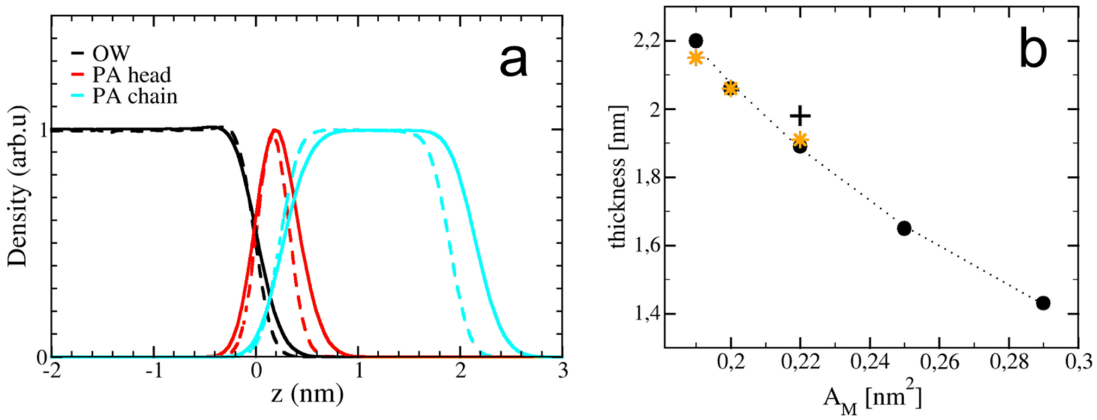

Figure 3.5: *(a) Density profiles along the z-axis for $A_M = 0.19$ nm^2 (solid line) and for $A_M = 0.22$ nm^2 (dashed line). The Gibbs dividing surfaces are used to set $z = 0$. (b) Thickness of the PA film calculated as the FWHM of both the C1 atom and the tail groups. For comparison (+) experimental [31] and (*) modeled values from [24] are plotted.*

To characterize the spatial ordering of the PA monolayer we calculated the RDF for C1–C1 headgroup atoms. Resulting C1–C1 distance distributions are plotted in Fig. 3.6b. The position of the first maximum for the most compressed state roughly defines the spacing d of the untilted hexagonal lattice structure (Fig. 3.6a) corresponding to the "molecular print" area. The extracted value of $d = 0.43$ nm is close to the size of the hexagonal unit cell ($d = 0.46$ nm) predicted by [24] using a different PA model. The hexagonal ordering of PA head groups disappears for increasing surface areas.

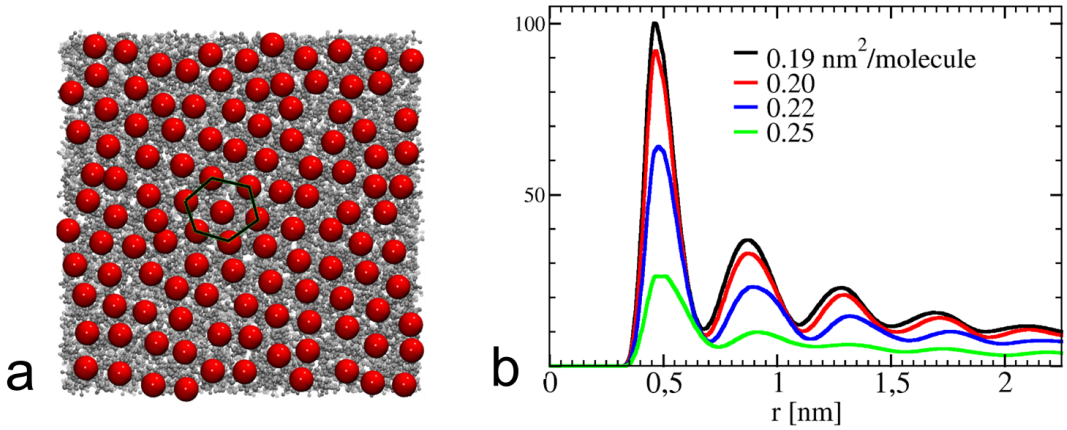

Figure 3.6: *(a) Top view of C1 atoms final positions (red beads) in the most compressed state ($A_M = 0.19$ nm^2) showing the hexagonal lattice structure. (b) RDFs of C1-C1 head group atoms calculated for different surface areas A_M.*

To complete the structural characterization of the PA monolayer we calculated order parameters S_z of the PA alkyl chains. The results for different A_M are plotted in Fig 3.7. With increasing compression, the order parameters increase, indicating untilted and more ordered alkyl chains. The midddle part of the order parameter curves exhibits a plateau indicating trans configuration of carbon

atoms. The lower order parameters in the head and tail group moieties are due to a higher orientational mobility of these parts of the PA molecule.

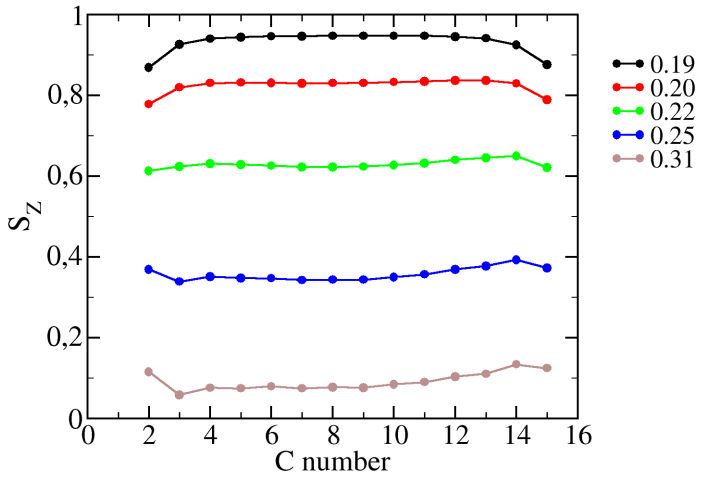

Figure 3.7: *Order parameters for the PA chain as a function of the surface area* A_M *[*nm^2*]*

3.3 Hydration

As a next step, we were interested, how the head group hydration of the PA molecule is affected by a monolayer compression. To see a detailed water structure in a vicinity of the PA head group, we calculated the RDF and the SDF of water oxygen atom OW around headgroup atoms (C1, O1=, O2, and H1). Results are shown in Fig. 3.8. Under compression, we noticed a decrease in the intensity of the O1–OW curve corresponding to a partial dehydration of the O1 atom. The spatial distribution is plotted for the isodensity value of water oxygen being 1.5 times higher than its density in bulk water. We can conclude that for all surface densities, two main binding motifs HW$\cdots$O1=C1 and OW$\cdots$H1 – O2 are conserved.

The palmitic acid monolayer is assumed to affect interfacial dynamics of the water molecules, which may influence freezing of the aerosol particles. Unfortunatelly, this analysis and also the planned calculation of the π-A isotherm, which would be the ultimate benchmarking of the model against the experiment, has not been completed, yet.

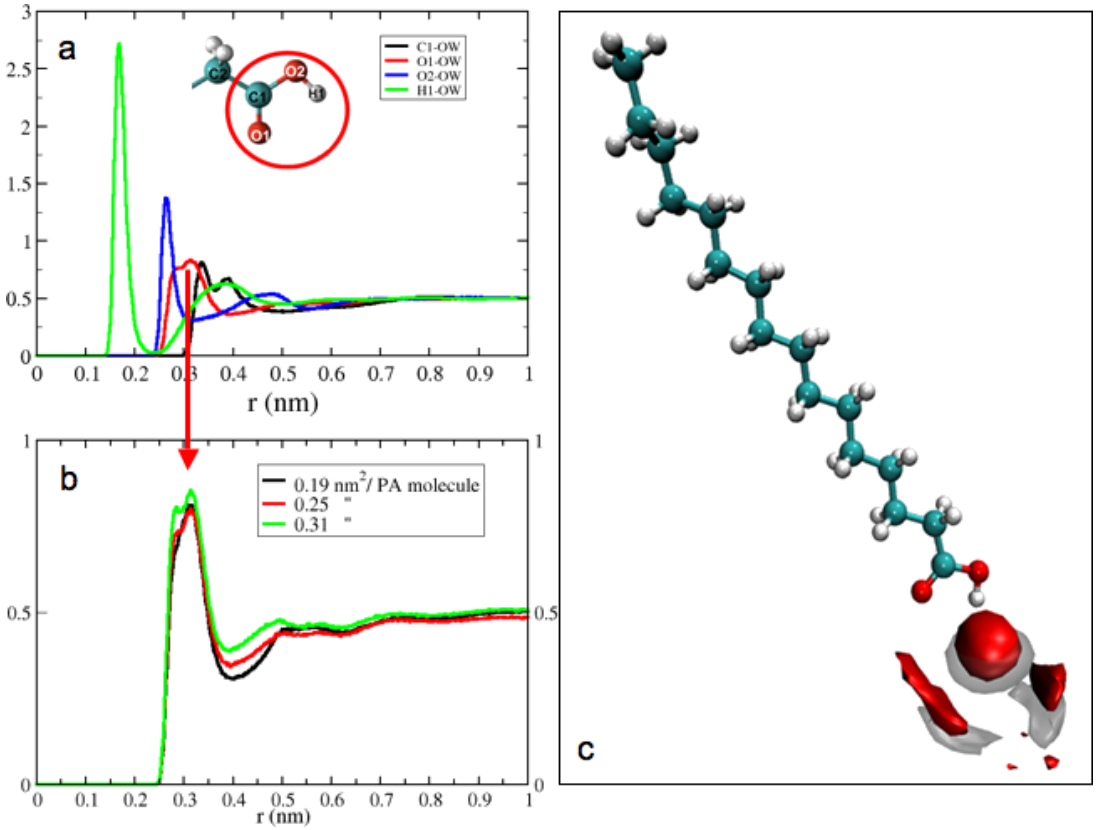

Figure 3.8: *(a) RDFs of water oxygen OW around the COOH head group atoms for* $A_M = 0.25\ nm^2$. *(b) A detail of the RDF of water oxygen OW around atom O1= for various* A_M. *(c) SDFs of water oxygen (in red) and hydrogen (in grey) around the COOH head group atoms calculated for* $A_M = 0.25\ nm^2$.

4. Interactions of the palmitic acid monolayer with haloalkanes

In previous chapters we explored the behaviour of haloalkanes on the neat water surface and structural properties of the palmitic acid film coating on the water surface. We ensured that the models provide a reliable description of a single component behavior. Finally, we put these components together to create systems closer to naturally occurring surfaces to address the following questions, such as: Does the monolayer prevent uptake of haloalcanes into water? Do haloalkanes adsorb at the monolayer/vapor interface or at the water/monolayer interface? Are haloalkanes incorporated into the monolayer?

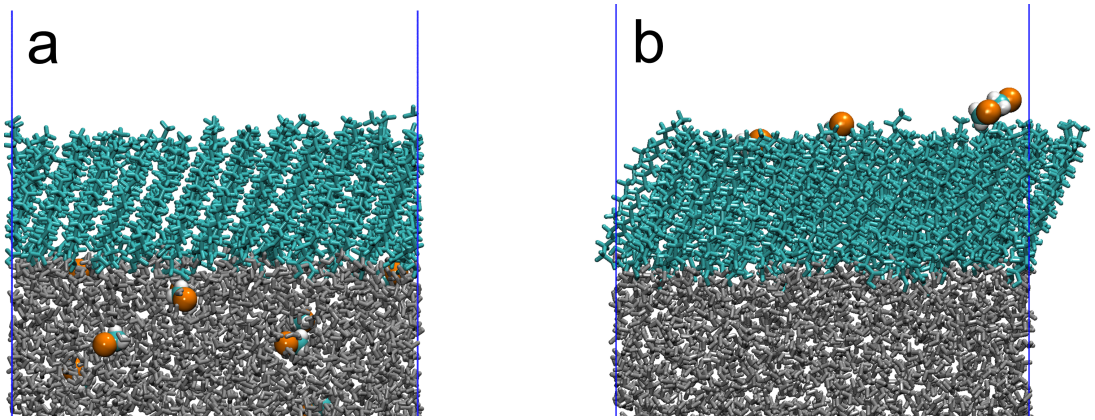

Figure 4.1: *Illustrations of systems consisted of the PA monolayer with (a) 20 solvated chloromethanes or (b) with 20 chloromethanes dispearsed in the vapor. Color coding: chlorine in orange, carbon in cyan, hydrogen in white, PA in cyan, and water in gray.*

4.1 Palmitic acid monolayer and short-chain haloalkanes

To study the mass transfer across the water/monolayer/vapor interface we consider two situations: chloromethanes solvated in bulk water and/or dispearsed in the vapor phase.

MD systems, initial conditions, and simulation runs. The simulated PA monolayer system described in the previous chapter was modified by 20 chloromethanes solvated in the central water slab or by 20 chloromethane molecules placed in the vapor phase (10 molecules were added to the proximity of each monolayer). The setup of the systems can be seen in Fig. 4.1. The rectangular box had x, y, and z-dimensions of 5.4, 5.4 and 25 nm, yielding $A_M = 0.25$ nm^2 in all cases. We run NVT simulation at $T = 293$ K. The starting configuration was always equilibrated for 10 ns, followed by a 40 ns production run.

The direct observations of trajectories reveal that chloromethanes initially fully solvated inside the water slab covered by the palmitic acid film slightly prefer the water/ monolayer interface. Nevertheless, neither incorporation of

chloromethanes into the monolayer, nor an evaporation event during the simulation were observed. For the other initial condition, the gas phase chloromethanes interacted weakly with the PA monolayer. The adsorbed chloromethanes diffused on the outer monolayer surface and underwent many desorption/absorption events. Due to the periodic boundary conditions, the desorbed molecule often left the simulation box and reentered it from the opposite side impinging to the other monolayer surface. But again, no incorporation into the PA monolayer occurred.

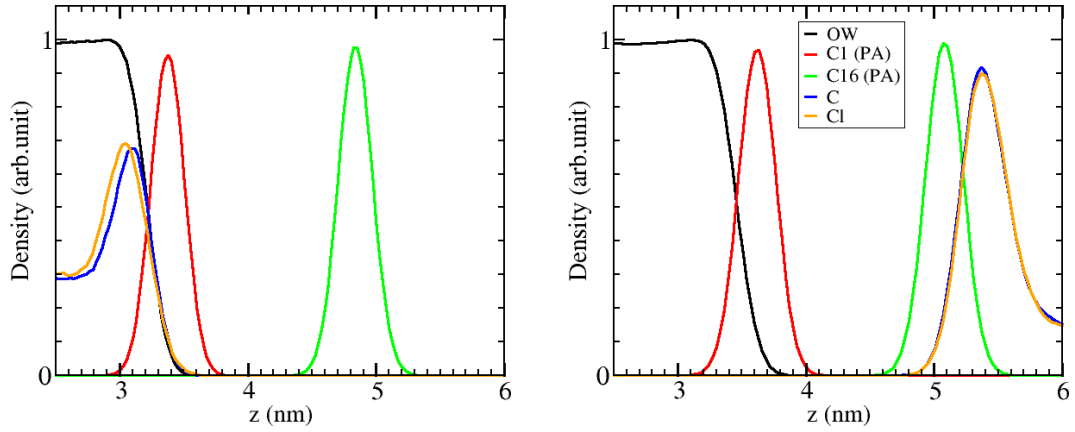

Figure 4.2: *Density profiles of the PA monolayer with 20 solvated chloromethanes (left) or 20 chloromethanes dispearsed in the vapor (right).*

The density profiles averaged over the last 40 ns of the trajectory are shown in Fig. 4.2. In each plot, the black curve corresponds to the density of water. The PA monolayer region is denoted by the density maxima of the C1 headgroup atom (in red) and the C16 tail group carbon (in green). Densities of chlorine (in orange), or carbon (in blue) atoms of solvated chloromethanes increase from their constant values in the bulk (left panel) to their maxima on the water/monolayer interface and then sharply decrease to zero in the PA monolayer region with negligible probability to enter gas phase. Focusing on the chlorine and carbon densities in the vicinity of the palmitic acid head group we can conclude that chloromethanes are preferentially oriented with chlorines pointing to the bulk. On the other hand, densities obtained for initially gas phase chloromethanes increase from their constant value in vapor to the maxima on the monolayer/vapor interface and then again decrease to zero in the PA monolayer region.

These results confirmed that the palmitic acid monolayer on the water/vapor interface at a medium surface packing ($A_M = 0.25$ nm^2) effectively prevents mass transfer of chloromethanes across the water/vapor interface, at least at the timescale of the simulations. To quantify the energy barrier caused by the PA monolayer, we calculated the free energy profile for a chloromethane molecule moving across the water/monolayer/vapor interface. (Fig. 4.3). The free energy profile calculated for the medium packing, has two shallow minima on both the water/monolayer (-2 kJ/mol with respect to water) and the monolayer/vapour (-5 kJ/mol with respect to vapor) interfaces. The free energy maximum inside the monolayer results in an energy barrier of $\approx$17 kJ/mol for a chloromethane entering the PA monolayer from either of the two interfaces. Moreover, the PA monolayer at a more compressed state of $A_M = 0.23$ nm^2 prevents the halo-

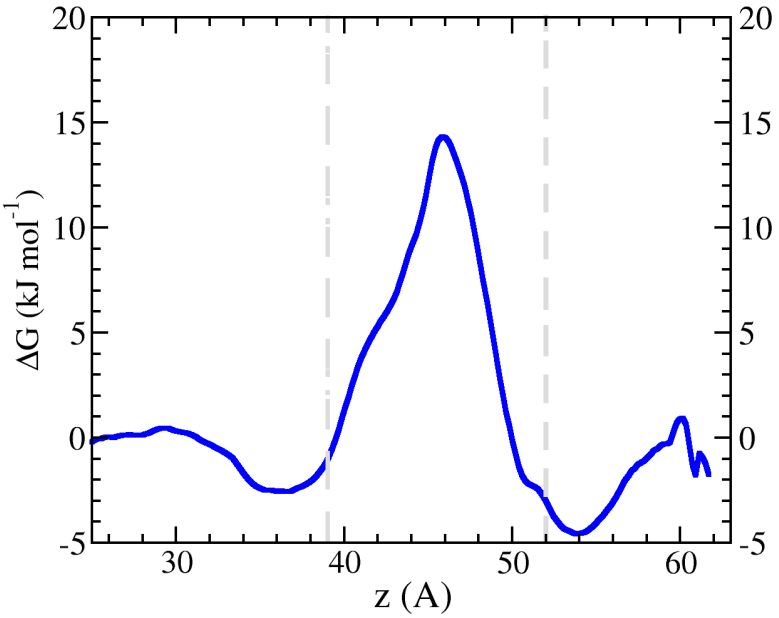

Figure 4.3: *Free energy profile for a chloromethane across the water/PA monolayer/vapor interface. The z-axis lies in the directon normal to the interface, $z = 0$ corresponds to the center of the water slab. ΔG is set to zero in the aqueous bulk. The vertical grey lines denote the monolayer region.*

methane transport across the water/vapor interface by twice that value (35 kJ/-mol). The error of the free energy calculation was about ±1 kJ/mol.

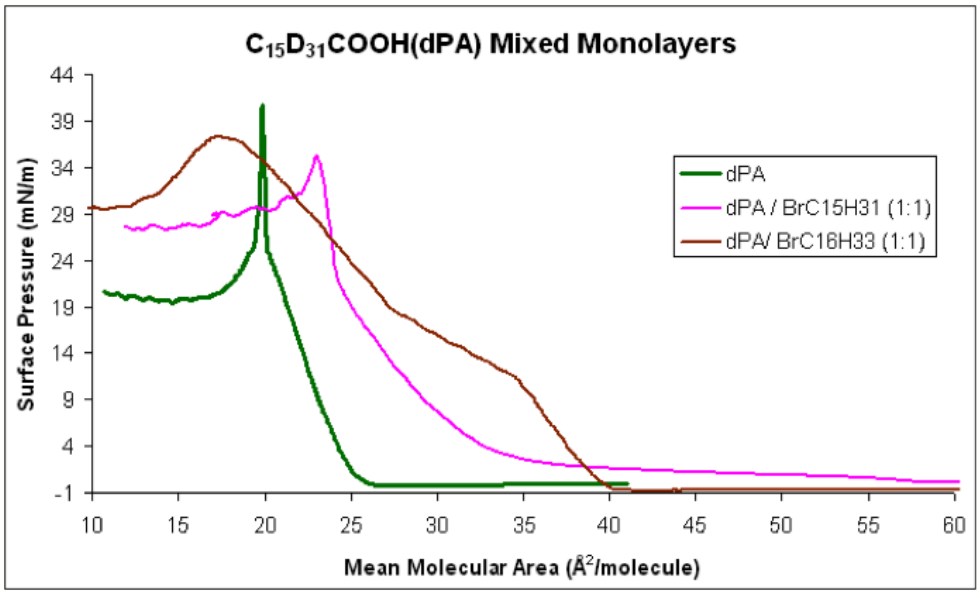

Figure 4.4: *Experimental π-A isotherms of deuterated d31-palmitic acid (dPA) and mixed monolayers with bromopentadecanes (BrC15) and bromohexadecanes (BrC16). A_M of mixed monolayers are with respect to the number of PA molecules. Data courtesy of R. Sierra-Hernandez.*

4.2 Palmitic acid monolayer and long-chain haloalkanes

The incorporation of long-chain haloalkanes into the PA monolayer was experimentally investigated by our collaborators [32]. The experimental palmitic acid π-A isotherm changes its shape and shifts to larger areas if haloalkanes are incorporated in the PA monolayer. The main experimental result is that a bromine atom and a chain length of at least 15 carbons are necessary for the alkane incorporation into a fatty acid monolayer (Fig. 4.4). However, when a lateral pressure is applied on the mixed monolayer, haloalkane molecules are squeezed out and form aggregates on the top of the monolayer.

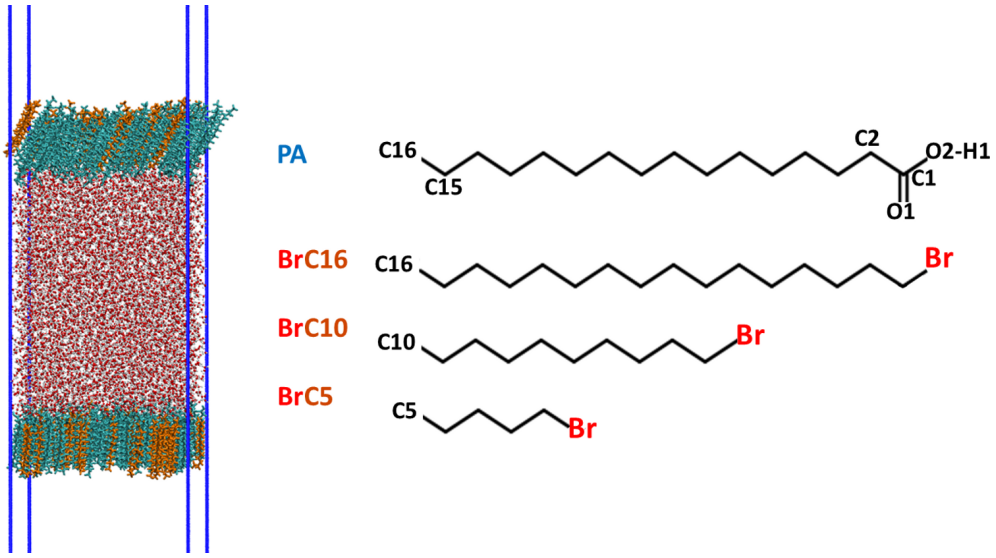

Figure 4.5: *Mixed monolayer system on the water subphase consisting of palmitic acids (PA) rendered in cyan and bromohexadecanes (BrC16), bromodecanes (BrC10), or bromopentanes (BrC5) depicted in orange.*

MD systems, initial conditions, and simulations. We mimic the experimental conditions using the above described system consisting of 6770 water molecules in the central slab geometry and 232 surfactant molecules forming a Langmuir monolayer (e.i., 116 molecules at each water-vapor interface). A snapshot of the system is presented in Fig. 4.5. The Langmuir monolayer was a 2-component mixture of palmitic acids and either 1-bromopentane BrC_5H_{11} (BrC5), 1-bromodecane $BrC_{10}H_{21}$ (BrC10), or 1-bromohexadecane $BrC_{16}H_{31}$ (BrC16) molecules. These mixed surfactant films were created from the equilibrated pure PA monolayer by a random replacement of one quarter, one half or three quarters of PA molecules by the 1-bromoalkane or hexadecane component yielding ratios of PA to the desired component of 3:1, 1:1, or 1:3 (Fig. 4.6). In all cases, bromoalkanes were initially oriented with bromine atoms pointing to the water phase.

The initial box had x-, y-, and z-dimension of 5.4 nm, 5.4 nm, and 25 nm and we refer to this box size as the medium state. By aplying a semiisotropic lateral pressure in the x- and y- dimension a)s we either reduced these dimensions stepwise to 4.8 nm (the compressed state), or these dimensions were extended stepwise to 6.0 nm (the relaxed state), resulting in various PA packings (Tab.

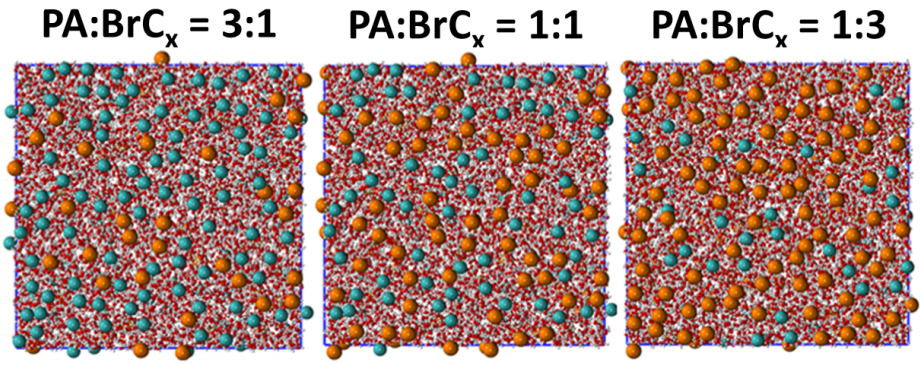

Figure 4.6: *Initial distribution of PA molecules (cyan beads) and admixed bromoalkanes (orange beads) BrC_x, $x = 5, 10, 16$.*

4.1). The thickness of the liquid water slab, depending on the compression state, varied between 6 nm for the relaxed state and 9 nm for the compressed state. The system was propagated for 100 ns at $T = 293$ K. The last 10 ns of the trajectory were used for the analysis.

Structure and dynamics of mixed monolayers

Our results showing the final snapshots of the medium states for different compositions and component ratios are presented in Fig. 4.9. The left panels illustrate the BrC5 separation from the PA monolayer for all studied ratios. This partitioning takes place in the course of a few ns. The final structures of the PA/BrC10 monolayer reveal flips of this admixture molecules, initially placed with bromine pointing to the water. In the equally mixed monolayer (1:1) about 10% of BrC10 changed their orientation in the course of 100 ns. For the prevalent BrC10 content (PA/BrC10 ratio of 1:3) both components are separated and PA molecules form small ordered islets. On the other hand, PA/BrC16 mixed monolayers are stable in all presented ratios. Our systems had the surface packing equal or larger than the "lift-off" point of the experimental dPA/BrC16 isotherm ($A_M = 0.40$ nm^2). It seems that interactions between hydrocarbon chains are slightly overestimated in our simulations as indicated by a stable structure of the control PA/hexadecane mixed monolayer, which failed to reproduce the experimental finding that the bromine atom is important for incorporation of long-chain

Table 4.1: *Mean surface area per PA molecule, A_M in nm^2, depending on the box sizes and the component ratios*

box x=y	PA:BrC$_x$			
nm	1:0	3:1	1:1	3:1
4.8	0.20	-	0.40	-
5.4	0.25	0.34	0.50	1.0
6.0	0.31	-	0.62	-

alkane into the PA monolayer. The time scale of 100 ns may be also too short to observe the separation of the two components and the atractive chain-chain interaction is too dominant compared to the bromine-water interaction. For this reason we conclude that further simulations of the PA monolayer/water interface and force field refinements are still needed. Next, we will focus only on the monolayers in a component ratio of 1:1.

The density profiles (Fig. 4.7) show positions of bromine atoms (in red) and the last carbons in the bromoalkane chains (in orange) with respect to water (black) and the ordered PA monolayer denoted by the C1 and C16 carbons (in dark and light blue). The results are drawn for the medium state (A_M = 0.50 nm^2). BrC16 molecules stay ordered within the PA monolayer as indicated by the narrow density profiles of both bromine and the last carbon (C16). The BrC10 profiles reveal that BrC10 molecules move further from the water interface, but stay ordered inside the monolayer. Moreover, the population of BrC10 with the inverted orientation is rather pronounced. In contrast, the density profiles of BrC5 are broad indicating no particular structure in separated patches.

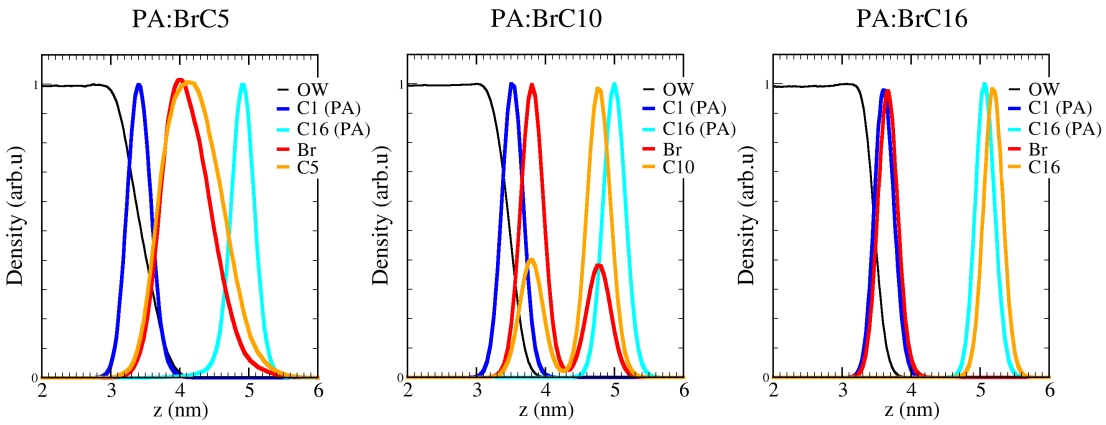

Figure 4.7: *Density profiles for the investigated mixed monolayers ($A_M = 0.50\ nm^2$).*

To evaluate the conformational order of PA in mixed monolayers, we calculated order parameters S_z for each carbon in the PA chain. Our results are plotted in Fig. 4.8. The flat central parts of the order parameter curves indicate all-trans conformation of the carbon chains. The head group and the tail carbons are more rotationally mobile and, consequently, their Sz is lower. We observe that while BrC16 doesn't affect the PA conformation, BrC10 and BrC5 increase PA order parameters. This is a consequence of the admixture separation. Upon spatial restriction given by separated bromoalkanes, PA molecules adopt less tilted all-trans conformations.

The last snapshots of the compressed and relaxed states are shown on Fig. 4.10. In the compressed state (A_M = 0.40 nm^2) immediate partitioning of BrC5 took place. Several BrC5 and BrC10 molecules were expelled from the monolayer, while the PA/BrC16 monolayer stays intact. In contrast to the mixed PA/BrC16 monolayer, neither PA/BrC5 nor PA/BrC10 monolayers in the relaxed state with A_M = 0.62 nm^2 are able to cover the whole water surface; the monolayer breaks and water pores are created.

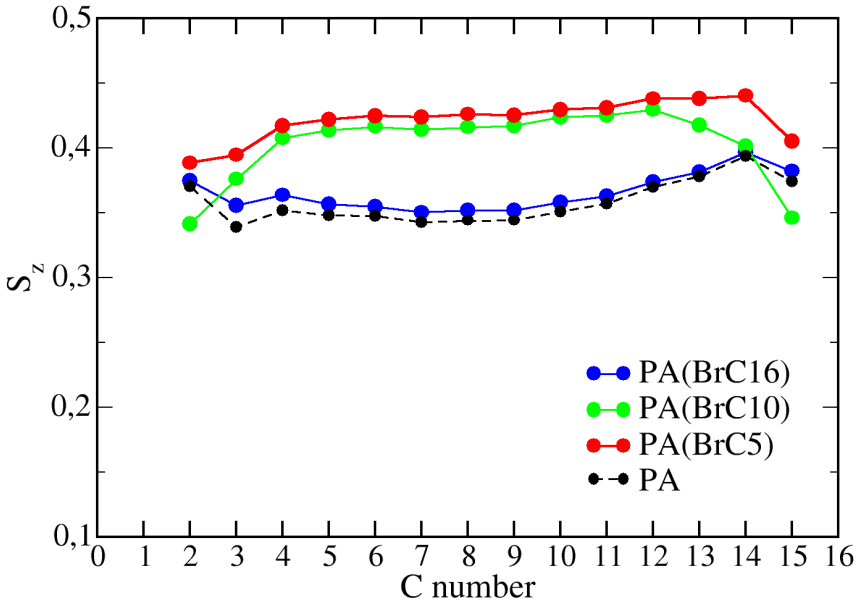

Figure 4.8: *Order parameters of the PA alkyl chain in the investigated mixed LMs ($A_M = 0.50\ nm^2$).*

The shape of the experimental dPA/BrC16 isotherm exhibits additional kinks in its slope. The first one appears at the surface pressure of 10 mN/m, the next one at 16 mN/m. These phenomena are attributed to the squeezing out of BrC16 molecules from the dPA monolayer. The final collapse pressure of 37 mN/m is similar to that of the pure dPA. To verify that, under compression, the bromoalkanes are expelled from the mixed monolayer prior the final collapse, we applied semi-isotropic pressure to the mixed monolayers. An expulsion of BrC10 was observed at the pressure of 100 atm. BrC16 molecules were squeezed out of the mixed monolayer and accumulated on the outer monolayer surface at the pressure of 350 atm (Fig. 4.11). The corresponding density profile shows an increased density of bromines in the proximity of the last carbon of PA as the BrC16 molecules are accumulated on the top of the monolayer.

Via MD simulations we have complemented the experimental data with a nano-scale resolution of the structure and the dynamics of mixed PA monolayers. We have confirmed that BrC16 is capable to create a stable mixed monolayer with palmitic acid in a wide range of composition ratios and compresion states, which is not the case for bromoalkanes with shorter hydrocarbon chains. We conclude that for an efficient incorporation into the monolayer, the haloalkane chain length plays a main role, optimally being the same size as that of palmitic acid. Our results also confirm that the Br – water interaction is weaker than the interaction of palmitic acid COOH group with water as the observed expulsion of bromoalkanes takes place prior to the collapse of the whole mixed monolayer.

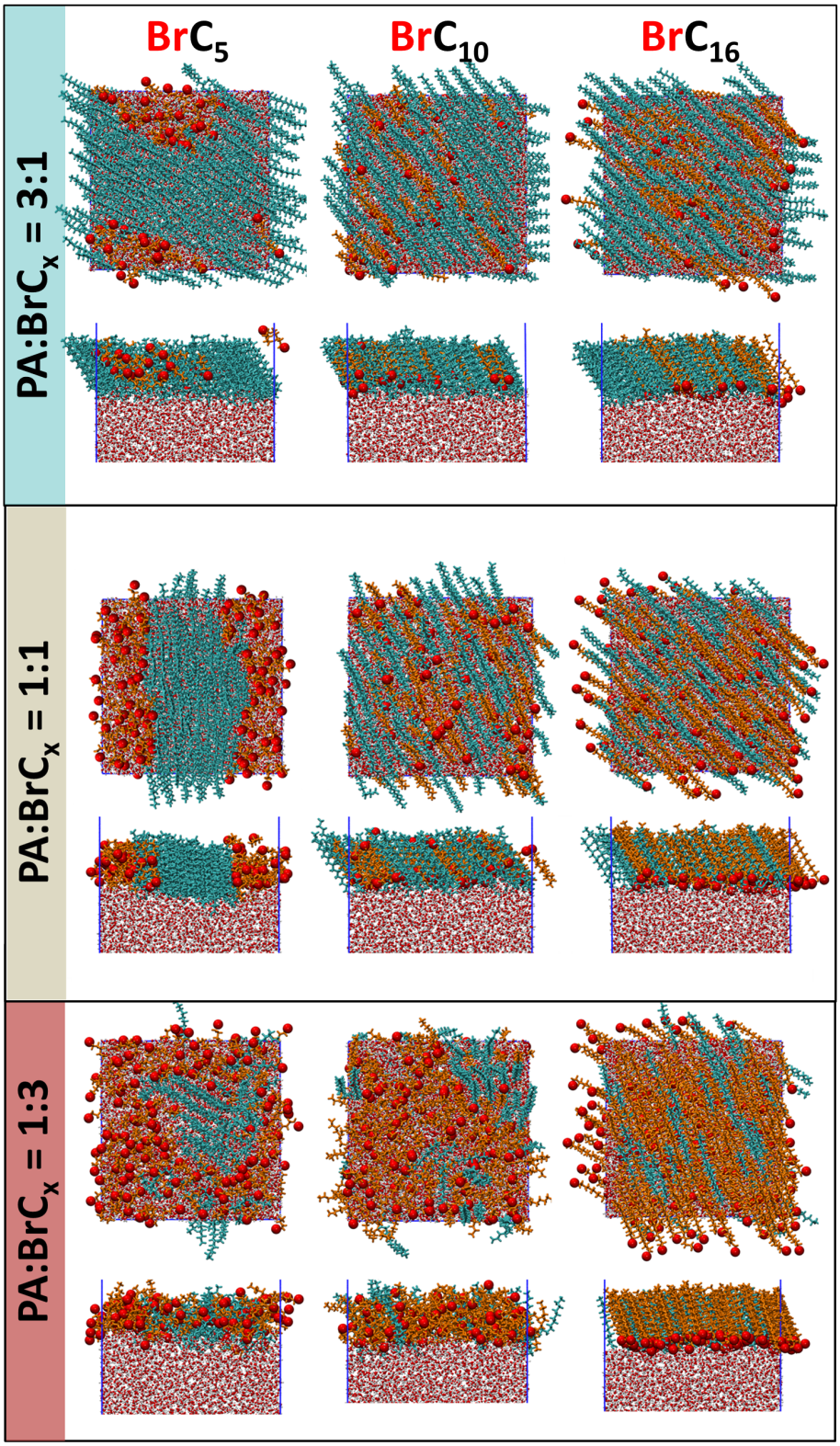

Figure 4.9: *The final snapshots (top and side views) of the mixed LMs for different component ratios and compositions. The box size x-, y-, and z-dimensions are 5.4, 5.4, and 25 nm, respectively. Color coding: PA in cyan, bromoalkane chain in orange, and bromine as a red bead.*

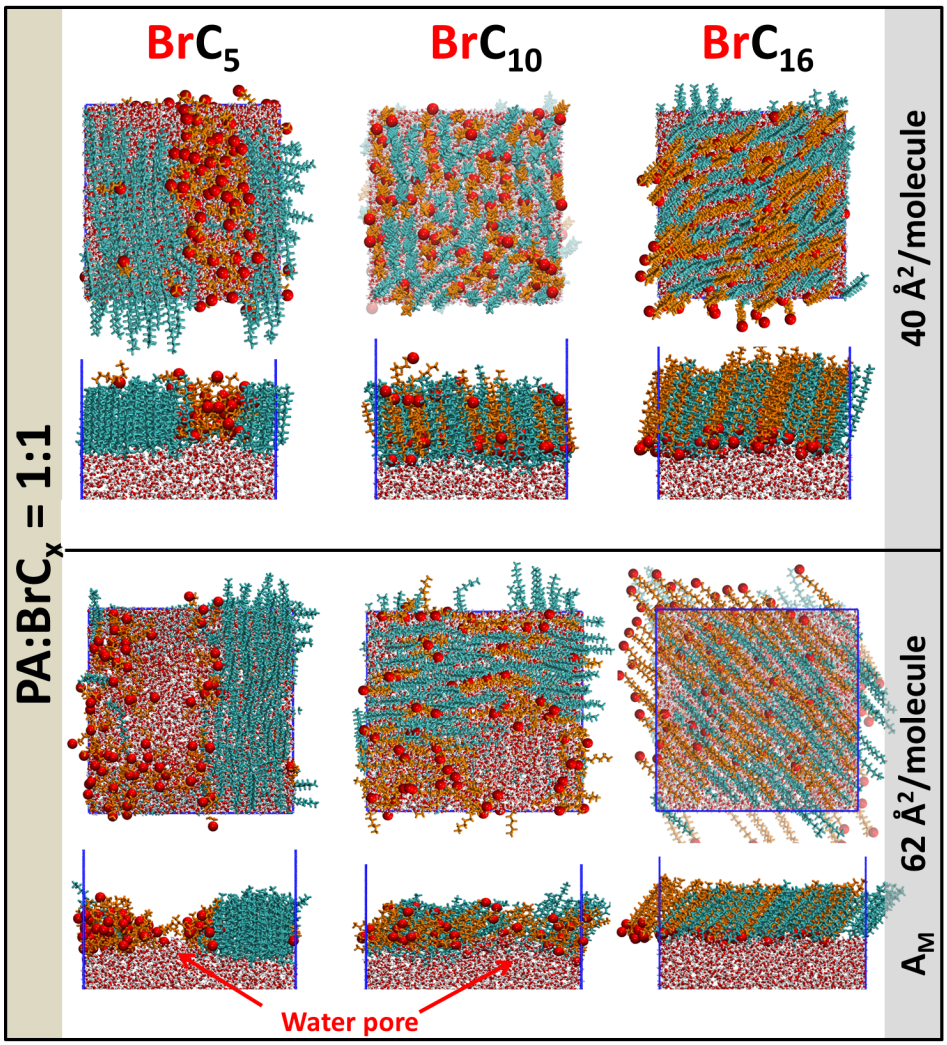

Figure 4.10: *Final snapshots of compressed and relaxed mixed LMs. Color coding: PA rendered in cyan, bromoalkane chain in orange, and bromines as red beads.*

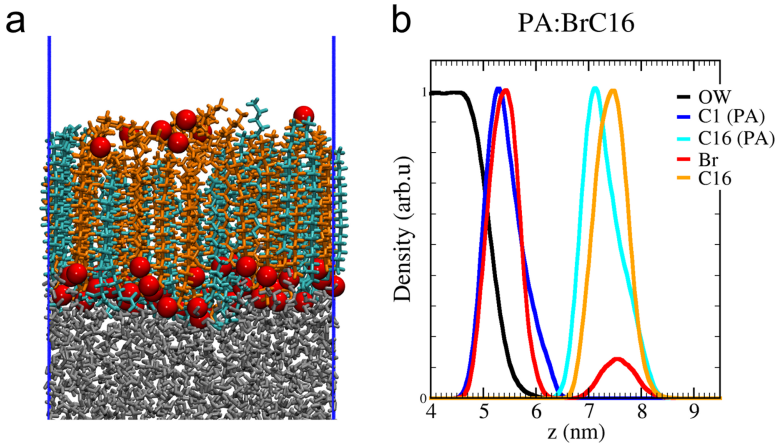

Figure 4.11: *(a) The last snapshot (100ns) of the compression of the Pa/BrC16 mixed LM by the lateral pressure of 350 atm. (b) Density profiles show accumulation of Br atoms on the top of the PA monolayer. Color coding: Water in grey, PA in cyan, bromoalkane chain in orange, bromines as red beads*

Conclusion

The principal goal of the present thesis was to show that MD simulations can provide an invaluable insight into the interfacial behavior of molecular species and contribute to the interpretation of the experimental data.

- We have shown via simulations that halocarbon molecules adsorbed on the surface of amorphous ice nanoparticles at the temperature of 100 K remain mostly isolated and do not form aggregates in spite of their mutual proximity. This is in strong contrast with their behavior on the surface of cryogenic argon nanoparticles, where they are mobile and coagulate efficiently. This can have important implications for astrochemistry and atmospheric chemistry. Our combined computational and experimental work on this topic was recently submitted for publishing. (Attached paper 1.)

- We can conclude that chloro-, bromo-, and iodoalkanes (C1-C5) interact weekly with the liquid water surface at room temperature. They tend to reside for several hundreds of ps to several ns in the outermost region of the water/vapor interface and undergo frequent desorption into the gas phase. Details of the calculated molecular orientations and the corresponding uncomplete hydration shells of the surface-adsorbed haloalkanes reveal that halogen atoms are rather desolvated and exposed to the gas phase. This hitherto unspecified molecular orientation may have important implications for heterogeneous (photo)chemical processes in the atmosphere. (Attached paper 2.)

- We quantitatively estimated enhanced interfacial concentrations of halomethanes based on free energy calculations. A minimum of the free energy that the haloalkanes exhibit at the water/vapour interface corresponds to 100 – 10000 times higher haloalkane concentrations at the aqueous surface relative to the gas phase, depending on a particular species. These enhanced concentrations in systems with a large surface area per volume, such as water droplets dispersed in air or air bubbles dispersed in water, can have consequences for atmospheric chemistry as well as for water treatment. (Attached paper 3.)

- We have shown that multi-substituted chloro- and bromomethane molecules adsorb readily on crystalline ice surfaces (at temperature 15 K below melting point of ice) and difuse freely on the outermost quasi liquid layer for several tents of nanoseconds. Their molecular orientation with respect to the ice surface is similar to the orientation that haloalkanes adopt on the liquid water surface, i.e., mostly the halide atoms point into the gas phase. Due to the ice structure an additional trapping of halide atoms in the ice lattice occurs. However, the behavior of tribromomethanes differs in terms of orientation and mobility from other studied halomethanes. $CHBr_3$ is mostly oriented with all three bromine atoms pointing to water resulting in a stronger interaction with the ice surface and a substantially lower mobility compared to other studied halomethanes. Our work on this subject is ready to be submitted (Attached paper 4.)

- We developed a new force field for PA, based on the OPLS Lennard-Jones parameters and atomic partial charges adopted from long-chain alcohols. We validated our force field against available experimental data and a recently published MD study of the PA monolayers. We conclude that our force field reproduces well overall structural properties of PA monolayer across the range of surface packing of 0.19 – 0.31 nm^2 per PA molecule and is suitable for further MD simulations. Based on the free energy calculations we conclude that PA monolayer at medium packing ($A_M = 0.25$ nm^2) effectively prevents mass transfer of chloromethanes across the water/vapor interface. We presented results of a systematic study of a pure PA monolayer and mixed monolayers of PA/1-bromoalkanes of different chain lengths (C5, C10, and C16) at the water/vapor interface. We performed a set of simulations at 293 K for several composition ratios and compression stages of the monolayer corresponding to a surface packing between 0.19 and 1.0 nm^2 per PA molecule. Our findings are in a good agreement with experimental data and have confirmed that long chain bromoalkanes (BrC16) are efficiently incorporated into the PA monolayer due to the attractive chain-chain interactions. We have also demonstrated that under compression BrC16 molecules are expelled from the mixed monolayer prior to its final collapse. Our MD simulations contribute to detailed molecular-level knowledge about the onset of processes characteristic for the experimental phase behavior of the mixed PA/bromoalkane monolayers and, in a broader context, about haloalkane partitioning in the organic-coated surfaces of aqueous aerosols. This work is prepared for publication.

Bibliography

[1] Tervahattu, H. "Identification of an organic coating on marine aerosol particles by TOF-SIMS". In: *Journal of Geophysical Research* 107.D16 (2002), p. 4319.

[2] Finlayson-Pitts, B. J. and J.Pitts., J. N. *Chemistry of the Upper and Lower Atmosphere: Theory, Experiments and Applications*. Academic Press, San Diego, USA, 2000.

[3] Ellison, G. B., Tuck, A. F., and Vaida, V. "Atmospheric processing of organic aerosols". In: *Journal of Geophysical Research* 104.D9 (1999), p. 11633.

[4] Gill, A. E. and Rasmusson, E. M. "The 1982–83 climate anomaly in the equatorial Pacific". In: *Nature* 306.5940 (1983), p. 229.

[5] Keene, W. C. et al. "Composite global emissions of reactive chlorine from anthropogenic and natural sources: Reactive Chlorine Emissions Inventory". In: *Journal of Geophysical Research* 104.D7 (1999), p. 8429.

[6] Low, J. C. "Measurements of ambient atmospheric C 2 H 5 Cl and other ethyl and methyl halides at coastal California sites and over the Pacific Ocean". In: *Journal of Geophysical Research* 108.D19 (2003), p. 4608.

[7] Greenberg, J. P., Guenther, A. B., and Turnipseed, A. "Marine organic halide and isoprene emissions near mace head, Ireland". In: *Environmental Chemistry* 2.4 (2005), p. 291.

[8] Solomon, S. "Stratospheric ozone depletion: A review of concepts and history". In: *Reviews of Geophysics* 37.3 (1999), p. 275.

[9] Langmuir, I. "The Shapes of Group Molecules Forming the Surfaces of Liquids." In: *Proceedings of the National Academy of Sciences of the United States of America* 3.4 (1917), p. 251.

[10] Ma, G. and Allen, H. C. "DPPC Langmuir monolayer at the air-water interface: probing the tail and head groups by vibrational sum frequency generation spectroscopy." In: *Langmuir : the ACS journal of surfaces and colloids* 22.12 (2006), p. 5341.

[11] VonNahmen, A. et al. "The structure of a model pulmonary surfactant as revealed by scanning force microscopy". In: *Biophysical Journal* 72.1 (1997), p. 463.

[12] Tragoulias, S. T. et al. "Surface Pressure Measurements of Human Tears and Individual Tear Film Components Indicate That Proteins Are Major Contributors to the Surface Pressure". In: *Cornea* 24.2 (2005), p. 189.

[13] Rhew, R. C., Miller, B. R., and Weiss, R. F. "Natural methyl bromide and methyl chloride emissions from coastal salt marshes." In: *Nature* 403.6767 (2000), p. 292.

[14] Keppler, F. et al. "Halocarbons produced by natural oxidation processes during degradation of organic matter." In: *Nature* 403.6767 (2000), p. 298.

[15] Bureau, H., Keppler, H., and Métrich, N. “Volcanic degassing of bromine and iodine: experimental fluid/melt partitioning data and applications to stratospheric chemistry”. In: *Earth and Planetary Science Letters* 183.1-2 (2000), p. 51.

[16] Guo, H. et al. “Source origins, modeled profiles, and apportionments of halogenated hydrocarbons in the greater Pearl River Delta region, southern China”. In: *Journal of Geophysical Research* 114.D11 (2009), p. D11302.

[17] Yagi, K. et al. “Atmospheric Methyl Bromide (CH3Br) from Agricultural Soil Fumigations.” In: *Science* 267.5206 (1995), p. 1979.

[18] Lorenz, C. D. and Travesset, A. “Atomistic simulations of langmuir monolayer collapse”. In: *Langmuir* 22.24 (2006), p. 10016.

[19] Duncan, S. L. and Larson, R. G. “Comparing experimental and simulated pressure-area isotherms for DPPC.” In: *Biophysical journal* 94.8 (2008), p. 2965.

[20] Baoukina, S., Mendez-Villuendas, E., and Tieleman, D. P. “Molecular view of phase coexistence in lipid monolayers.” In: *Journal of the American Chemical Society* 134.42 (2012), p. 17543.

[21] Khabiri, M., Roeselova, M., and Cwiklik, L. “Properties of oxidized phospholipid monolayers: An atomistic molecular dynamics study”. In: *Chemical Physics Letters* 519-520 (2012), p. 93.

[22] Höltje, M. et al. “Molecular dynamics simulations of stratum corneum lipid models: fatty acids and cholesterol”. In: *Biochimica et Biophysica Acta (BBA) - Biomembranes* 1511.1 (2001), p. 156.

[23] Lee, H., Kandasamy, S. K., and Larson, R. G. “Molecular dynamics simulations of the anchoring and tilting of the lung-surfactant peptide SP-B1-25 in palmitic acid monolayers.” In: *Biophysical journal* 89.6 (2005), p. 3807.

[24] Lin, W., Clark, A. J., and Paesani, F. “Effects of surface pressure on the properties of Langmuir monolayers and interfacial water at the air-water interface.” In: *Langmuir : the ACS journal of surfaces and colloids* 31.7 (2015), p. 2147.

[25] Tervahattu, H. “Fatty acids on continental sulfate aerosol particles”. In: *Journal of Geophysical Research* 110.D6 (2005), p. D06207.

[26] "Voss, L. F., Hadad, C. M., and Allen, H. C. “"Competition between Atmospherically Relevant Fatty Acid Monolayers at the Air/Water Interface"”. In: *J.Phys. Chem. B* 110 (2006), p. 19487.

[27] Mochida, M. et al. “Bimodal size distributions of various organic acids and fatty acids in the marine atmosphere: Influence of anthropogenic aerosols, Asian dusts, and sea spray off the coast of East Asia”. In: *Journal of Geophysical Research* 112.D15 (2007), p. D15209.

[28] Adams, E. and Allen, H. “Palmitic Acid on Salt Subphases and in Mixed Monolayers of Cerebrosides: Application to Atmospheric Aerosol Chemistry”. In: *Atmosphere* 4.4 (2013), p. 315.

[29] Sláčík, S. *Structural characterization of the interface between a fatty acid Langmuir monolayer and water using molecular simulations.* Bachelor thesis. Charles University in Prague, 2011.

[30] Weidemann, G et al. "Comparing Molecular Packing and Textures of Langmuir Monolayers of Fatty Acids and Their Methyl and Ethyl Esters". In: *Journal of Physical Chemistry B* 5647.102 (1998), p. 148.

[31] Lee, K. Y. et al. "Synchrotron X-ray study of lung surfactant-specific protein SP-B in lipid monolayers." In: *Biophysical journal* 81.1 (2001), p. 572.

[32] Sierra-Hernández, M. R. and Allen, H. C. "Incorporation and exclusion of long chain alkyl halides in fatty acid monolayers at the air-water interface." In: *Langmuir : the ACS journal of surfaces and colloids* 26.24 (2010), p. 18806.

[33] Fárník, M. and Poterya, V. "Atmospheric processes on ice nanoparticles in molecular beams." In: *Frontiers in chemistry* 2 (2014), p. 4.

[34] Fedor, J. et al. "Cluster cross sections from pickup measurements: Are the established methods consistent?" In: *The Journal of Chemical Physics* 135.10 (2011), p. 104305.

[35] Gunstone, F. D., Harwood, J. L., and Dijkstra, A. J. *The Lipid Handbook with CD-ROM, Third Edition.* Amazon.com.

[36] Lambert, A. G., Davies, P. B., and Neivandt, D. J. "Implementing the Theory of Sum Frequency Generation Vibrational Spectroscopy: A Tutorial Review". In: *Applied Spectroscopy Reviews* 40.2 (2005), p. 103.

[37] Mendelsohn, R., Mao, G., and Flach, C. R. "Infrared reflection-absorption spectroscopy: principles and applications to lipid-protein interaction in Langmuir films." In: *Biochimica et biophysica acta* 1798.4 (2010), p. 788.

[38] Hoenig, D. and Moebius, D. "Direct visualization of monolayers at the air-water interface by Brewster angle microscopy". In: *The Journal of Physical Chemistry* 95.12 (1991), p. 4590.

[39] Jungwirth, P. *Klasická a kvantová molekulová dynamika.* URL: `http://marge.uochb.cas.cz/~jungwirt/`.

[40] Allen, M. and Tildesley, D. *Computer Simulation of Liquids.* Oxford University Press Inc., New York, 1991.

[41] Frenkel, D. and Smith, B. *Understanding Molecular Simulations,* Academic Press, San Diego, 2002.

[42] G, S. "Quantum Simulations of Complex Many-Body Systems:From Theory to Algorithms, Lecture Notes". In: vol. 10. NIC Series. John von Neumann Institute for Computing, Juelich, 2002. Chap. Classical Molecular Dynamics, p. 211.

[43] Hinchliffe, A. *Molecular Modelling for Beginners.* John Wiley & Sons Ltd., England, 2003.

[44] Rapaport, D. C. *The Art of Molecular Dynamics Simulation.* Cambridge University Press, UK, 2004.

[45] Verlet, L. “Computer "Experiments" on Classical Fluids. I. Thermodynamical Properties of Lennard-Jones Molecules”. In: *Physical Review* 159.1 (1967), p. 98.

[46] Hockney, R., Goel, S., and Eastwood, J. “Quiet high-resolution computer models of a plasma”. In: *Journal of Computational Physics* 14.2 (1974), p. 148.

[47] Hess, B. et al. “GROMACS 4: Algorithms for Highly Efficient, Load-Balanced, and Scalable Molecular Simulation”. In: *Journal of Chemical Theory and Computation* 4.3 (2008), p. 435.

[48] Case, D. A. et al. “The Amber biomolecular simulation programs.” In: *Journal of computational chemistry* 26.16 (2005), p. 1668.

[49] Wang, J. et al. “Development and testing of a general amber force field”. In: *Journal of Computational Chemistry* 25.9 (2004), p. 1157.

[50] Kaminski, G. A. et al. “Evaluation and Reparametrization of the OPLS-AA Force Field for Proteins via Comparison with Accurate Quantum Chemical Calculations on Peptides”. In: *The Journal of Physical Chemistry B* 105.28 (2001), p. 6474. eprint: `http://dx.doi.org/10.1021/jp003919d`.

[51] Frisch, M. J. et al. *Gaussian 09 Revision D.01*. Gaussian Inc. Wallingford, 2009.

[52] Bayly, C. I. et al. “A well-behaved electrostatic potential based method using charge restraints for deriving atomic charges: the RESP model”. In: *The Journal of Physical Chemistry* 97.40 (1993), p. 10269. eprint: `http://dx.doi.org/10.1021/j100142a004`.

[53] Darden, T., York, D., and Pedersen, L. “Particle mesh Ewald: An N·log(N) method for Ewald sums in large systems”. In: *The Journal of Chemical Physics* 98.12 (1993), p. 10089.

[54] Essmann, U. et al. “A smooth particle mesh Ewald method”. In: *The Journal of Chemical Physics* 103.19 (1995), p. 8577.

[55] Ryckaert, J.-P., Ciccotti, G., and Berendsen, H. J. “Numerical integration of the cartesian equations of motion of a system with constraints: molecular dynamics of n-alkanes”. In: *Journal of Computational Physics* 23.3 (1977), p. 327.

[56] Hess, B et al. “LINCS: A linear constraint solver for molecular simulations”. In: *The Journal of Computational Chemistry* 18.12 (1997), p. 1463.

[57] Bussi, G., Donadio, D., and Parrinello, M. “Canonical sampling through velocity rescaling”. In: *Journal of Chemical Physics* 126.1 (2007), p. 14101.

[58] Berendsen, H. J. C. et al. “Molecular dynamics with coupling to an external bath”. In: *The Journal of Chemical Physics* 81.8 (1984), p. 3684.

[59] Parrinello, M. “Polymorphic transitions in single crystals: A new molecular dynamics method”. In: *Journal of Applied Physics* 52.12 (1981), p. 7182.

[60] Nosé, S. “A molecular dynamics method for simulations in the canonical ensemble”. In: *Molecular Physics* 100.1 (2002), p. 191.

[61] Hoover, W. “Canonical dynamics: Equilibrium phase-space distributions”. In: *Physical Review A* 31.3 (1985), p. 1695.

[62] Humphrey, W., Dalke, A., and Schulten, K. “VMD: Visual molecular dynamics”. In: *Journal of Molecular Graphics* 14.1 (1996), p. 33.

[63] *Grace*. URL: `http://plasma-gate.weizmann.ac.il/Grace/`.

[64] MATLAB. *version 7.10.0 (R2010a)*. Natick, Massachusetts: The MathWorks Inc., 2010.

[65] Torrie, G. and Valleau, J. “Nonphysical sampling distributions in Monte Carlo free-energy estimation: Umbrella sampling”. In: *Journal of Computational Physics* 23.2 (1977), p. 187.

[66] Kumar, S. et al. “The weighted histogram analysis method for free-energy calculations on biomolecules. I. The method”. In: *Journal of Computational Chemistry* 13.8 (1992), p. 1011.

[67] Pašalić, H., Roeselová, M., and Lischka, H. “Methyl and pentyl chloride in a microhydrated environment and at the liquid water-vapor interface: a theoretical study.” In: *The journal of physical chemistry. B* 115.8 (2011), p. 1807.

[68] Sander, R. *Compilation of Henry’s Law Constants for Inorganic and Organic Species of Potential Importance in Environmental Chemistry, Version 3*. 1999.

[69] Habartová, A., Valsaraj, K. T., and Roeselová, M. “Molecular Dynamics Simulations of Small Halogenated Organics at the Air–Water Interface: Implications in Water Treatment and Atmospheric Chemistry”. In: *The Journal of Physical Chemistry A* 117.38 (2013), p. 9205.

[70] Grecea, M. et al. “Mobility of haloforms on ice surfaces”. In: *Chemical Physics Letters* 385.3-4 (2004), p. 244.

[71] McMullen, R. L. and Kelty, S. P. “Molecular dynamic simulations of eicosanoic acid and 18-methyleicosanoic acid langmuir monolayers”. In: *Journal of Physical Chemistry B* 111.37 (2007), p. 10849.

[72] Tang, C. Y. and Allen, H. C. “Ionic binding of Na+ versus K+ to the carboxylic acid headgroup of palmitic acid monolayers studied by vibrational sum frequency generation spectroscopy.” In: *The journal of physical chemistry. A* 113.26 (2009), p. 7383.

[73] Plazzer, M. B. et al. “Comparative study of commonly used molecular dynamics force fields for modeling organic monolayers on water”. In: *Journal of Physical Chemistry B* 115.14 (2011), p. 3964.

[74] Pasenkiewicz-Gierula, M. et al. “Orientation of lutein in a lipid bilayer - revisited.” In: *Acta biochimica Polonica* 59.1 (2012), p. 115.

List of Tables

List of Figures

List of Abbreviations

A_M	mean surface Area per Molecule
AMBER	Assisted Model Building with Energy Refinement
BrC5	Bromopentane
BrC10	Bromodecane
BrC16	Bromohexadecane
CHARMM	Chemistry at HARvard Macromolecular Mechanics
FWHM	Full Width at Half Maximum
GID	Grazing incidence synchrotron X-ray diffraction
GROMACS	GROningen MAchine for Computer Simulation
GROMOS	GROningen MOlecular Simulation
LINCS	LINear Constraint Solver
LM	Langmuir monolayer
MD	Molecular Dynamics
NpT	constant number of particles, pressure and temperature
NVT	constant number of particles, pressure and volume
PA	Palmitic Acid
π-A	surface pressure (π) - Area isotherm
RDF	Radial Distribution Function
RESP	Restrained ElectroStatic Potential
SDF	Spatial Distribution Function
SFG	Sum Frequency Generation spectroscopy
VMD	Visual Molecular Dynamics

Attachments

List of attached papers

1. Pysanenko A., Habartová A., Svrčková P., Lengyel J., Poterya V., Roeselová M., Fedor J. and Fárník M. "Lack of Aggregation of molecules on ice nanoparticles". *Submitted to: The Journal of Physical Chemistry A*

2. Habartová A., Obisesan A., Minofar B. and Roeselová, M. "Partial hydration of n-alkyl halides at the water–vapor interface: a molecular simulation study with atmospheric implications". In: *Theoretical Chemistry Accounts*, 133, 1455 (2014).

3. Habartová A., Valsaraj K. T. and Roeselová, M. "Molecular dynamics simulations of small halogenated organics at the air-water interface: implications in water treatment and atmospheric chemistry". In: *Journal of Physical Chemistry A* 117, 9205–15 (2013).

4. Habartová A., Hormain L., Pluhařová E., Briquez S., Monnerville M., Toubin C. and Roeselová M. "Molecular Simulations of Halomethanes at the Air/ice Interface". *Submitted to:The Journal of Physical Chemistry A*

Lack of aggregation of molecules on ice nanoparticles

Andriy Pysanenko,[†] Alena Habartová,[*,‡] Pavla Svrčková,[†,¶] Jozef Lengyel,[†,¶] Viktoriya Poterya,[†] Martina Roeselová,[‡] Juraj Fedor,[*,†] and Michal Fárník[*,†]

J. Heyrovský Institute of Physical Chemistry v.v.i., Czech Academy of Sciences, Dolejškova 3, 18223 Prague 8, Czech Republic, and Institute of Organic Chemistry and Biochemistry v.v.i., Czech Academy of Sciences, Flemingovo nám. 2, 16610 Prague 6, Czech Republic

E-mail: alena.habartova@marge.uochb.cas.cz; juraj.fedor@jh-inst.cas.cz; michal.farnik@jh-inst.cas.cz

[*]To whom correspondence should be addressed

[†]J. Heyrovský Institute of Physical Chemistry v.v.i., Czech Academy of Sciences

[‡]Institute of Organic Chemistry and Biochemistry v.v.i., Czech Academy of Sciences

[¶]*Also at: Department of Physical Chemistry, University of Chemistry and Technology, Technická 5, 16628 Prague 6, Czech Republic*

Abstract

Multiple molecules adsorbed on the surface of nano-sized ice particles can either remain isolated or form aggregates, depending on their mobility. Such (non)aggregation may subsequently drive the outcome of chemical reactions which play an important role in atmospheric chemistry or astrochemistry. We present a molecular beam experiment where the controlled number of guest molecules is deposited on the water and argon nanoparticles in a pickup chamber and their aggregation is studied mass spectrometrically. The studied molecules (HCl, CH_3Cl, $CH_3CH_2CH_2Cl$, C_6H_5Cl, CH_4 and C_6H_6) form relatively large aggregates on argon nanoparticles. On the other hand, no aggregation is observed on ice nanoparticles. Molecular simulations confirm the experimental results, they reveal high degree of aggregation on the argon nanoparticles and show that the molecules remain mostly isolated on the water ice surface. This finding will influence efficiency of ice-grain mediated synthesis (e.g., in outer space) and is also important for the cluster science community since it shows some limitations of pickup experiments on water clusters.

Introduction

Heterogeneous chemistry of molecules adsorbed on ice particles with nano- to micrometer dimensions plays central role in several environments. An obvious example is photochemistry of halogenated species on polar stratospheric clouds and other ice particles in the atmosphere, where the presence of such nanoparticles triggers chemical changes of global importance (ozone hole).[1] Also, it is believed that in outer space, where molecular density is very low, molecular ice particles (water ice in particular) represent "sponges" where guest molecules are adsorbed and meet other molecules yielding reactions, often assisted by high energy radiation.[2,3]

One factor that will strongly influence both the photochemistry and ice-assisted synthesis is whether molecules remain isolated on the particle surface or form aggregates prior to the

triggering radiation event. It can result in a dramatically different outcome of the subsequent reaction. The examples include change in photochemistry of HCl in complexes when compared to that of monomers,[4] or cosmic-ray induced glycine synthesis from simpler molecules on extraterrestrial ices.[3] The aggregation will be influenced by the molecules' mobility and migration upon their uptake on the particle. Surprisingly little data on molecular mobility on ice surfaces exists even for bulk ices.[5,6]

In laboratory experiments the above-mentioned environments are often mimicked by water clusters (ice nanoparticles) with guest molecules adsorbed on their surface. The pickup technique which is used to adsorb the guest molecules on the clusters has been introduced in 80's by Gough et al.[7] A subsequent aggregation of adsorbed/embedded molecules have been exploited extensively for large superfluid helium nanodroplets.[8–14] and to limited extent for argon nanoparticles.[4,15–18] We are not aware of any study addressing the question of aggregation on the surface of ice nanoparticles.

In this paper we examine the aggregation of guest molecules on ice nanoparticles (water clusters $(H_2O)_N$, $\bar{N} = 10^2$-10^3). These particles have diameters in a nanometer range and possess low temperatures - as discussed in the Computational methods section, we assume the temperature of ≈100 K. We successively dope the nanoparticles with a controlled number of guest molecules by pickup[19–21] and probe them mass-spectrometrically. Surprisingly, no aggregation of guest molecules is observed. In order to examine the reliability of our technique and to provide a chemically inert reference, we perform analogous experiments with Ar_N clusters. In this case, strong aggregation of guest molecules is observed, in spite of the lower particle temperature of ≈37 K.[22] The experimental results are confirmed by molecular dynamics (MD) simulations. As the guest molecules, we study mainly Cl-containing species due to their atmospheric relevance. To probe different types of bonding we proceed from diatomic HCl to chloroalkanes with various chain lengths (CH_3Cl and $CH_3CH_2CH_2Cl$), and to aromatic compound C_6H_5Cl which can bind via π-interactions. For comparison, non-polar CH_4 and C_6H_6 molecules are also considered.

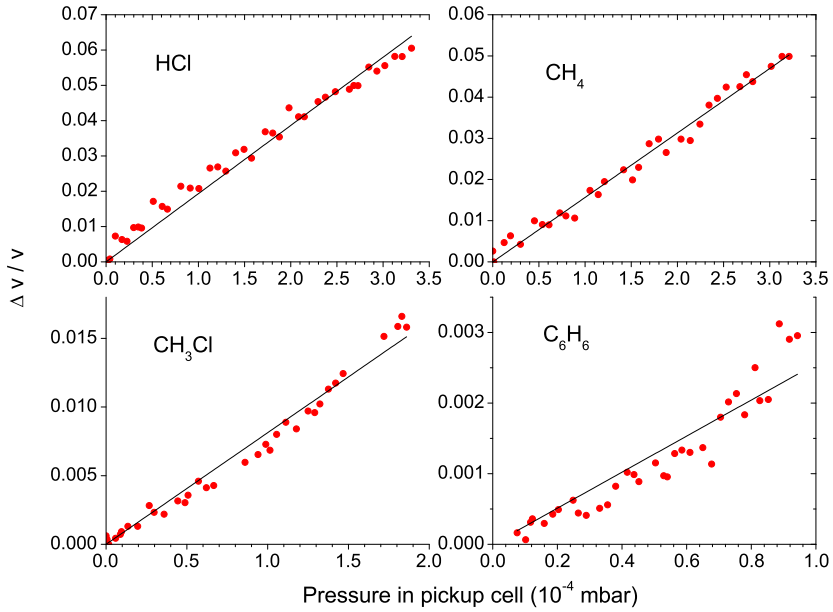

Figure 1: Dependence of the relative velocity decrease of the beam $\frac{\Delta \mathrm{V}}{\mathrm{V}}$ on pressure. Pickup on $(H_2O)_N$, $\bar{N} \approx 430$.

Experimental methods

The experiments were performed on the CLUster Beam apparatus (CLUB) which is a versatile molecular beam setup allowing for a range of experiments including photochemistry, mass spectrometry and pickup experiments with clusters and nanoparticles.[17,18,21,23] The Ar_N and $(H_2O)_N$ nanoparticles are generated in continuous supersonic expansion of Ar and water vapour, respectively, through a conical nozzle into the vacuum. The mean cluster size is controlled by the source conditions (stagnation pressure, temperature and geometrical nozzle parameters). The present mean sizes are $\bar{N} \approx 330$ and 430 for Ar_N and $(H_2O)_N$, respectively. They correspond approximately to the same geometrical cross section of nanoparticles $\sigma_g \approx 660$ Å^2. The mean cluster size determination and calculation of geometrical cross section are described in the Supplementary Information (SI). The cluster beam is skimmed and passes through a differentially pumped chamber where the guest molecules are introduced.

In the first type of measurement we determine the amount of picked-up guest molecules from deceleration of the beam after it passes the pickup chamber. For this purpose the beam velocity is determined by modulating the beam with a pseudorandom mechanical chopper

and measuring its time-of-flight. The chopper is located in the next differentially pumped chamber after the pickup chamber and the flight time is measured on a subsequent 151 cm path into a detector. There the clusters are ionized by 70 eV electrons, and fragment ions selected by quadrupole analyzer are detected. The arrival time to the detector is measured and converted to the velocity distribution. Assuming that the cluster with the mass $\bar{N}m_C$ is slowed down by picking up m_p guest molecules, the relative change of the cluster velocity is

$$\frac{\Delta \mathrm{v}}{\mathrm{v}} = \frac{m_M}{\bar{N}m_C} m_p, \tag{1}$$

where m_M and m_C are masses of guest molecule and cluster constituent, respectively. Despite the simplified assumptions (sticking collisions), this formula was proved to deliver reliable results confirmed by molecular dynamics simulations of the pickup process several species previously.[19–21] The m_p is linearly dependent on the pickup cell pressure p and consequently $\frac{\Delta \mathrm{V}}{\mathrm{V}} = \alpha p$. Figure 1 shows typical pressure dependences of the relative deceleration $\frac{\Delta \mathrm{V}}{\mathrm{V}}$. The linear dependence was verified for each guest molecule, and m_p during subsequent mass spectrometry measurement (performed at fixed p) was determined from the measured slope α.

The pressure p was monitored with a Bayard-Alpert ionization gauge (Varian type 571). The measured pressures for various gasses were divided by the correction factor listed in the gauge instruction manual. Since this is a crucial factor for m_p determination, we have calibrated the ionization gauge independently with a capacitance manometer (Pfeiffer CMR 365) and the absolute pressures were found in very good agreement with the corrected pressures based on the ionization gauge manual. The uncorrected pressure limit of the ionization gauge is $5{\times}10^{-4}$ mbar which for benzene and chlorobenzene leads to very low calibrated pressures (shown in Table 1) where the determination of α (and consequently of m_p) is subject to relatively large error.

In the second type of measurement the beam is not chopped and we measure the mass spectra of the doped nanoparticles in another differentially pumped chamber with a high-

resolution reflectron time-of-flight mass spectrometer (RTOF).[24–26] The RTOF is mounted orthogonally to the molecular beam.The clusters are ionized by 70 eV electrons at 10 kHz repetition frequency, and the mass spectra are recorded with a resolution of $\frac{M}{\Delta M} \approx 5{\times}10^3$. In the perpendicular arrangement, attention must be paid to the mass discrimination due to the different cluster energies along the beam direction. The spectrometer was calibrated with perfluorotributylamine (FC-43) and known spectra of large Ar_N clusters so that no discrimination occurs in the mass range up to $\sim 10^3$ amu.

Computational methods

To provide further insight, we simulated motion of several guest molecules on both types of nanoparticles. Spherical nanoparticles consisting of 300 Ar atoms or H_2O molecules were carved out from a previously simulated liquid argon ($T \approx 100$ K)/liquid water ($T \approx 300$ K) system. Each nanoparticle was then placed in the center of a cubic simulation cell with the edge size of 80 Å (the diameters of the argon and water nanoparticles were about 30 Å). To equilibrate the nanoparticles to the known target temperature of 37 K (for argon)[22] and 100 K (for water)[27,28] , 50 ns isochoric-isothermal (NVT) simulations were performed. The temperatures correspond to experimental conditions. For argon nanoparticles created in supersonic expansion, the commonly accepted value is 37 K as measured by electron diffraction.[22] For water nanoparticles a range of temperatures has been put forward. 180 ±20 K was reported by electron diffraction experiment for $N < 200$.,[29] temperatures between 50 K and 100 K were estimated in a recent perspective[28] and vibrational spectroscopy of size-selected nanoparticles with 200 - 500 molecules reported temperatures 90 - 115 K.[30] We therefore assume the nanoparticle temperature of ≈ 100 K.

Subsequently, 12 identical molecules from the list of studied pick-up species were added into the simulation cell. The molecules were initially evenly (pseudo-randomly) distributed around the argon/amorphous ice nanoparticle at a distance of several Å from the surface.

The entire system was again shortly equilibrated ($\approx$ 10 ps) at the respective experimental temperature. During that period, most of the molecules landed on the surface, and the resulting configurations of the argon/amorphous ice nanoparticle with 12 adsorbed molecules were used as initial conditions for the subsequent production runs. The systems were propagated for 50 ns in the NVT simulation at the above given experimental temperatures to sample structural characteristics. Periodic boundary conditions were applied in all three dimensions. For each combination of the argon nanoparticle and the pick-up species, 5 different initial configurations of molecules around the argon nanoparticle were created and the simulations were propagated independently. Close contacts of picked-up molecules were considered as an aggregate (cluster) when no molecule of argon/H_2O was found between them.

Interaction potentials: Water molecules were described using the TIP4P/2005 model,[31] while for argon the OPLS parameters[32] were used. Topologies for the pick-up molecules were obtained from the Automated Topology Builder[33] and the general Amber force field (GAFF) parameter set[34] was employed to describe their interactions. Chemical bonds were kept intact during the simulations, including that in HCl (i.e., no acidic dissociation of molecular HCl on the clusters was considered, which will be discussed below). The atomic partial charges were calculated by the RESP method.[35] For CH_3Cl and C_6H_6 these charges were enhanced by a factor of 1.7[36] and 1.24,[37] respectively. Further details of the theoretical simulations and the atomic partial charges and topologies of studied molecular species are attached as itp-files in the SI.

Results

Mass spectra of doped nanoparticles

Pickup on ice nanoparticles: Figure 2 shows example mass spectra following the pickup of HCl and CH_3Cl on H_2O nanoparticles. Further spectra for all studied molecules are

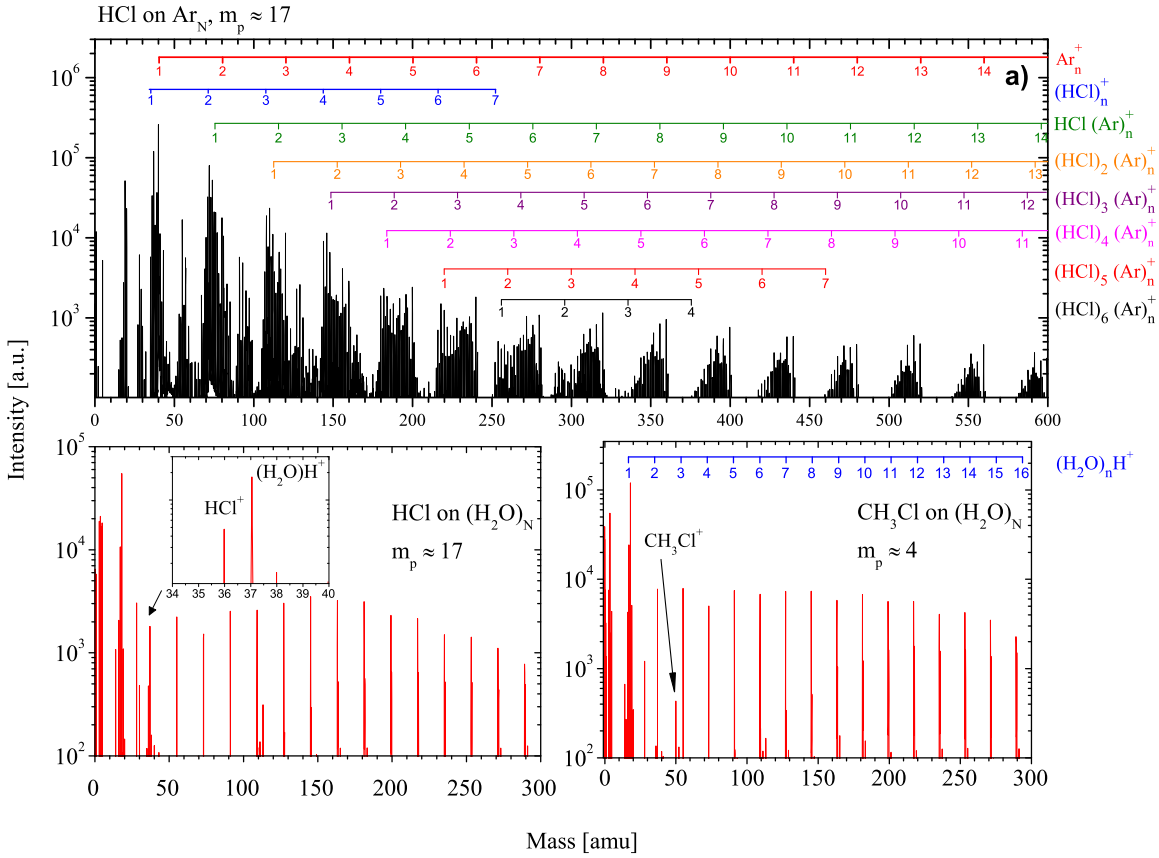

Figure 2: Representative time-of-flight mass spectra. Top panel: HCl molecules adsorbed on argon nanoparticles with $\bar{N} \approx 330$. Bottom panels: HCl and CH_3Cl molecules adsorbed on water ice nanoparticles with $\bar{N} \approx 430$.

presented in Supporting Information (SI). No ions corresponding to aggregates of guest molecules (either pure or mixed water-guest aggregates) were observed, only the monomer ions and their fragments are present in the spectra.

We are certain that these peaks originate from species deposited on the nanoparticles as the background signals measured with the blocked beam were carefully subtracted. The presence of molecules on ice nanoparticles was confirmed in some cases by our previous photodissociation studies[18,38,39] where features corresponding to nanoparticle-guest interactions (acidic dissociation) clearly dominate the spectra. Further evidence comes from the measured velocities shown in figure 1. The increasing relative deceleration $\frac{\Delta V}{V}$ with pressure shows that the clusters are slowed down by a momentum transfer from multiple guest molecules. Additionally, in a similar experiment, Ahmed and co-workers[40–42] reported sticking of a number

of similar organic molecules on the surface of water clusters.

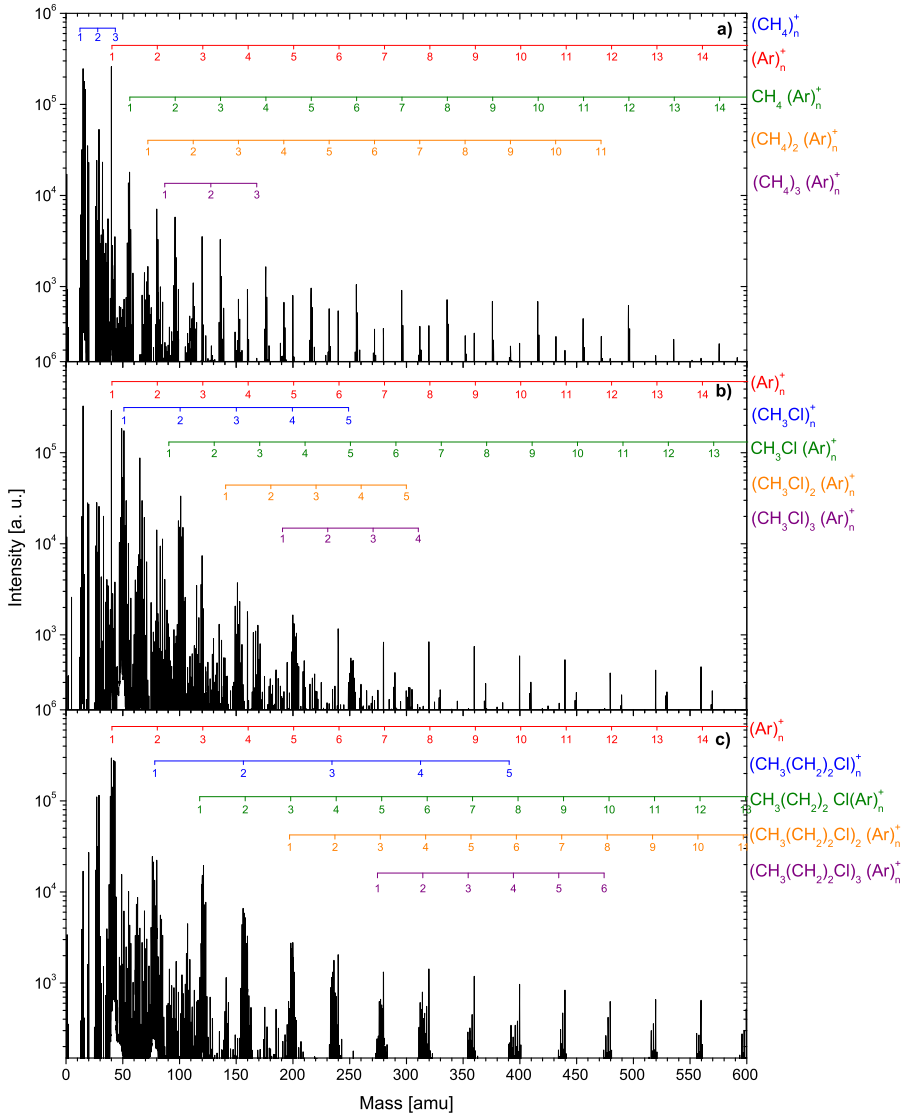

Figure 3: The mass spectrum of Ar_N, $\bar{N}$= 330, clusters after the pickup of CH_4 at p= 2.0×10^{-4} mbar (a), CH_3Cl at p= 1.0×10^{-4} mbar (b), and $CH_3CH_2CH_2Cl$ at p= 0.6×10^{-4} mbar (c). The series corresponding to the different cluster ion fragments are labeled.

Pickup on argon nanoparticles: Mass spectra following pickup of guest molecules on argon nanoparticles are shown in figure 2 for HCl and in figure 3 for CH_4, CH_3Cl and $CH_3CH_2CH_2Cl$. Due to overlap of multiple spectra a detailed analysis based on isotope ratios was required to assign all the mass peaks unambiguously. This analysis, as well as mass spectra corresponding to the pickup of other guest molecules, are shown in SI.

As opposed to the ice nanoparticles, relatively large aggregate ions of the adsorbed molecules were observed on Ar_N: the mass spectra exhibited M_m^+ with $m \geq 10$ as well as mixed species $Ar_n \cdot M_k^+$. Figure 4 summarizes the mass peak intensities corresponding to M_m^+ cluster ions generated on Ar_N at the highest exploited pickup pressures. We denote the largest detected molecular cluster size as m_{max}. For the ice nanoparticles $m_{max} = 1$ for all guest molecules. The results are summarized in table 1.

For HCl the mass spectra showed evidence for $(HCl)_m^+$ clusters up to the maximum cluster fragment size $m_{max} = 11$. For chloromethane also relatively large $(CH_3Cl)_m^+$ clusters ions with $m_{max} = 7$ were observed. On the other hand, the clustering of methane molecule on Ar_N was inefficient. Cluster fragments $(CH_4)_m^+$ were observed, but the maximum cluster size was only $m_{max} = 3$. This is nonetheless an interesting result: methane is notoriously known as a non-clustering gas, it is thus interesting to note that on the argon surface it still forms aggregates that do not decay upon the electron ionization.

To investigate the influence of the hydrocarbon chain length on the molecule coagulation we have studied the pickup of chloropropane where again the spectra exhibited $(CH_3CH_2CH_2Cl)_m^+$ cluster ions up to $m_{max} = 7$. Since the linear chain length of the adsorbed molecule did not have any significant influence on the clustering on Ar_N, we exploited aromatic molecules chlorobenzene C_6H_5Cl and benzene C_6H_6, if the interaction of the ring π-electrons would change the coagulation behavior. However, the spectra exhibit essentially the same clustering as the linear molecules above: $(C_6H_6)_m^+$ fragments with $m_{max} = 9$ for benzene and $(C_6H_5Cl)_m^+$ with $m_{max} = 7$ for chlorobenzene.

MD simulations

The MD simulations were performed for 50 ns in order to visualize possible coagulation of 12 individual molecules of the tested molecules on Ar_N or $(H_2O)_N$, $N = 300$, nanoparticles. Within the first 10 ps the guest molecules were adsorbed on the nanoparticle surfaces. Once adsorbed, they remained so on both argon or ice for the entire simulation run. The only

exceptions were the molecules of HCl and methane, which underwent desorption/absorption cycles on amorphous ice. In the period of 50 ns, an isolated molecule of HCl desorbed approximately 4 times, while an isolated CH_4 molecule desorbed about 200 times. However, for HCl one has to consider that the molecule acidically dissociates on the ice nanoparticles which has not been taken into account in present simulations (see discussion below). All other adsorbed molecules were moving on the nanoparticle surface roughly for the first 10 ns. During this period molecular aggregates were formed, submerged and a practically final orientation of the molecules took place. For the next 40 ns, the molecules remained mostly fixed, except of benzene aggregates submerging in the argon nanoparticle. Figure 5 shows typical snapshots at the end of the simulation (see SI for further snapshots and videos).

Coagulation on argon. All studied molecules formed aggregates on argon (Fig. 5). To eliminate the influence of initial conditions, for each molecular species several separate simulations were run and the maximal cluster size was determinated from the last snapshot. HCl molecules created molecular chains with the average maximal size of 8 molecules. Methylchloride and propylchloride generated on aver clusters of 5 and 4 molecules, respectively. Benzene (without dipole moment) and chlorobenzene (dipole moment of 2.1 Debye) coagulate to the same extent (average maximal size $m_{cal} = 5$ molecules). This points out to dominant role of π-interaction of aromatic rings. The largest aggregates of methane consisted on average of only 2 molecules (Tab. 1). Interestingly, chloromethanes, chlorobenzenes, and benzenes submerged into argon nanoparticles while chloropropanes stayed localized more at the surface. Chlorine atoms of both chloropropane and chlorobenzene were mostly oriented outside of the argon cluster.

Coagulation on ice. We observe mostly individual molecules on the $(H_2O)_N$ ice nanoparticles since the picked-up molecules do not aggregate. Only chloromethane, benzene, and chlorobenzene formed in each simulation one dimer, and choloropropane formed one trimer. The non-aggregation on the ice particles results from a combination of kinetic and thermodynamic effects. The interaction of guest molecules with polar water molecules inhibits

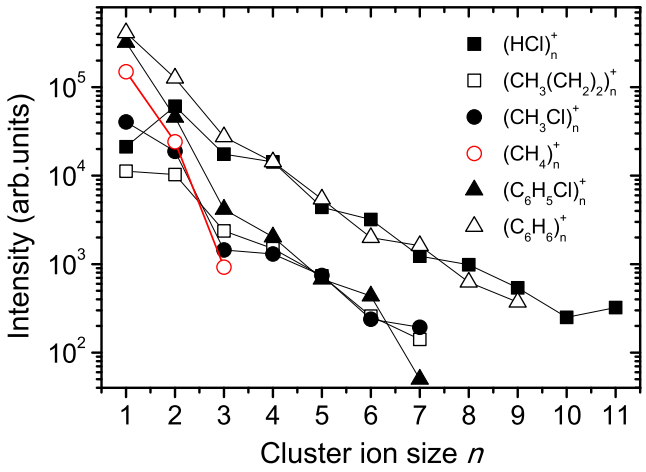

Figure 4: The mass peak intensities corresponding to M_m^+ aggregate ions following pickup of M on Ar_N nanoparticles, $\bar{N} \approx 330$.

their mobility. They generally remain at the position of the first contact with the surface and merely reorient themselves with respect to the closest water molecules (kinetic effect). A similar finding has been observed experimentally for chloroform $CHCl_3$ molecules which remain immobile on the bulk ice surface up to its desorption temperature.[5] Additionally, the amorphous surface layer effectively solvates the guest molecule and in some cases this solvation prevents aggregation of guest molecules in spite of their physical proximity (thermodynamic effect).

Discussion

The unambiguous experimental observation is that while large aggregate ions of guest molecules M are detected from argon nanoparticles - both the pure M_n^+ and mixed $M_n.Ar_m^+$ ions - only the monomer ions are formed on the ice nanoparticles. To be certain that this observation leads to the conclusion outlined in the title of this paper, several issues have to be addressed. First, we have to consider the possibility of electron-induced aggregate fragmentation. Generally, the electron-impact ionization in the gas phase leads to strong fragmentation, which opens a speculation that molecular aggregates on ice particles could be formed but are decomposed in the ionization process. Even though we cannot fully exclude certain amount of

Table 1: The maximum aggregate fragment size observed in the mass spectra m_{max} and the mean number of adsorbed molecules m_p at the pressure p, and the maximum aggregate size from MD simulations m_{cal}. The numbers in brackets correspond to standard deviations. The m_p value for methane on ice nanoparticles* is judged to be overestimated, and for benzene and chlorobenzene** on both argon and ice have lower confidence level (see text).

M	p	Ar_N			$(H_2O)_N$		
	10^{-4}mbar	m_p	m_{max}	m_{cal}	m_p	m_{max}	m_{cal}
HCl	3.0	17(3)	11(2)	8(3)	17(5)	1	1
CH_4	3.3	22(2)	3(1)	2(1)	18(4)*	1	1
CH_3Cl	1.7	10(3)	7(2)	5(1)	4(2)	1	2(1)
C_3H_7Cl	0.9	7(1)	7(2)	4(1)	3(1)	1	3(1)
C_6H_6	0.9	4(2)**	9(1)	5(1)	1(1)**	1	2(1)
C_6H_5Cl	0.7	3(2)**	7(1)	5(1)	1(1)**	1	2(1)

fragmentation, there is a strong evidence that ionization is much softer when the aggregate is on the surface of a nanoparticle. This is clearly experimentally demonstrated in this work in the case of argon nanoparticles when comparing m_p and m_{max} in table 1. The number of picked up molecules m_p corresponds to the cluster ion size observed on Ar_N. This shows that molecules coagulate efficiently into their aggregates and these do not fragment significantly upon the ionization. The reason is that the nanoparticle serves as efficient heat-baths and can dissipate the excess energy upon the ionization, e.g., via evaporation of Ar atoms. Second, the ionization on nanoparticles is less destructive, since it can proceed via ionization of argon atom and a subsequent charge transfer process to the guest molecule with release of much less excess energy than a direct ionization.[25,26]

We are aware of only one experimental confirmation of soft ionization for molecules deposited on ice nanoparticles: Moro et al.[43,44] reported almost negligible fragmentation of amino acids after they were picked-up on water clusters, in contrast to rich fragmentation patterns of these molecules in the gas phase. The excess energy transfer to the water solvent can be even more efficient than in the argon case since the water molecules poses internal degrees of freedom, where the energy can be transferred. Besides, a lower ionization energy of water compared to argon leads to less excess energy in case of the host molecule/cluster

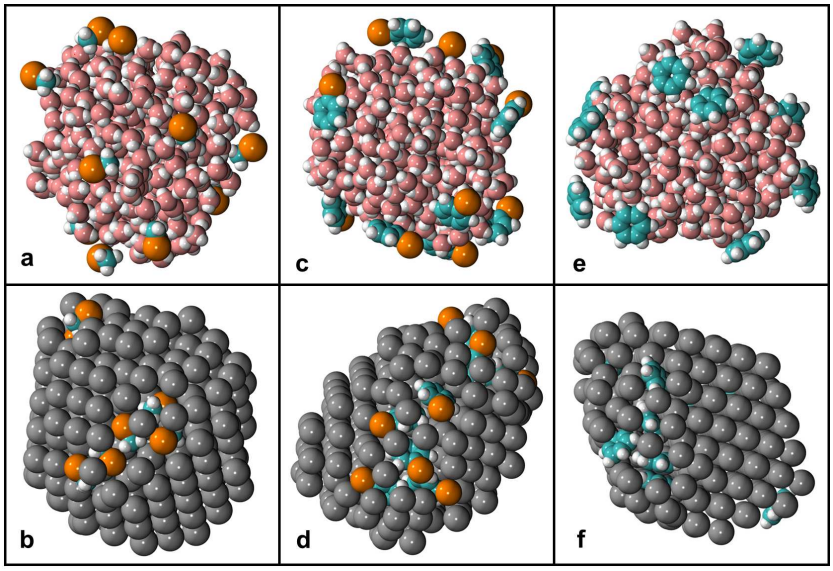

Figure 5: Last snapshot of the 50 ns MD simulation ice (top) and argon (bottom) nanoparticles and 12 adsorbed pick-up molecules: chloromethane (a,b), chlorobenzene (c,d) and benzene (e,f). Color coding: chlorine in orange, carbon in cyan and hydrogen in white.

ionization by charge transfer from water/argon. In addition, relatively soft proton transfer ionization is possible in $(H_2O)_N$. It is thus reasonable to assume soft ionization of aggregates on the surface of ice nanoparticles.

Another critical factor is the number of picked-up molecules m_p. Its determination relies on two assumptions about the deceleration of nanoparticles in the pickup chamber: (i) the sticking collisions during which guest molecules land on the surface are the dominant contributor to the momentum transfer; and (ii) guest molecules do not spontaneously desorb. We have previously shown[19–21] by extensive Monte Carlo simulations that assumption (i) is fulfilled both for argon and water particles, the statistical weight of non-sticking scattering events is much smaller than that of the sticking events. The relatively low collision energies (undisturbed beam velocities being 1450 ms^{-1} for H_2O and 490 ms^{-1} for Ar particles) lead to 'soft landing' on the particle surface. The assumption (ii) is verified in present MD simulations. The guest molecules, once adsorbed, remained on the surface of both argon or ice for the entire simulation run - with two exceptions, HCl and CH_4 as described above. Therefore the m_p value for methane can be overestimated. This is also suggested by the

negligible intensity of the methane peaks in the mass spectra (SI). The situation is different for HCl which has been shown experimentally to undergo acidic dissociation to $Cl^- \cdot H_3O^+$ ion pair on ice nanoparticles.[18,38,39,45] A simulation of this process goes beyond the present MD model where the chemical bonds were kept intact. Acidic dissociation will prohibit desorption of HCl from the surface and probably further inhibit the aggregation of the guest molecules. Thus the m_p determination for HCl is reliable. As to the possible desorption of other guest molecules, it should be noted that MD simulations probe timescale that is approximately five orders of magnitude shorter than the experimental time window, thus do not fully exclude possible desorption in the experiment. However, in our previous systematic investigation of chloroalkanes at liquid water interfaces we have shown that the free energy-profiles have minima at water-vapor interface and molecules prefer to stay adsorbed on the water surface even at 300 K.[36] The present, much lower temperature, will only decrease the desorption probability.

For benzene and chlorobenzene on argon nanoparticles the m_p values are lower then m_{max}. This is possible since m_p is a mean number of picked-up molecules - their actual number follows a Poisson distribution[19] and can be larger. However, we consider these m_p values to be underestimated, no other molecule shows $m_{max} > m_p$ and the pickup chamber pressures for these two molecules are low due to high correction factors. All pressures in table 1 correspond to the maximal reliable pressure of the ionization gauge of 5×10^{-4} mbar. The slope determination of $\frac{\Delta V}{V}$ pressure dependence (described in SI) at these low pressures has large error bars.

The present MD simulations were actually inspired by the experimental results and were performed to account for the main uncertainty in the experimental interpretation: whether the lack of observation of aggregate ions in the mass spectra on ice nanoparticle can be interpreted as the lack of neutral aggregates prior to the ionization. As described in the results section, they fully support this interpretation. Again, the shorter time scale of the simulations when compared the that of the experiment comes into a question. The aggre-

gation degree would be strongly influenced by a time scale if it were limited solely by the mobility of guest molecules on the particle. However, the low mobility on the ice surface is only part of the reason for the non-aggregation. We have observed a number of trajectories where two guest molecules came into a physical proximity on the ice surface but did not form dimers since they were solvated by water molecules. The important role of binding of guest molecules to water has been pointed out by Ahmed and co-workers[41,42] . The fact that the guest molecules remain on the surface and do not submerge into the nanoparticle can be attributed to the fact that guest-H_2O interaction is weaker than the H_2O-H_2O interaction. On the other hand, the guest-H_2O and guest-guest interaction energies have similar magnitudes which leads to surface solvation of the guest molecules. The detailed analysis of energetics and temperature dependence of the mobility and aggregation process will be a subject of a separate publication.

Conclusions

In conclusion we have shown experimentally that adsorption of multiple molecues on the surface of water ice nanoparticles and the subsequent ionization do not lead to formation of any aggregate ions. MD simulations confirm that the molecules stay mostly iosolated and do not form aggregates in spite of their physical proximity. This is in strong contrast with their behavior on the surface of argon nanoparticles, where they are mobile and coagulate efficiently. In the mass spectra this is reflected in a rich progression of either pure aggregate or mixed aggregate-argon ions. Even methane after adsorption on argon and ionization forms pure aggregates $(CH_4)_n^+$ up to $n = 3$. Methane is known to be a difficult gas to cluster in co-expansions probably due to its small c_p/c_v ratio.[46] The use of argon nanoparticles as a cold support could represent a way for generating interesting methane-containing aggregates, e.g., clathrates. Additional interesting result for doped argon nanoparticles is shown by MD simulations: while some of the aggregates submerge into the nanoparticle (chloromethanes,

chlorobenzenes, and benzenes) some remain on its surface (methane, chloropropane). Both chlorinated species are oriented with chlorine atoms pointing out of the surface. These two finding will have consequences in the amount of caging observed in photodissociation studies.

As to the implications in astro- and atmospheric chemistry outlined in the introduction, it is important to note that the present findings apply to water ices with temperature around 100 K and an amorphous surface layer.[47] Naturally occurring nano- to micro-sized ices encompass a range of temperatures in different regions. The timescales should also not be overlooked: experimentally, we probed processes on a milisecond timescale, theoretically on a nanosecond timescale while, for example, the interstellar chemistry often requires millions of years. The present results are also of fundamental interest to the cluster physics research. Rare gas nanoparticles or helium nanodroplets are often used as support for forming cold clusters of picked-up molecules. This will be apparently difficult with water clusters. Several research groups have envisioned the use of water clusters as a supporting microsolvation system, e.g., for providing support for Watson-Crick pairs formation by successive pickup of nucleobases. The low mobility and non-aggregation of guest molecules can represent an obstructive factor for such approach. A more promising way for generating such species would be co-expansion with the water vapor instead of the pickup, as it has been demonstrated for a number of biomolecules.[48–50] However, in such case the molecules are generally incorporated into the bulk water and composition of the resulting nanoparticles (number of water molecules vs. number of 'guest' molecules) is difficult to control.

Acknowledgement

This work has been supported by the Czech Science Foundation projects 15-12386S and 13-06181S. We thank Prof. Pavel Jungwirth, Prague, for fruitful discussions.

Supporting Information Available

The Supporting Information contains: (1) Detailed description of the experiment, expansion

conditions, geometrical cross sections; (2) Detailed analysis of mass spectra and their discussion. Also available are the topology files and videos with final configurations from MD simulations. This material is available free of charge via the Internet at `http://pubs.acs.org/`.

References

(1) Peter, T. Microphysics and heterogeneous chemistry of polar stratospheric clouds. *Ann. Rev. Phys. Chem.* **1997**, *48*, 785–822.

(2) Herbst, E.; van Dishoeck, E. F. Complex Organic Interstellar Molecules. *Annu. Rev. Astron. Astrophys.* **2009**, *47*, 427.

(3) Holtom, P. D.; Bennet, C. E.; Osamura, Y.; Mason, N. J.; Kaiser, R. I. A combined experimental and theoretical study on the formation of the amino acid glycine (NH(2)CH(2)COOH) and its isomer (CH(3)NHCOOH) in extraterrestrial ices. *Astrophys. J.* **2005**, *626*, 940.

(4) Nahler, N. H.; Fárník, M.; Buck, U.; Vach, H.; Gerber, R. B. Photodissociation of HCl and small $(HCl)_m$ complexes in and on large Ar_n clusters. *J. Chem. Phys.* **2004**, *121*, 1293.

(5) Grecea, M.; Backus, E.; Fraser, H.; Pradeep, T.; Kleyn, A.; Bonn, M. Mobility of haloforms on ice surfaces. *Chem. Phys. Lett.* **2004**, *385*, 244.

(6) Park, S. C.; Moon, K. S.; Kang, H. Some fundamental properties and reactions of ice surfaces at low temperatures. *Phys. Chem. Chem. Phys.* **2010**, *12*, 12000.

(7) Gough, T. E.; Mengel, M.; Rowntree, P. A.; Scoles, G. Infrared spectroscopy at the surface of clusters: SF_6 on Ar. *J. Chem. Phys.* **1985**, *83*, 4958.

(8) Lewerenz, M.; Schilling, B.; Toennies, J. P. Successive capture and coaugulation of atoms and molecules to small clusters in large liquid helium clusters. *J. Chem. Phys.* **1995**, *102*, 8191.

(9) Behrens, M.; Fröchtenicht, R.; Hartmann, M.; Siebers, J. G.; Buck, U. Vibrational spectroscopy of methanol and acetonitrile clusters in cold helium droplets. *J. Chem. Phys.* **1999**, *111*, 2436.

(10) Scoles, G.; Lahmann, K. K. Nanomatrices are cool. *Science* **2000**, *287*, 2429.

(11) Toennies, J. P.; Vilesov, A. F. Superfluid helium droplets: A uniquely cold nanomatrix for molecules and molecular complexes. *Angew. Chem. Int. Ed.* **2004**, *43*, 2622.

(12) Choi, M. Y.; Douberly, G. E.; Falconer, T. M.; Lewis, W. K.; Lindsay, C. M.; Merritt, J. M.; Stiles, P. L.; Miller, R. E. Infrared spectroscopy of helium nanodroplets: novel methods for physics and chemistry. *Int. Rev. Phys. Chem.* **2006**, *25*, 15.

(13) Denifl, S.; Zappa, F.; Mähr, I.; da Silva, F. F.; Aleem, A.; Mauracher, A.; Probst, M.; Urban, J.; Mach, P.; Bacher, A. et al. IonMolecule Reactions in Helium Nanodroplets Doped with C_60 and Water Clusters. *Angew. Chem. Int. Ed.* **2009**, *121*, 9102 – 9105.

(14) Lehnig, R.; Sebree, J. A.; Slenczka, A. Structure and Dynamics of Phthalocyanine-Argon$_n$ (n = 1-4) Complexes Studied in Helium Nanodroplets. *J. Phys. Chem. A* **2007**, *111*, 7576 – 7584.

(15) Huisken, F.; Stemmler, M. Infrared spectroscopy of methanol clusters adsorbed on large Ar$_x$ host clusters. *J. Chem. Phys.* **1993**, *98*, 7680.

(16) Ehbrecht, M.; Stemmler, M.; Huisken, F. Enhanced production of unprotonated hydrogen-bonded cluster ions. *Int. J. Mass Spectrom.* **1993**, *123*, R1.

(17) Poterya, V.; Kočišek, J.; Lengyel, J.; Svrčková, P.; Pysanenko, A.; Hollas, D.; Slavíček, P.; Fárník, M. Clustering and Photochemistry of Freon CF2Cl2 on Argon and Ice Nanoparticles. *J. Phys. Chem. A* **2014**, *118*, 4740 – 4749.

(18) Poterya, V.; Lengyel, J.; Pysanenko, A.; Svrčková, P.; Fárník, M. Imaging of hydrogen

halides photochemistry on argon and ice nanoparticles. *J. Chem. Phys.* **2014**, *141*, 074309–1 – 10.

(19) Fedor, J.; Poterya, V.; Pysanenko, A.; Fárník, M. Cluster cross sections from pickup measurements Are the established methods consistent. *J. Chem. Phys.* **2011**, *135*, 104305.

(20) Lengyel, J.; Kočišek, J.; Poterya, V.; Pysanenko, A.; Svrčková, P.; Fárník, M.; Zaouris, D.; Fedor, J. Uptake of atmospheric molecules by ice nanoparticles: Pickup cross sections. *J. Chem. Phys.* **2012**, *137*, 034304.

(21) Lengyel, J.; Pysanenko, A.; Poterya, V.; Slavíček, P.; Fárník, M.; Kočišek, J.; Fedor, J. Irregular shapes of water clusters generated in supersonic expansions. *Phys. Rev. Lett.* **2014**, *112*, 113401.

(22) Farges, J.; de Feraudy, M. F.; Raoult, B.; Torchet, G. Structure and temperature of rare gas clusters in a supersonic expansion. *Sur. Sci.* **1981**, *106*, 95.

(23) Poterya, V.; Kočišek, J.; Pysanenko, A.; Fárník, M. Caging of Cl atoms from photodissociation of CF_2Cl_2 in clusters. *Phys. Chem. Chem. Phys.* **2014**, *16*, 421 – 429.

(24) Lengyel, J.; Pysanenko, A.; Kočišek, J.; Poterya, V.; Pradzynski, C.; Zeuch, T.; Slavíček, P.; Fárník, M. Nucleation of Mixed Nitric AcidWater Ice Nanoparticles in Molecular Beams that Starts with a HNO_3 Molecule. *J. Phys. Chem. Lett.* **2012**, *3*, 3096 – 3109.

(25) Kočišek, J.; Lengyel, J.; Fárník, M. Ionization of large homogeneous and heterogeneous clusters generated in acetylene Ar expansions: Cluster ion polymerization. *J. Chem. Phys.* **2013**, *138*, 124306.

(26) Kočišek, J.; Lengyel, J.; Fárník, M.; Slavíček, P. Energy and charge transfer in ionized argon coated water clusters. *J. Chem. Phys.* **2013**, *139*, 214308.

(27) Jansen, R.; Wysong, I.; Gimelshein, S.; Zeifman, M.; Buck, U. Nonequilibrium numerical model of homogeneous condensation in argon and water vapor expansions. *J. Chem. Phys.* **2010**, *132*, 244105.

(28) Buck, U.; Pradzinski, C. C.; Zeuch, T.; Dieterich, J. M.; Hartke, B. A size resolved investigation of large water clusters. *Phys. Chem. Chem. Phys.* **2014**, *16*, 6859 – 6871.

(29) Torchet, G.; Schwartz, P.; Farges, J.; de Feraudy, M. F.; Raoult, B. Structure of solid water clusters formed in a free jet expansion. *J. Chem. Phys.* **1983**, *79*, 6196.

(30) Pradzynski, C. C.; Forck, R. M.; Zeuch, T.; Slavíček, P.; Buck, U. A fully size-resolved perspective on the crystallization of water clusters. *Science* **2012**, *337*, 1529–1532.

(31) Abascal, J. L. F.; Vega, C. A general purpose model for the condensed phases of water: TIP4P/2005. *The Journal of Chemical Physics* **2005**, *123*, –.

(32) Kaminski, G. A.; Friesner, R. A.; Tirado-Rives, J.; Jorgensen, W. L. Evaluation and Reparametrization of the OPLS-AA Force Field for Proteins via Comparison with Accurate Quantum Chemical Calculations on Peptides. *The Journal of Physical Chemistry B* **2001**, *105*, 6474–6487.

(33) Malde, A. K.; Zuo, L.; Breeze, M.; Stroet, M.; Poger, D.; Nair, P. C.; Oostenbrink, C.; Mark, A. E. An Automated Force Field Topology Builder (ATB) and Repository: Version 1.0. *Journal of Chemical Theory and Computation* **2011**, *7*, 4026–4037.

(34) Wang, J.; Wolf, R. M.; Caldwell, J. W.; Kollman, P. A.; Case, D. A. Development and testing of a general amber force field. *Journal of Computational Chemistry* **2004**, *25*, 1157–1174.

(35) Bayly, C. I.; Cieplak, P.; Cornell, W.; Kollman, P. A. A well-behaved electrostatic potential based method using charge restraints for deriving atomic charges: the RESP model. *The Journal of Physical Chemistry* **1993**, *97*, 10269–10280.

(36) Habartová, A.; Valsaraj, K. T.; Roeselová, M. Molecular Dynamics Simulations of Small Halogenated Organics at the AirWater Interface: Implications in Water Treatment and Atmospheric Chemistry. *The Journal of Physical Chemistry A* **2013**, *117*, 9205–9215.

(37) Vácha, R.; Jungwirth, P.; Chen, J.; Valsaraj, K. Adsorption of polycyclic aromatic hydrocarbons at the air-water interface: Molecular dynamics simulations and experimental atmospheric observations. *Phys. Chem. Chem. Phys.* **2006**, *8*, 4461–4467.

(38) Poterya, V.; Fárník, M.; Slavíček, P.; Buck, U.; Kresin, V. V. Photodissociation of hydrogen halide molecules on free ice nanoparticles. *J. Chem. Phys.* **2007**, *126*, 071101.

(39) Poterya, V.; Fedor, J.; Pysanenko, A.; Tkáč, O.; Lengyel, J.; Ončák, M.; Slavíček, P.; Fárník, M. Photochemistry of HI on Argon and water nanoparticles: Hydronium radical generation in $HI{\cdot}(H_2O)_n$. *Phys. Chem. Chem. Phys.* **2011**, *13*, 2250 – 2258.

(40) Ahmed, M.; Apps, C. J.; Hughes, C.; Whitehead, J. C. The adsorption of methanol on large water clusters. *Chem. Phys. Lett.* **2007**, *240*, 216.

(41) Ahmed, M.; Apps, C. J.; Hughes, C.; Watt, N. E.; Whitehead, J. C. Adsorption of organic molecules on large water clusters. *J. Phys. Chem. A* **1997**, *101*, 1250.

(42) Ahmed, M.; Apps, C. J.; Hughes, C.; Watt, N. E.; Whitehead, J. C. Adsorption of NxOy-Based Molecules on Large Water Clusters: An Experimental and Theoretical Study. *J. Phys. Chem. A* **1997**, *101*, 1254.

(43) Moro, R.; Rabinovitch, R.; Kresin, V. V. Amino-acid and water molecules adsorbed on water clusters in a beam. *J. Chem. Phys.* **2005**, *123*, 074301.

(44) Moro, R.; Rabinovitch, R.; Kresin, V. V. Pickup cell for cluster beam experiments. *Rev. Sci. Instrum.* **2005**, *76*, 156104.

(45) Ončák, M.; Slavíček, P.; Fárník, M.; Buck, U. Photochemistry of Hydrogen Halides on

Water Clusters: Simulations of Electronic Spectra and Photodynamics, and Comparison with Photodissociation Experiments. *J. Phys. Chem. A* **2011**, *115*, 6155–6168.

(46) Ding, A.; Cassidy, R. A.; Futrell, J. H.; Cordis, L. Ion-molecule reactions within methane clusters initiated by photoionization. *J. Phys. Chem.* **1987**, *91*, 2562.

(47) Buch, V.; Bauerecker, S.; Devlin, J. P.; Buck, U.; Kazimirski, J. K. Solid water clusters in the size range of tens-thousands of H2O: a combined computational/spectroscopic outlook. *Int. Rev. Phys. Chem.* **2004**, *23*, 375.

(48) Kim, W.; Felker, P. M. *J. Chem. Phys.* **1996**, *104*, 1147.

(49) Belau, L.; Wilson, K. R.; Leone, S. R.; Ahmed, M. Vacuum ultraviolet (VUV) photoionization of small water clusters. *J. Phys. Chem. A* **2007**, *111*, 10075–10083.

(50) Nosenko, Y.; Kunitski, M.; Riehn, C.; Harbach, P. H. P.; Dreuw, A.; Brutschy, B. The structure of adenine monohydrates studied by femtosecond multiphoton ionization detected IR spectroscopy and quantum chemical calculations. *Phys. Chem. Chem. Phys.* **2010**, *12*, 863.

Graphical TOC Entry

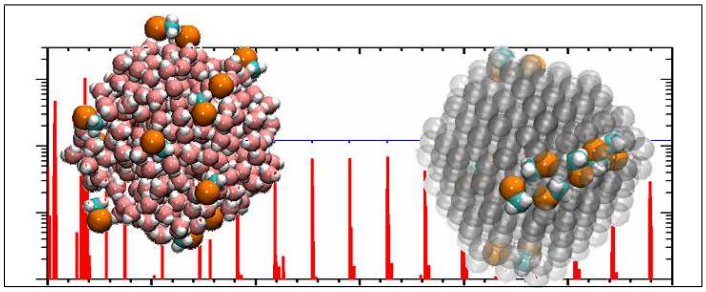

Lack of aggregation of molecules on ice nanoparticles

SUPPORTING INFORMATION

Andriy Pysanenko,[†] Alena Habartová,[*,‡] Pavla Svrčková,[†,¶] Jozef Lengyel,[†,¶] Viktoriya Poterya,[†] Martina Roeselová,[‡] Juraj Fedor,[*,†] and Michal Fárník[*,†]

J. Heyrovský Institute of Physical Chemistry v.v.i., Czech Academy of Sciences, Dolejškova 3, 18223 Prague 8, Czech Republic, and Institute of Organic Chemistry and Biochemistry v.v.i., Czech Academy of Sciences, Flemingovo nám. 2, 16610 Prague 6, Czech Republic

E-mail: alena.habartova@marge.uochb.cas.cz; juraj.fedor@jh-inst.cas.cz; michal.farnik@jh-inst.cas.cz

[*]To whom correspondence should be addressed

[†]J. Heyrovský Institute of Physical Chemistry v.v.i., Czech Academy of Sciences

[‡]Institute of Organic Chemistry and Biochemistry v.v.i., Czech Academy of Sciences

[¶]*Also at: Department of Physical Chemistry, University of Chemistry and Technology, Technická 5, 16628 Prague 6, Czech Republic*

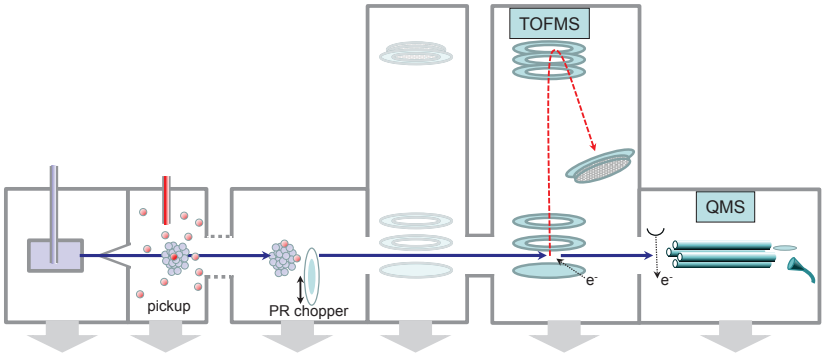

Figure 1: Scheme of the present experimental setup.

Experimental methods

Figure 1 shows the parts of universal CLUB (cluster beam) apparatus that were utilized in the present experiments. Clusters (nanoparticles) in the beam are generated via continuous supersonic expansion of either argon gas or heated water vapor through a conical nozzle. The mean cluster size $\bar{N}$ is determined from the source conditions using well-established scaling formulas[1,2] as described in our previous publications.[3,4] The mean size of argon clusters is

$$\bar{N} = K \cdot \left(\frac{\Gamma^*}{1000}\right)^{\zeta}, \Gamma^* = \frac{p_0[mbar] \cdot d_e[\mu m]^{0.85}}{T_0[K]^{2.2875}} \cdot K_c, \quad (1)$$

where $K = 38.4$ and $\zeta = 1.64$ were determined from the diffractive He atom scattering on large Ar_N clusters,[5] K_c =1646 is a characteristic constant of the expanding gas for Ar, and $d_e = d/\mathrm{tg}(\alpha/2)$ is the equivalent nozzle diameter.

Similarly, for water clusters

$$\bar{N} = D \cdot \left(\frac{\Gamma^*}{1000}\right)^{a}, \Gamma^* = \frac{\Gamma}{K_c} = \frac{n_0 \cdot d_e^q \cdot T_0^{q-3}}{K_c}, \quad (2)$$

where parameters $D = 11.6$, $a = 1.886$ and $q = 0.634$ were determined from fitting the measured size distributions of large $(H_2O)_N$ clusters.[6] The characteristic constant of the expanding gas $K_c = (r_c \cdot T_c)^{q-3}$ for water was evaluated from $r_c = 3.19$ Å and $T_c = 5684$ K.

We point out that the applicability of these formulas has been demonstrated by Buck's

Table 1: Purities and suppliers of the used chemicals

Compound	Purity	Supplier
Ar	99.998%	Messer
H_2O	distilled	Jarda Srol & Co.
HCl	anhydrous, >99%	Praxair
CH_4	99.97%	Praxair
CH_3Cl	>99.5%	Sigma-Aldrich
C_3H_7Cl	98%	Sigma-Aldrich
C_6H_6	99.8%	Lachema
C_6H_5Cl	>99.5%	Sigma-Aldrich

group in Göttingen[5,6] with the same cluster sources that are used in the present experiments. For water clusters, the reservoir temperature 420 K, stagnation pressure 4.3 bar, and nozzle with 90 μm diameter kept at 428 K lead to $\bar{N} = 430$. For argon clusters, the stagnation pressure of 7.0 bar and the 60 μm nozzle kept at 223 Kelvin leads to $\bar{N} = 330$. Both nozzles have 30 ° opening angle and 2 mm thickness.

We chose these expansion conditions to obtain argon and water clusters of approximately the same geometrical size. The geometrical cross section σ_g of the Ar_N and $(H_2O)_N$ nanoparticles is

$$\sigma_g = \pi R_N^2, R_N = R_0 N^{1/3}, R_0 = \left(\frac{3m_C}{4\pi\rho N_A}\right)^{1/3} \quad (3)$$

(N_A is Avogadro's constant). From the density ρ of solid Ar and ice we get R_0= 2.09 Å and 1.93 Å, respectively. Subsequently, the geometrical cross section is approximately the same $\sigma_g \approx 660$ Å^2 for both Ar_N and $(H_2O)_N$ of the mean sizes $\bar{N} \approx 330$ and 430. It ought to be mentioned that the geometrical cross section often includes also the radius of the molecule r_M, $\sigma_g = \pi (R_N + r_M)^2$, which is also included intrinsically in the measured cross section.[7–9] However, for the purpose of the pickup of different molecules with different radii, the geometrical cross section of the pure nanoparticles is presented here.

Table 1 shows suppliers and purities of the used chemicals.

Computational methods

All molecular dynamics calculations were performed using the GROMACS (version 4.5.4) program package.[10] The equations of motion were integrated by the leap-frog algorithm[11] with a 2 fs time step. A cut-off scheme was employed and both the Lennard-Jones and the short-range part of the Coulomb interactions were truncated to zero at 10 Å. The long-range part of the Coulomb interaction was evaluated using the smooth Particle-Mesh Ewald method[12,13] with a relative tolerance of 10^{-5}, fourth order cubic interpolation and a Fourier spacing parameter of 0.15. Temperature was controlled by the Bussi-Donadio-Parrinello (velocity rescaling with a stochastic term) thermostat[14] with a coupling time of 1 ps. All bonds were constrained by LINCS algorithm.[15] System configurations were saved at 2 ps intervals. The VMD program[16] was used for visualisation of saved trajectories to investigate structural features.

Mass spectra of adsorbed aggregates

HCl pickup: The mass spectra provide the experimental evidence for aggregation of the adsorbed molecules on Ar_N clusters. Figure 2 (a) shows the mass spectrum of pure Ar_N, $\bar{N}$= 330, clusters, and the lower panel (b) shows the spectrum of the Ar_N clusters which passed through the pickup chamber filled with HCl gas at the pressure p= 1.8×10^{-4} mbar. The upper scales label the series corresponding to the generation of HCl aggregates on Ar_N, namely the cluster ion fragments $(HCl)_m^+$ and $Ar_n\cdot(HCl)_k^+$. The spectra were measured at pickup pressures from 0.6×10^{-4} mbar to 3×10^{-4} mbar exhibiting gradual decrease of the Ar_n^+ fragment series and increase of $(HCl)_m^+$ and $Ar_n\cdot(HCl)_k^+$ series. At the highest pressure the spectrum was dominated by $(HCl)_m^+$ series. The maximum aggregate fragment size m_{max} for which the $(HCl)_m^+$ clusters were still discernible in the spectrum increased from m_{max}= 4 to 11 in the investigated pressure range, and k for the mixed fragments $Ar_n\cdot(HCl)_k^+$ increased from $k = 2$ to 6.

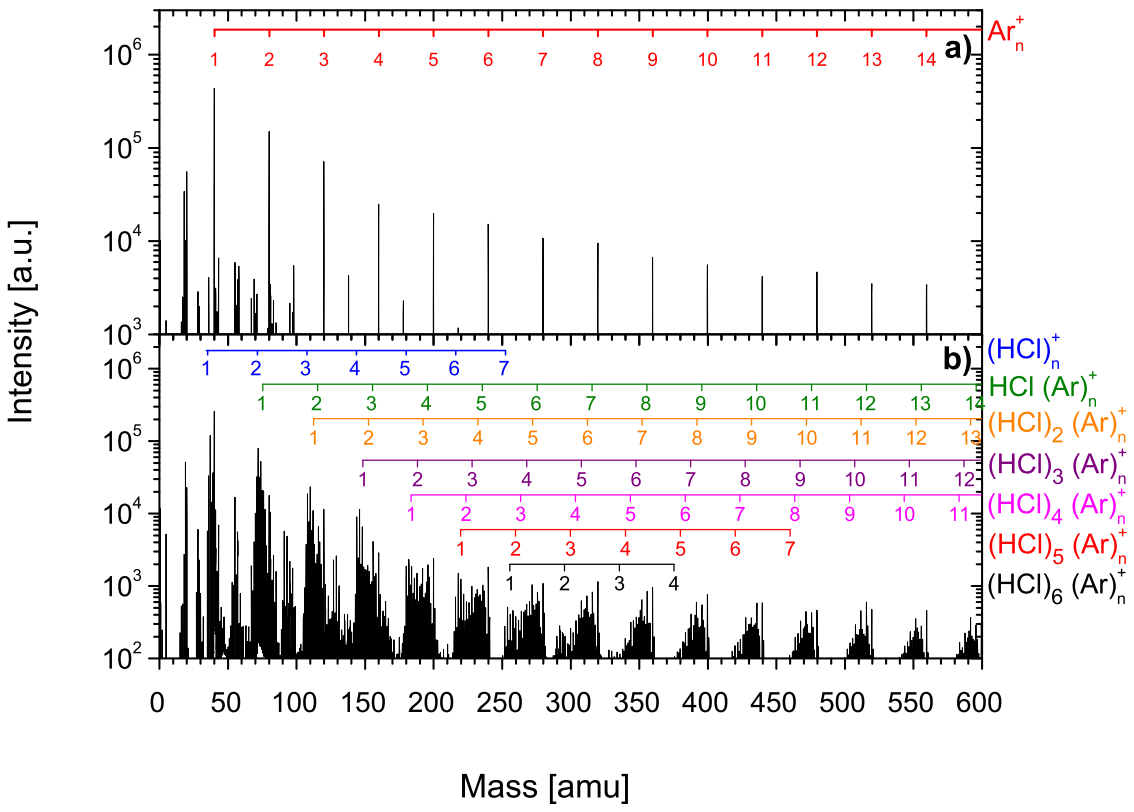

Figure 2: The mass spectrum of pure Ar_N, $\bar{N}$= 330, clusters after 70 eV electron ionization (a). The spectrum of the Ar_N clusters which passed through the pickup chamber filled with HCl gas at the pressure of 1.8×10^{-4} mbar (b). The series corresponding to the $(HCl)_m^+$ and $Ar_n\cdot(HCl)_k^+$ cluster ion fragments are labeled.

It ought to be mentioned, that due to the overlap of multiple spectra a detailed analysis was required to assign all the mass peaks unambiguously. Figure 3 shows a detail analysis of the part of the spectrum showing mass peaks corresponding to the $(HCl)_5^+$, $Ar_n\cdot(HCl)_k^+$, n= 1-4 and k= 4-1, and Ar_5^+ ion fragments. Multiple mass peaks assigned to the same cluster species occur due to the ^{35}Cl and ^{37}Cl isotopes present in the natural ratio of 3:1, and due to the presence of protonated $(HCl)_mH^+$ as well as "dehydrogenated" $(HCl)_{m-1}Cl^+$ fragments. These species appear also for the Ar containing fragments. The analysis based on the isotope ratio is outlined by the stick plot below in figure 3.

Aromatics C_6H_5Cl and C_6H_6: Extending the linear chain length of the adsorbed molecule did not have a significant influence on the clustering on Ar_N, therefore we used molecules with aromatic rings where we expected that the interaction of the ring π-electrons could change

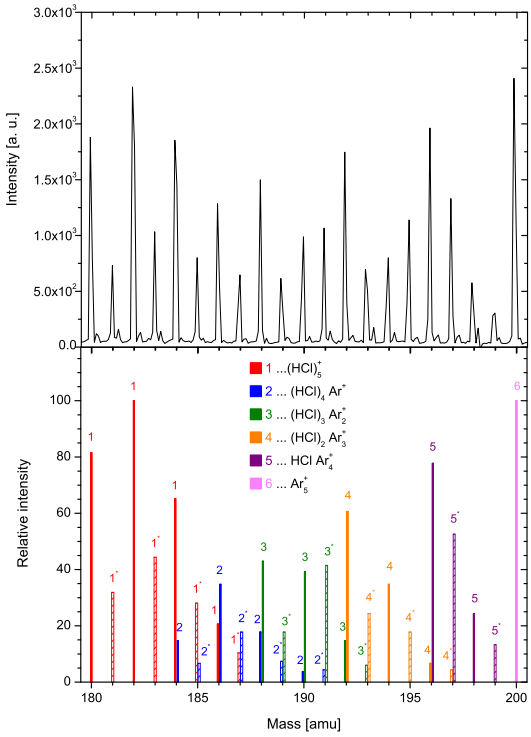

Figure 3: Detailed analysis of the mass spectrum of $Ar_N \cdot (HCl)_m$ clusters generated by pickup of HCl at the pressure of 1.8×10^{-4} mbar on Ar_N, $\bar{N}$= 330, clusters. Stick plots below show the decomposed spectra corresponding the $(HCl)_5^+$, $Ar_n \cdot (HCl)_k^+$, n= 1-4 and k= 4-1, and $Ar-5^+$ ion fragments, considering the ^{35}Cl and ^{37}Cl isotope ratio of 3:1. See text for more details.

the coagulation behavior. Figure 4 (a) and (b) show the Ar_N cluster mass spectra after the pickup of C_6H_6 (a), and C_6H_5Cl (b). However, the spectra exhibit essentially the same clustering behavior as the linear molecules above: $(C_6H_6)_m^+$, and $Ar_n \cdot (C_6H_6)_k^+$,fragments with m_{max}= 9 and k= 1-5, for benzene at the highest pickup pressure p= 0.9×10^{-4} mbar; and $(C_6H_5Cl)_m^+$, and $Ar_n \cdot (C_6H_5Cl)_k^+$,fragments with m_{max}= 7 and k= 1-3, for chlorobenzene at the highest pickup pressure p= 0.7×10^{-4} mbar. Thus these aromatic molecules clearly coagulate to the larger clusters on Ar_N as well.

Pickup on water clusters $(H_2O)_N$: No evidence for the generation of any molecular aggregates was found in any mass spectra after the uptake of all the molecules on the ice nanoparticles $(H_2O)_N$, $\bar{N}$= 430 under analogical conditions as above. Figure 5 shows an example of the water cluster spectrum after the benzene pickup at the pickup pressure

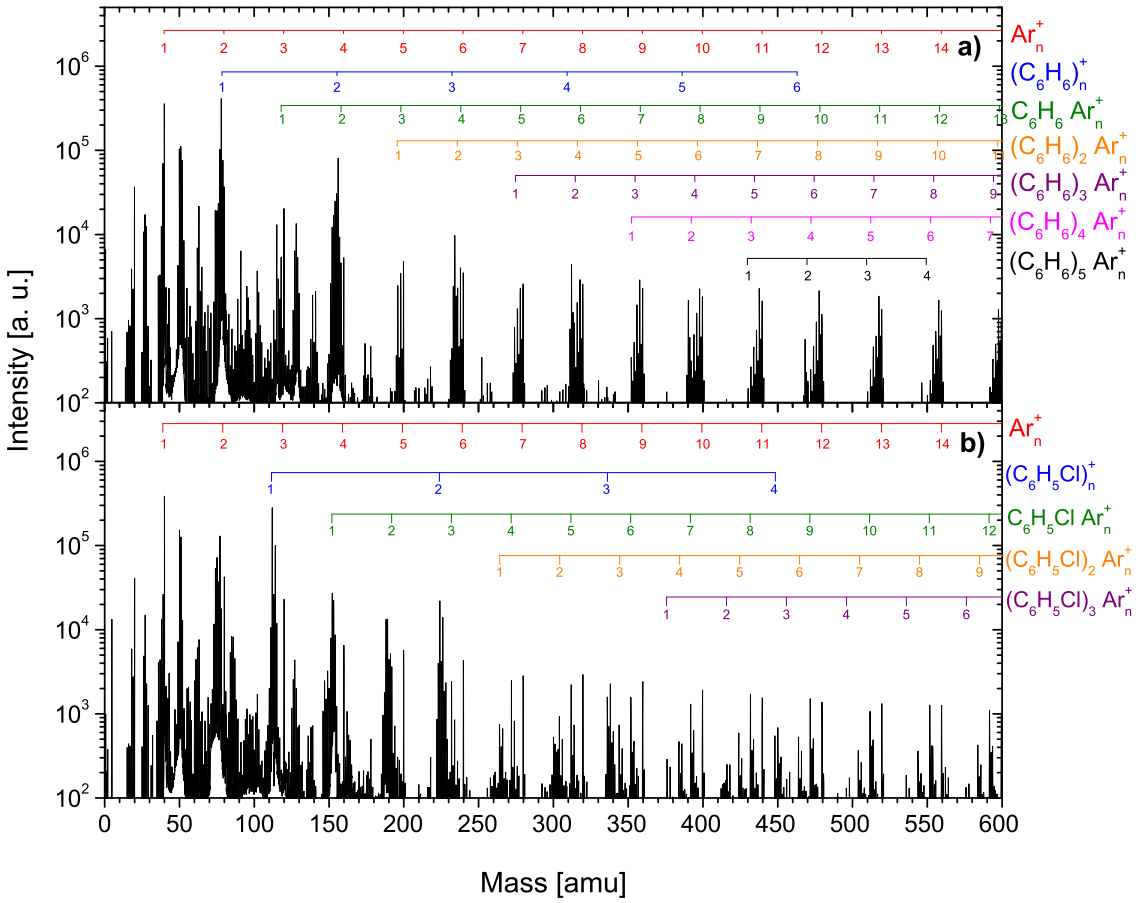

Figure 4: The mass spectrum of Ar_N, $\bar{N}$= 330, clusters after the pickup of C_6H_6 at p= 0.5×10^{-4} mbar (a), C_6H_5Cl at p= 0.4×10^{-4} mbar (b). The series corresponding to the different cluster ion fragments are labelled.

p= 0.7×10^{-4} mbar. Besides the series of protonated water cluster fragments $(H_2O)_nH^+$ there is only the mass peak corresponding to parent benzene ion $C_6H_6^+$ at 78 amu. It ought to be mentioned that the background of any C_6H_6 molecules diffused more than 1 m from the pickup chamber through the two separate differentially pumped chambers into the TOF chamber was small and carefully subtracted. Thus the C_6H_6 molecules could arrive in the TOF only with the $(H_2O)_N$ clusters. In the article, we provide further proofs that the molecules are adsorbed on the $(H_2O)_N$ nanoparticles but the mass spectra show that they do not coagulate into clusters on $(H_2O)_N$. Similar conclusions can be drawn from the mass spectra after the pickup of chlorobenzene C_6H_5Cl (figure 6), HCl and CH_3Cl (shown in the article).

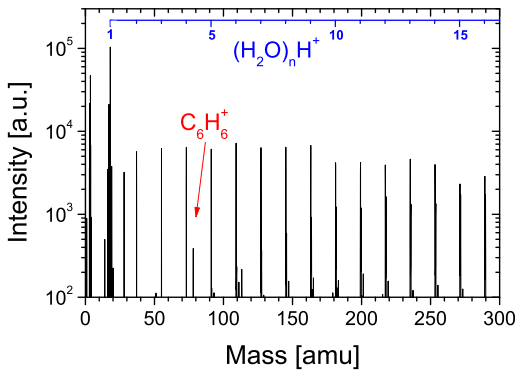

Figure 5: The mass spectrum of $(H_2O)_N$, $\bar{N}$= 430, clusters after the pickup of C_6H_6 at the pickup pressure p= 0.9×10^{-4} mbar.

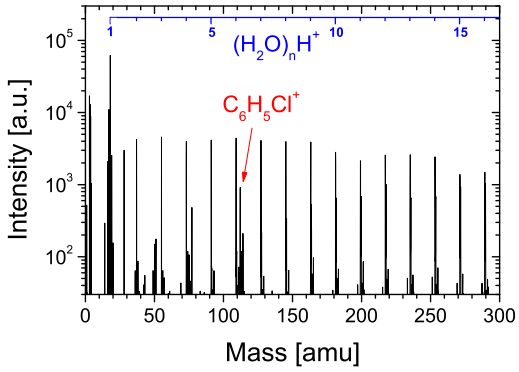

Figure 6: The mass spectrum of $(H_2O)_N$, $\bar{N}$= 430, clusters after the pickup of C_6H_5Cl at the pickup pressure p= 0.7×10^{-4} mbar.

References

(1) Hagena, O. F. *Surf. Sci.* **1981**, *106*, 101 – 116.

(2) Hagena, O. F. Condensation in free jets: comparison of rare gases and metals. *Z. Phys. D* **1987**, *4*, 291 – 299.

(3) Fedor, J.; Poterya, V.; Pysanenko, A.; Fárník, M. Cluster cross sections from pickup measurements Are the established methods consistent. *J. Chem. Phys.* **2011**, *135*, 104305.

(4) Lengyel, J.; Kočišek, J.; Poterya, V.; Pysanenko, A.; Svrčková, P.; Fárník, M.; Za-

ouris, D.; Fedor, J. Uptake of atmospheric molecules by ice nanoparticles: Pickup cross sections. *J. Chem. Phys.* **2012**, *137*, 034304.

(5) Buck, U.; Krohne, R. Cluster size determination from diffractive He atom scattering. *J. Chem. Phys.* **1996**, *105*, 5408 – 5415.

(6) Bobbert, C.; Schütte, S.; Steinbach, C.; Buck, U. Fragmentation and reliable size distributions of large ammonia and water clusters. *Eur. Phys. J. D* **2002**, *19*, 183–192.

(7) Zamith, S.; Feiden, P.; Labastie, P.; L'Hermite, J.-M. Sticking Properties of Water Clusters. *Phys. Rev. Lett.* **2010**, *104*, 103401.

(8) Zamith, S.; Feiden, P.; Labastie, P.; L'Hermite, J.-M. Attachment cross sections of protonated water clusters. *J. Chem. Phys.* **2010**, *133*, 154305.

(9) Zamith, S.; de Tournadre, G.; Labastie, P.; L'Hermite, J.-M. Attachment cross-sections of protonated and deprotonated water clusters. *J. Chem. Phys.* **2013**, *138*, 034301.

(10) Hess, B.; Kutzner, C.; van der Spoel, D.; Lindahl, E. GROMACS 4: Algorithms for Highly Efficient, Load-Balanced, and Scalable Molecular Simulation. *Journal of Chemical Theory and Computation* **2008**, *4*, 435–447.

(11) Hockney, R.; Goel, S.; Eastwood, J. Quiet high-resolution computer models of a plasma. *Journal of Computational Physics* **1974**, *14*, 148–158.

(12) Darden, T.; York, D.; Pedersen, L. Particle mesh Ewald: An Nlog(N) method for Ewald sums in large systems. *The Journal of Chemical Physics* **1993**, *98*, 10089.

(13) Essmann, U.; Perera, L.; Berkowitz, M. L.; Darden, T.; Lee, H.; Pedersen, L. G. A smooth particle mesh Ewald method. *The Journal of Chemical Physics* **1995**, *103*, 8577.

(14) Bussi, G.; Donadio, D.; Parrinello, M. COMP 8-Canonical sampling through velocity rescaling. *Abstract of papers of the American Chemical Society* **2007**, *234*.

(15) Hess, B.; Bekker, H.; Berendsen, H.; Fraaije, J. LINCS: A linear constraint solver for molecular simulations. *The Journal of Computational Chemistry* **1997**, *18*, 1463–1472.

(16) Humphrey, W.; Dalke, A.; Schulten, K. VMD: Visual molecular dynamics. *Journal of Molecular Graphics* **1996**, *14*, 33–38.

Theor Chem Acc (2014) 133:1455
DOI 10.1007/s00214-014-1455-z

REGULAR ARTICLE

Partial hydration of *n*-alkyl halides at the water–vapor interface: a molecular simulation study with atmospheric implications

Alena Habartová · Anthony Obisesan · Babak Minofar · Martina Roeselová

Received: 14 October 2013 / Accepted: 18 January 2014

Abstract Classical molecular dynamics simulations with a polarizable force field were used to study adsorption of gas-phase alkyl halides to the surface of liquid water and their hydration properties in the interfacial environment. A systematic investigation has been performed for a set of monosubstituted alkyl chlorides, bromides and iodides of the alkyl chain length from one to five carbon atoms ($C_nH_{2n+1}X$, $n = 1$–5, X = Cl, Br, or I). All alkyl halides readily adsorb to the water surface and exhibit a strong preference for interfacial (partial) hydration. When adsorbed, the alkyl halide molecules reside primarily in the outermost region of the water–vapor interface. The (incomplete) hydration shell of the surface-adsorbed methyl halide species is centered on the methyl end of the molecule, with the halogen atom largely exposed and facing away from water into the gas phase. The maximum hydration of the longer-chain alkyl halides is localized around the α-CH_2 group next to the halogen. With an increasing chain length, the alkyl halide molecules align more parallel to the surface. However, ethyl and propyl halides still have the halogen atom rather exposed, pointing almost freely into the gas phase. The behavior of butyl and pentyl halides on the water surface resembles that of alcohols, with the polar region of the CH_2X group interacting with water and the rest of the increasingly nonpolar hydrocarbon chain pointing on average away from water. Consequently, the halogen atom becomes more, albeit not fully, hydrated. The propensity of alkyl halides for the water–vapor interface along with the specific character of the partial hydration of the surface-adsorbed alkyl halides and their preferred interfacial orientation is likely to be of importance for heterogeneous chemical processes, involving alkyl halides adsorbed on the surface of aqueous aerosol droplets or ice particles in the atmosphere.

Keywords Halogenated organics · Haloalkanes · Adsorption · Interfacial solvation · Interfacial partitioning · Surface orientation · Heterogeneous chemistry

Electronic supplementary material The online version of this article (doi:10.1007/s00214-014-1455-z) contains supplementary material, which is available to authorized users.

A. Habartová · A. Obisesan · M. Roeselová (✉)
Institute of Organic Chemistry and Biochemistry, Academy of Sciences of the Czech Republic, Flemingovo nám. 2, 16610 Prague 6, Czech Republic
e-mail: martina.roeselova@uochb.cas.cz

A. Obisesan
Department of Chemistry, California State University Los Angeles, 5151 State University Drive, Los Angeles, CA 90032, USA

B. Minofar
Institute of Nanobiology and Structural Biology, Academy of Sciences of the Czech Republic, Zámek 136, 37333 Nové Hrady, Czech Republic

B. Minofar
Faculty of Science, University of South Bohemia, Branišovská 31, 37005 České Budějovice, Czech Republic

1 Introduction

Halogenated organic compounds are abundant throughout the atmosphere [1–3]. They are emitted from a number of different sources, both biogenic and anthropogenic. The main natural source has been attributed to oceanic origin [4–6], including the coastal marine biota [7] and salt marshes [8, 9]. Terrestrial sources have also been determined [10], and they include biomass burning [11], oxidative degradation of organic matter in soils [12], and

Published online: 01 February 2014

volcanic emissions [13]. In addition, halogenated organics are produced in industry for the use as pesticides, herbicides, insecticides, fungicides, refrigerants, flame retardants and anesthetics [14–18]. Other anthropogenic sources include human-caused biomass burning [19], and gasoline combustion [20]. Of the halogenated organic compounds, small haloalkane species are particularly abundant in the atmosphere and play an important role in atmospheric reactions. Specifically, short-chain alkyl halides, such as methyl chloride (CH_3Cl), methyl bromide (CH_3Br), methyl iodide (CH_3I), ethyl chloride (C_2H_5Cl), ethyl bromide (C_2H_5Br), ethyl iodide (C_2H_5I), as well as 1-propyl iodide (C_3H_7I) and other propyl halides, have been observed in field studies, along with various multi-substituted halomethanes and haloethanes [4, 6, 7, 12, 14, 21–24].

Most of the alkyl halides are relatively short-lived, as they are rapidly oxidized in the troposphere (the primary sink being the reaction with OH radical) or undergo photochemical degradation [1]. For example, CH_3I has an atmospheric lifetime of 1 week [18], the lifetimes of C_2H_5Cl and C_2H_5Br in the troposphere are of the order of 1 month [14]. (Photo)chemical processing of alkyl halides in the troposphere can release free halogen radicals, which then react with hydrocarbons and are involved in the chemistry of tropospheric ozone, odd nitrogen species (NO, NO_2, HNO_3) and odd hydrogen radicals ($HO_x = HO_2 + OH + H$) [14, 25, 26]. Unlike the other alkyl halides, however, CH_3Cl and CH_3Br are not subject to tropospheric removal. Their relatively long tropospheric lifetimes ($\sim$1 year), combined with their large fluxes into the atmosphere, result in significant amounts of these two species reaching the stratosphere, where their halogen atoms, released through photolysis, contribute to ozone depletion [24, 27–29]. Methyl bromide, in particular, has a large ozone-depleting potential, because bromine is about 50 times more effective than chlorine in destroying ozone as it reacts with reservoir chlorine species, freeing the chlorine to react with additional ozone. Methyl bromide is included in the set of substances controlled under the 1987 Montreal Protocol and its production has been subject to an international phaseout [18, 24].

Alkyl halides contribute significantly to the total amount of halogenated organic gases in the atmosphere. Research to determine the distribution and relative magnitudes of natural and anthropogenic fluxes of alkyl halides has led to much progress, however, their sources and sinks are not yet fully clarified and their global budgets remain imbalanced [30–32]. Thus, in addition to further field measurements and atmospheric modeling studies, there is a need for better understanding of the molecular mechanisms that play a role in the complex biogeochemical cycles of alkyl halides on the local as well as global scales.

Naturally, gas-phase chemical reactions are very important in the atmosphere, as are the reactions taking place in the liquid phase—inside aqueous aerosol, cloud and fog droplets or other kinds of atmospheric moisture. Furthermore, aqueous-phase reactions occurring in the oceans, lakes, rivers, etc., greatly affect atmospheric composition and processes. It has been shown, however, that homogeneous, single-phase reactions may not be sufficient in characterizing the complex atmospheric processes, and heterogeneous reactions occurring at the air–water and air–ice interfaces need to be taken into account. The prime example is the heterogeneous reactions on the surfaces of polar stratospheric clouds resulting in the "ozone hole" formation in the Antarctic [33]. (Photo)chemical reactions on aqueous and ice surfaces in the troposphere play an equally important role [1, 34, 35].

As far as alkyl halides are concerned, a number of photochemical reactions have been studied in the gas phase as well as in solution [36–39], in cryogenic matrices [40] and in amorphous solid water [41, 42]. Interaction of haloalkanes with water vapor, formation of alkyl chloride–water complexes and hydrolysis of alkyl halides to the respective alcohols have been investigated theoretically by means of quantum chemical methods [43–46]. Heterogeneous processes involving alkyl halides received considerably less attention. Interaction of methyl chloride (CH_3Cl) with D_2O co-adsorbed on Pd(111) surfaces was studied using femtosecond sum frequency generation spectroscopy [47], photoinduced reaction dynamics of methyl bromide (CH_3Br) and iodide (CH_3I) on MgO(100) was probed by time delayed multi photon ionization mass spectrometry [48], photodissociation dynamics of methyl iodide (CH_3I) adsorbed on amorphous solid water has been investigated using laser resonance-enhanced multiphoton ionization [49], and photochemistry of CD_3Br co-adsorbed with oxygen on Ru(001) was studied by temperature programmed desorption [50]. While these studies provided significant insight into heterogeneous reaction dynamics of alkyl halides, showing for instance the importance of surface adsorption structure and alignment of the alkyl halide molecules, they have focused predominantly on methyl halides, CH_3X, at solid and/or low temperature surfaces, such as surfaces of metals or amorphous solid water.

Alkyl halide species have been observed in the polar regions and at high altitudes, where they can interact with deep-frozen water surfaces. However, a variety of alkyl halides are found in the boundary layer at mid-latitudes [51, 52] where there is significant potential for interfacial chemistry on liquid surfaces of aqueous aerosols, fog and cloud droplets, the open ocean and also on the quasi-liquid layer of ice. Understanding the adsorption, solvation and dynamics of alkyl halides at the surface of liquid water, which can provide vital information for characterizing such

chemical reactions, is therefore as important as on ice or amorphous solid water. Surface-sensitive techniques such as the sum frequency generation spectroscopy are, in principle, well suited for investigation of molecules at aqueous interfaces. However, the relatively weak alkyl halide–water interaction compared to more traditional surface-active species (e.g., alcohols), resulting in significantly lower surface density and higher orientational disorder, makes the detection of surface-adsorbed alkyl halides a challenging task for this method at ambient temperatures [53].

In the absence of experimental data, computational chemistry methods can be a useful tool to learn about alkyl halide–water interactions. Ab initio calculations have been used to study microhydration of methyl chloride, methyl bromide and pentyl chloride in small water clusters [43, 44, 54]. In addition, hydration properties of a few selected chlorinated and brominated haloalkanes at an extended water–vapor interface have been explored using classical and ab initio molecular dynamics (MD) simulations [53–55]. The latter studies, co-authored by some of us, showed for all of the alkyl halides investigated (methyl chloride/bromide, butyl chloride/bromide and pentyl chloride) a strong preference to reside at the water–vapor interface, similar to other small organic molecules and atmospheric gases [56–61]. Both the classical and ab initio MD simulations also showed that the surface-adsorbed methyl chloride and bromide molecules are preferentially oriented with the methyl group toward water. For butyl and pentyl chloride/bromide, due to their longer nonpolar hydrocarbon chain, a parallel alignment at the water surface was found with the hydrocarbon chain pointing on average slightly to the gas phase.

Heterogeneous reactions occurring in interfacial (multiphase) environments often proceed via different mechanisms and/or with different outcomes than chemical reactions of the same reactants in a homogeneous medium (such as in the gas phase or in aqueous solution) [35]. Unlike in the homogeneous phase, where all spatial orientations of a molecule are equally probable, the alignment imposed by the contact of the molecule with a surface is an important aspect of its interfacial chemical reactivity [50, 62, 63]. While in some cases the confining environment of a surface results in photochemical activity that is sensitive to the molecular orientation [50], in other cases the photochemistry of surface-adsorbed species is not significantly different from that of its gas-phase counterpart [64]. In addition, the asymmetric solvation and/or the reduced cage effect of an incomplete solvent shell may enhance certain reaction channels, while suppressing other ones [65–67].

The distinctly different surface orientation of methyl chloride/bromide and their longer-chain counterparts (butyl and pentyl chloride/bromide) observed in the previous computational studies [53, 54] indicates that significant changes in the character of the hydration of the C–X bond occur as one proceeds along the homologous series of alkyl halides. This, in turn, is likely to have consequences for the heterogeneous (photo) chemistry of alkyl halides on aqueous surfaces. While the previous studies were performed only for selected alkyl halide species, it is the aim of the present paper to systematically investigate the interfacial behavior of a series of *n*-alkyl halides (R–X, where X = Cl, Br, or I, and R = C_nH_{2n+1}, n = 1–5), in order to obtain a more complete picture of molecular orientation and hydration structure of alkyl halides, when adsorbed on the surface of liquid water. In addition to a full set of alkyl chlorides and bromides, the current study includes also alkyl iodides, which, to the best of our knowledge, have not been previously investigated as regards their adsorption at the liquid water–vapor interface.

We report results of classical MD simulations in which individual alkyl halide molecules interact with the surface of a liquid water slab at room temperature. The MD trajectories were analyzed in terms of propensity for interfacial solvation, surface residence times, interfacial alignment and hydration shell structure of the surface-adsorbed alkyl halide molecules. The comparison within the set of *n*-alkyl halide species allows us to characterize the trends in interfacial hydration properties of alkyl halides, depending on the type of the halogen substituent and the length of the hydrocarbon chain. The results are discussed in the context of heterogeneous reactions of alkyl halides on atmospheric aqueous-vapor and ice-vapor interfaces.

2 Computational methods

Interaction of alkyl halides with the aqueous surface was studied by classical MD simulations with polarizable force fields. We focused on *n*-alkyl halides with a general formula R–X, where X stands for Cl, Br or I, and R = C_nH_{2n+1}. The number of carbon atoms in the alkyl chain, n, was varied from 1 to 5. In the rest of the paper, the alkyl halide species with the chain length of 1 through 5 carbon atoms will be referred to as MeX, EtX, ProX, BuX, and PenX, X = Cl, Br or I. The simulated systems consisted of 2 (identical) alkyl halide molecules and 863 water molecules, forming a slab of liquid in the central part of the simulation box, with two water–vapor interfaces perpendicular to the z-axis. The x-, y- and z-dimensions of the rectangular parallelepiped simulation box were set to 30.0, 30.0 and 100.0 Å, respectively. Periodic boundary conditions were applied in all three dimensions. The setup of the systems can be seen in Fig. 1, showing typical snapshots from simulations of MeCl through PenCl.

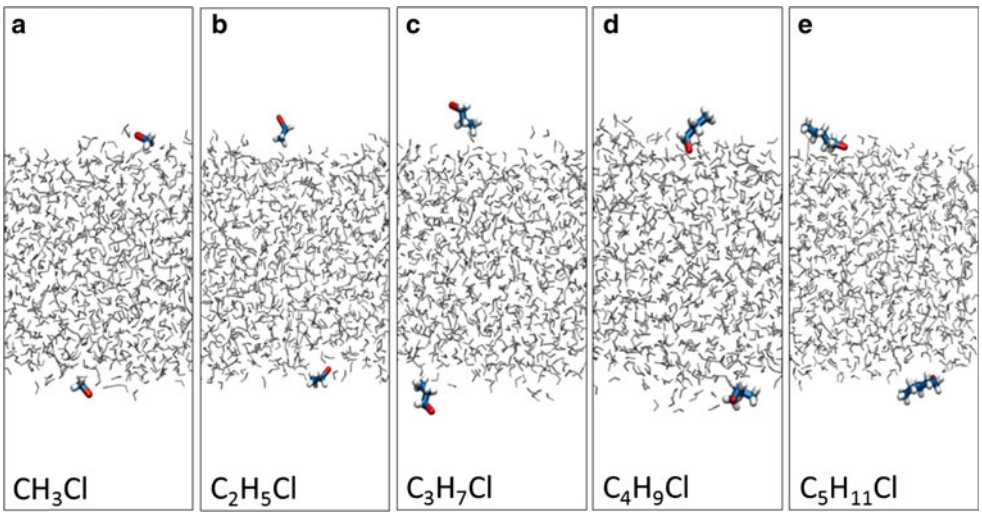

Fig. 1 Examples of the simulated systems showing the water slab placed in the central part of the simulation box and two identical alkyl halide molecules, each at one of the water–vapor interfaces: **a** methyl chloride, **b** ethyl chloride, **c** propyl chloride, **d** butyl chloride and **e** pentyl chloride. Color coding: water—*dark gray*, carbon—*cyan*, hydrogen—*light gray*, chlorine—*red*. The same system setup was employed for alkyl bromides and iodides

The alkyl halide species were modeled using the general amber force field (GAFF) [68], whereas for water molecules the POL3 model [69] was employed. Thus, in addition to the standard Lennard-Jones repulsion and dispersion interactions and the Coulomb forces between the charged sites, description of both water and alkyl halides included an explicit treatment of polarization interaction. This approach has been successfully used in a previous MD study of selected alkyl chlorides and bromides [53] and has been validated by comparison with ab initio structure calculations on alkyl halide–water clusters [43, 44, 54, 70] and ab initio MD of alkyl chlorides on water surface [54]. To obtain partial charges at the atom sites of the alkyl halide molecules, ab initio geometry optimization using the Gaussian 03 package [71] was performed, employing the MP2/cc-pVDZ method. The cc-pVDZ basis set for the iodine atom was downloaded from the Basis Set Exchange web page of the EMSL basis set library [72–74]. The ab initio calculation was followed by the restrained electrostatic potential (RESP) fitting according to the Merz–Singh–Kollman scheme [75] using the Antechamber program [76] of the Amber program package [68, 77]. The optimized geometries, atomic charges and other force field parameters of all alkyl halide molecules considered in this study are summarized in the Supplementary Information.

As the starting configuration for each simulation, two identical alkyl halide molecules were added into the simulation box containing a pre-equilibrated liquid water slab. The alkyl halide molecules were placed in the gas-phase region of the box, approximately 2 Å away from either of the two interfaces. Upon energy minimization, all systems were equilibrated for several hundred picoseconds, followed by a 20 ns production run. The simulations were carried out in the NVT ensemble at 300 K, and the temperature was controlled by the Berendsen thermostat [78] with the coupling constant of 0.05 ps. Equations of motion were integrated using the leap-frog algorithm [79] with a timestep of 1 fs. The short-range nonbonded interactions were truncated to zero beyond the cut-off distance of 12.0 Å, and the long-range part of the electrostatic interactions was accounted for by the particle mesh Ewald method [80, 81]. In the alkyl halide molecules, all bonds involving hydrogen atoms were constrained using the SHAKE algorithm [82], water molecules were kept rigid by SETTLE [83]. Atomic coordinates were sampled for analysis at 5 ps intervals. All simulations were performed employing Amber8 [68] or Amber11 [77] program packages. VMD program was utilized for visualizations [84].

3 Results

Typical results of MD simulations of alkyl halide molecules interacting with a liquid water slab are shown for alkyl chlorides in Fig. 2, where the z-coordinate of the chlorine atom is plotted versus time for a 2 ns segment selected from the 20 ns simulation. The simulations of alkyl bromides and alkyl iodides yielded essentially the same picture and, therefore, are not shown here. In each case, the simulation box contained two (identical) alkyl chloride molecules marked red and green. The center of the slab is set to $z = 0$, the bulk water region is situated approximately between $z = \pm 12$ Å. The two pairs of horizontal dashed lines indicate the approximate location of the two water–vapor interfaces, corresponding to the interval of z-coordinates, in which water density decreases from 90 to 10 % of its bulk value (the so-called "90–10" definition of the liquid–vapor interface). As can be seen from Fig. 2, alkyl chlorides remain most of the time within the interfacial water layer. Visual inspection of the

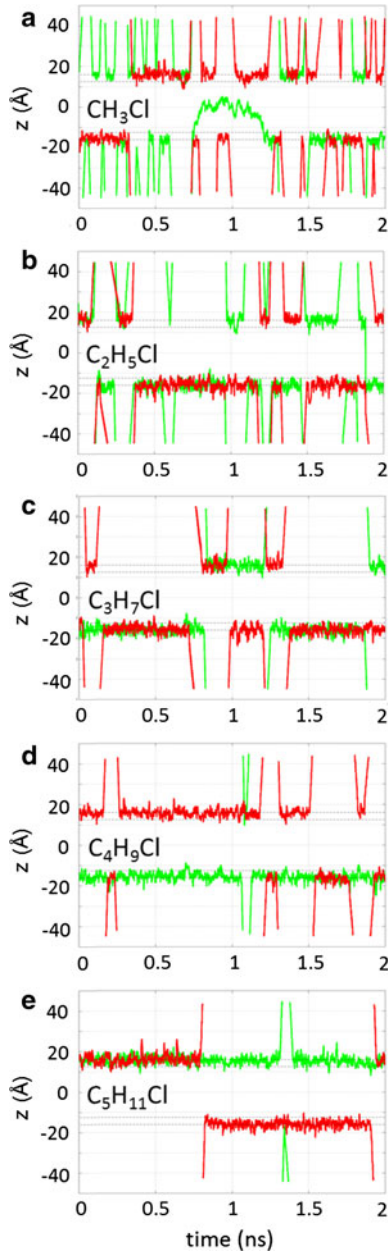

Fig. 2 Trajectories of two identical alkyl chloride molecules interacting with the water slab (one depicted in *red* and the other one in *green*), projected onto the z-coordinate normal to the water–vapor interface: **a** methyl chloride, **b** ethyl chloride, **c** propyl chloride, **d** butyl chloride and **e** pentyl chloride. A 2 ns section of the simulation data is shown in each case. The approximate location of the two water–vapor interfaces of the water slab is indicated by the horizontal dashed lines, $z = 0$ corresponds to the middle of the slab

simulation trajectories reveals that, while adsorbed, the alkyl chloride molecules readily diffuse on the surface of water. They, however, only seldom become fully solvated in the bulk liquid. On the other hand, they frequently undergo desorption into the gas phase. Due to the periodic boundary conditions, if a molecule evaporates from the water surface and leaves the simulation box, it will re-enter the box from the opposite side and impinge onto the other surface of the aqueous slab. A molecule can also diffuse from one interface to the other through the water slab. Thus, both alkyl chloride molecules are sometimes present at the same interface during the simulation, although they mostly remain laterally well-separated and rarely get into the vicinity of each other.

The series of Fig. 2a through e illustrates the effect of the chain length on the behavior of an alkyl chloride molecule. While MeCl did occasionally enter the interior of the water slab and became fully solvated, such episodes were rare and on average shorter with EtCl and ProCl. In the course of the 20 ns trajectory, EtCl exhibited only four absorption events, one of which can be seen in Fig. 2, and a single absorption event of ProCl occurred (not shown in Fig. 2). No uptake of BuCl and PenCl was observed during the entire 20 ns simulations. At the same time, as the alkyl chain gets longer, the volatility of alkyl halides decreases; the molecule spends more time at the surface and its interfacial residence times get (on average) longer. Alkyl bromides and iodides show similar trends, albeit with increasingly longer residence times (from chlorides to bromides to iodides), which can be rationalized in terms of increasing strength of their interaction with the surface of water due to stronger dispersion and induction forces between the larger halogen atoms and water.

To quantify the above trends obtained from the computed MD trajectories, we identified the individual surface residence events and determined their duration for each alkyl halide species. The duration of a residence event was defined as the time continuously spent by a molecule within one of the liquid–vapor interfacial regions of the water slab, i.e., either within the z-coordinate interval from 6 to 25 Å or from −6 to −25 Å. Note that these z-coordinate limits differ from the standard (averaged) "90–10" definition of the water–vapor interface; they were chosen so as to account for fluctuations of the instantaneous position of alkyl halide molecules along the interface normal when adsorbed at the water surface. By assuming first-order kinetics, we obtained a characteristic surface residence time, τ, of each compound as the e-folding lifetime calculated by fitting the residence times distribution to an exponential function $f(t) = A \exp(-t/\tau)$. An example of the analysis of the residence events is shown for MeCl in the Supplementary Information, Figure S1. Results for the full set of alkyl chloride species, obtained using the above described procedure, are summarized in Table 1. The residence times increase systematically with the chain length, from about one or two hundred picoseconds for MeCl and EtCl to about one nanosecond for PenCl. Similar increase by roughly an order of magnitude between the methyl and pentyl species was observed also for alkyl bromides and iodides, albeit their residence times are on average

Table 1 Average residence times of alkyl chlorides at the water–vapor interface (numbers in parenthesis correspond to the 95 % confidence interval)

	CH_3Cl	C_2H_5Cl	C_3H_7Cl	C_4H_9Cl	$C_5H_{11}Cl$
τ (ps)	140 (124,158)	197 (162,250)	535 (437,690)	662 (492,1010)	1007 (684,1915)

Table 2 Average residence times of methyl chloride, methyl bromide and methyl iodide at the water–vapor interface (numbers in parenthesis correspond to the 95 % confidence interval)

	CH_3Cl	CH_3Br	CH_3I
τ (ps)	140 (124,158)	161 (144, 183)	178 (157,205)

somewhat longer with respect to the corresponding alkyl chlorides. The increase of residence times in the series chloride–bromide–iodide is illustrated in Table 2 for the case of methyl halides. However, it should be noted that these calculations were performed to provide only a qualitative picture of the surface residence times and the effects due to the increasing chain length and the size of the halogen. We would like to emphasize that the precision, with which the values of τ were determined (expressed using the 95 % confidence interval in Tables 1 and 2), decreases substantially for the longer-chain species because as the individual residence events get longer with increasing molecular size (and, hence, larger attraction with the water surface), the total number of events within a fixed simulation time drops down dramatically (see Fig. 2). For example, less than 80 residence events were detected for ProCl and only about 20 for PenCl during a 20 ns long simulation, compared to over 200 events for MeCl.

The overall solvation preferences of alkyl halide species at the water–vapor interface can be visualized in terms of the probability distribution (density profile) in the direction normal to the interface. The results are shown in Fig. 3. In each plot, the gray curve corresponds to the density of water that gradually decreases across the water–vapor interfacial region from its constant bulk liquid value to (almost) zero in the vapor phase. The thin dashed horizontal line represents the Gibbs dividing surface (GDS), which is approximated by the position along the z-axis halfway between where the water density is 10 and 90 % of the bulk value. This is to provide a common point of reference for the location of water surface in each system and guide the eye in the figures. The blue curves denote the terminal carbon of the alkyl chain (the CH_3 carbon), and the curves corresponding to the halogen atoms are depicted in orange (Cl), brown (Br) and purple (I). All density

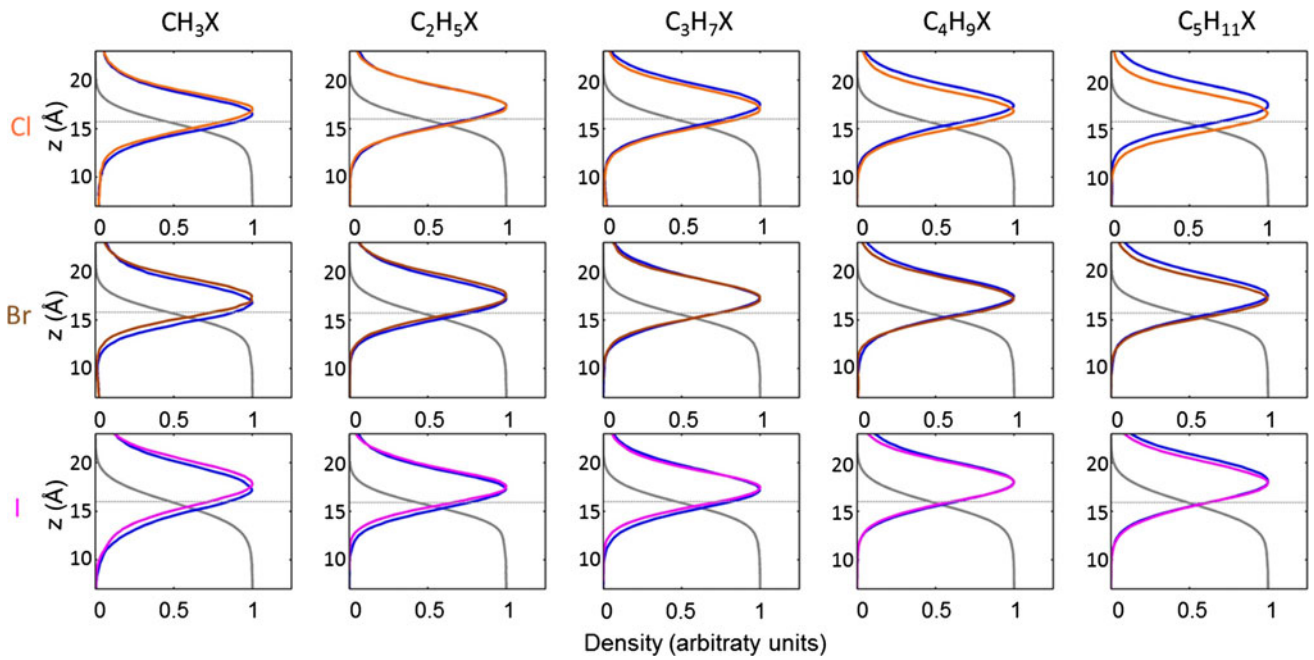

Fig. 3 Density profiles of alkyl halides across the water–vapor interface of the water slab. Color coding: *gray*—water, *blue*—carbon atom of the terminal CH_3 group, *orange*—chlorine, *brown*—bromine, *purple*—iodine. The *horizontal dashed line* denotes the Gibbs dividing surface representing the approximate location of the water–vapor interface. All density profiles were averaged over the two equivalent interfaces, the halogen and carbon profiles were normalized by the corresponding density maximum

profiles were averaged over the two equivalent interfaces and scaled by the respective density maximum.

In Fig. 3, all alkyl halide densities are significantly enhanced in the interfacial region compared to the gas as well as the bulk liquid phases. This corroborates the overall picture obtained from the trajectories (Fig. 2) and demonstrates the propensity of all of the present alkyl halide species for the water–vapor interface. As discussed above, the smaller molecules (especially methyl halides) were observed to occasionally enter the interior of the water slab, albeit only for short periods of time relative to the total length of the simulation. This is reflected in the corresponding density profiles penetrating somewhat deeper into the aqueous phase and having non-zero value in the bulk region of the water slab when compared to the longer-chain species. At the same time, the interaction of all alkyl halides with the water surface is rather weak and, while adsorbed at the surface, they are found predominantly in the outermost region of the aqueous interface. This can be seen from the positions of the density profile maxima, which are all located outside of the GDS. Finally, a non-zero value of density profiles in the gas-phase region, in particular for the smaller alkyl halides, is due to their frequent desorption from the aqueous surface. The above described solvation behavior is characteristic for all of the alkyl halides investigated here, with only minor differences between alkyl chlorides, bromides and iodides.

In addition to the propensity of alkyl halides to reside in the aqueous interfacial region, the density profiles displayed in Fig. 3 also provide information on the preferred molecular orientation of each species at the water surface. This can be inferred from the relative displacement between the density profiles of the halogen atom and the carbon of the CH_3 group in each case. In accord with previous studies [53, 54], the interfacial density peak of the carbon atom of all three methyl halides is shifted toward the interior of water slab relative to the halogen atom, indicating that the methyl halide molecules are oriented with the CH_3 group on average closer to water and with halogen atom pointing to the gas phase. As one proceeds in Fig. 3 along the homologous series for Cl, Br and I, the relative positions of the two density profile curves change. With an increasing chain length, both the curves first overlap, indicating parallel alignment of the molecule with the surface. Eventually, the CH_3 carbon curve moves further away from water relative to the halogen one, as can be seen in the density profiles of the PenX species. This general trend is present in all three alkyl halide series, albeit the details differ somewhat depending on the halogen atom.

To explore the orientation preferences of alkyl halides at the water–vapor interface in more detail, we analyzed the MD trajectories of individual alkyl halide species in terms of the orientation distribution P(cos θ), where θ is the angle between the interface normal (z-axis) and the molecular vector X $\rightarrow$ C(H_3) pointing from the halogen atom X (=Cl, Br, or I) to the carbon atom of the terminal methyl group. (Note that the molecular vector simply connects the two ends of a molecule, while the molecules are flexible and undergo conformational changes during the simulation, as can be seen for instance from the snapshots in Fig. 1). Using this definition, cos $\theta = 0$ means that the molecule is aligned with the molecular vector parallel to the surface, cos $\theta = 1$ corresponds to the molecular vector-oriented perpendicular to the surface with the methyl group pointing to the gas phase, and cos $\theta = -1$ denotes a perpendicular orientation of the molecular vector relative to the surface with the methyl group pointing toward water.

The orientation distributions for the series of alkyl chlorides, from MeCl to PenCl, are plotted in Fig. 4. In agreement with previous studies [53, 54], the results show that the MeCl orientations with the chlorine atom facing the water surface are the least probable, whereas orientations parallel to the interface and, in particular, tilted orientations with the methyl group pointing toward the water surface are preferred. The maximum around cos $\theta = -0.5$ corresponds to a tilt angle of 120 degrees between the MeCl molecular vector and the surface normal. The orientation distribution is, however, rather broad and relatively flat, indicating that the MeCl molecules adsorbed at the water–vapor interface are rotationally highly mobile and sample a large range of orientations with respect to water surface. The P(cos θ) is subject to relatively large uncertainty close to cos $\theta = \pm 1$ due to limited sampling when the angle θ approaches 0 and 180 degrees, therefore, the P(cos θ) values close to cos $\theta = \pm 1$ are less reliable than the "central" part of the distribution. The error of

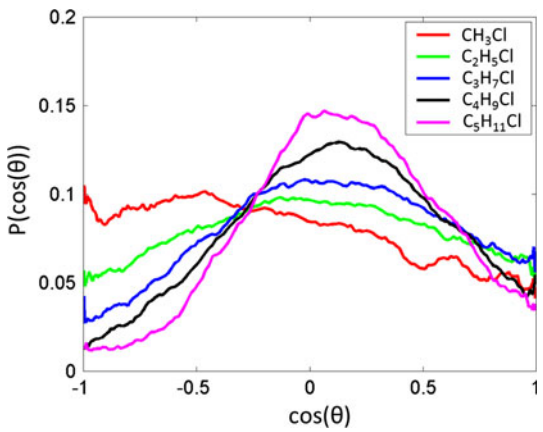

Fig. 4 Orientation distributions of alkyl chlorides at the water–vapor interface. Angle θ is the angle between the interface normal (z-axis) and the molecular vector X $\rightarrow$ C(H_3) pointing from the halogen atom X (=Cl, Br, or I) to the carbon atom of the terminal methyl group

calculated P(cos θ) values, estimated based on block averaging, amounts to ± 0.01 everywhere except for cos θ approaching the limits of the $(-1, 1)$ interval; within the intervals corresponding to $0.9 < |\cos\theta| < 1$, the error of P(cos θ) increases from ± 0.01 to ± 0.03. Nevertheless, even after taking into account the uncertainty in P(cos θ), the preference for the MeCl orientations with the methyl group pointing toward the water surface and the Cl atom toward the gas phase remain statistically significant. (The errors of the P(cos θ) distributions of the rest of the alkyl halide molecules, discussed below, are similar to those given here for MeCl.) With an increasing length of the molecule, the distributions become less broad, which implies gradual reduction of orientational flexibility. At the same time, the distribution maxima shift systematically toward higher cos θ values: While the maxima of EtCl and ProCl distributions are located around cos $\theta \sim 0$, corresponding to parallel alignment of the molecules with the water–vapor interface, the maxima for BuCl and PenCl are found at cos $\theta \sim 0.15$, indicating tilted orientation with the hydrocarbon chain pointing on average slightly away from water at an angle of approx. 10 degrees between the molecular vector and water surface.

Alkyl bromides and iodides follow the same trends as described above for the chlorinated species. The comparison of the orientation distributions of alkyl bromides and iodides with those of alkyl chlorides (see Supplementary Information, Figure S2) shows that alkyl halides of the same chain length exhibit similar behavior (the distributions corresponding to one chain length agree with each other within the statistical uncertainty). Specifically, all methyl halides have a broad distribution of orientations with a maximum corresponding to the methyl group closer to the aqueous phase than the halide end of the molecule, which is more exposed to the vapor phase. The longer-chain molecules, on the other hand, preferably align parallel to the surface, with a slight tendency for the hydrocarbon tail to point away from the aqueous surface. In summary, the orientation analysis thus confirms the conclusions drawn from the density profiles (Fig. 3). We note that the present findings regarding the preferred interfacial orientation of alkyl halides are relevant for individual molecules interacting with water surface, i.e., for the case of low surface number densities. At higher surface coverage (larger number densities), when the alkyl halide molecules get in contact with each other, their mutual interaction may result in re-orientation of some or all of the surface-adsorbed molecules. This concerns in particular the longer-chain alkyl halides that tend to orient more perpendicular to the water surface with increasing surface coverage, albeit to a significantly lesser degree than the corresponding alcohols [53].

The orientation distribution P(cos θ), discussed above, describes molecular orientation with respect to the z-axis perpendicular to both (parallel) global interface planes of the water slab. However, the P(cos θ) distribution does not take into account instantaneous local corrugations of the aqueous surface. In addition, it gives only limited information about hydration of an alkyl halide adsorbate at the local, molecular level. To take into consideration the effect of surface flexibility and to obtain more detailed knowledge about local hydration of alkyl halides at the water–vapor interface, we evaluated the spatial distribution function (SDF) of water around the individual alkyl halides. SDF represents a spatial (3D) histogram of particle number (spatial number density) relative to a central particle. It thus combines information on both radial and angular distribution of solvent molecules around a solute or, as in the present case, an adsorbate.

Figure 5 shows spatial distributions of water oxygen atoms around the surface-adsorbed alkyl halide molecules, averaged over 20 ns simulations. One randomly selected conformation is shown for each alkyl halide species. To construct the spatial density maps, each system configuration (saved at regular intervals along the trajectory) was transformed into a coordinate system having the halide atom X as the origin, the *x*-axis coinciding with the X–C1 bond, the X, C1, and one of the adjacent H atoms defining the *xy*-plane (with the *z*-axis perpendicular to it). The spatial coordinates of all water oxygen atoms were then recorded with respect to this molecule-fixed coordinate system. In this way, positions of water molecules around the alkyl halide molecule are obtained regardless of the instantaneous orientation of the alkyl halide molecule relative to the global water–vapor interface. The distributions plotted in Fig. 5 represent the density isovalue corresponding to 1.5 times the density of bulk water. The SDF plots show that methyl halides have the (incomplete) hydration shell centered on the methyl end of the molecule, leaving the halogen atom fully exposed. For the rest of the species, the maximum hydration is localized around the α-CH_2 group next to the halogen, in accord with the results of ab initio calculations for pentyl chloride [54]. As one proceeds along each of the alkyl halide series, however, there are important differences as regards the hydration of the halogen atom. While in ethyl halides the C–X bond still essentially points away from water, the increasing length—and, hence, hydrophobicity—of the alkyl chain results in gradual re-orientation of the C–X bond relative to the hydration shell, which thereby extends to the vicinity of the halogen. Consequently, ethyl and, to a large degree, also propyl halides have the halogen atom fairly exposed, whereas in butyl and pentyl halides the halogen becomes partially hydrated. The SDF analysis thus supplements the above discussed orientation distributions and provides additional, more specific information on the hydration structure of alkyl halides. In particular, it shows that while

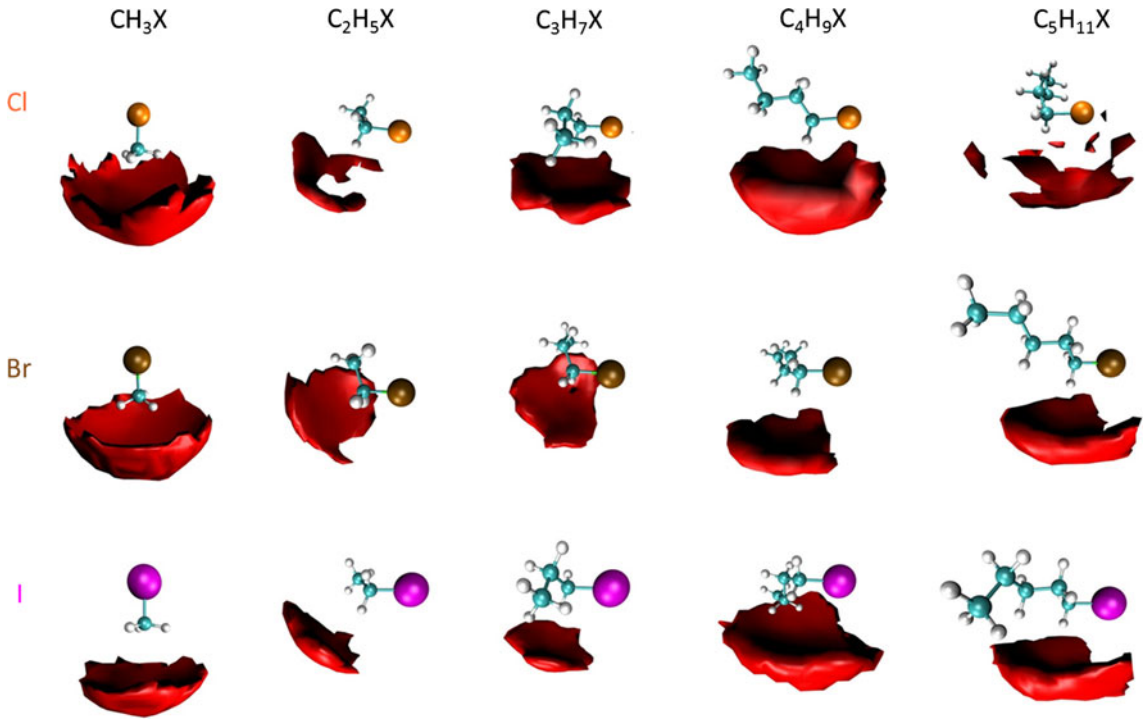

Fig. 5 Spatial density distributions of water around alkyl halide molecules as obtained by averaging over 20 ns MD simulations. Color coding: carbon—*cyan*, hydrogen—*light gray*, chlorine—*orange*, bromine—*brown*, iodine—*purple*. The spatial distributions (*red*) are plotted for the isodensity value of water oxygen corresponding to 1.5 times the density of bulk water

the alkyl halides sample a rather broad range of orientations at the water–vapor interface, sufficient translational and rotational mobility enables the interfacial water molecules to adopt energetically favorable configurations around the surface-adsorbed alkyl halide molecule even if its instantaneous orientation relative to the global water–vapor interface is quite far from optimal.

4 Discussion

The MD simulations of full series of monosubstituted chloro-, bromo- and iodoalkanes with 1–5 carbon atoms in the alkyl chain, the results of which are presented in the preceding section, allow us to identify common features relevant for alkyl halide–water interaction, and to characterize the trends in interfacial hydration properties of alkyl halides, as they change with the type of the halogen atom and the length of the alkyl chain.

While the alkyl halides can be classified as hydrophobic, our results show that they readily adsorb to the water surface. This is in accord with the findings of previous studies [53, 54, 56–59, 61, 85], which indicated that the propensity of gaseous molecules for the water–vapor interface is a generic effect, present for both hydrophobic and hydrophilic species [57]. The underlying reason is the opportunity for the surface-adsorbed molecules to make use of the attractive van der Waals and electrostatic interactions with the aqueous medium without significantly perturbing the hydrogen-bonded network of liquid water. Naturally, the details of the interfacial behavior, such as the extent of surface enhancement or characteristic surface residence times, may differ substantially between different classes of compounds (as well as between individual compounds of the same class), depending on the character and strength of the interaction with water and other molecular properties. The present MD simulations demonstrate that although the interaction of alkyl halides with water is relatively weak, they adsorb to aqueous surfaces and can accumulate in the air–water interfacial region, although they are traditionally not viewed as being "surface active."

In addition to the tendency to preferentially reside at the water–vapor interface, which is common for all of the alkyl halide species investigated here, the MD trajectories also revealed the differences in the interfacial behavior of individual compounds. Methyl halides, being the smallest of the species, are the most volatile and exhibit the shortest surface residence times ($\sim 10^{-10}$ s with the present model). At the same time, they become most easily dissolved in bulk water. With increasing molecular mass within each of the chloro-, bromo-, and iodoalkane series, the molecules get increasingly confined to the interfacial region, as they desorb less frequently into the gas phase and

do not enter the bulk liquid phase. Consequently, the surface residence times grow by about an order of magnitude (to $\sim 10^{-9}$ s) between methyl and pentyl halides. The effect of the halogen atom is less pronounced: The behavior of the compounds of the same chain length, but with a different halogen substituent, is rather similar, with only a moderate increase of the residence times from the alkyl chloride to the corresponding alkyl bromide and iodide.

The above discussed properties and trends are in agreement with low solubility [86] and relatively small Henry's law constants [87] of alkyl halides, and agree well also with the changes in solubility and Henry's law constant along the homologous series of *n*-alkyl halides (see Supplementary Information). This gives us confidence that qualitatively the present MD simulations provide a reliable picture of alkyl halide solvation in aqueous interfacial environment. The quantitative results, such as the precise values of the residence times (Tables 1, 2) or the exact details of the liquid phase—interface—gas-phase partitioning (Figs. 2, 3), depend to a certain degree on the specific model employed in the MD simulations. In particular, the present model was not optimized to reproduce the hydration free energy of the alkyl halide species. This leads to underestimation of the strength of the alkyl halide–water interactions and, thus, of the magnitude of the surface effect, as shown in our recent study for methyl chloride [55]. The results can, therefore, be viewed as a lower estimate of the surface residence times and the interfacial preference of the alkyl halide investigated. At the same time, since polarization interaction is explicitly included in the current model, the model is likely to provide a reliable description of the asymmetric hydration of alkyl halides in the interfacial aqueous environment [56, 88].

The propensity of a compound for the air–water interface becomes important in systems with large interface area. In atmospheric chemistry, the most typical case, in which the air–water interface often dominates, is water droplets dispersed in air (as cloud and fog droplets, dew and mist). Another example is air bubbles dispersed in ocean water, the bursting of which gives rise to aqueous aerosol. While water droplets play a crucial role in scavenging organic compounds from the air, air bubbles can transport dissolved organics to the ocean surface, where the organics are further transferred to the aerosol phase. In the above systems, characterized by one phase (liquid or gas) dispersed in another (bulk) phase, the conventional approach based on the bulk phase gas–liquid partitioning (e.g., the Henry's law) is insufficient. In such cases, the surface has to be taken into account, as surface adsorption can affect the mass transfer across the interface, and reactions at the interface between the two phases may become significant.

The results of the present study, showing interfacial enhancement for a large set of alkyl halides, indicate that partitioning to the interface—in addition to the partitioning between the air and the droplet (bulk liquid) phase—may need to be included to correctly describe the uptake of gas-phase alkyl halides into aqueous droplets dispersed in air. While experimental and/or modeling studies of uptake by aqueous droplets are missing for alkyl halides, the importance of the interface partitioning of these compounds has been demonstrated in the field of water treatment, in separation processes using minute air bubbles to remove pollutants from water by surface adsorption. Experimental and mathematical modeling of the bubble columns has shown that the mass transfer rate of alkyl halides from the aqueous phase to air bubbles as well as the adsorption capacity of the air bubbles for alkyl halides increased with decreasing size of the air bubbles [89–91]. Similar mechanisms are thus likely to play a role also in the behavior of alkyl halides toward wet deposition (uptake by dispersed aqueous droplets) in the atmosphere.

As far as the reactivity is concerned, alkyl halides are known to be subject to photolysis and oxidation reactions in the atmosphere. The preference of alkyl halides for interfacial hydration opens up the possibility for their heterogeneous atmospheric processing at the surface of aerosols and other dispersed droplets. Previous studies have also shown that atmospheric oxidants, including the OH and HO_2 radicals, prefer the air–water interface [56, 57, 61, 92]. The partial hydration of alkyl halides at the aqueous surface (together with the interfacial presence of the oxidizing agent) will potentially affect the heterogeneous photolysis and oxidation reaction rates at the atmospheric aqueous surfaces in contrast to the gas phase or species fully solvated within the bulk liquid phase [67, 93, 94].

Unlike in the homogeneous-phase reactions, one of the important aspects of heterogeneous processes affecting their mechanisms and reaction rates is the alignment of reactants due to the orienting effect of the interface. For alkyl halides, the interfacial orientation is a result of a subtle balance of electrostatic, dispersion, induction and hydrogen-bonded interactions. Previous MD simulations showed interesting differences between the smallest molecules of the series, methyl halides (MeX), oriented preferentially with the CH_3 group into water and the halogen atom into the gas phase, and the molecules with 4- or 5-carbon chain, oriented parallel to the interface with the flexible nonpolar alkyl chain pointing on average slightly away from water [53, 54]. The present study reveals the details of the molecular orientation and the corresponding hydration at the water–vapor interface along the whole alkyl halide series. In particular, it shows that (a) the change in orientation from the alkyl chain (terminal methyl group) toward water to the alkyl chain (terminal methyl

group) away from water occurs gradually within the alkyl halide series, (b) the methyl halide molecules have their (incomplete) hydration shell centered on the methyl end of the molecule, while the hydration shell of the 2- to 5-carbon chain molecules is localized around the CH_2 group immediately next to the halogen, and (c) not only the methyl species, but also the ethyl and propyl halides have the halogen atom exposed, pointing essentially freely into the gas phase. Only as the length of the hydrophobic alkyl chain increases substantially beyond the polar region of the CH_2X group (i.e., for the 4- and 5-carbon chain), the halogen atom becomes more hydrated. The present MD simulations thus corroborate the conclusions of the previous studies carried out for only a few selected alkyl chlorides and bromides [53, 54], and show similar behavior also for alkyl iodides. The identity of the halogen substituent plays relatively minor role in the above general trend.

Ab initio studies [43, 44, 54, 70] have shown that the key factor for the alkyl halide hydration is a simultaneous occurrence of $X\cdots H_2O$ and $CH\cdots OH_2$ hydrogen bonds, with the hydrogen atoms of the α-CH_2 group (or, in the case of methyl halides, the CH_3 group) having the most positive electrostatic potential and being the preferential site for hydrogen bonding. In all alkyl halides, the region around the halogen atom possesses the most negative electrostatic potential, indicating its ability to act as proton acceptor. In methyl chloride, however, this negative region was shown to be less pronounced compared to pentyl chloride. Consequently, the $X\cdots H_2O$ hydrogen bonds of methyl chloride at the liquid water surface were found to be weaker and less frequent than the $CH\cdots OH_2$ bonds of the CH_3 group to the interfacial water molecules [54]. The character of the molecular electrostatic potential of alkyl halides and the resulting hydrogen-bonding patterns, as obtained from ab initio studies, thus provide rationalization of the orientational preferences of alkyl halides at the water–vapor interface predicted by MD simulations. Further ab initio investigations of a more complete set of alkyl halides, including the brominated and iodinated compounds, are needed to better understand their molecular properties and the nature of their interaction with water, as well as to test the adequacy of the present empirical model. The fact that the force field employed in the current MD simulations reproduces correctly the ab initio-based results for alkyl chlorides strongly suggests that the model is able to reliably describe, at least qualitatively, the interfacial hydration also for alkyl bromides and iodides.

As discussed above, the propensity of alkyl halides for interfacial solvation and the asymmetric hydration due to a particular molecular orientation is important for reactions of these compounds at aqueous atmospheric interfaces (on aerosols, cloud and fog droplets, and also on thin films of water on solid surfaces, on ice and snow). The differences in preferential orientation of the small alkyl halides versus the longer-chain ones relative to the aqueous surface are likely to have consequences for example in photochemical processes, in which caging by the solvent molecules plays a crucial role. The cage effect can be reduced at the water–vapor interface as a result of a less complete hydration shell of the interfacial species [65]. The present study shows that as the length of the alkyl chain increases, the halogen atom becomes increasingly (albeit still partially) hydrated. This indicates that partial caging of the halogen fragment upon photolysis of the C–X bond may occur for the longer-chain alkyl halides. For the small alkyl halides, however, such caging will be absent or substantially limited, as the short-chain compounds, when adsorbed at the water surface, tend to have the halogen atom exposed, with the C–X bond pointing into the gas phase. This concerns methyl, ethyl and propyl halides, which are the most atmospherically relevant ones, and thus suggests that the release of the reactive halogen radicals from photolysis of alkyl halides may be essentially unaffected by the interaction of alkyl halides with aqueous aerosols and other liquid droplets dispersed in air compared to the photochemical processing in the gas phase. While experimental studies of interfacial processes with sensitivity to molecular alignment remain challenging at ambient conditions, more information on the uptake and photochemistry of alkyl halides on aqueous surfaces may be obtained from molecular beam experiment with water clusters [95–97]. These experiments, employing the pickup technique, have been performed for a range of atmospherically relevant molecules (e.g., HCl, HBr, CH_3OH and CH_3CH_2OH) [96] and should thus be feasible also for the short-chain alkyl halides. In addition to providing validation of our theoretical predictions made on the basis of a computational model, such experiments would be valuable in regards to the reactivity of low molecular weight alkyl halides on atmospheric ice particles, which is important from the point of view of the ozone layer depletion in polar regions.

Finally, we note that adsorption behavior of alkyl halides can be significantly influenced by organics present at the interface. In many environments, field studies have shown that a major fraction of aqueous aerosol particles as well as fog and rain droplets comprises a variety of surface-active organic material, from long chain fatty acids [98] to shorter chain compounds [99] to complex humic-like substances [100]. Depending on the type of surfactant and its surface coverage, interfacial partitioning, residence times and orientation of alkyl halides at the surfactant-coated aqueous or ice surfaces may be different than those at the neat air–water or air–ice interfaces [101, 102]. Further work is needed to bring insight into how the presence of surfactants will affect the interfacial behavior of alkyl halides.

5 Conclusions

Adsorption of gas-phase *n*-alkyl halides to the surface of a liquid water slab and their hydration at the water–vapor interface were studied using classical MD simulations. The investigated alkyl halide species included monosubstituted methyl to pentyl halides, R–X, where X = Cl, Br, or I, and R = C_nH_{2n+1}, n = 1–5. Our results show that all of the alkyl halides have a strong tendency to reside at the water–vapor interface, in accord with the findings of previous studies for a few selected chloro- and bromoalkanes [53–55] as well as other small organics and gases [56–59, 61, 85]. This phenomenon may result in considerable adsorption or even accumulation of alkyl halides at the air–water interface, although the low molecular weight alkyl halides investigated here are rather volatile and, at the same time, are not viewed as particularly "surface active."

The present MD study reveals the details of the molecular orientation and the corresponding hydration at the water–vapor interface for the alkyl halide series. In particular, it shows that all methyl halide molecules, including methyl iodide which has not been previously studied, have their (incomplete) hydration shell centered on the methyl end of the molecule, while the halogen atom is facing the gas phase essentially unsolvated. The hydration shell of the 2- to 5-carbon chain molecules is localized around the α-CH_2 group next to the halogen, in accord with ab initio results for pentyl chloride [54]. However, ethyl and, to a large degree, also propyl halides, with their relatively short alkyl chain, still have the halogen atom rather exposed, pointing almost freely into the gas phase. The behavior of butyl and pentyl halides on the water surface begins to resemble that of alcohols, with the polar region of the CH_2X group interacting with water and the rest of the increasingly nonpolar hydrocarbon chain pointing on average away from water. Consequently, the halogen atom becomes more, albeit not fully, hydrated. The identity of the halogen substituent plays only a minor role in this general trend.

The above findings regarding the solvation behavior of alkyl halides at the water–vapor interface have possible important consequences for atmospheric chemistry. In systems with large air–water interface area, such as the aqueous aerosols and other airborne liquid droplets, the propensity of alkyl halides for the water–vapor interface may result in significant enhancement of their surface concentrations. While the importance of interfacial adsorption of haloalkanes has been demonstrated experimentally in the field of water treatment for air bubbles dispersed in water [89–91], uptake and heterogeneous atmospheric processing on the surface of aqueous aerosol and cloud droplets has not received much attention so far. Our results show that the interfacial partitioning of alkyl halides may need to be taken into account when interpreting the results of field studies or laboratory experiments involving the aerosol phase. In addition, the partitioning of alkyl halides to the aqueous aerosol surfaces should be considered in tropospheric models. At the same time, the specific character of the partial hydration of the surface-adsorbed alkyl halides is likely to affect the reactivity of these species when adsorbed on the surface of aqueous or ice particles in the atmosphere. The distinct difference in preferred alignment and solvation structures at the aqueous surface between the short-chain alkyl halides and their longer-chain counterparts is of potential importance particularly for heterogeneous photochemistry of alkyl halides on atmospheric aqueous and/or ice interfaces. Experimental investigation of such systems and processes, for example in molecular beam experiments with the pickup and photodissociation of alkyl halides on water clusters, would be of high relevance for atmospheric science.

Acknowledgments The authors wish to thank Jan Heyda for technical assistance with the computations of the spatial distribution functions. The research in Prague was supported by the Czech Science Foundation Grant no. P208/10/1724 and by RVO 61388963. B.M. would like to acknowledge financial support from the Czech Science Foundation (Grant no. 13-08651S). A.H. acknowledges the support from SVV265304. Support to A.O. and M.R. via the KONTAKT program of the Ministry of Education, Youth and Sports of the Czech Republic (Grant ME09064), and to M.R. by the AirUCI Institute funded by the U.S. National Science Foundation (Grant no. 0909227) is also gratefully appreciated. Part of the work has been carried out by A.O. as a student research project at an international summer school Schola Ludus 2009 in Nove Hrady (http://auc.cz/scholaludus), which received financial support from the European Social Fund and from the government of the Czech Republic.

References

1. Finlayson-Pitts BJ, Pitts JN Jr (2000) Chemistry of the upper and lower atmosphere: theory, experiments, and applications. Academic Press, San Diego
2. Carpenter LJ (2003) Iodine in the marine boundary layer. Chem Rev 103(12):4953–4962. doi:10.1021/cr0206465
3. Barrie LA, Bottenheim JW, Schnell RC, Crutzen PJ, Rasmussen RA (1988) Ozone destruction and photochemical reactions at polar sunrise in the lower Arctic atmosphere. Nature 334:138–141
4. Keene WC, Khalil MAK, Erickson DJ, McCulloch A, Graedel TE, Lobert JM, Aucott ML, Gong SL, Harper DB, Kleiman G, Midgley P, Moore RM, Seuzaret C, Sturges WT, Benkovitz CM, Koropalov V, Barrie LA, Li YF (1999) Composite global emissions of reactive chlorine from anthropogenic and natural sources: reactive Chlorine Emissions Inventory. J Geophys Res Atmos 104(D7):8429–8440. doi:10.1029/1998jd100084
5. Lovelock JE (1975) Natural halocarbons in air and in sea. Nature 256:193–194
6. Khalil MAK, Moore RM, Harper DB, Lobert JM, Erickson DJ, Koropalov V, Sturges WT, Keene WC (1999) Natural emissions of chlorine-containing gases: reactive chlorine emissions inventory. J Geophys Res Atmos 104(D7):8333–8346. doi:10.1029/1998jd100079

7. Greenberg JP, Guenther AB, Turnipseed A (2005) Marine organic halide and isoprene emissions near Mace Head, Ireland. Environ Chem 2:291–294
8. Bill M, Rhew RC, Weiss RF, Goldstein AH (2002) Carbon isotope ratios of methyl bromide and methyl chloride emitted from a coastal salt marsh. Geophys Res Lett 29:4/1–4/4
9. Rhew RC, Miller BR, Weiss RF (2000) Natural methyl bromide and methyl chloride emissions from coastal salt marshes. Nature 403:292–295
10. Yokouchi Y, Noljiri Y, Barrle LA, Toom-Sauntry D, Machlda T, Inuzuka Y, Aklmoto H, Li HJ, Fujinuma Y, Aoki S (2000) A strong source of methyl chloride to the atmosphere from tropical coastal land. Nature 403:295–298
11. Crutzen PJ, Heidt LE, Krasnec JP, Pollock WH, Seiler W (1979) Biomass burning as a source of atmospheric gases CO, H_2, N_2O, NO, CH_3Cl and COS. Nature 282:253–256
12. Keppler F, Eiden R, Niedan V, Pracht J, Scholer HF (2000) Halocarbons produced by natural oxidation processes during degradation of organic matter. Nature 403:298–301
13. Rasmussen RA, Rasmussen LE, Khalil MAK, Dalluge RW (1980) Concentration distribution of methyl chloride in the atmosphere. J Geophys Res Oceans 85(C12):7350–7356. doi:10.1029/JC085iC12p07350
14. Low JC, Wang NY, Williams J, Cicerone RJ (2003) Measurements of ambient atmospheric C_2H_5Cl and other ethyl and methyl halides at coastal California sites and over the Pacific Ocean. J Geophys Res Atmos 108(D19):4608. doi:10.1029/2003JD003620
15. Yagi YL, Williams J, Wang N-Y, Cicerone RJ (1993) Agricultural soil fumigation as a source of atmospheric methyl bromide. Proc Natl Acad Sci 90:8420–8423
16. Yagi YL, Williams J, Wang N-Y, Cicerone RJ (1995) Atmospheric methyl bromide (CH_3Br) from agricultural soil fumigations. Science 267:1979–1981
17. Yates SR, Wang D, Ernst FF, Gan J (1997) Methyl bromide emissions from agricultural fields: bare soil, deep injection. Environ Sci Technol 31:1136–1143
18. Ristaino JB, Thomas W (1997) Agriculture, methyl bromide and the ozone hole. Can we fill the gaps? Plant Dis 81:964–977
19. Andreae MO, Atlas E, Harris GW, Helas G, de Kock A, Koppmann R, Maenhaut W, Mano S, Pollock WH, Rudolph J, Scharffe D, Schebeske G, Welling M (1996) Methyl halide emissions from savanna fires in southern Africa. J Geophys Res Atmos 101(D19):23603–23613. doi:10.1029/95JD01733
20. Thomas VM, Bedford JA, Cicerone RJ (1997) Bromine emissions from leaded gasoline. Geophys Res Lett 24:1371–1374
21. Thornton JA, Kercher JP, Riedel TP, Wagner NL, Cozic J, Holloway JS, Dube WP, Wolfe GM, Quinn PK, Middlebrook AM, Alexander B, Brown SS (2010) A large atomic chlorine source inferred from mid-continental reactive nitrogen chemistry. Nature 464:271–274
22. Graedel TE, Keene WC (1995) Tropospheric budget of reactive chlorine. Global Biogeochem Cycles 9:47–77
23. Carpenter LJ, Sturges WT, Penkett SA, Liss PS, Alicke B, Hebestreit K, Platt U (1999) Short-lived alkyl iodides and bromides at Mace Head, Ireland: links to biogenic sources and halogen oxide production. J Geophys Res Atmos 104(D1):1679–1689. doi:10.1029/98JD02746
24. Butler JH (2000) Atmospheric chemistry: better budgets for methyl halides? Nature 403:260–261
25. Platt U, Janssen C (1995) Observaton and role of the free radicals NO_3, ClO, BrO, and IO in the troposphere. Faraday Discuss 100:175–198
26. Sekusak S, Gusten H, Sablijic A (1995) An ab initio investigation on transition states and reactivity of chloroethane with OH radical. J Chem Phys 102:7504–7518
27. Mellouki A, Talukdar RK, Schmoltner A, Gierczak T, Mills MJ, Solomon S, Ravishankara AR (1992) Atmospheric lifetimes and ozone depletion potentials of methyl bromide and dibromomethane. Geophys Res Lett 19:2059–2062
28. Solomon S, Mills M, Heidt LE, Pollock WH, Tuck AF (1992) On the evaluation of ozone depletion potential. J Geophys Res Atmos 97(D1):825–842
29. Khalil MAK, Rasmussen RA (1999) Atmospheric methyl chloride. Atmos Environ 33:1305–1321
30. Yvon-Lewis SA, Saltzman ES, Montzka SA (2009) Recent trends in atmospheric methyl bromide: analysis of post-Montreal Protocol variability. Atmos Chem Phys 9:5963–5974
31. Yoshida Y, Wang Y, Shim C, Cunnold D, Blake DR, Dutton GS (2006) Inverse modeling of the global methyl chloride sources. J Geophys Res Atmos 111:D16307
32. Bell N, Hsu L, Jacob DJ, Schultz MG, Blake DR, Butler JH, King DB, Lobert JM, Maier-Reimer E (2002) Methyl iodide: atmospheric budget and use as a tracer of marine convection in global models. J Geophys Res Atmos 107(D17):4340
33. Molina MJ, Tso T-L, Molina LT, Wang FC-Y (1987) Antarctic stratospheric chemistry of chlorine nitrate, hydrogen chloride, and ice: release of active chlorine. Science 238:1253–1257
34. Grecea ML, Backus EHG, Kleyn AW, Bonn M (2005) Surface photochemistry of bromoform on ice: cross section and competing reaction pathways. J Phys Chem B 109(37):17574–17578. doi:10.1021/jp052586n
35. Finlayson-Pitts BJ (2009) Reactions at surfaces in the atmosphere: integration of experiments and theory as necessary (but not necessarily sufficient) for predicting the physical chemistry of aerosols. PCCP 11(36):7760–7779. doi:10.1039/b906540g
36. Pal SK, Mereshchenko AS, El-Khoury PZ, Tarnovsky AN (2011) Femtosecond photolysis of CH_2Br_2 in acetonitrile: capturing the bromomethyl radical and bromine-atom charge transfer complex through deep-to-near UV probing. Chem Phys Lett 507(1–3):69–73. doi:10.1016/j.cplett.2011.02.046
37. Zhu R, Tang B, Ji L, Tang Y, Zhang S, Zhang B (2004) Photodissociation dynamics of n-alkyl bromide at 234 and 267 nm. Opt Commun 235(4–6):325–331. doi:10.1016/j.optcom.2004.02.055
38. Karras G, Danakas S, Kosmidis C (2011) Formation of molecular halide ions from alkyl-halide clusters irradiated by ps and fs laser pulses. J Phys Chem A 115(17):4186–4194. doi:10.1021/jp2015947
39. Miranda MA, Pérez-Prieto J, Font-Sanchis E, Scaiano JC (2001) One- vs two-photon processes in the photochemistry of 1, n-dihaloalkanes. Acc Chem Res 34(9):717–726. doi:10.1021/ar000107r
40. Preston TJ, Dutta M, Esselman BJ, Kalume A, George L, McMahon RJ, Reid SA, Crim FF (2011) Formation and relaxation dynamics of iso-CH_2Cl–I in cryogenic matrices. J Chem Phys 135(11):114503–114510
41. Lilach Y, Asscher M (2003) Photochemistry of caged molecules: CD_3Cl@Ice. J Chem Phys 119(1):407–412
42. Ayoub Y, Asscher M (2008) Photochemistry of ethyl chloride caged in amorphous solid water. Phys Chem Chem Phys 10(43):6486–6491
43. Dozova N, Krim L, Alikhani ME, Lacome N (2005) Vibrational spectra and structure of CH_3Cl:H_2O, CH_3Cl:HDO, and CH_3Cl:D_2O complexes. IR matrix isolation and ab initio calculations. J Phys Chem A 109(45):10273–10279. doi:10.1021/jp053895g
44. Dozova N, Krim L, Alikhani ME, Lacome N (2007) Vibrational spectra and structure of CH_3Cl:$(H_2O)_2$ and CH_3Cl:$(D_2O)_2$ complexes. IR matrix isolation and ab initio calculations. J Phys Chem A 111(40):10055–10061. doi:10.1021/jp074028
45. Aida M, Yamataka H, Dupuis M (1998) Ab initio molecular dynamics simulations on the hydrolysis of methyl chloride with

explicit consideration of three water molecules. Chem Phys Lett 292(4–6):474–480. doi:10.1016/S0009-2614(98)00706-4
46. Aida M, Yamataka H, Dupuis M (1999) Ab initio MD simulations of a prototype of methyl chloride hydrolysis with explicit consideration of three water molecules: a comparison of MD trajectories with the IRC path. Theor Chem Acc 102(1–6):262–271. doi:10.1007/s002140050497
47. Fournier F, Dubost H, Carrez S, Zheng W, Bourguignon B (2005) Interaction of coadsorbed CH_3Cl and D_2O layers on Pd(111) studied by sum frequency generation. J Chem Phys 123(18):184705–184707
48. Vaida ME, Bernhardt TM (2012) Surface-aligned femtochemistry: photoinduced reaction dynamics of CH_3I and CH_3Br on MgO(100). Faraday Discuss 157:437–449
49. DeSimone AJ, Olanrewaju BO, Grieves GA, Orlando TM (2013) Photodissociation of methyl iodide adsorbed on low-temperature amorphous ice surfaces. J Chem Phys 138(8): 084703–084709
50. Berger R, Lilach Y, Ayoub Y, Asscher M (2005) Photochemistry of molecules at confined environment: CD_3Br/O/Ru(001) and CO_2 @ Ice. Isr J Chem 45(1–2):97–109. doi:10.1560/veyg-4lq8-dtpt-tdu4
51. Swanson AL, Blake NJ, Blake DR, Sherwood Rowland F, Dibb JE, Lefer BL, Atlas E (2007) Are methyl halides produced on all ice surfaces? Observations from snow-laden field sites. Atmos Environ 41(24):5162–5177. doi:10.1016/j.atmosenv.2006.11.064
52. Swanson AL, Blake NJ, Dibb JE, Albert MR, Blake DR, Sherwood Rowland F (2002) Photochemically induced production of CH_3Br, CH_3I, C_2H_5I, ethene, and propene within surface snow at Summit, Greenland. Atmos Environ 36(15–16):2671–2682. doi:10.1016/S1352-2310(02)00127-9
53. Harper K, Minofar B, Sierra-Hernandez MR, Casillas-Ituarte NN, Roeselova M, Allen HC (2009) Surface residence and uptake of methyl chloride and methyl alcohol at the air/water interface studied by vibrational sum frequency spectroscopy and molecular dynamics. J Phys Chem A 113:2015–2024
54. Pasalic H, Roeselova M, Lischka H (2011) Methyl and pentyl chloride in a microhydrated environment and at the liquid water-vapor interface: a theoretical study. J Phys Chem B 115: 1807–1816
55. Habartová A, Valsaraj KT, Roeselová M (2013) Molecular dynamics simulations of small halogenated organics at the air-water interface: implications in water treatment and atmospheric chemistry. J Phys Chem A. doi:10.1021/jp405292k
56. Vieceli J, Roeselova M, Potter N, Dang LX, Garrett BC, Tobias DJ (2005) Molecular dynamics simulations of atmospheric oxidants at the air-water interface: solvation and accommodation of OH and O_3. J Phys Chem B 109(33):15876–15892. doi:10.1021/jp051361
57. Vacha R, Slavicek P, Mucha M, Finlayson-Pitts BJ, Jungwirth P (2004) Adsorption of atmospherically relevant gases at the air/water interface: free energy profiles of aqueous solvation of N_2, O_2, O_3, OH, H_2O, HO_2, and H_2O_2. J Phys Chem A 108: 11573–11579
58. Vacha R, Jungwirth P, Chen J, Valsaraj KT (2006) Adsorption of polycyclic aromatic hydrocarbons at the air-water interface: molecular dynamics simulations and experimental atmospheric observations. PCCP 8(38):4461–4467. doi:10.1039/b610253k
59. Liyana-Arachchi TP, Valsaraj KT, Hung FR (2011) Molecular simulation study of the adsorption of naphthalene and ozone on atmospheric air/ice interfaces. J Phys Chem A 115(33): 9226–9236. doi:10.1021/jp205246z
60. Hub JS, Caleman C, van der Spoel D (2012) Organic molecules on the surface of water droplets: an energetic perspective. PCCP 14:9537–9545. doi:10.1039/c2cp40483d
61. Roeselova M, Vieceli J, Dang LX, Garrett BC, Tobias DJ (2004) Hydroxyl radical at the air-water interface. J Am Chem Soc 126(50):16308–16309. doi:10.1021/ja045552m
62. Harrison I, Polanyi JC, Young PA (1988) Photochemistry of adsorbed molecules. 3.Photodissociation and photodesorption of CH3Br adsorbed on LiF(001). J Chem Phys 89(3):1475–1497. doi:10.1063/1.455148
63. Slavicek P, Roeselova M, Jungwirth P, Schmidt B (2001) Preference of cluster isomers as a result of quantum delocalization: potential energy surfaces and intermolecular vibrational states of Ne···HBr, Ne···HI, and $HI(Ar)_n$ ($n = 1 - 6$). J Chem Phys 114(4):1539–1548
64. Rieley H, McMurray DP, Haq S (1996) Adsorption and photochemistry of dinitrogen tetroxide on low temperature ice layers. J Chem Soc Faraday Trans 92(6):933–939. doi:10.1039/ft9969200933
65. Donaldson DJ, Valsaraj KT (2009) Adsorption and reaction of trace gas-phase organic compounds on atmospheric water film surfaces: a critical review. Environ Sci Technol 44:865–873
66. Wingen LM, Moskun AC, Johnson SN, Thomas JL, Roeselova M, Tobias DJ, Kleinman MT, Finlayson-Pitts BJ (2008) Enhanced surface photochemistry in chloride-nitrate ion mixtures. PCCP 10(37):5668–5677. doi:10.1039/b806613b
67. Nissenson P, Knox CJH, Finlayson-Pitts BJ, Phillips LF, Dabdub D (2006) Enhanced photolysis in aerosols: evidence for important surface effects. PCCP 8(40):4700–4710. doi:10.1039/B609219e
68. Case DA, Darden TA, Cheatham TEI, Simmerling CL, Wang J, Duke RE, Luo R, Merz KM, Wang B, Pearlman DA, Crowley M, Brozell S, Tsui V, Gohlke H, Mongan J, Hornak V, Cui G, Beroza P, Schafmeister C, Caldwell JW, Ross WR, Kollman PA (2004) AMBER 8. University of California, San Francisco
69. Dang LX (1992) The nonadditive intermolecular potential for water revised. J Chem Phys 97:2659–2660
70. Wang W, Tian A, Wong N-B (2005) Theoretical study on the bromomethane-water 1:2 complexes. J Phys Chem A 109: 8035–8040
71. Frisch MJ, Trucks GW, Schlegel HB, Scuseria GE, Robb MA, Cheeseman JR, Montgomery JA, Jr, Vreven T, Kudin KN, Burant JC, Millam JM, Iyengar SS, Tomasi J, Barone V, Mennucci B, Cossi M, Scalmani G, Rega N, Petersson GA, Nakatsuji H, Hada M, Ehara M, Toyota K, Fukuda R, Hasegawa J, Ishida M, Nakajima T, Honda Y, Kitao O, Nakai H, Klene M, Li X, Knox JE, Hratchian HP, Cross JB, Bakken V, Adamo C, Jaramillo J, Gomperts R, Stratmann RE, Yazyev O, Austin AJ, Cammi R, Pomelli C, Ochterski JW, Ayala PY, Morokuma K, Voth GA, Salvador P, Dannenberg JJ, Zakrzewski VG, Dapprich S, Daniels AD, Strain MC, Farkas O, Malick DK, Rabuck AD, Raghavachari K, Foresman JB, Ortiz JV, Cui Q, Baboul AG, Clifford S, Cioslowski J, Stefanov BB, Liu G, Liashenko A, Piskorz P, Komaromi I, Martin RL, Fox DJ, Keith T, Al-Laham MA, Peng CY, Nanayakkara A, Challacombe M, Gill PMW, Johnson B, Chen W, Wong MW, Gonzalez C, Pople JA (2004) Gaussian 03, Revision D.01. Gaussian, Inc., Wallingford, CT
72. Hirose C, Akamatsu N, Domen K (1992) Formulas for the analysis of surface sum-frequency generation spectrum by CH stretching modes of methyl and methylene groups. J Chem Phys 96:997–1004
73. Feller D (1996) The role of databases in support of computational chemistry calculations. J Comput Chem 17:1571–1586
74. Schuchardt KL, Didier BT, Elsethagen TO, Sun L, Gurumoorthi V, Chase JM, Li J, Windus TL (2007) Basis set exchange: a community database for computational sciences. J Chem Inf Model 47(3):1045–1052. doi:10.1021/ci600510j

75. Bayly CI, Cieplak P, Cornell WD, Kollman PA (1993) A well-behaved electrostatical potential based method using charge restraints for deriving atomic charges: the RESP model. J Phys Chem 97(40):10269–10280. doi:10.1021/j100142a004
76. Wang J, Wang W, Kollman PA, Case DA (2006) Automatic atom type and bond type perception in molecular mechanical calculations. J Mol Graph Modell 25:247–260
77. Case DA, Darden TA, Cheatham TE, Simmerling CL, Wang J, Duke RE, Luo R, Walker RC, Zhang W, Merz KM, Roberts B, Wang B, Hayik S, Roitberg A, Seabra G, Kolossvary I, Wong KF, Paesani F, Vanicek J, Liu J, Wu X, Brozell SR, Steinbrecker T, Gohlke H, Cai Q, Ye X, Wang J, Hsieh M-J, Cui G, Roe DR, Mathews DH, Seetin MG, Sagui C, Babin V, Luchko T, Gusarov S, Kovalenko A, Kollman PA (2010) AMBER 11. University of California, San Francisco
78. Berendsen HJC, Postma JPM, van Gunsteren WF, DiNola A, Haak JR (1984) Molecular dynamics with coupling to an external bath. J Chem Phys 81:3684–3690
79. Hockney RW, Goel SP, Eastwood JW (1974) Quiet high-resolution computer models of a plasma. J Comput Phys 14(2): 148–158
80. Darden T, York D, Pedersen LG (1993) Particle mesh Ewald: an N.Log(N) method for Ewald sums in large systems. J Chem Phys 98(12):10089–10092
81. Essmann U, Perera L, Berkowitz ML, Darden T, Lee H, Pedersen LG (1995) A smooth particle mesh Ewald method. J Chem Phys 103(null):8577–8593
82. Ryckaert JP, Ciccotti G, Berendsen HJC (1977) Numerical integration of the cartesian equations of motion of a system with constraints: molecular dynamics of n-alkanes. J Comput Phys 23:327–341
83. Miyamoto S, Kollman PA (1992) SETTLE: an analytical version of the SHAKE and RATTLE algorithm for rigid water models. J Comput Chem 13:952–962
84. Humphrey W, Dalke A, Schulten K (1996) VMD: visual molecular dynamics. J Molec Graph 14:33–38
85. Murdachaew G, Varner ME, Phillips LF, Finlayson-Pitts BJ, Gerber RB (2013) Nitrogen dioxide at the air-water interface: trapping, absorption, and solvation in the bulk and at the surface. PCCP 15(1):204–212. doi:10.1039/c2cp42810e
86. Lide DR (ed) (2007-2008) Aqueous solubility of organic compounds. In CRC Handbook of Chemistry and Physics, 88th ed. Taylor and Francis, Boca Raton, FL
87. Sander R (1999) Compilation of Henry's law constants for inorganic and organic species of potential importance in environmental chemistry. http://www.henrys-law.org
88. Vrbka L, Mucha M, Minofar B, Jungwirth P, Brown EC, Tobias DJ (2004) Propensity of soft ions for the air/water interface. Curr Opin Colloid Interface Sci 9(1–2):67–73. doi:10.1016/j.cocis.2004.05.028
89. Smith JS, Burns LF, Valsaraj KT, Thibodeaux LJ (1996) Bubble column reactors for wastewater treatment. 2. The effect of sparger design on sublation column hydrodynamics in the homogeneous flow regime. Ind Eng Chem Res 35(5): 1700–1710. doi:10.1021/ie950366y
90. Smith JS, Valsaraj KT (1997) Bubble column reactors for wastewater treatment. 3. Pilot-scale solvent sublation of pyrene and pentachlorophenol from simulated wastewater. Ind Eng Chem Res 36(3):903–914. doi:10.1021/ie9605241
91. Smith JS, Valsaraj KT, Thibodeaux LJ (1996) Bubble column reactors for wastewater treatment.1. Theory and modeling of continuous countercurrent solvent sublation. Ind Eng Chem Res 35(5):1688–1699. doi:10.1021/ie9503656
92. Morita A, Kanaya Y, Francisco JS (2003) Uptake of HO_2 radical by water: molecular dynamics calculations and their implications for atmospheric modeling. J Geophys Res 109:Article No. D09210
93. Valsaraj KT (2009) Trace gas adsorption thermodynamics at the air-water interface: implications in atmospheric chemistry. Pure Appl Chem 81(10):1889–1901. doi:10.1351/pac-con-08-07-06
94. Watanabe H, Yamaguchi S, Sen S, Morita A, Tahara T (2010) "Half-hydration" at the air/water interface revealed by heterodyne-detected electronic sum frequency generation spectroscopy, polarization second harmonic generation, and molecular dynamics simulation. J Chem Phys 132(14):144701
95. Poterya V, Farnik M, Slavicek P, Buck U, Kresin VV (2007) Photodissociation of hydrogen halide molecules on free ice nanoparticles. J Chem Phys 126(7). doi:10.1063/1.2709635
96. Lengyel J, Kocisek J, Poterya V, Pysanenko A, Svrckova P, Farnik M, Zaouris DK, Fedor J (2012) Uptake of atmospheric molecules by ice nanoparticles: pickup cross sections. J Chem Phys 137(3). doi:10.1063/1.4733987
97. Pradzynski CC, Forck RM, Zeuch T, Slavicek P, Buck U (2012) A fully size-resolved perspective on the crystallization of water clusters. Science 337(6101):1529–1532. doi:10.1126/science.1225468
98. Tervahattu T, Juhanoja J, Vaida V, Tuck AF, Niemi JV, Kupiainen K, Kulmala M, Vehkamäki H (2005) Fatty acids on continental sulfate aerosol particles. J Geophys Res 110:D06207
99. Russell LM, Maria SF, Myneni SCB (2002) Mapping organic coatings on atmospheric particles. Geophys Res Lett 29. 10.1029/2002GL014874
100. Raja S, Raghunathan R, Yu XY, Lee TY, Chen J, Kommalapati RR, Murugesan K, Shen X, Qingzhong Y, Valsaraj KT, Collett JL (2008) Fog chemistry in the Texas-Louisiana gulf coast corridor. Atmos Environ 42:2048
101. Liyana-Arachchi TP, Valsaraj KT, Hung FR (2012) Adsorption of naphthalene and ozone on atmospheric air/ice interfaces coated with surfactants: a molecular simulation study. J Phys Chem A 116(10):2519–2528. doi:10.1021/jp3002417
102. Wick CD, Chen B, Valsaraj KT (2010) Computational investigation of the influence of surfactants on the air-water interfacial behavior of polycylic aromatic hydrocarbons. J Phys Chem C 114(34):14520–14527. doi:10.1021/jp1039578

THE JOURNAL OF PHYSICAL CHEMISTRY A

Article

pubs.acs.org/JPCA

Molecular Dynamics Simulations of Small Halogenated Organics at the Air−Water Interface: Implications in Water Treatment and Atmospheric Chemistry

Alena Habartová,[†] Kalliat T. Valsaraj,*[,‡] and Martina Roeselová*[,†]

[†]Institute of Organic Chemistry and Biochemistry, Academy of Sciences of the Czech Republic, Flemingovo nám. 2, 16610 Prague 6, Czech Republic

[‡]Cain Department of Chemical Engineering, Louisiana State University, Baton Rouge, Louisiana 70803, United States

Supporting Information

ABSTRACT: Free energy profiles associated with transfer of chlorinated and brominated halomethane molecules from the gas phase across the water−vapor interface to the aqueous phase were calculated using classical molecular dynamics simulations. The investigated species include chloromethane (CH_3Cl), bromomethane (CH_3Br), dichloromethane (CH_2Cl_2), dibromomethane (CH_2Br_2), chloroform ($CHCl_3$), and bromoform ($CHBr_3$). The employed halomethane force field was tuned by scaling up the atomic charges to reproduce the experimental hydration free energies. The computed free energy profiles have a minimum at the water−vapor interface of about 12−15 kJ·mol^{-1} relative to full hydration in the bulk liquid. This implies that the halomethanes exhibit enhanced interfacial concentrations in systems with large surface area per unit volume, such as air bubbles dispersed in water or water droplets dispersed in air. Implications for water treatment as well as for atmospheric chemistry are discussed.

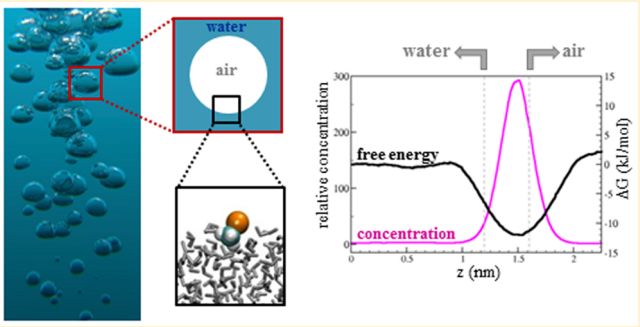

1. INTRODUCTION

Haloalkanes are a group of organic compounds derived from alkanes and containing one or more halogen substituents. They are prevalent pollutants in waste waters, groundwater, and in the atmosphere.[1,2] This results from their widespread use in industrial and agricultural operations as excellent solvents, flame retardants, and fumigants. Leaking valves and fugitive emissions are among the sources of these pollutants. Low molecular weight chlorinated haloalkanes are also formed in drinking water during treatment such as disinfection. A number of separation processes are used to remediate the water environment. These include the use of air stripping, activated carbon, and other adsorbent media.[3] Air stripping includes conventional bubble aeration and packed tower stripping, both of which are economically feasible. Adsorbent use for removing pollutants requires regeneration or proper disposal of the adsorbent after use.

Most of air stripping process designs involve the use of air−water bulk phase relationships (Henry's constant) and the rate of mass transfer of pollutants between the bulk air and water phases. The efficiency of the process depends on increasing the air−water interfacial contact and this can be brought about by decreasing the bubble size in conventional bubble aeration.[4] It has, however, been known that for systems that involve very high surface area to volume ratios (such as minute air bubbles in water), surface adsorption mechanisms for pollutants should be considered in addition to bulk phase relationships.[5] One such process that made use of the air−water surface adsorption of pollutants is an adsorptive bubble separation process (bubble fractionation) called "solvent sublation".[6] In solvent sublation, very fine air bubbles remove pollutants by adsorption from the aqueous phase and the materials are stripped into an immiscible organic solvent floated on top of the aqueous phase.[7,8] The process has been found to be very successful in removing a variety of organic pollutants such as chlorinated organics, aromatic hydrocarbons, and pesticides. Solvent sublation has been extensively tested on the laboratory scale and further tested on a pilot-scale as well on the industrial scale.[9−14] The success of solvent sublation in removing organic hydrophobic compounds was proven to be as a result of the air−water interface having the capability to transport volatile, semivolatile, and nonvolatile compounds from the aqueous phase.

The inverse problem arises in the atmosphere for water droplets scavenging organic compounds from the gas phase, which is termed "wet deposition" by rain, fog, dew, and mist. This process is important for atmospheric aerosols that affect both climate change and atmospheric chemistry. In this context, understanding the heterogeneous processes that occur on the

Received: May 29, 2013
Revised: August 22, 2013
Published: August 26, 2013

surfaces of atmospheric dispersoids (cloud droplets, fog droplets, dew, and mist) becomes significant. Hence, for wastewater treatment and atmospheric wet deposition the essential element is the presence of one phase dispersed (as bubbles or drops) in another bulk phase to affect mass transfer and reaction at the interface between the two phases.

Although a number of experimental and correlation data on the air−water interfacial adsorption is available in the literature,[15−20] theoretical work has only recently begun to explore the adsorption phenomena at the air−water interface for natural surfactants[21−24] as well as for small organic molecules that are traditionally not called "surface-active".[25−27] Molecular dynamics simulation work has shown that a number of molecules including oxidants have the propensity for the air−water interface since they display substantial free energy minima at this interface.[21,25,26,28−31] Most of these computational studies have been performed on larger aromatic compounds such as polycyclic aromatic hydrocarbons (PAHs). Halogenated organics at the air−water interface have received little attention up to this point. Recent classical and ab initio MD simulation studies[32,33] of several monosubstituted haloalkanes showed their strong preference for interfacial solvation rather than full solvation in bulk liquid water even for the smallest and most water-soluble of these compounds, methyl chloride (CH_3Cl) and bromide (CH_3Br). It is important to investigate the free energy profiles at the air−water interface for halogenated organics so that their equilibrium and reaction rates at the interface can be better understood. This will help in not only improving the design of separation processes but also in understanding how water droplets in air can support reactions leading to atmospheric processing by clouds and fogs.[34]

This paper reports molecular dynamics investigation of a series of chlorinated and brominated halomethane species, including chloromethane (CH_3Cl), bromomethane (CH_3Br), dichloromethane (CH_2Cl_2), dibromomethane (CH_2Br_2), chloroform ($CHCl_3$), and bromoform ($CHBr_3$). For each compound, we have obtained the free energy profile associated with moving the molecule from the gas phase across the water−vapor interface to the aqueous phase. Our calculations are compared to the available experimental free energies of hydration derived from measured Henry's law constants,[35] and the computed free energy profiles are used to elucidate the interfacial partitioning of the halomethane species. Implications of our observations for water remediation using the air stripping method as well as potential impacts on atmospheric chemistry of halogenated organics are discussed.

An important contribution of the paper is the force field for interaction of halomethanes with water, which was tuned to the experimental free energy of hydration of each compound (obtained from Henry's law constants) via scaling of the atomic charges. This force field, albeit simple and nonpolarizable, is shown to provide quantitative results for the present set of halomethane compounds at the water−vapor interface, and is expected to be reliable when used in more complex MD simulations involving halomethanes.

2. METHODOLOGY

2.1. Computational Approach. Classical molecular dynamics (MD) simulations were used to investigate the aqueous hydration and surface propensity of the following set of halomethane molecules: CH_3Cl, CH_2Cl_2, $CHCl_3$, CH_3Br, CH_2Br_2, and $CHBr_3$. The simulated systems consisted of one halomethane molecule from the above list and 863 water molecules forming a slab of liquid with two water−vapor interfaces. The water slab was placed in the middle of a rectangular parallelepiped simulation box, with the *x*-, *y*-, and *z*-dimension of 3.0, 3.0, and 10.0 nm, respectively. The *z*-axis coincides with the direction normal to the two water−vapor interfaces. The thickness of the liquid water slab was approximately 3 nm. Periodic boundary conditions were applied in all three dimensions. This setup was utilized to evaluate the free energy profile associated with moving each halomethane molecule along the *z*-axis from the gas phase across the water−vapor interface into the bulk liquid, and then across the other water−vapor interface back into the gas phase. The simulation setup is shown in Figure 1a, and a schematic free energy profile of a halomethane molecule along the *z*-axis is depicted in Figure 1b.

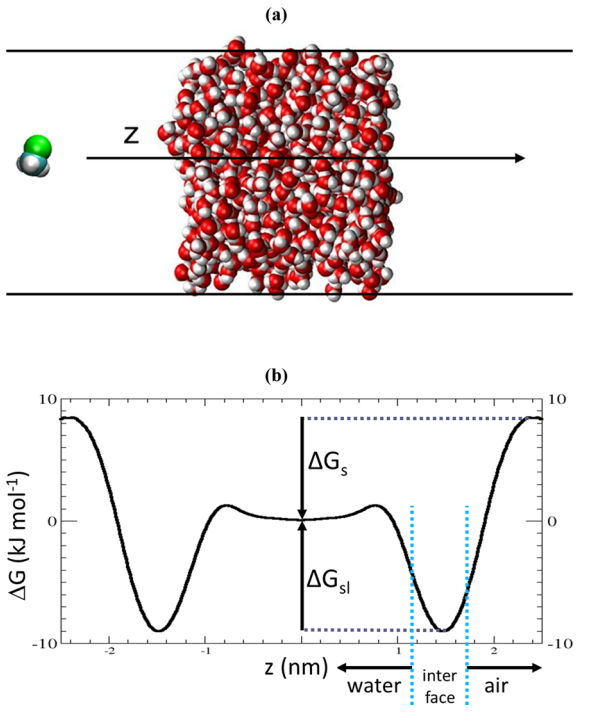

Figure 1. (a) Schematic depiction of the free energy profile coordinate across a liquid water slab. (b) Typical free energy profile of a haloalkane molecule.

As the molecule moves from the gas phase toward the bulk liquid water, its free energy goes through a minimum at the water−vapor interface, then increases again, and finally reaches a plateau in the interior of the water slab. The free energy difference of the transition of the solute from the gas to the liquid phase, ΔG_s, represents the free energy of hydration of the given species, and ΔG_{sl} is the free energy of the transition from the water surface into the bulk liquid. We note that the ΔG profile corresponds to the limit of infinite dilution. The experimental hydration free energy, ΔG_s^0, corresponding to the standard state of p_0 = 1 atm gas pressure and c_0 = 1 mol·L^{-1} aqueous concentration differs from the ΔG_s value pertinent to the present simulations with a single solute molecule by a constant according to[31,35]

$$\Delta G_s = \Delta G_s^0 + RT\left(\frac{p_0}{c_0 RT}\right) = \Delta G_s^0 - 7.9\ \text{kJ·mol}^{-1} \quad (1)$$

dx.doi.org/10.1021/jp405292k | J. Phys. Chem. A 2013, 117, 9205−9215

Table 1. Henry's Law Constant (k_H) and the Corresponding Experimental Free Energy of Hydration (ΔG_s^H), Calculated Free Energy of Hydration (ΔG_s), Interfacial Free Energy Minimum (ΔG_{sl}) Relative to the Liquid Phase, and the Relative Aqueous and Interfacial Concentrations with Respect to the Gas Phase As Obtained from the Calculated Free Energy Profiles for the Set of Halomethanes Studied[a]

	k_H	ΔG_s^H	ΔG_s	ΔG_{sl}	relative concentration			
molecule	(M/atm)	(kJ·mol^{-1})	(kJ·mol^{-1})	(kJ·mol^{-1})	gas phase	aqueous bulk	surface (maximum)	surface (averaged)
CH_3Cl	0.10	−2.2	−2	12	1	2	300	200
CH_2Cl_2	0.40	−5.6	−6	11	1	9	900	600
$CHCl_3$	0.25	−4.5	−4	12	1	6	800	500
CH_3Br	0.16	−3.4	−4	11	1	4	400	300
CH_2Br_2	1.10	−8.1	−6	15	1	26	8700	5600
$CHBr_3$	1.90	−9.5	−11	12	1	45	6500	5100

[a]For the interfacial concentration, both the maximum and averaged values are shown (see text for details). ΔG is set to 0 in the aqueous phase. For definition of ΔG_s and ΔG_{sl} see Figure 1b.

where R is the universal gas constant and T stands for temperature (T = 298.15 K for the standard state). The experimental free energy of hydration, ΔG_s^0, can be obtained from the Henry's law constant, k_H, using the following relation[35]

$$\Delta G_s^0 = -RT \ln\left(\frac{p_0}{c_0} k_H\right) \quad (2)$$

The Henry's law constant, k_H, in the above equation is defined as the equilibrium ratio of the molar concentration of a compound in the aqueous phase and its partial pressure above the liquid and is expressed in the units of M·atm^{-1}. Equation 1 is used to compare the MD-computed free energies of hydration with the experimental ones and to verify the quality of the employed force fields.

In addition, the free energy difference ΔG_{12} between any two points 1 and 2 selected along the free energy path can be used to evaluate the molar concentration ratio of the given species at these points

$$\frac{c_1}{c_2} = \exp\left(-\frac{\Delta G_{12}}{RT}\right) \quad (3)$$

Specifically, by setting the reference point 1 into the gas phase and selecting point 2 in the aqueous phase or at the liquid−vapor interface, one can use the corresponding ΔG values, namely ΔG(gas→liquid) = ΔG_s and ΔG(gas→interface) = $\Delta G_s - \Delta G_{sl}$, to calculate the partitioning of a species between the gas phase, the aqueous phase, and the liquid−vapor interface.

2.2. Computational Details and Potential Parameters. The free energy profiles were computed from a set of umbrella sampling simulations.[36−38] A single halomethane molecule was introduced into the gas phase region of the simulation box containing a pre-equilibrated liquid water slab, approximately 1.0 nm away from the water surface. First, a 4 ns constant volume and temperature (NVT) simulation was performed in which the center of mass (CoM) of the halomethane molecule was pulled along the z-direction (normal to the interface) toward the center of the water slab and then across the opposite interface into the gas phase using a harmonic restraining potential with the force constant of 1000 kJ·mol^{-1}·nm^{-2} and a pull rate of 0.002 nm·ps^{-1}. From this simulation, 60 configurations ("windows") with different positions of the halomethane molecule along the z-axis were extracted. Two different widths of the windows were employed: The first 10 and the last 10 windows (i.e., the windows located in the gas phase within −2.5 nm ≤ z ≤ −2.0 nm and 2.0 nm ≤ z ≤ 2.5 nm) were spaced by 0.05 nm, the remaining 40 windows within −2.0 nm ≤ z ≤ 2.0 nm were spaced by 0.1 nm. The finer spacing of the outermost windows was chosen in order to increase the precision of the ΔG calculation in the gas phase region far away from the water surface where the force exerted on the solute molecule by the water slab is subject to large fluctuations. For each of the 60 windows, a separate 6 ns NVT simulation was then carried out in which a biasing harmonic potential with the force constant of 3000 kJ·mol^{-1}·nm^{-2} was applied to the halomethane CoM. From the instantaneous values of the z-coordinate of the halomethane CoM, collected at 4 ps intervals, the umbrella sampling population histograms were constructed for the individual windows. Finally, the free energy profile was obtained from the umbrella sampling histograms using the weighted histogram analysis method (WHAM).[39,40] The MD simulations were carried out by the GROMACS 4.5.1[41] molecular dynamics package; the Gromacs utility g_wham[38] was utilized to perform the WHAM calculation and to estimate the statistical errors along the free energy profile with the bootstrapping analysis. A total of 100 bootstrap cycles were used.

The TIP4P-2005 force field[42] was used for water. This force field is currently one of the most universal water models that provides good description of water phase diagram over a wide range of temperatures and pressures.[43,44] The general Amber force field (GAFF)[45] was employed for the halomethanes. The Lennard-Jones parameters for the C, H, Cl, and Br centers are given in the Supporting Information, Table S1. The atomic partial charges were evaluated from molecular structures optimized at the B3LYP/cc-pVTZ level by the restrained electrostatic potential (RESP) method, fitting the electrostatic potential generated by the molecular charge distribution at points selected according to the Merz−Singh−Kollman scheme.[46] The ab initio calculations were conducted using Gaussian09 package,[47] the RESP calculations were performed by Antechamber.[48] The force fields employed in our MD simulations are nonpolarizable, that is, the model does not explicitly include the description of electronic polarization. However, polarization effects are implicitly taken into account in the interaction potentials. First of all, the parametrization of the TIP4P/2005 water model includes an average increase of the molecular dipole moment relative to its gas phase value due to polarization forces experienced by a water molecule in the condensed phase. In a similar way, the increase of the atomic partial charges of the halomethane molecules relative to their gas-phase values accounts for the average polarization effects of

dx.doi.org/10.1021/jp405292k | J. Phys. Chem. A 2013, 117, 9205−9215

the aqueous environment. The atomic charges of the halomethane molecules evaluated by the RESP procedure, the charge scaling factors and the atomic charges after scaling are given in the Supporting Information, Table S2. An individual charge scaling factor was chosen for each of the halomethane species so as to yield a good agreement with the experimental hydration free energy, as obtained from the available Henry's law constants. The values of the Henry's law constants used in this study (see Table 1) were obtained as an average of the Henry's law constant values reported by different authors as summarized in the compilation by Sander.[35] With the exception of one or two outliers, the range of the experimental Henry's law constant values corresponds to an uncertainty in the free energy of hydration (ΔG_s^H, see Table 1), which is comparable to the ± 2 kJ·mol^{-1} error of our free energy calculation.

All MD simulations were performed in an NVT ensemble at T = 300 K using the leapfrog integrator[49] with a time step of 1 fs. The system temperature was controlled by the v-rescale thermostat (temperature coupling using velocity rescaling with a stochastic term)[50] with a coupling time of 1 ps. The cutoff distance of 1.0 nm was employed for the Lennard-Jones and the short-range part of the Coulomb interactions. The neighbor list was updated every 10 integration steps. The long-range part of the Coulomb interaction was evaluated using the Particle-Mesh Ewald method[51,52] with a relative tolerance of 10^{-5}, fourth order cubic interpolation and a Fourier spacing parameter of 0.12. All bonds were constrained using LINCS.[53]

3. RESULTS

3.1. Free Energy Profiles and Interfacial Concentrations. The calculated free energy profiles of the set of chlorinated and brominated halomethane molecules (CH_3Cl, CH_2Cl_2, $CHCl_3$, CH_3Br, CH_2Br_2, and $CHBr_3$) are displayed in Figure 2. While the free energy profiles were calculated by moving each molecule from the gas phase through the entire water slab back into the gas phase at the opposite side of the slab, only the profiles for $z > 0$ are shown (with $z = 0$ corresponding to the middle of the water slab). They were obtained by averaging the computed ΔG values over the two equivalent half-spaces in the simulation system. The original free energy curves for both halves of the aqueous slab are available in the Supporting Information (Figure S1). They provide proof that the free energy profiles computed across the water slab (i.e., before averaging) were sufficiently symmetric. The deviations from perfect symmetry across the two equivalent water−vapor interfaces can serve as a measure of uncertainty of the computed ΔG values and of the convergence of the umbrella sampling calculations. The largest deviation observed is ± 2 kJ·mol^{-1}. Another way to estimate the statistical error is using the bootstrapping analysis (see Section 2.2. above). The free energy profiles from Figure 2 including the error bars computed by the bootstrapping technique are shown in Figure S2 of the Supporting Information. The largest error obtained by this approach is ± 1 kJ·mol^{-1}. The ΔG uncertainties of the order of 1−2 kJ·mol^{-1} are comparable with the errors reported in similar calculations for other small organic molecules at the water−vapor interface.[54]

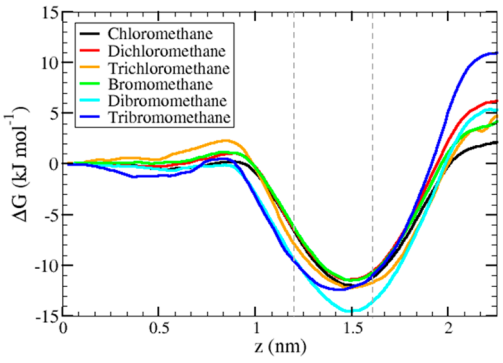

Figure 2. Computed free energy profiles of the chlorinated and brominated halomethanes across the liquid−vapor interface. The z-coordinate values represent the CoM of chloromethane. The z-axis lies in the direction normal to the liquid−vapor interface, z = 0 corresponds to the center of the water slab. The two vertical dashed lines denote the interfacial water layer.

The free energy difference between the gas phase and bulk liquid corresponds to the hydration free energy, ΔG_s. As discussed above, the hydration free energy can be obtained from the experimentally measured Henry's law constant. Thus, reproducing the ΔG_s value in a simulation helps to properly set the parameters of the molecular model. The comparison between the experimental hydration free energies (as obtained from the respective Henry's law constants) and the MD-calculated values is given in Table 1 and shows a good agreement. This was achieved by increasing the atomic partial charges of the halomethane molecules in order to account on average for the polarization effects due to the aqueous environment. The charge scaling factors needed to reproduce the free energy of hydration of the individual halomethane species range between 1.7 and 2.0 (see Supporting Information, Table S2).

For all of the halomethanes studied, the free energy profiles in Figure 2 exhibit a minimum in the liquid−vapor interfacial region corresponding to ΔG_{sl} of 12−15 kJ·mol^{-1} (ΔG_{sl} is defined as the free energy of the transition from the water surface into the bulk liquid, see Figure 1b). The ΔG_{sl} values for the individual compounds are given in Table 1. Unlike the free energy of hydration, which can be obtained from experimental measurements, the depth of the interfacial free energy minimum is experimentally very difficult to access. MD simulations thus provide an invaluable insight into the interfacial behavior of the halomethane species. Results of any classical MD simulation, however, depend critically on the quality of the underlying model. In the present case, as specified above in Section 3, the halomethane force field parametrization is a combination of the standard GAFF[55] parameters and ab initio/RESP-calculated atomic partial charges, which were uniformly increased by applying a scaling factor. For each halomethane species, free energy profile calculations were performed using several different scaling factors; the final results shown in Figure 2 and Table 1 were obtained with the atomic charges that reproduced best the experimental free energies of hydration. The free energy profiles calculated with different values of the charge scaling factor (see Supporting Information, Figure S3) can be used to assess the sensitivity of the results with respect to the charge distribution of each halomethane compound. Our results show that the computed free energy of hydration, ΔG_s, is highly sensitive to the charge scaling factor: ΔG_s values typically range between -10 kJ·mol^{-1} and $+10$ kJ·mol^{-1} for the charge scaling factor between 1.0 and 2.0. However, regardless of the scaling factor, the interfacial free energy minimum is always present and its depth (relative to the bulk liquid) is rather independent of the atomic charges. In the

dx.doi.org/10.1021/jp405292k | J. Phys. Chem. A 2013, 117, 9205−9215

majority of cases, the ΔG_{sl} values obtained with the scaling factor between 1.0 and 2.0 fall within or only slightly beyond the 4 kJ·mol^{-1} interval corresponding to the ±2 kJ·mol^{-1} uncertainty in the free energy calculation. Therefore, we conclude that the present MD simulations provide robust results as regards the free energy minimum of halomethane molecules at the water−vapor interface. Similar, albeit less deep interfacial free energy minima ($\Delta G_{sl} \approx 2-6$ kJ·mol^{-1}) have been reported for a set of atmospheric gases (N_2, O_2, O_3, OH, H_2O, HO_2, and H_2O_2).[28,30,31] The depths of the interfacial free energy minima of the halomethanes, as yielded by the present calculations ($\Delta G_{sl} \approx 12-15$ kJ·mol^{-1}), reflects the stronger attractive interaction between the halogenated compounds and water surface compared to the above gas molecules and radicals. The ΔG_{sl} values obtained for halomethanes are comparable to those predicted for benzene and small polycyclic aromatic hydrocarbons.[25,26] Similar free energy minima, ranging between 6 kJ·mol^{-1} for methanol and 28 kJ·mol^{-1} for neopentane, were also found for a set of small organic molecules of varying degree of hydrophobicity at the surface of water droplets.[54]

A recently published thermodynamic analysis[54] demonstrated that the preference of organic molecules to be partially solvated at the water−vapor interface rather than inside the bulk liquid is primarily an enthalpic effect, which is modulated by entropy. For molecules containing large nonpolar groups, however, the entropic component becomes significant, resulting in further enhancement of the magnitude of surface preference due to the hydrophobic effect. Following the previous studies of solutes at the surface of water droplets[54,56] and infinite water slab,[21] we have attempted to decompose the free energy profiles $\Delta G(z)$ into the enthalpic component $\Delta H(z)$ and the entropic component $-T\Delta S(z)$. The enthalpic component was determined as the average potential energy of the system over the simulation in each of the umbrella sampling windows along the z-coordinate. The average potential energy of the system was computed as the average of the sum of the respective Lennard-Jones and Coulomb interactions. The entropic component was calculated as the difference between the free energy profile and the enthalpic contribution at a given value of the z-coordinate: $-T\Delta S(z) = \Delta G(z) - \Delta H(z)$. The results are shown in the Supporting Information, Figure S4. Qualitatively, the overall character of the $\Delta H(z)$ and $-T\Delta S(z)$ curves agrees with what has been reported in the previous studies:[21,54,56] The enthalpic curves tend to exhibit a minimum at the interface, indicating that the solutes are stabilized in the interfacial region mainly due to the energy interactions with the water molecules. At the same time, the entropic components $-T\Delta S$ tend to increase as the solutes move from the gas phase across the interface into the bulk liquid phase. We wish to stress, however, that in contrast to the previous work on organic solutes at the surface of small water droplets[54] both the enthalpic and entropic contributions in the present case are subject to very large uncertainty due to large fluctuations of the system's potential energy with a standard deviation of ±200 kJ·mol^{-1} (see Figure S5, Supporting Information). This uncertainty is significantly greater than the range of changes of $\Delta H(z)$ or $-T\Delta S$ across the entire interfacial system. Thus, in the present case of halomethanes at the extended water−vapor interface, the attempt to split the free energy profiles into their enthalpic and entropic components does not yield meaningful results.

From the free energy profile, $\Delta G(z)$, along the z-coordinate normal to the two liquid−vapor interfaces of the water slab, one can evaluate the corresponding relative concentration profile $c_{rel}(z)$ of the halomethane species across the liquid bulk/interface/gas phase system. Equation 3, upon setting the reference point into the gas phase, can be rewritten in terms of the concentration profile relative to the gas phase concentration, c_g, as

$$c_{rel}(z) = \frac{c(z)}{c_g} = \exp\left(-\frac{\Delta G(z) - \Delta G_s}{RT}\right) \quad (4)$$

As an example, the free energy profile and the corresponding concentration profile for chloromethane is shown in Figure 3.

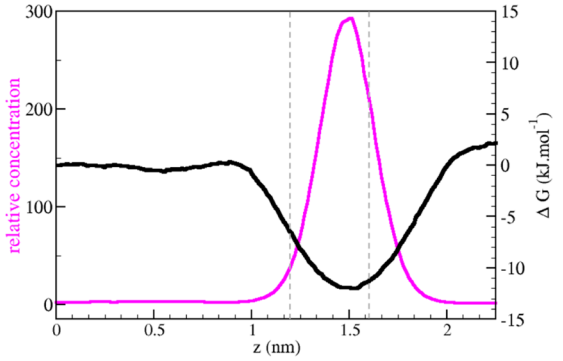

Figure 3. Free energy profile (black line) and the corresponding concentration profile (purple line) of chloromethane across the water−vapor interface. The concentration profile is calculated using eq 4 relative to the gas phase concentration ($c_{rel} = 1$ in the gas phase). The z-coordinate values represent the CoM of chloromethane. The z-axis lies in the direction normal to the liquid−vapor interface, $z = 0$ corresponds to the center of the water slab. The two vertical dashed lines denote the interfacial water layer.

The free energy minimum at the liquid−vapor interface gives rise to a substantial enhancement of chloromethane concentration in the interfacial region with respect to both the gas phase and liquid phase concentrations. Similar results were obtained for all of the halomethane species under investigation. The results are summarized in Table 1, which shows for each of the species studied their aqueous bulk concentrations (relative to the gas phase) and the maximum relative concentrations at the water−vapor interface (corresponding to the point of the free energy minimum). In addition, the relative concentrations averaged over the entire interfacial layer are reported. For the purpose of the integration, the liquid−vapor interface is defined as the region between the z-coordinate values z_{90} and z_{10} for which the water density reaches 90% and 10% of its bulk liquid value, respectively. For our slab system, $|z_{90}| = 1.23$ nm and $|z_{10}| = 1.62$ nm with $z = 0$ in the middle of the water slab. The averaged interfacial concentrations are likely to reflect more realistically the situation at the dynamic liquid−vapor interface. Albeit lower than the maximum values, the averaged values still imply enhanced surface concentrations by 2−3 orders of magnitude compared to the gas phase, and an appreciable surface enhancement with respect to the aqueous phase concentration ranging from a factor of ∼70 to ∼200, depending on the halomethane species.

The significant surface enhancement, indicating a strong preference for interfacial solvation, has been previously predicted for two of the present molecules (chloromethane and bromomethane) from unconstrained classical MD trajectories that sampled the time development of the

dx.doi.org/10.1021/jp405292k | J. Phys. Chem. A 2013, 117, 9205−9215

molecular position along the direction normal to the water−vapor interface of liquid water slab.[32] For chloromethane, a similar result was obtained by ab initio (DFTB-D) molecular dynamics simulations.[33] The position distribution (density profile) obtained from such direct sampling should in principle agree with the concentration profile computed from the free energy profile (Figure 3). In this particular case, however, the comparison is not straightforward, because the sampling trajectories of ref 32 and the present free energy calculations were each based on a different interaction model. While in both cases the GAFF parameters were used for CH_3Cl and CH_3Br, the former MD simulations utilized a polarizable CH_3Cl/CH_3Br model with unscaled RESP charges based on an MP2/cc-pvdz calculation combined with polarizable POL3 water force field, whereas the free energy profiles in this work were computed using a nonpolarizable model for CH_3Cl/CH_3Br with scaled atomic charges (RESP charges based on an B3LYP/cc-pvtz calculation enlarged by a factor of 1.7 for CH_3Cl and 1.95 for CH_3Br) and nonpolarizable TIP4P-2005 water force field.

To enable direct comparison between the two methods of computing the concentration profile across the water−vapor interface (direct sampling vs free energy profile calculation), we performed a 100 ns MD simulation of chloromethane and bromomethane interacting with the water slab using the present (nonpolarizable) model. The simulated system and computational details were the same as in the free energy profile calculations (see Sections 2.1 and 2.2), except that two (instead of one) CH_3Cl or CH_3Br molecules in the simulation box were used to enhance the sampling efficiency. The resulting CH_3Cl trajectories are available in the Supporting Information, Figure S6. The corresponding position distribution of chloromethane along the z-coordinate, equivalent to the concentration (or number density) profile across the water−vapor interface, is shown in Figure 4 (green line) together with the concentration profiles obtained from the present free energy profile calculation (purple line) and from the previous simulation with a polarizable force field[32] (blue line). All concentration profiles are normalized relative to the gas phase concentration (i.e., c_{rel} = 1 in the gas phase). Similar results were obtained for bromomethane (not shown). The broadening of the interfacial concentration peaks obtained by direct sampling compared to the concentration profile derived from the free energy calculation (more pronounced for the longer nonpolarizable simulation than for the considerably shorter polarizable one) can be attributed to frequent evaporation of chloromethane from the water surface (see Figure S6 in the Supporting Information), which leads to a somewhat ill-defined center of mass of the water slab. Upon averaging over the trajectory, this results in an effective broadening of the interfacial layer. This effect is not present in the umbrella sampling simulations, in which the chloromethane position along the interfacial normal is restrained by the umbrella potential.

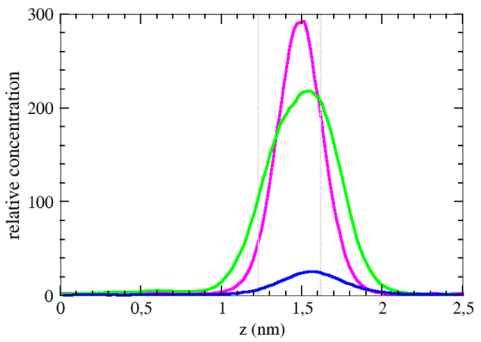

Figure 4. Concentration profiles of chloromethane across the water−vapor interface as obtained from the free energy profile calculation (purple line) and direct sampling simulations (green line) using the present nonpolarizable force field combined with the TIP4P-2005 water model. For comparison, results of previous simulation with a polarizable chloromethane force field in combination with POL3 water model are shown in blue. All concentration profiles are normalized relative to the gas phase concentration (c_{rel} = 1 in the gas phase). The z-axis lies in the direction normal to the liquid−vapor interface, z = 0 corresponds to the center of the water slab. The two vertical dashed lines denote the interfacial water layer.

As can be seen in Figure 4, the agreement of the concentration profile calculated for the present model by direct sampling with that derived from the free energy profile is rather satisfactory. In both cases, the region of the maximum concentration is located in the outer (vapor-side) layer of the interface, and both methods yield the enhancement of the interfacial concentration by 2 orders of magnitude with respect to the gas phase. The maximum relative interfacial concentration determined by direct sampling (c_{rel} = 220) agrees within the error bars with the value obtained from the free energy calculation (c_{rel} = 300 ± 170). On the other hand, the direct sampling predicts somewhat higher value (c_{rel} = 10) of the relative concentration in the bulk liquid than the free energy profile calculation (c_{rel} = 2 ± 1). The errors in c_{rel} were estimated based on the maximum uncertainty (±1 kJ·mol^{-1}) of the computed ΔG values obtained from the bootstrapping analysis (see above) using standard error propagation. The comparison with the previous MD simulation that employed the polarizable Amber force field is less favorable. While qualitatively similar, the predicted surface enhancement is an order of magnitude smaller than that obtained with the present nonpolarizable model. It is important to note that the results of the polarizable simulation are based on a significantly shorter sampling (20 ns trajectory) compared to the nonpolarizable simulation (100 ns trajectory). A more critical factor, however, is the fact that unlike the present nonpolarizable model the polarizable Amber force field used in ref 32 in combination with the POL3 water model was not optimized to reproduce the hydration free energy of the haloalkane species. In the light of the comparison with the results of the current study (Figure 4), it seems likely that the polarizable model[32] underestimates the strength of the haloalkane−water interactions and, therefore, also the magnitude of the haloalkane concentration enhancement at the aqueous surface. Thus, the present model, albeit based on a simpler, nonpolarizable force field with scaled charges, is nevertheless expected to provide more reliable results. Further work is needed to understand and quantify the role of polarization forces in the interfacial hydration of the haloalkane compounds and to refine the currently available polarizable force fields for MD simulations of haloalkanes in interfacial environments.

In summary, the computed free energy profiles indicate a significant propensity of single- and multisubsituted halomethanes to reside at the water−vapor interface. The present work thus corroborates the conclusions of previous MD simulation studies carried out for chloromethane (CH_3Cl)[32,33] and bromomethane (CH_3Br)[32] and provides a more quantitative picture regarding the interfacial hydration preferences of small halogenated organic species.

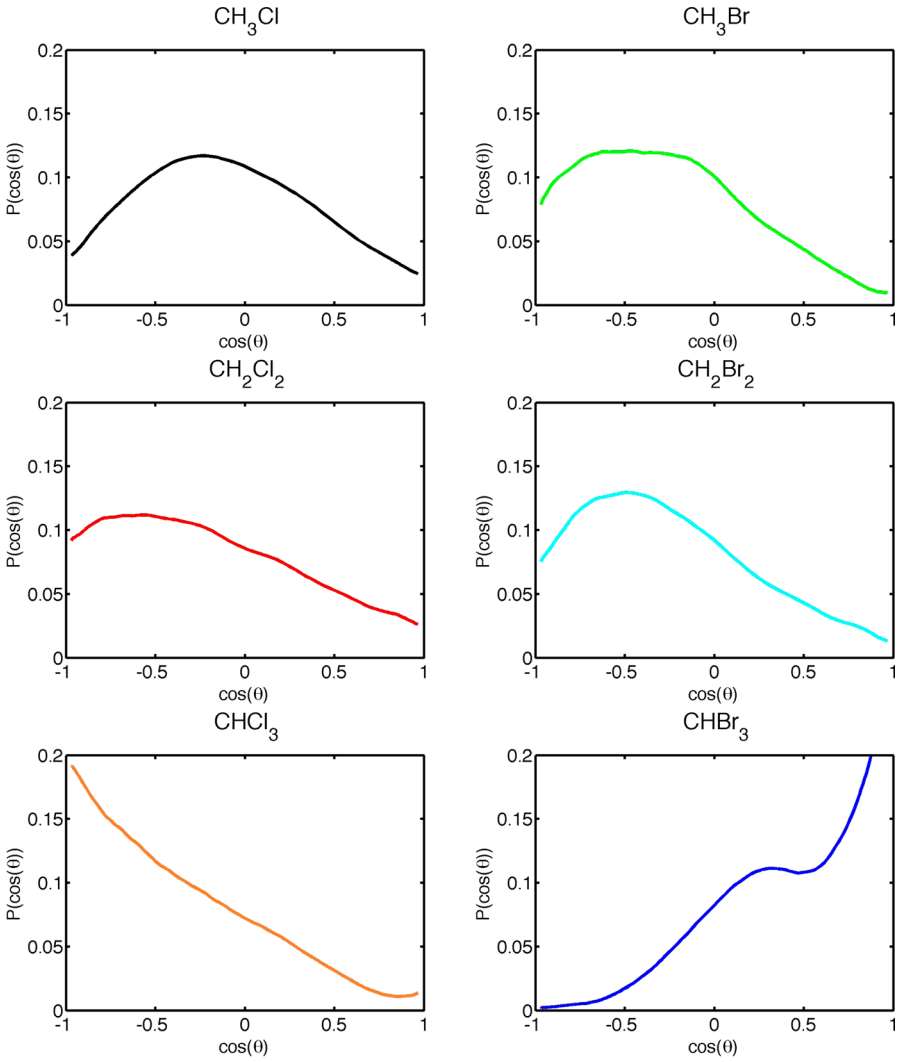

Figure 5. Orientation distributions of chlorinated and brominated halomethanes at the water−vapor interface. θ is the angle between the interface normal (z-axis) and the molecular vector $\vec{v}$, defined in the following way: (1) For the CH_3X species (upper two panels), the molecular vector points from the halogen atom X toward the carbon of the methyl group, $\vec{v}$ = X → C. (2) For the CH_2X_2 species (middle two panels), the molecular vector coincides with the bisector of the X−C−X angle and points toward the carbon atom. (3) For the CHX_3 species (bottom two panels), the molecular vector points from the carbon atom to the hydrogen, $\vec{v}$ = C → H.

3.2. Interfacial Orientation. The previous classical[32] and ab initio molecular dynamics simulations[33] showed that the surface-adsorbed chloromethane and bromomethane are (surprisingly) preferentially oriented with the methyl group toward the water. This has been rationalized on the basis of ab initio calculations in terms of the subtle balance of electrostatic, dispersion, induction, and hydrogen-bonded interactions. While in general the hydrogen bonds between alkyl halides and water are considered weak, in chloro- and bromomethane the large polarity of the C−H bonds of the methyl group immediately next to the halogen substituent makes the methyl group a preferential site for $CH_3\cdots OH_2$ hydrogen bonding. Indeed, ab initio calculations[33] showed that chloromethane primarily interacts with the water surface via the CH···O hydrogen bonds between the methyl group and water oxygen, whereas the OH···Cl hydrogen bonds between chlorine and water are weaker and less frequent. The empirical force field employed in the previous MD simulations[32] that included explicit treatment of polarization interactions was able to reproduce this behavior of chloromethane and bromomethane at the water−vapor interface.

In order to check the performance of the present force field as far as the preferential surface orientation of chloro- and bromomethane is concerned, we analyzed the 100 ns MD trajectories of two CH_3Cl or CH_3Br molecules interacting with a water slab in terms of the orientation distribution $P(\cos\theta)$, where θ is the angle between the interface normal (z-axis) and the molecular vector $\vec{v}$ = X → C pointing from the halogen atom X (= Cl or Br) to the carbon of the methyl group. In addition, we evaluated the $P(\cos\theta)$ distribution for chloromethane and bromomethane also from the respective umbrella sampling simulations in the z-coordinate window corresponding to the interfacial free energy minimum. Both approaches yielded practically the same results, therefore only the orientation distributions obtained from the umbrella sampling simulations are shown in Figure 5 (upper two panels). For the molecular vector $\vec{v}$ = X → C, $\cos\theta = 0$ means that the CH_3X molecule is aligned with the molecular axis parallel to the surface, $\cos\theta = 1$ corresponds to the molecular axis oriented perpendicular to the surface with the methyl group pointing to the gas phase, whereas $\cos\theta = -1$ denotes a perpendicular orientation of the molecular axis relative to the surface with the

dx.doi.org/10.1021/jp405292k | J. Phys. Chem. A 2013, 117, 9205−9215

methyl group facing toward water. The $P(\cos\theta)$ distributions of chloromethane and bromomethane show that molecular orientations parallel to the interface as well as tilted orientations with the methyl group pointing toward water are preferred (see the snapshots in upper two panels of Figure 6), whereas the

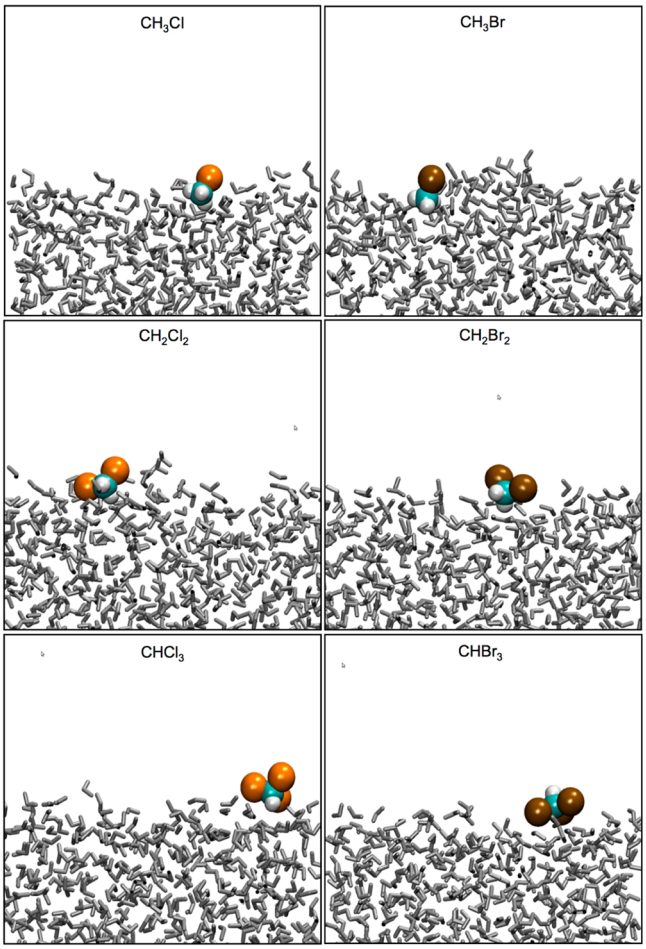

Figure 6. Example of snapshots showing the preferential orientation of chloro- and bromomethanes at the water−vapor interface.

orientations with the halogen atom facing the water surface are disfavored. This is consistent with the results of the previous MD studies of CH_3Cl and CH_3Br at the water−vapor interface[32,33] and demonstrates that the present nonpolarizable force field is able to represent reliably the preferential orientation of chloro- and bromomethane in the aqueous interfacial layer, observed in the earlier simulations that employed more sophisticated description of the interaction potential, either at the ab initio (DFTB-D) level (cf. Figure 7 of ref 33) or at the empirical force field level with polarization interaction explicitly included (see Figure 6 of ref 32).

It would be of interest to know the preferred interfacial orientation also for the other halomethanes investigated here. To this end, we calculated their orientation distributions from the respective umbrella sampling simulations in the z-coordinate window corresponding to the interfacial free energy minimum of each compound. For dichloro- and dibromomethane (CH_2X_2, middle two panels of Figure 5) the molecular vector $\vec{v}$ coincides with the bisector of the X−C−X angle and points toward the carbon atom. Thus, $\cos\theta = 1$ corresponds to the molecular vector oriented perpendicular to the surface with the halogen atoms pointing toward water and the hydrogen atoms toward the vapor phase, whereas $\cos\theta = -1$ means a perpendicular orientation of the molecular vector relative to the surface with the hydrogen atoms facing toward water and the halogen atoms toward the vapor phase. For $\cos\theta = 0$, the molecular vector of CH_2X_2 is aligned parallel to the surface. As can be seen from the distributions, dichloro- and dibromomethane exhibit orientation behavior similar to chloro- and bromomethane. The configurations with the hydrogen atoms facing toward water are preferred over the configurations with the hydrogen atoms pointing away from water, into the gas phase (typical snapshots are shown in Figure 6). For trichloro- and tribromomethane (CHX_3, bottom two panels of Figure 5), the molecular vector points from the carbon atom to the hydrogen, $\vec{v}$ = C → H. Once again, for this definition $\cos\theta = 1$ corresponds to the molecular vector of CHX_3 oriented perpendicular to the surface with the hydrogen atoms pointing toward the vapor phase, whereas $\cos\theta = -1$ represents a perpendicular orientation of the molecular vector relative to the surface with the hydrogen atoms facing toward water. The bottom left panel of Figure 5 shows that the latter configuration (i.e., with the hydrogen atom facing water) is strongly preferred for trichloromethane. However, a quite different behavior is seen for tribromomethane (bottom right panel, Figure 5). The distribution is bimodal with a secondary maximum corresponding to tilted orientation and the main maximum to perpendicular orientation of the molecular vector relative to the interface in both cases with the hydrogen atom of $CHBr_3$ pointing into the gas phase rather than toward water.

The dramatically different interfacial orientation of $CHBr_3$ compared to $CHCl_3$ (see Figure 6, bottom two panels) which falls outside the trends exhibited by the rest of the halomethane molecules studied may be an indication of the limitations of the present model. An ab initio study of trihalomethane−water complexes ($X_3CH\cdots OH_2$, X = F, Cl, Br, I) showed that all members of the trihalomethane series interact with the water molecule via the CH···O hydrogen bond.[57] Also the molecular electrostatic potential exhibits the same character for all trihalomethanes with the most positive region around the hydrogen atom.[58] On the other hand, the situation may be different for the halomethanes interacting with liquid water. The orientation of a molecule at the water surface is a result of the balance of hydrogen-bonding, electrostatic, induction, and dispersion interactions. This balance is particularly subtle for halomethanes since their hydrogen bonds with water are weak. Therefore, while the stabilization of the halomethane−water complexes comes predominantly from hydrogen-bonding, the dispersion, and induction terms may become comparable, or even dominant, at the water−vapor interface, especially for bromoform, with its three large and polarizable bromine atoms. This may result in a different orientation behavior of bromoform from the rest of the present halomethanes possessing either fewer or smaller and less polarizable halogen atoms. While it is possible to quantitatively reproduce the overall interaction of halomethanes with liquid water using an empirical force field, as demonstrated above by our free energy calculations, it is very difficult to represent all of the different contributions to the interaction energy reliably with such a simple model. More detailed study of the nature of the halomethane−water interaction, including a high-level ab initio investigation of larger halomethane−water complexes, is needed to rationalize the preferential surface orientations of di- and trihalomethanes observed in our MD simulations and to

dx.doi.org/10.1021/jp405292k | J. Phys. Chem. A 2013, 117, 9205−9215

test the adequacy of the model in this respect. Such study is, however, beyond the scope of the present paper.

To summarize, the nonpolarizable halomethane force field employed in this work reproduces well the preferential orientation of surface-adsorbed chloromethane and bromomethane with the methyl group toward water, predicted by a previous MD study with a polarizable force field[32] and subsequently confirmed by ab initio calculations.[33] Similar verification is necessary as far as the interfacial orientation of di- and trihalomethanes is concerned. We wish to emphasize, however, that even though the preferential surface orientation of some (or possibly all) of the multisubstituted halomethanes, as predicted by the present force field, may be incorrect, this does not affect the main result of this work, which is the significant concentration enhancement of all of the halomethanes at the water−vapor interface due to the existence of a pronounced interfacial free energy minimum. As shown by our present calculations (see Section 3.1 above and Figure S3 of the Supporting Information) as well as by an earlier work,[30] while the computed value of the free energy of hydration depends rather strongly on the choice of the force field, the calculated depth of the free energy minimum, and hence the magnitude of the concentration enhancement at the surface, is robust and much less sensitive to the underlying model and the particular choice of its parameters. Thus, although further refinement of the halomethane force field, which may be needed for correct description of the molecular orientation at the water surface, is likely to result in certain quantitative changes to the computed free energy profile and relative concentrations, we do not expect these changes to be of such an order as to significantly alter the overall picture obtained from the present study.

4. IMPLICATIONS FOR WATER TREATMENT AND ATMOSPHERIC CHEMISTRY

As stated in the introduction, the air−water interface plays a dominant role in two areas: (a) the use of bubble fractionation or aeration (air bubbles dispersed in water) for treatment of dissolved haloalkanes, and (b) in wet deposition scavenging of gaseous haloalkanes from air (water droplets dispersed in air). In both cases, the air−water interface area and the adsorption of haloalkanes at the interface will increase the overall efficiency of the process. The conventional partition constant (Henry's law constant) for bulk phase air−water relationship is insufficient to capture the process. Consider, for example, the case of water droplets dispersed in the atmosphere (as in cloud or fog) that contains a haloalkane compound in the gas phase. The uptake of the haloalkane into the droplet is determined by the partitioning between the air and the droplet phase. An effective Henry's constant (dimensionless molar ratio of aqueous to gas phase concentrations), K_H^* can be defined[5]

$$K_H^* = RTk_H + a_v K_{ia} \quad (5)$$

that accounts for both the conventional bulk water−air Henry's law constant, k_H/M·atm^{-1} (ratio of aqueous molar concentration in mol·L^{-1} to gas phase partial pressure in atm), and the interface−air adsorption constant, K_{ia}/cm (ratio of aqueous surface concentration in mol·cm^{-2} to molar gas phase concentration in mol·cm^{-3}). In the above equation, a_v is the surface area per unit volume of the dispersed phase. Note that although k_H remains constant, the effective Henry's constant K_H^* increases with the interface area and the partitioning to the air−water interface.

As the surface area per unit volume for the dispersed phase increases, the additional term that involves the surface area and interface partition constant has to be included. In the realm of bubble fractionation (and solvent sublation), the significance of the same has been shown via experimental and mathematical modeling of the bubble columns.[59−61] It has been shown that both mass transfer rate for the haloalkanes from water to air bubbles and the adsorption capacity of the air bubbles for haloalkanes increased with decreasing size of the air bubbles. In atmospheric chemistry, the behavior of haloalkanes toward wet deposition by dispersed droplets (aqueous aerosol, cloud droplets, fog, rain, and mist) and via adsorption on thin water films on solid surfaces (as well as on ice and snow) will also depend on the adsorption capacity at the air−water interface from air. The fact that the haloalkane compounds are preferentially partially hydrated at the surface will lead to their effective capture and transport from the air to water droplets. Techniques such as the sum frequency generation and other second order spectroscopic probes should provide support for the MD simulations, although the relatively weak haloalkane−water interaction compared to more traditional surface active species (e.g., alcohols), resulting in comparatively lower surface density and lower degree of orientation order, makes the detection of surface-adsorbed haloalkanes a challenging task for these methods, at least at ambient temperature.[32] It has also been shown that many atmospheric oxidants prefer the air−water interface.[28] Thus, the partial solvation phenomena of haloalkanes and atmospheric oxidants will potentially affect the heterogeneous oxidation reaction rates at the surface of aerosols and other dispersed droplets in contrast to fully solvated species within the aqueous phase.[62−64] In particular, it would be useful to further understand the reactivity of low molecular weight haloalkanes on thin films of water in ice and snow, as they are important from the perspective of ozone layer depletion in the Arctic and Antarctic regions.

5. CONCLUSIONS

Molecular dynamics simulations were used to calculate the free energy profiles of chlorinated and brominated halomethane molecules (CH_3Cl, CH_2Cl_2, $CHCl_3$, CH_3Br, CH_2Br_2, and $CHBr_3$) across the water−vapor interface. Our calculations reproduce well the experimental free energies of solvation derived from measured Henry's law constants. For all of the above halomethane species, the computed free energy profiles exhibit a minimum at the water−vapor interface of about 12−15 kJ·mol^{-1} relative to full hydration in the bulk liquid. This translates into enhanced interfacial concentrations by 2−3 orders of magnitude compared to the gas phase, and by a factor of ∼70 to ∼200 with respect to the aqueous phase concentration, depending on the particular halomethane. The present results indicate that small halogenated organics readily adsorb to aqueous surfaces and can accumulate in the water−vapor interfacial region. This has important implications for systems and processes in which the air−water interface plays a dominant role, for example, for air bubbles dispersed in water (such as in bubble aeration used in water treatment) or water droplets dispersed in air (wet deposition by aqueous aerosols, cloud droplets, fog, rain, and mist). The propensity of the haloalkane compounds for the water−vapor interface will lead to their effective transfer from water to air bubbles or, in the inverse case, to their capture and transport from the air to water droplets. The overall efficiency of the process will increase with increasing surface area of the dispersed phase per unit volume.

The fact that the low molecular weight haloalkanes are preferentially partially hydrated at the aqueous−air interfaces is of importance also for understanding heterogeneous chemical processes occurring at the surface of aerosols and other liquid droplets dispersed in air, on thin water films adsorbed on surfaces, or at the quasi-liquid layer on ice.

■ ASSOCIATED CONTENT

Supporting Information

Halomethane force field: Lennard-Jones parameters (Table S1), atomic charges and scaling factor values (Table S2). Unsymmetrized free energy profiles (Figure S1), free energy profiles with error bars computed by the bootstrapping technique (Figure S2), free energy profiles calculated using several different values of the scaling factor of atomic partial charges (Figure S3), decomposition of computed free energy profiles into enthalpic and entropic components (Figure S4), plot of the enthalpic components with a typical error bar shown (Figure S5), unconstrained trajectories of two chloromethane molecules interacting with a water slab (Figure S6). This material is available free of charge via the Internet at http://pubs.acs.org.

■ AUTHOR INFORMATION

Corresponding Authors

*E-mail: roesel@uochb.cas.cz (M.R.).
*E-mail: valsaraj@lsu.edu (K.T.V.).

Notes

The authors declare no competing financial interest.

■ ACKNOWLEDGMENTS

The authors wish to thank Robert Vácha, Ivan Gladich, Morteza Khabiri, Jana Hladílková, and Pavel Jungwirth for helpful discussions. The research was supported by the Czech Science Foundation (Grant 13-06181S) and by the funding to the Institute of Organic Chemistry and Biochemistry AS CR via RVO 61388963. Travel support to M.R. from the AirUCI Institute funded by the U.S. National Science Foundation (Grant 0909227) is also gratefully appreciated. K.T.V. acknowledges grants from the U.S. National Science Foundation (AGS 1106569) and the Gulf of Mexico Research Initiative (GoMRI) (LSU GRI Subaward TUL-629-11/12).

■ REFERENCES

(1) Symons, J. M.; Bellar, T. A.; Carswell, J. K.; DeMarco, J.; Kropp, K. L.; Robeck, G. G.; Seeger, D. R.; Slocum, C. J.; Smith, B. L.; Stevens, A. A. National Organics Reconnaissance Survey for Halogenated Organics. *J. Am. Water Works Assoc.* **1975**, *67*, 634.

(2) Finlayson-Pitts, B. J.; Pitts, J. N., Jr. *Chemistry of the Upper and Lower Atmosphere: Theory, Experiments, and Applications*; Academic Press: San Diego, 2000.

(3) Tchobanoglous, G.; Burton, F.; Stensel, H. D. *Metcalf & Eddy: Wastewater Engineering - Treatment and Reuse*; McGraw Hill Book Co.: New York, 2002.

(4) Eckenfelder, W. W., Jr. *Industrial Water Pollution Control*; McGraw-Hill: New York, 1966.

(5) Valsaraj, K. T. Adsorption of Polycyclic Aromatic Hydrocarbons at the Air-Water Interface and Its Role in Atmospheric Deposition by Fog Droplets. *Environ. Toxicol. Chem.* **2004**, *23*, 2318−2323.

(6) Karger, B. L. Solvent Sublation. In *Adsorptive Bubble Separation Techniques*; Lemlich, R., Ed.; Academic Press: New York, 1972.

(7) Valsaraj, K. T.; Thoma, G. J.; Thibodeaux, L. J.; Wilson, D. J. Studies in Batch and Continuous Solvent Sublation. 1. A Complete Model and Mechanisms of Sublation of Neutral and Ionic Species from Aqueous Solution. *Sep. Technol.* **1991**, *1*, 234−244.

(8) Clarke, A. N.; Wilson, D. J. *Foam Flotation: Theory and Applications*; Marcel Dekker: New York, 1983.

(9) Bryson, B. G.; Valsaraj, K. T. Solvent Sublation for Waste Minimization in a Process Water Stream - a Pilot-Scale Study. *J. Hazard. Mater.* **2001**, *82*, 65−75.

(10) Smith, J. S.; Valsaraj, K. T. The Promise of Solvent Sublation. *Chem. Eng. Progr.* **1998**, *94*, 69−76.

(11) Huang, S. D.; Valsaraj, K. T.; Wilson, D. J. Removal of Refractory Organics by Aeration. 5. Solvent Sublation of Naphthalene and Phenanthrene. *Sep. Sci. Technol.* **1983**, *18*, 941−968.

(12) Valsaraj, K. T.; Porter, J. L.; Liljenfeldt, E. K.; Springer, C. Solvent Sublation for the Removal of Hydrophobic Chlorinated Compounds from Aqueous-Solutions. *Water Res.* **1986**, *20*, 1161−1175.

(13) Valsaraj, K. T.; Wilson, D. J. Removal of Refractory Organics by Aeration. 4. Solvent Sublation of Chlorinated Organics and Nitrophenols. *Colloids Surf.* **1983**, *8*, 203−224.

(14) Lionel, T.; Wilson, D. J.; Pearson, D. E. Removal of Refractory Organics from Water by Aeration. 1. Methyl Chloroform. *Sep. Sci. Technol.* **1981**, *16*, 907−923.

(15) Valsaraj, K. T. On the Physicochemical Aspects of Partitioning of Non-Polar Hydrophobic Organics at the Air-Water-Interface. *Chemosphere* **1988**, *17*, 875−887.

(16) Hartkopf, A.; Karger, B. L. Study of Interfacial Properties of Water by Gas-Chromatography. *Acc. Chem. Res.* **1973**, *6*, 209−216.

(17) Roth, C. M.; Goss, K.-U.; Schwarzenbach, R. P. Adsorption of a Diverse Set of Organic Vapors on the Bulk Water Surface. *J. Colloid Interface Sci.* **2002**, *252*, 21−30.

(18) Kelly, C. P.; Cramer, C. J.; Truhlar, D. G. Predicting Adsorption Coefficients at Air−Water Interfaces Using Universal Solvation and Surface Area Models. *J. Phys. Chem. B* **2004**, *108*, 12882−12897.

(19) Goss, K.-U. Predicting Adsorption of Organic Chemicals at the Air-Water Interface. *J. Phys. Chem. A* **2009**, *113*, 12256−12259.

(20) Jubb, A. M.; Hua, W.; Allen, H. C. Organization of Water and Atmospherically Relevant Ions and Solutes: Vibrational Sum Frequency Spectroscopy at the Vapor/Liquid and Liquid/Solid Interfaces. *Acc. Chem. Res.* **2012**, *45*, 110−119.

(21) Liyana-Arachchi, T. P.; Stevens, C.; Hansel, A. K.; Ehrenhauser, F. S.; Valsaraj, K. T.; Hung, F. R. Molecular Simulations of Green Leaf Volatiles and Atmospheric Oxidants on Air/Water Interfaces. *Phys. Chem. Chem. Phys.* **2013**, *15*, 3583−3592.

(22) Hede, T.; Li, X.; Leck, C.; Tu, Y.; Ågren, H. Model Hulis Compounds in Nanoaerosol Clusters − Investigations of Surface Tension and Aggregate Formation Using Molecular Dynamics Simulations. *Atmos. Chem. Phys.* **2011**, *11*, 6549−6557.

(23) Li, X.; Hede, T.; Tu, Y.; Leck, C.; Ågren, H. Surface-Active cis-Pinonic Acid in Atmospheric Droplets: A Molecular Dynamics Study. *J. Phys. Chem. Lett.* **2010**, *1*, 769−773.

(24) Ma, X.; Chakraborty, P.; Henz, B. J.; Zachariah, M. R. Molecular Dynamic Simulation of Dicarboxylic Acid Coated Aqueous Aerosol: Structure and Processing of Water Vapor. *Phys. Chem. Chem. Phys.* **2011**, *13*, 9374−9384.

(25) Vacha, R.; Jungwirth, P.; Chen, J.; Valsaraj, K. T. Adsorption of Polycyclic Aromatic Hydrocarbons at the Air-Water Interface: Molecular Dynamics Simulations and Experimental Atmospheric Observations. *Phys. Chem. Chem. Phys.* **2006**, *8*, 4461−4467.

(26) Liyana-Arachchi, T. P.; Valsaraj, K. T.; Hung, F. R. Molecular Simulation Study of the Adsorption of Naphthalene and Ozone on Atmospheric Air/Ice Interfaces. *J. Phys. Chem. A* **2011**, *115*, 9226−9236.

(27) Hede, T.; Leck, C.; Sun, L.; Tu, Y.; Ågren, H. A Theoretical Study Revealing the Promotion of Light-Absorbing Carbon Particles Solubilization by Natural Surfactants in Nanosized Water Droplets. *Atmos. Sci. Lett.* **2013**, *14*, 86−90.

(28) Vacha, R.; Slavicek, P.; Mucha, M.; Finlayson-Pitts, B. J.; Jungwirth, P. Adsorption of Atmospherically Relevant Gases at the Air/Water Interface: Free Energy Profiles of Aqueous Solvation of N_2,

O_2, O_3, OH, H_2O, HO_2, and H_2O_2. *J. Phys. Chem. A* **2004**, *108*, 11573−11579.
(29) Wick, C. D.; Chen, B.; Valsaraj, K. T. Computational Investigation of the Influence of Surfactants on the Air-Water Interfacial Behavior of Polycylic Aromatic Hydrocarbons. *J. Phys. Chem. C* **2010**, *114*, 14520−14527.
(30) Vieceli, J.; Roeselova, M.; Potter, N.; Dang, L. X.; Garrett, B. C.; Tobias, D. J. Molecular Dynamics Simulations of Atmospheric Oxidants at the Air-Water Interface: Solvation and Accommodation of OH and O_3. *J. Phys. Chem. B* **2005**, *109*, 15876−15892.
(31) Roeselova, M.; Vieceli, J.; Dang, L. X.; Garrett, B. C.; Tobias, D. J. Hydroxyl Radical at the Air-Water Interface. *J. Am. Chem. Soc.* **2004**, *126*, 16308−16309.
(32) Harper, K.; Minofar, B.; Sierra-Hernandez, M. R.; Casillas-Ituarte, N. N.; Roeselova, M.; Allen, H. C. Surface Residence and Uptake of Methyl Chloride and Methyl Alcohol at the Air/Water Interface Studied by Vibrational Sum Frequency Spectroscopy and Molecular Dynamics. *J. Phys. Chem. A* **2009**, *113*, 2015−2024.
(33) Pasalic, H.; Roeselova, M.; Lischka, H. Methyl and Pentyl Chloride in a Microhydrated Environment and at the Liquid Water-Vapor Interface: A Theoretical Study. *J. Phys. Chem. B* **2011**, *115*, 1807−1816.
(34) Blando, J. D.; Turpin, B. J. Secondary Organic Aerosol Formation in Cloud and Fog Droplets: A Literature Evaluation of Plausibility. *Atmos. Environ.* **2000**, *34*, 1623−1632.
(35) Sander, R. *Compilation of Henry's Law Constants for Inorganic and Organic Species of Potential Importance in Environmental Chemistry*, Version 3, 1999; http://www.henrys-law.org (accessed September 9, 2011).
(36) Lemkul, J. A.; Bevan, D. R. Assessing the Stability of Alzheimer's Amyloid Protofibrils Using Molecular Dynamics. *J. Phys. Chem. B* **2010**, *114*, 1652−1660.
(37) Jagoda-Cwiklik, B.; Cwiklik, L.; Jungwirth, P. Behavior of the Eigen Form of Hydronium at the Air/Water Interface. *J. Phys. Chem. A* **2011**, *115*, 5881−5886.
(38) Hub, J. S.; de Groot, B. L.; van der Spoel, D. g_wham - A Free Weighted Histogram Analysis Implementation Including Robust Error and Autocorrelation Estimates. *J. Chem. Theory Comput.* **2010**, *6*, 3713−3720.
(39) Kumar, S.; Bouzida, D.; Swendsen, R. H.; Kollman, P. A.; Rosenberg, J. M. The Weighted Histogram Analysis Method for Free-Energy Calculations on Biomolecules. 1. The Method. *J. Comput. Chem.* **1992**, *13*, 1011−1021.
(40) Kumar, S.; Rosenberg, J. M.; Bouzida, D.; Swendsen, R. H.; Kollman, P. A. Multidimensional Free-Energy Calculations Using the Weighted Histogram Analysis Method. *J. Comput. Chem.* **1995**, *16*, 1339−1350.
(41) Hess, B.; Kutzner, C.; van der Spoel, D.; Lindahl, E. GROMACS 4: Algorithms for Highly Efficient, Load-Balanced, and Scalable Molecular Simulation. *J. Chem. Theory Comput.* **2008**, *4*, 435−447.
(42) Abascal, J. L. F.; Vega, C. A general purpose model for the condensed phases of water: TIP4P/2005. *J. Chem. Phys.* **2005**, *123*, 234505.
(43) Vega, C.; Abascal, J. L. F. Simulating Water with Rigid Non-Polarizable Models: A General Perspective. *Phys. Chem. Chem. Phys.* **2011**, *13*, 19663−19688.
(44) Vega, C.; Abascal, J. L. F.; Conde, M. M.; Aragones, J. L. What Ice Can Teach Us About Water Interactions: A Critical Comparison of the Performance of Different Water Models. *Faraday Discuss.* **2009**, *141*, 251−276.
(45) Wang, J.; Wolf, R. M.; Caldwell, J. W.; Kollman, P. A.; Case, D. A. Development and Testing of a General Amber Force Field. *J. Comput. Chem.* **2004**, *25*, 1157−1174.
(46) Bayly, C. I.; Cieplak, P.; Cornell, W. D.; Kollman, P. A. A Well-Behaved Electrostatic Potential Based Method Using Charge Restraints for Deriving Atomic Charges - the RESP Model. *J. Phys. Chem.* **1993**, *97*, 10269−10280.
(47) Frisch, M. J.; Trucks, G. W.; Schlegel, H. B.; Scuseria, G. E.; Robb, M. A.; Cheeseman, J. R.; Scalmani, G.; Barone, V.; Mennucci, B.; Petersson, G. A.; et al. *Gaussian 09, Revision A.1*; Gaussian, Inc.: Wallingford, CT, 2009.
(48) Case, D. A.; Darden, T. A.; Cheatham, T. E.; Simmerling, C. L.; Wang, J.; Duke, R. E.; Luo, R.; Merz, K. M.; Pearlman, D. A.; Crowley, M.; et al. *AMBER 9*; University of California: San Fransisco, 2006.
(49) Hockney, R. W.; Goel, S. P.; Eastwood, J. W. Quiet High-Resolution Computer Models of a Plasma. *J. Comput. Phys.* **1974**, *14*, 148−158.
(50) Bussi, G.; Donadio, D.; Parrinello, M. Canonical Sampling through Velocity Rescaling. *J. Chem. Phys.* **2007**, *126*, 014101.
(51) Darden, T.; York, D.; Pedersen, L. Particle Mesh Ewald - an N.Log(N) Method for Ewald Sums in Large Systems. *J. Chem. Phys.* **1993**, *98*, 10089−10092.
(52) Essmann, U.; Perera, L.; Berkowitz, M. L.; Darden, T.; Lee, H.; Pedersen, L. G. A Smooth Particle Mesh Ewald Method. *J. Chem. Phys.* **1995**, *103*, 8577−8593.
(53) Hess, B.; Bekker, H.; Berendsen, H. J. C.; Fraaije, J. Lincs: A Linear Constraint Solver for Molecular Simulations. *J. Comput. Chem.* **1997**, *18*, 1463−1472.
(54) Hub, J. S.; Caleman, C.; van der Spoel, D. Organic Molecules on the Surface of Water Droplets − an Energetic Perspective. *Phys. Chem. Chem. Phys.* **2012**, *14*, 9537−9545.
(55) Feller, D. The Role of Databases in Support of Computational Chemistry Calculations. *J. Comput. Chem.* **1996**, *17*, 1571−1586.
(56) Caleman, C.; Hub, J. S.; van Maaren, P. J.; van der Spoel, D. Atomistic Simulation of Ion Solvation in Water Explains Surface Preference of Halides. *Proc. Natl. Acad. Sci. U.S.A.* **2011**, *108*, 6838−6842.
(57) Zierkiewicz, W.; Michalska, D.; Havlas, Z.; Hobza, P. Study of the Nature of Improper Blue-Shifting Hydrogen Bonding and Standard Hydrogen Bonding in the $X_3CH—OH_2$ and $XH—OH_2$ Complexes (X = F, Cl, Br, I): A Correlated Ab Initio Study. *ChemPhysChem* **2002**, *3*, 511−518.
(58) Zhao, X.; Pang, X.; Yan, X.; Jin, W. Halogen Bonding or Hydrogen Bonding between 2,2,6,6-Tetramethyl-Piperidine-Noxyl Radical and Trihalomethanes CHX_3 (X = Cl, Br, I). *Chin. J. Chem. Phys.* **2013**, *26*, 172−180.
(59) Smith, J. S.; Valsaraj, K. T.; Thibodeaux, L. J. Bubble Column Reactors for Wastewater Treatment. 1. Theory and Modeling of Continuous Countercurrent Solvent Sublation. *Ind. Eng. Chem. Res.* **1996**, *35*, 1688−1699.
(60) Smith, J. S.; Burns, L. F.; Valsaraj, K. T.; Thibodeaux, L. J. Bubble Column Reactors for Wastewater Treatment. 2. The Effect of Sparger Design on Sublation Column Hydrodynamics in the Homogeneous Flow Regime. *Ind. Eng. Chem. Res.* **1996**, *35*, 1700−1710.
(61) Smith, J. S.; Valsaraj, K. T. Bubble Column Reactors for Wastewater Treatment. 3. Pilot-Scale Solvent Sublation of Pyrene and Pentachlorophenol from Simulated Wastewater. *Ind. Eng. Chem. Res.* **1997**, *36*, 903−914.
(62) Valsaraj, K. T. Trace gas adsorption thermodynamics at the air-water interface: Implications in atmospheric chemistry. *Pure Appl. Chem.* **2009**, *81*, 1889−1901.
(63) Nissenson, P.; Knox, C. J. H.; Finlayson-Pitts, B. J.; Phillips, L. F.; Dabdub, D. Enhanced Photolysis in Aerosols: Evidence for Important Surface Effects. *Phys. Chem. Chem. Phys.* **2006**, *8*, 4700−4710.
(64) Watanabe, H.; Yamaguchi, S.; Sen, S.; Morita, A.; Tahara, T. "Half-Hydration" at the Air/Water Interface Revealed by Heterodyne-Detected Electronic Sum Frequency Generation Spectroscopy, Polarization Second Harmonic Generation, and Molecular Dynamics Simulation. *J. Chem. Phys.* **2010**, *132*, 144701.

MOLECULAR SIMULATIONS OF HALOMETHANES AT THE AIR/ICE INTERFACE.

A. Habartová[(a)], L. Hormain [(b)], E. Pluharova [(a),(c)], S. Briquez [(b)], M. Monnerville [(b)], C. Toubin [(b)] and M. Roeselova [(a)]*

(a) Institute of Organic Chemistry and Biochemistry, Academy of Sciences of the Czech Republic, Flemingovo nám. 2, 16610 Prague 6,

Czech Republic

(b) PhLAM Laboratory, UMR CNRS 8523,

Université de Lille, Cité Scientifique,

59655 VILLENEUVE D'ASCQ, France

(c) Department of Chemistry, École Normale Supérieure, UMR ENS-CNRS-UPMC 8640, 24 rue Lhomond, 75005 Paris, France

KEYWORDS.

Molecular dynamics, ice, adsorption, halocarbons, haloalkanes, halomethanes, methylchloride, methylbromide, trichloromethane, tribromomethane, atmosphere.

ABSTRACT. Halogenated organics are emitted into the atmosphere from a variety of sources of both natural and anthropogenic origin. Their uptake at the surface of aerosols can affect their reactivity, for example in processes which take part in ozone destruction due to production of reactive chlorine, bromine and iodine radicals. Classical molecular dynamics (MD) simulations are carried out to investigate the interaction of small halomethane molecules of atmospheric relevance with a crystalline ice surface. The following halomethanes were studied: CH_3Cl, CH_2Cl_2, $CHCl_3$, CH_3Br, CH_2Br_2 and $CHBr_3$. MD simulations thus provide an invaluable insight into the adsorption behavior of halomethanes species. The adsorption energy is increasing as the number of halogen atoms is increasing. Moreover brominated methanes exhibit a stronger interaction with the ice than their chlorinated analogs. Implications for the atmospheric chemistry are discussed.

INTRODUCTION

There are still many open questions about the activation of halogens in the Polar Boundary Layer and its implication in the strastrospheric ozone loss. A comprehensive account of the different mechanisms for halogen activation in environmental ice and snow is included in the reviews by Saiz Lopez and Glasow [1] and Abbatt et al [2]. Recent studies have shown that halocarbons are also important contributors to stratospheric bromine or chlorine loading, through their

transport and photodegradation.[3, 4] Volatile halogenated compounds were also measured in the water column, in the air and in sea ice brine across the Arctic Ocean.[5-7]

CH_3Cl is a naturally occurring, ozone-depleting trace gas and one of the most abundant chlorinated compounds in the atmosphere.[8] The relatively long tropospheric lifetime of CH_3Cl (>1 year) results in a significant amount of CH_3Cl being transported into the stratosphere, where it undergoes photolysis or reactions with OH radical to release ozone-destroying Cl atoms or convert to the temporary reservoirs of HCl, $ClONO_2$, and HOCl.[9]

By contrast, CHX_3, and CH_2X_2 (X=Cl or Br) have shorter lifetimes in the troposphere – with lifetimes <6 months - and are thus called Very Short Lived Species (VSLS). The most abundant chlorinated VSLS are CH_2Cl_2 and $CHCl_3$ for which anthropogenic activity accounts for 90% and 25 % respectively of their tropospheric abundances. Indeed ,there is an observed growth of tropospheric CH_2Cl_2 that could be due, in particular, to its use in as a feedstock in the production of HFCs, the second generation of CFC replacement gases.[4]

High concentrations of tribromomethane have been reported in sea ice, originating from biogenic production by algae[10] and in the Arctic stratosphere.[5] Halomethanes may transfer from clouds to ice particles. Some of these enriched ice particles may be transported up to the Troposphere Tropopause Layer (TTL) where they could evaporate releasing the chemical species in the gas phase. As a consequence, the contribution of bromocarbons has been increasingly recognized, especially given the enhanced ozone destruction potential of bromine in the lower stratosphere[3]– two orders of magnitude higher than that of chlorine.

One pioneering experimental work[11] studied, by infrared spectroscopy (IR), the series of twenty-three halocarbon compounds interacting with water ice at 12 K. Perturbations to the water (D_2O) sites which are not saturated (dangling atoms) in the absence of guest molecules

showed distinct trends (shifts of the dangling bond spectral position) depending on the type and extent of halogen substitution in the occluded molecules. Moreover, the ozonation of chlorinated methanes on polycrystalline ice was studied by IR spectroscopy over the temperature range 77–292 K.[12] Under the conditions of the model experiments, ozonation does not occur at temperatures below 210 K (characteristic of the upper troposphere). At higher temperatures, chloromethanes can, however, effectively destroy ozone with possible formation of chlorine oxides in low oxidation states decreasing as the number of chlorine atoms increases in the series CH_3Cl, CH_2Cl_2,$CHCl_3$, CCl_4.

The chemical sputtering technique has been used to investigate the diffusive mixing of chloromethanes in different molecular solids H_2O, D_2O, and CH_3OH, focusing on amorphous solid water.[13] It has been found that while the diffusion of CCl_4 in amorphous solid water (ASW) is hindered, other chloromethanes such as $CHCl_3$ and CH_2Cl_2 undergo diffusive mixing over the same temperature range.

By contrast, the adsorption of trichloromethane ($CHCl_3$) on ice layers has been studied extensively by various experimental techniques: temperature-programmed desorption (TPD), infrared reflection absorption spectroscopy (IRAS)[14], X-ray photoemission spectroscopy (XPS)[5] metastable impact electron spectroscopy.[15] It was found that the interaction of $CHCl_3$ with the ice is relatively weak and physisorptive, as expected from a hydrophobic nature of the molecule. The mobility of tribromomethane ($CHBr_3$) and trichloromethane ($CHCl_3$) on amorphous solid water and crystalline ice surfaces have been compared using temperature programmed desorption spectroscopy and reflection absorption infrared spectroscopy.[16] The experiments concluded that $CHBr_3$ is more strongly bound than $CHCl_3$, as evidenced by its higher desorption temperature. Nevertheless they also observe a lower barrier for surface

diffusion of CH_3Br compared to $CHCl_3$. Computer calculations as those carried in the present study will provide quantitative estimates of these interactions.

From a theoretical point of view, the halomethanes have received less attention than HCl and HBr, whose interaction with the ice surface has been extensively studied in the context of stratospheric ozone loss.[2] To improve our understanding of the role of 'hydration' for the removal of inorganic bromine or chlorine from the troposphere to the stratosphere, it is, therefore, crucial to further extend our knowledge about surface and uptake processes for other species than HCl and HBr[17]. Theoretical studies were actually carried on the CH_3X-H_2O dimer. One ab initio study characterized the geometry and binding energy of the CH_xCl_{4-x} –H_2O dimer (x=0,..3)[18] The bromomethane - water 1:2 complexes have been also studied with the Second-order Møller-Plesset theory (MP2) to reveal the role of hydrogen bond and halogen bond in the formation of different aggregates[19] More recently, free energy profiles associated with the transfer of chlorinated and brominated halomethane molecules across the vapor-liquid water interface were calculated using classical molecular dynamics simulations[20]. There is no report available on the interaction of haloalkanes with ice at the molecular level. In this context, we have investigated by means of classical molecular dynamics simulation the interaction of the series of halomethanes ($CH_{4-n}X_n$, n=1-3, X=Cl, Br) with a model crystalline ice surface. The MD simulation results provide molecular-level insight into the adsorption behavior and residence time of halomethane species contributing to a better understanding of some heterogeneous chemical processes in the atmosphere.

COMPUTATIONAL DETAILS

Molecular dynamics simulations of the halomethanes adsorption at T=235 K were performed for a hexagonal (I_h) ice slab with the basal (0001) facet exposed to the vapor phase. For the halomethane molecules ($CH_{4-n}X_n$, n=1-3, X=Cl, Br), the general Amber force field (GAFF) parameters set was employed. The atomic partial charges of the halomethane molecules along with the rest of the force field parameters are given in our previous work[20, 21]. Water molecules were described using the TIP4P/2005 model[22]. The ice sample, consisting of 1344 water molecules, was constructed as an ideal ice crystal at 0 K using the algorithm of Buch et al [23] which yields a proton-disordered ice structure satisfying the Bernal-Fowler rules.[24] The dimensions of the initial ice sample were approximately 26.9 × 31.0 × 46.5 $Å^3$ in the x, y, and z directions, respectively. To equilibrate the ice to the target temperature, periodic boundary conditions were applied in all three dimensions, and a 200ps isobaric-isothermal (NPT) simulation of bulk ice was performed. The ice sample was first annealed from 0 K to 235 K over the course of 130 ps, and then equilibrated at T=235 K for additional 70 ps. The Berendsen weak-coupling scheme [25] with time steps for heat bath coupling and pressure relaxation of 0.1 and 0.5 ps, respectively, was employed to control the temperature and pressure in the annealing and equilibration run. The pressure of the barostat was set to zero in order to avoid any unwanted stress to the equilibrated ice structure after the ice–vacuum interface has been generated.[26]

Once the bulk ice sample had been equilibrated at the desired temperature, the z-dimension of the simulation cell was extended to 160 Å, resulting in an ice slab with two flat ice–vacuum interfaces located in the middle of the simulation cell, with a layer of vacuum on each side. The thickness of the ice slab was approximately 47 Å, corresponding to 14 ice crystal bilayers. The z axis is normal to the ice–vacuum interface. Two halocarbon molecules ($CH_{4-n}X_n$, n=1-3, X=Cl,

Br) were then added to the simulation cell, one to each of the two ice surfaces, at randomly selected x and y positions, and about 10 Å away from the ice surface along the z coordinate. The haloalkane molecules were assigned a small initial velocity (sampled randomly from the Maxwell-Boltzmann distribution corresponding to T = 10 K) pointing toward the respective ice surface. For each of the halomethanes species, the system was propagated for 50 ns in an isochoric-isothermal (NVT) simulation at T=235 K to sample structural and dynamical characteristics of the adsorbed halomethanes. The first 2 ns of each trajectory were excluded from analysis to allow the formation and equilibration of the disordered interfacial layer on the free basal planes of the ice slab. In the production run, the system's temperature was controlled by the Bussi-Donadio-Parrinello thermostat (velocity rescaling with a stochastic term)[27] with a coupling time of 0.5 ps. The melting point of the TIP4P/2005 model being T_m ~250 K,[26] the simulation at T=235 K therefore corresponds to a 15 K undercooling with respect to the melting point of the model ice ($T = T_m$ -15 K).

All molecular dynamics calculations were performed using the GROMACS[28] (version 4.5.3) program package.[28] The equations of motion were integrated by the leap-frog algorithm[29] with a 1fs time step. The twin range cut-off scheme was employed, and both the Lennard-Jones and the short-range part of the Coulomb interactions were smoothly truncated to zero between 7 and 9 Å. The long-range part of the Coulomb interaction was evaluated using the smooth Particle-Mesh Ewald method[30, 31] with a relative tolerance of 10^{-5}, fourth order cubic interpolation and a Fourier spacing parameter of 0.12. Water molecules were treated as rigid bodies using SETTLE,[32] whereas no constrain was applied to the halomethane molecules. System configurations were saved at 1 ps intervals. Analysis of the trajectories was done using GROMACS tools, VMD program[33] was used for visualization.

RESULTS

All halomethane molecules ($CH_{4-n}X_n$, n=1-3, X=Cl, Br) stick to the ice surface and remain adsorbed for the duration of the simulation. The adsorption properties are characterized in terms of configuration, orientation, bonding properties and interaction energies.

1. Configuration of the admolecule

Figure 1 shows some typical configurations obtained from the MD trajectory for each halomethane adsorbed at the gas/ice interfaces. From these snapshots, we can notice that in the simulated conditions (T=235 K, T = T_m - 15 K) only the outermost interfacial layer of ice exhibits substantial disorder. All halomethane molecules are adsorbed on the top of the ice surface but with orientations and distances to the surface layer that differ from one to the other.

This qualitative view of the system can be rationalized by analyzing the density profiles of relevant atoms along the normal (z) to the ice surface. This is illustrated on Figure 2. The water oxygen density profiles are represented for simulations with all six halomethane admolecules, and they exhibit only minor differences. The inner layers of the ice slab are well ordered as evidenced by the double peaks corresponding to the water bilayers of the ice crystal lattice. The disappearance of the double peak for the outermost layer on both sides of the ice slab is indicative of some translational disorder of water molecules at the interface.

Now, considering the adsorption of the halomethane molecules, the methylchloride and methylbromide (Fig. 2(a) and 2(b)) density profiles shapes are very similar to each other. The carbon density profiles exhibit a two component signature: a sharp peak at about 2 Å

from the surface water oxygen layer, and a shoulder, less pronounced, corresponding to the admolecule incorporated deeper in the outermost ice layer. The chlorine density profile of CH_3Cl (Figure 2a) is almost completely superimposed onto the carbon one, indicating that methyl chloride is adsorbed nearly flat on the surface. The 'outer' peak being more intense than the one relative to the 'buried' site indicates that the more loosely physisorbed outer configuration is favored over the duration of the simulation. For CH_3Br (Figure 2d), the bromine density profile is also very close from the carbon one for the surface state. The fact that the bromine density is not so clearly superimposed to the carbon one, compared to CH_3Cl, suggests a slightly more tilted orientation (with respect to the surface normal) for CH_3Br than for CH_3Cl.

For the di-halo (Figure 2(b) and (2e)), the carbon density profile resembles the ones of CH_3Cl or CH_3Br with the evidence of two types of adsorption sites. The halogen atoms are distributed on both sides of the carbon atoms, which can be interpreted in terms of two orientations: one with the C-Cl axis pointing toward the surface, and the other one nearly parallel to the surface (see next section). For CH_2Br_2, the carbon atom can occupy two positions at the ice surface with nearly the same probability, by contrast with CH_2Cl_2, CH_3Cl and CH_3Br, where the carbon tends to be adsorbed predominantly in the site located at a larger distance from the surface layer.

The tri-halo compounds (Figure 2(c) and 2(f)) have similar behaviors with two preferential positions of the carbon at the interface. However, the carbon and halogen density profiles indicate some differences between the trichloro- and tri-bromo methane. For $CHCl_3$, the carbon is essentially pointing toward the film and the chlorine atoms directed toward the vapor phase. By contrast, $CHBr_3$'s atomic distributions exhibit narrower peaks more

especially for the bromine atoms. The halogens are occupying nearly the same plane upwards from the carbon, we can thus expect that the C-H axis is nearly aligned with the surface normal. This will be confirmed in the next section when characterizing the orientation of the molecule.

The projection of the trajectory along the x and y degrees of freedom, parallel to the surface plane, (Figure 3) shows that the methylchloride and methylbromide has a significant mobility and can explore various adsorption sites while remaining adsorbed. CH_2Cl_2, CH_2Br_2 and $CHCl_3$ exhibit also significant surface diffusion motion (Figure 3b), e) and c)), but less homogeneous, since some preferential sites can be identified for CH_2Br_2 and $CHCl_3$ from the regions with high density plots. This is even more pronounced for $CHBr_3$ (Figure 3f)), that appears to be confined in some regions of the surface with a reduced surface diffusion. This is the sign of a stronger binding of $CHBr_3$ to the surface layer than for the other compounds, as shown in part 4.

Finally, for all species, no diffusion trough the ice layers is observed since only the outermost layer exhibits some substantial disorder. Getting closer to the melting temperature or performing the same calculations on a porous surface would of course promote diffusion through the ice lattice.

2. Orientation at the surface

The snapshots shown in Fig. 1 and the comparison of the carbon and halogen density profiles in Fig. 2 already provide a rough idea of the orientation of the various admolecules at the ice surface, but it is nevertheless useful to investigate the surface orientation in a more quantitative way. Orientational distributions P (cos θ) have been

calculated, where θ is the angle between the interface normal (z -axis) and the molecular vector $\vec{v}$ whose definition varies with the different investigated halomethane compounds. These orientational distributions have been calculated separately for each interface. Figure 4 shows the distributions obtained for the upper interface.

For CH_3X (X=Cl or Br), the molecular vector $\vec{v}$= X → C points from the halogen atom to the carbon atom. $\cos\theta = 0$ means that the CH_3X molecule is aligned with the C-X axis parallel to the surface, $\cos\theta = 1$ corresponds to the molecular axis oriented perpendicular to the surface with the halogen (X) atom pointing toward the ice layer, whereas $\cos\theta = -1$ denotes a perpendicular orientation of the molecular axis relative to the surface with the methyl group directed toward the gas phase. Figure 4(a) and (d) represent the distributions calculated respectively for CH_3Cl and CH_3Br. Both angular distributions are similar and characterized by a single broad peak. The distribution is centered around $\cos\theta = -0.15$ for CH_3Cl and $\cos\theta = -0.4$ for CH_3Br, characteristic of a tilted orientation of the X-C axis of the chloromethane and bromomethane molecules at the angle $\theta = 99°$ and 113 °, respectively, relative to the surface normal. CH_3Br molecule is thus slightly more tilted with respect to the normal to the surface than CH_3Cl, the hydrogens of the halomethane being directed toward the surface. This is fully consitent with the z density profiles previously described, characteristic of a flat configuration of the two halomethanes on the surface.

CH_2X_2 (X=Cl or Br) orientation is defined by the molecular vector $\vec{v}$= C → H with taking into account only one of the two (equivalent) hydrogen atoms for the analysis. We note that the molecular vector defined using the other hydrogen atom (or both of them) would lead to an identical distribution. The orientational distributions obtained for both CH_2Cl_2

and CH_2Br_2 exhibit two peaks, for the same angle, corresponding to two possible orientations of one of the C-H bond. The maxima correspond to configurations where one C-H axis is directed toward the surface tilted by around 155° degrees with respect to the surface normal and the second one, where the same C-H bond is directed toward the gas phase (tilted by 72° from the surface normal). As a consequence, one of the halogens is pointing toward the gas phase and the second one toward the interface, as shown on Figure 1(b) and 1(e).

Finally, for the tri-halomethanes, we define the molecular vector $\vec{v}$= C → H, i.e. from the carbon to the hydrogen atom. $CHCl_3$ and $CHBr_3$ differ strongly in their orientation as shown from the angular distributions (Fig. 4(c) and 4(f)). The trichloromethane molecule orientational distribution (Fig. 4(c)) is characterized by a broad peak centered around cos θ = 0.3 (θ= 72°) and by a second broad peak, less intense, for θ close to 180°, corresponding to the halogens directed toward the gas phase. The orientation obtained from our calculations is consistent with Aoki's experimental results[15] showing that the $CHCl_3$ molecules are adsorbed on the topmost ice layer with their H atoms pointing toward the substrate at 35 K and with their Cl atoms away from the ice layers. The orientation of $CHBr_3$, shown in Figure 4(f), is characterized by bimodal distribution with a broad peak centered around cos θ = 0.4 (θ= 66°) and a second peak, more intense, for cos θ close to 1. For this latter orientation, the hydrogen is the only atom pointing toward the gas phase, the three bromine atoms facing the ice layer. The orientation of the tribromomethane is thus very different from its chlorinated analog as illustrated on the snapshots shown in Figure 1 panel (c) and (f). The orientation of these halocarbons has been characterized in a previous study at the air/liquid water interface with using the same

semiempirical description[20]. For halomethanes, the orientation on liquid water and on ice is rather similar (even if broader at the liquid interface). By contrast, for CH_2Cl_2, $CHCl_3$ and CH_2Br_2, some preferential orientations are evidenced on ice. We should actually relate these differences to the temperature at which the simulations have been performed, 300 K for the liquid interface and 235 K for the ice surface. The thermal energy present for the liquid film calculations allows both the admolecules to adopt various orientations, and the interface to relax upon the adsorption of the haloalkane. As a result, the distributions at the liquid interface are smoothed out compared to the ones obtained for ice. For $CHBr_3$, the signature of two preferential orientations can also be distinguished, even if less pronounced, at the liquid interface, similarly to the ice surface.

1.3. Bonding properties from geometric criteria

Figure 5 shows radial distribution functions (RDFs) g(r) characterizing the bonding of the various halomethanes with the water molecules. The first interesting distance used in g(r) is the distance between the halogen atom (X=Cl or Br) in the halomethane molecule and the hydrogen atoms (H) in the water molecules. These distributions are represented in Figure 5 for the halomethanes series. Except for CH_2Cl_2 and $CHCl_3$, the $g_{X...Hw}(r)$ distributions, are characterized by a pronounced peak for distances from 0.21 to 0.25 nm indicating that the corresponding halomethane molecules bind to water through the formation of a X…H bond with unsaturated hydrogens of the surface layer. Halomethanes can also bind to the oxygen atom of water through their hydrogen atoms thanks to the polarity of the C – H bonds, this is characterized by the $g_{H...Ow}(r)$ radial distribution. The $g_{H...Ow}(r)$ distributions (Figure 5) exhibit peaks for H…O distances ranging between 0.2 and 0.25 nm for all species except for CH_3Cl and CH_3Br. Most of

the species adopt orientations allowing the formation of weak hydrogen bonds between the halomethane hydrogens and unsaturated oxygen atoms of the surface. The orientation of $CHCl_3$ at the surface, with the hydrogen atom pointing toward the innerlayers, optimizes this type of binding. Among the series, CH_2Br_2 and $CHBr_3$ combine both types of bonding by forming Br…H_w and H…O_w bonds. This binding is possible thanks to the tilted orientation of the two molecules at the interface. When $CHBr_3$ is adsorbed with the hydrogen pointing straight to the gas phase ($\cos \theta=1$), the formation of Br…H bonds is evidently favored in this case.

The orientation and bonding features obtained from our calculations indicate that, for all brominated halomethanes and for CH_3Cl, the bonding to the ice surface occurs mainly through the halogen atoms. For CH_2Cl_2 and $CHCl_3$, the chlorine atoms do not seem to be attached to a dangling H atom of the surface and point freely toward the gas phase. These results are in agreement with the IR investigation by Holmes et al, [11] particularly for the brominated halomethanes, since they evidenced, that in the series CBr_nH_{4-n}, with n=1-4, the bonding to a 12K amorphous ice film is through the bromine atom(s).

The differences we evidence in the nature of the bonding of the studied halomethanes with the ice surface may be of importance regarding their photodissociation and the ability of the photoproducts, like the halogen radicals, to be released in the gas phase or trapped at the surface.

1.4. Interaction energy

The strength of the interaction of the admolecule with the ice surface is also an important parameter that can be compared with experiments. From the MD simulations, the short range interaction energy can be obtained and averaged over the simulation time. The total short range interaction energy is obtained from the sum of the short range dispersion-repulsion and

electrostatic contributions. The long-range correction of the interaction between the admolecule and the surface cannot be distinguished from all the interactions, including the water – water interaction, with using the PME summation method. Still, the comparison between the short-range adsorption energies of the various haloalkanes provides a useful qualitative description of the relative strength of the binding. The general observations that can be addressed from the energy distributions given in Figure 6, are the following: i) the strength of the interaction increases with the number of halogen substituents; ii) the distribution gets also broader as the number of halogens is increasing and iii) the bromine compounds exhibit larger adsorption energies than their chlorinated analogs. For all the studied adsorbates, the electrostatic contribution is dominating. CH_3Cl exhibits the weakest interaction (-22 kJ/mol) and the interaction is increasing from CH_2Cl_2 (-30 kJ/mol) to $CHCl_3$ (-38 kJ/mol).

The distribution in energy for CH_3Br is slightly narrower than the one of CH_3Cl but with a maximum for a comparable value (-22 kJ/mol). Because CH_2Br_2 is forming both Br…H(water) and H...O(water) bonds, it has a larger interaction, by about 10 kJ/mol, with the water ice than CH_2Cl_2. As supposed from the mobilities of the admolecules (Figure 3 and part 1.1), the strongest adsorption energy (-70 kJ/mol) is obtained for tribromomethane, twice larger than $CHCl_3$ one, certainly because of the formation of Br…H(water) bond. The present comparison agrees well with the experimental results of Grecea et al[16], who concluded from their desorption temperature that $CHBr_3$ is more strongly bound to ice than $CHCl_3$, but the agreement is only limited to this property. Actually, they also observed a lower barrier for surface diffusion of $CHBr_3$ on ice compared to $CHCl_3$, which is in contradiction with the binding strength they suppose and our results presented previously (Figure 3). To resolve this ambiguity, the diffusion

of the tri-halo compounds would need to be investigated in more details on a defective surface to allow the molecules to percolate throught defects (cracks, grains boundaries) in the ice lattice. Finally, the trend we observe on the bonding properties can be compared with studies of the hydrogen bonding between chlorinated methanes and the oxygen atom of liquid water dimers by Hobza and co-workers[18]. They found that the interaction energy increased in the order CCl_4>$CHCl_3$>CH_2Cl_2>CH_3Cl, the order being consistent with our results.

CONCLUSION:

This MD study addresses a detailed analysis of the adsorption properties of a single halomethane molecule $CH_{4-n}X_n$, n=1-3, X=Cl, Br at the air/ice interface at the nominal temperature of 235 K that corresponds to 15 K undercooling relative to the melting point of the water model employed. All of the studied molecules remain adsorbed at the surface during the entire 50 ns simulation runs. The surface orientation of the admolecules varies from one species to another and as a result the bonding properties of the individual admolecules are also slightly different. No substantial difference is observed for the orientation of the studied molecules at the air/ice interface in comparison with the air/water interface except that the more structured character of the ice surface compared to that of a liquid supports several more pronounced preferential orientations. We might expect more differences for lower temperatures since the simulations have been carried out close to the melting point (15K) to mimic the tropospheric conditions. In general, the adsorbate binds to water through either the halogen ($X\ldots H_w$) or the hydrogen ($H\ldots O_w$) atoms. The interaction energy, mainly electrostatic in nature, is increasing with the number of halogen substituents, the brominated compounds showing significantly

stronger interactions than their chlorinated analogs. The range of the interactions is qualitatively consistent with previous experimental data.

$CHBr_3$ and CH_2Br_2, known as VSLS, are produced in principle in the troposphere. The present study shows that these two species may stick to the ice surface. We can thus propose that upon adsorption on ice particles, they may be able to reach higher altitudes and contributing to stratospheric bromine loading.

Another important result is that the halogen atoms of the monochloro or monobromomethane are clearly pointing toward the gas phase making it easily releasable upon photodissociation; for the disubstituted species, even if one halogen is embedded in the ice lattice, the second one is also directed to the vapor phase. The same trend is observed for $CHCl_3$. By contrast, $CHBr_3$ is adsorbed with having the three halogens encapsulated in the ice, making them less available for reactions with gas phase species or less releasable in the gas phase upon photodissociation. As consequence, the adsorption of these species at the ice surface may alter their photodissociation properties and the direct release of the photoproducts.

FIGURES

Figure 1. Side views of snapshots obtained from the MD simulation showing only the upper ice interface and the adsorbed halomethane with the corresponding legend: (a) CH_3Cl, (b) CH_2Cl_2, (c) $CHCl_3$, (d) CH_3Br, (e) CH_2Br_2, (f) $CHBr_3$. For clarity, the water molecules are represented by bonds. The halogen atoms, Cl and Br, are represented by yellow and orange balls respectively.

Figure 2. Density profiles along the z axis perpendicular to the interface for the oxygen atoms of water (black line), the carbon (red line) and halogen atoms (green line) of (a) CH_3Cl, (b) CH_2Cl_2,

(c) $CHCl_3$, (d) CH_3Br, (e) CH_2Br_2, (f) $CHBr_3$. For clarity, only the upper interface is shown. In each panel, the density curves have been normalized to their respective maximum peak for a better representation.

Figure 3. Diffusion of the halomethane parallel to the surface plane for (a) CH_3Cl, (b) CH_2Cl_2, (c) $CHCl_3$, (d) CH_3Br, (e) CH_2Br_2, (f) $CHBr_3$. The blue dots represent the successive x and y positions of the carbon atom.

Figure 4. Orientation of the halomethane adsorbed on the ice surface. θ is the angle between the interface normal (z-axis) and the molecular vector $\vec{v}$. For the CH_3X molecules (X=Cl or Br) (a and d), the molecular vector points from the carbon atom C of the methyl group toward the halogen X, $\vec{v}$= C → X. (2) For the CH_2X_2 species (b and e), the molecular vector is taken as one C-H bond. For the CHX_3 species (c and f), the molecular vector points from the carbon atom to the hydrogen, $\vec{v}$= C → H.

Figure 5. Radial distribution functions characterizing the X halogen atom(s) -H atoms of water distance (green line) and H atom(s) of the halomethane- Oxygen atom of water distance (black line) respectively for (a) CH_3Cl, (b) CH_2Cl_2, (c) $CHCl_3$, (d) CH_3Br, (e) CH_2Br_2, (f) $CHBr_3$.

Figure 6. Energy distribution (in kJ/mol) for the total short range interaction energy between the ice surface and CH_3X (black curve) or CH_2X_2 (red curve) or CHX_3 (green line) with (a) X=Cl and (b) X=Br.

ASSOCIATED CONTENT

(Word Style "TE_Supporting_Information"). **Supporting Information**. A brief statement in non-sentence format listing the contents of material supplied as Supporting Information should be included, ending with "This material is available free of charge via the Internet at http://pubs.acs.org." For instructions on what should be included in the Supporting Information, as well as how to prepare this material for publication, refer to the journal's Instructions for Authors.

AUTHOR INFORMATION

Corresponding Author

celine.toubin@univ-lille1.fr and alena.habartova@marge.uochb.cas.cz

Present Addresses

†If an author's address is different than the one given in the affiliation line, this information may be included here.

Author Contributions

The manuscript was written through contributions of all authors. All authors have given approval to the final version of the manuscript. ‡These authors contributed equally. (match statement to author names with a symbol)

Funding Sources

Czech Science Foundation (Grant 13-06181S), Institute of Organic Chemistry and Biochemistry (AS CR via RVO 61388963), PHC-Barrande (26513PA) funded by the french Ministry of Foreign Affairs and the Czech Ministry of Education, the CaPPA project (Chemical and Physical Properties of the Atmosphere) funded by the French National Research Agency (ANR) through the PIA (Programme d'Investissement d'Avenir) under contract ANR-10-LABX-005, CNRS and Université Lille 1.

Notes

Any additional relevant notes should be placed here.

ACKNOWLEDGMENT

The authors wish to thank Ivan Gladich and Pavel Jungwirth for helpful discussions. The authors dedicate this paper in fond memory of co-author Martina Roeselova: a great teacher and scientist.
Access to computing and storage facilities owned by parties and projects contributing to the National Grid Infrastructure MetaCentrum, provided under the programme "Projects of Large Infrastructure for Research, Development, and Innovations" (LM2010005), is greatly appreciated.

ABBREVIATIONS

MD: Molecular Dynamics, PME: Particle Mesh Ewald,

(Word Style “TF_References_Section”). References are placed at the end of the manuscript.

Authors are responsible for the accuracy and completeness of all references. Examples of the recommended format for the various reference types can be found at http://pubs.acs.org/page/4authors/index.html. Detailed information on reference style can be found in *The ACS Style Guide*, available from Oxford Press.

BRIEFS (Word Style “BH_Briefs”). If you are submitting your paper to a journal that requires a brief, provide a one-sentence synopsis for inclusion in the Table of Contents.

SYNOPSIS (Word Style “SN_Synopsis_TOC”). If you are submitting your paper to a journal that requires a synopsis, see the journal’s Instructions for Authors for details.

REFERENCES

1. Saiz-Lopez, A; von Glasow, R. Reactive halogen chemistry in the troposphere. *Chem Soc Rev*. **2012**, *41* (19), 6448-6472.
2. Abbatt, J.P.D.; Thomas, J. L.; Abrahamsson, K.; Boxe, C.; Granfors, A.; Jones, A. E.; King, M. D.; Saiz-Lopez, A.; Shepson, P. B.; Sodeau, J.; Toohey, D. W.; Toubin, C.;

von Glasow, R.; Wren, S. N.; Yang, X. Halogen activation via interactions with environmental ice and snow in the polar lower troposphere and other regions. *Atmospheric Chemistry and Physics* **2012**, *12(14),* 6237-6271.

3. Aschmann, J.; Sinnhuber, B.M. Contribution of very short-lived substances to stratospheric bromine loading: uncertainties and constraints. *Atmospheric Chemistry and Physics* **2013**, *13(3)*, 1203-1219.

4. Hossaini, R.; Chipperfield, M.P.; Saiz-Lopez, A.; Harrison, J.J.; von Glasow, R.; Sommariva, R.; Atlas, E.; Navarro, M.; Montzka, S.A.; Feng, W.; Dhomse, S.; Harth, C.; Mühle, J.; Lunder, C.; O'Doherty, S.; Young, D.; Reimann, S.; Vollmer, M.K.; Krummel, P.B.; Bernath, P.F. Growth in stratospheric chlorine from short-lived chemicals not controlled by the Montreal Protocol. *Geophysical Research Letters* **2015**, *42*.

5. Karlsson, A.; Theorin, M.; Abrahamsson, K. Distribution, transport, and production of volatile halocarbons in the upper waters of the ice-covered high Arctic Ocean. *Global Biogeochemical Cycles* **2013**, *27(4)*, 1246-1261.

6. Verhulst, K.R.; Aydin, M.; Saltzman, E.S. Methyl chloride variability in the Taylor Dome ice core during the Holocene. *Journal of Geophysical Research: Atmospheres* **2013**, *118(21)*, 12,218-12,228.

7. Saltzman, E.S.; Aydin, M.; Tatum, C.; Williams, M.B. 2000-year record of atmospheric methyl bromide from a South Pole ice core. *Journal of Geophysical Research: Atmospheres* **2008**, *113(D5)*, 2156-2202.

8. Harper, K.; Minofar, B.; Roxana Sierra-Hernandez, M.; Casillas-Ituarte, Nadia N.; Roeselova, M.; Allen, H.C. Surface residence and uptake of methyl chloride and methyl alcohol at the air/water interface studied by vibrational sum frequency spectroscopy and molecular dynamics. *J Phys Chem A* **2009**, *113(10)*, 2015-24.

9. Rowland, F.S. Stratospheric ozone depletion. *Philos Trans R Soc Lond B Biol Sci*. **2006**, *361(1469)*, 769-790.

10. Sturges, W.T.; Cota, G.F.; Buckley, P.T. Bromoform emission form arctic ice algae. *Nature* **1992***, 358*, 660.

11. Holmes, N.S.; Sodeau, J.R. A Study of the Interaction between Halomethanes and Water-Ice. *J. Phys. Chem. A* **1999**, *103*, 4673-4679.

12. Vysokikh, T.A., Mukhamedzyanova, D.F.; Yagodovskaya, T.V.; Savilov, S.V.; Lunin V.V. The interaction of CH3Cl, CH2Cl2, CHCl3, and CCl4 with ozone on the surface of ice under stratospheric conditions. *Russian Journal of Physical Chemistry A* **2007**, *81(11)*, 1836-1839.

13. Cyriac, J.; Pradeep, T. Probing Difference in Diffusivity of Chloromethanes through Water Ice in the Temperature Range of 110-150 K. *Journal of Physical Chemistry C*, **2007**, *111*, 8557-8565.

14. Schaff, J.E.; Roberts, J.T. Toward an Understanding of the Surface Chemical Properties of Ice: Differences between the Amorphous and Crystalline Surfaces. *J. Phys. Chem.* **1996**, *100*, 14151-14160.

15. Aoki, M.; Ohashi, Y.; Masuda, S. Interactions of CHCl3 molecules with a crystalline ice grown on Pt(111) studied by metastable impact electron spectroscopy. *Surface Science* **2003**, *532-535*, p. 137-141.

16. Grecea, M.L.; Backus, E.H.G.; Fraser, H.J.; Pradeep, T.; Kelyen, A.W.; Bonn, M. Mobility of haloforms on ice surfaces. *Chemical Physics Letters* **2004,** *385(3-4)*, 244-248.
17. Crowley, J.N.; Amman, M.; Cox, R.A.; Hynes, R.G.; Jenkin, M.E.; Mellouki, A.; Rossi, M.J.; Troe, J.; Wallington, T.J. Evaluated kinetic and photochemical data for atmospheric chemistry: Volume V – heterogeneous reactions on solid substrates. *Atmospheric Chemistry and Physics* **2010**, *10(18)*, 9059-9223.
18. Hobza, P.; Sandorfy, C. Quantum chemical and statistical thermodynamic investigations of anesthetic activity. 3. The interaction between CH4, CH,Cl, CH2C12, CHCI, CCl, and an 0-H.. -0 hydrogen bond. *Can. J. Chem.* **1984**, *62*, 606.

19. Wang, W.; Tian, A.; Wong, N.B. Theoretical Study on the Bromomethane-Water 1:2 Complexes. *Journal of Physical Chemistry A* **2005**, *109,* 8035-8040.
20. Habartova, A.; Valsaraj, K.T.; Roeselova, M. Molecular dynamics simulations of small halogenated organics at the air-water interface: implications in water treatment and atmospheric chemistry. *J Phys Chem A* **2013**, *117(38)*, 9205-9215.
22. Abascal, J.L.F.; Vega, C. A general purpose model for the condensed phases of water: TIP4P/2005. *J. Chem. Phys.* **2005**, 123, 234505.

23. Buch, V.; Sandler, P.; Sadlej; J. Simulations of H2O Solid, Liquid, and Clusters, with an Emphasis on Ferroelectric Ordering Transition in Hexagonal Ice. *J. Phys. Chem. B* **1998**, *102*, 8641–8653.
24. Bernal, J.D.; Fowler, R.H. A Theory of Water and Ionic Solution, with Particular Reference to Hydrogen and Hydroxyl Ions. *J. Chem. Phys.* **1933**, *1*, 515.

25. Berendsen, H.J.C.; Postma, J.P.M.; van Gunsteren, W.F.; DiNola, A.; Haak, J.R. *Molecular dynamics with coupling to an external bath. J. Chem. Phys.* **1984**, *81(8)*, 3684-3690.
26. Vega, C.; Martin-Conde, M.; Patrykiejew, A. Absence of superheating for ice Ih with a free surface: a new method of determining the melting point of different water models. *Molecular Physics* **2006**, *104(22-24)*, 3583–3592.
27. Bussi, G.; Donadio, D.; Parrinello, M. Canonical sampling through velocity rescaling. *J. Chem. Phys.* **2007**, *126*, 014101.
28. Hess, B., et al., *GROMACS 4: Algorithms for highly efficient, load-balanced, and scalable molecular simulation. Journal of Chemical Theory and Computation* **2008**, *4(3)*, 435-447.
29. Hockney, R.W.; Goel, S.P.; Eastwood, J.W. Quiet High-resolution computer models of plasma. *Journal of Computational Physics* **1974**, *14(2)*, 148-158.
30. Darden, T.; York, D.; Pedersen, L. Particle Mesh Ewald - an N.Log(N) Method for Ewald Sums in Large Systems. *J. Chem. Phys.* **1993**, *98(12)*, 10089-10092.
31. Essmann, U.; Perera, L.; Berkowitz, M.L.; Darden, T.; Lee, H.; Pedersen, L.G. A Smooth Particle Mesh Ewald Method. *J. Chem. Phys.* **1995**, *103(19)*, 8577-8593.
32. Miyamoto, S.; Kollman, P.A. *SETTLE:* An analytical version of the SHAKE and RATTLE algorithm for rigid water models. *J. Comput. Chem.* **1992**, *13*, 952–962.
33. Humphrey, W.; Dalke, A.; Schulten, K. VMD - Visual Molecular Dynamics. *J. Molec. Graphics* **1996**, *14*, 33-38.

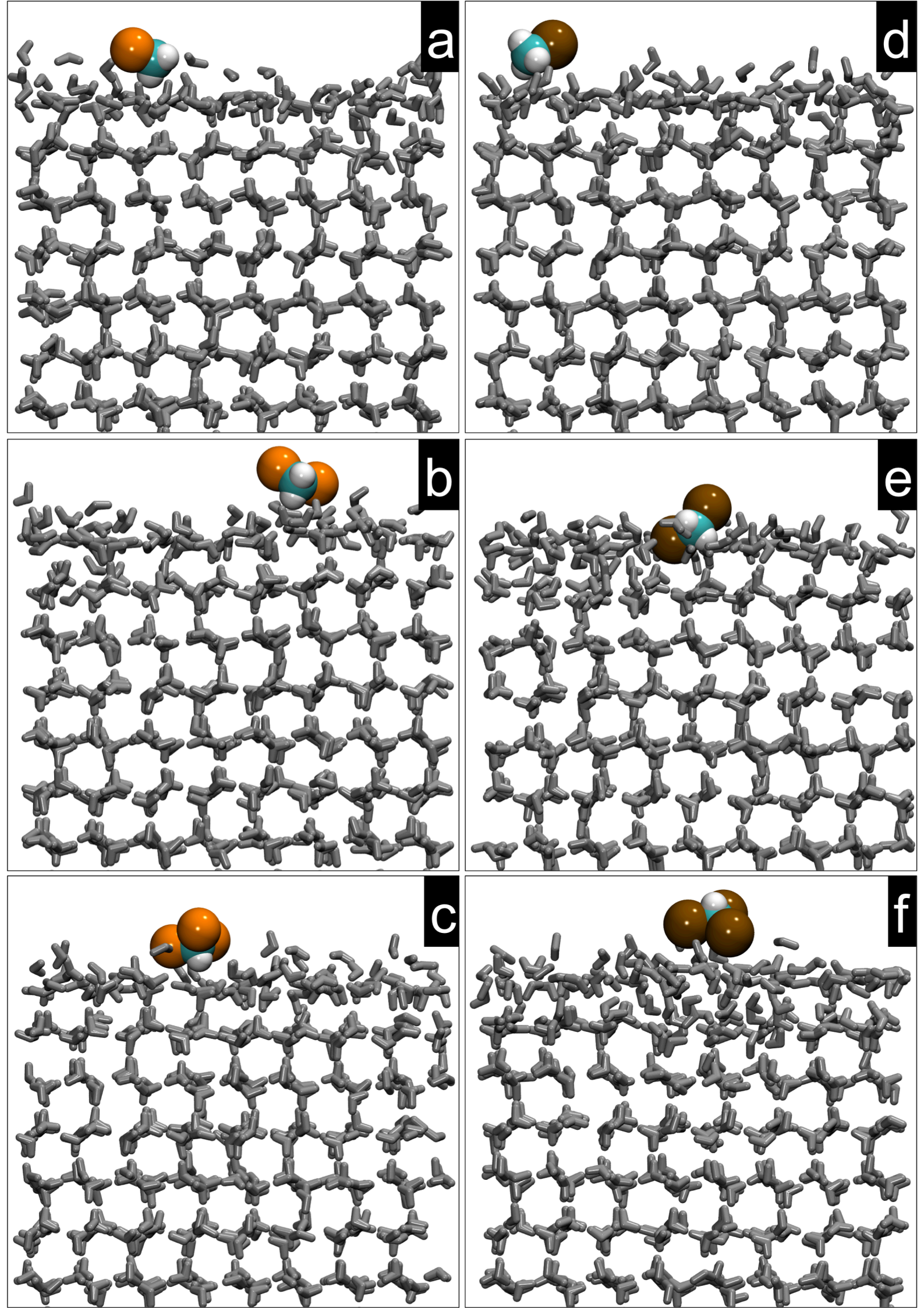
a
d
b
e
c
f

a

b

c

d

e

f

OW

C

X

Density (arb.u.)

0,5

1

0

1

2

3

4

z (nm)

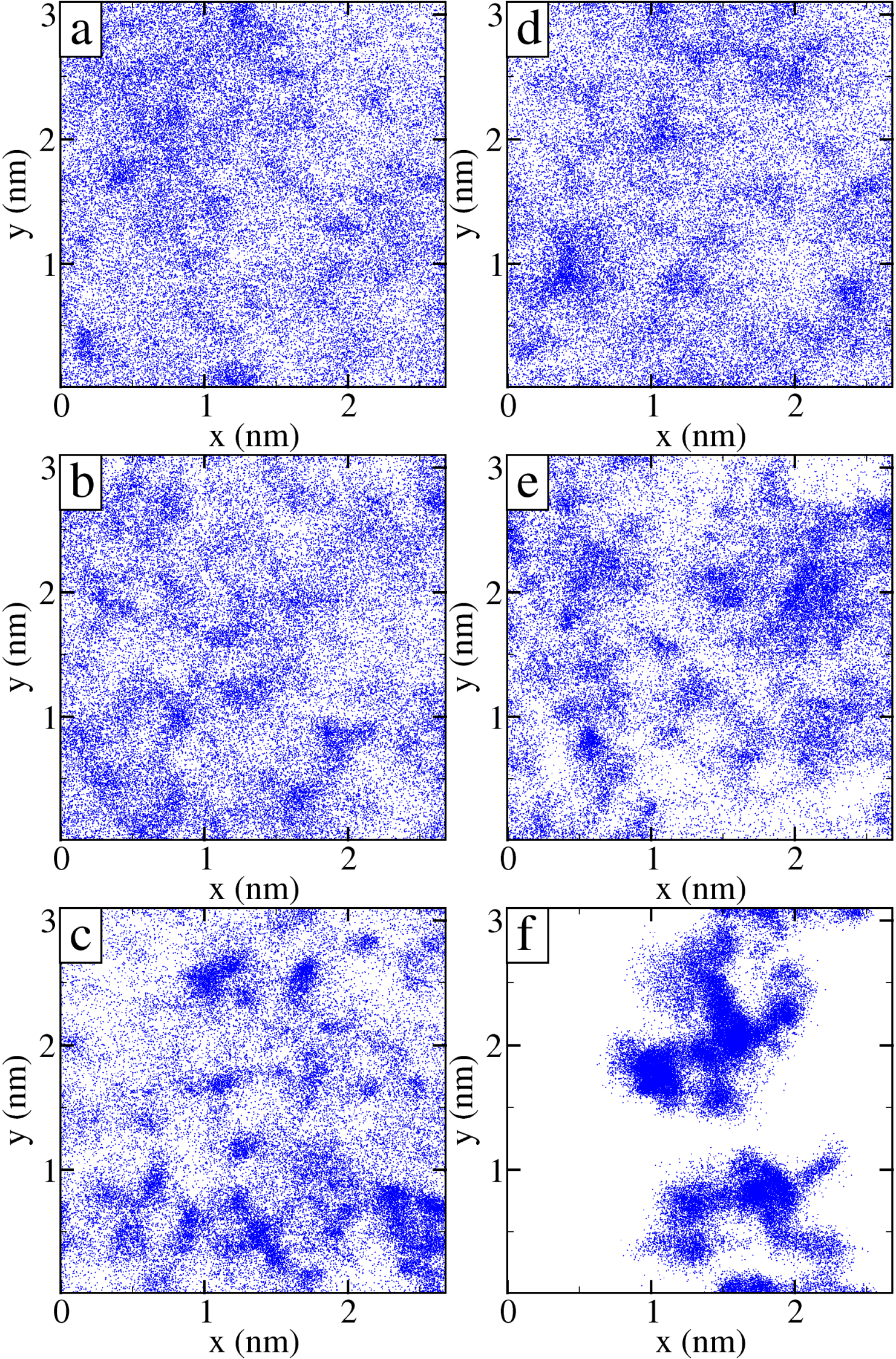
a
b
c
d
e
f
y (nm)
x (nm)
0
1
2
3

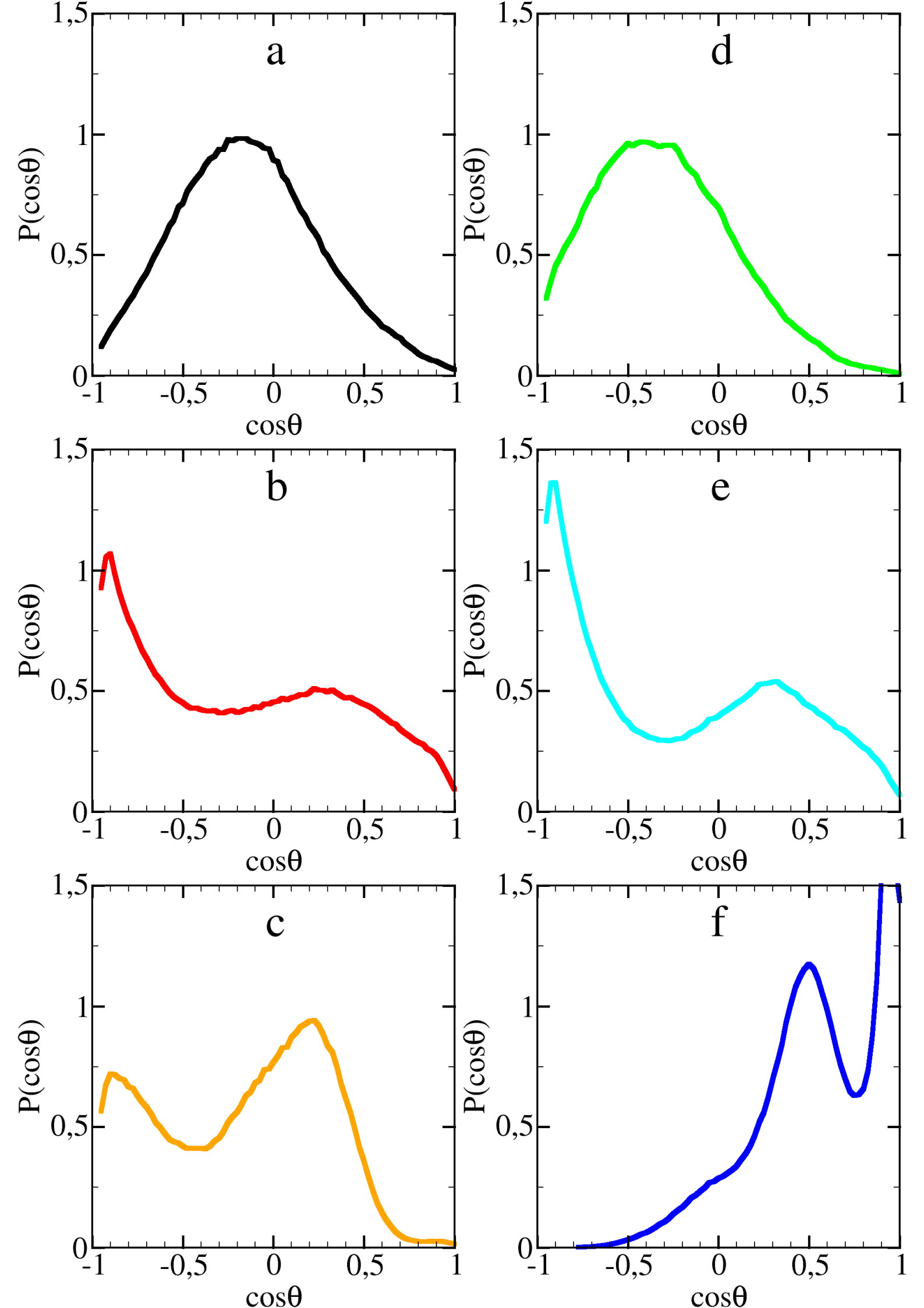
a
b
c
d
e
f
P(cosθ)
cosθ
1,5
1
0,5
0
-1
-0,5
0
0,5
1

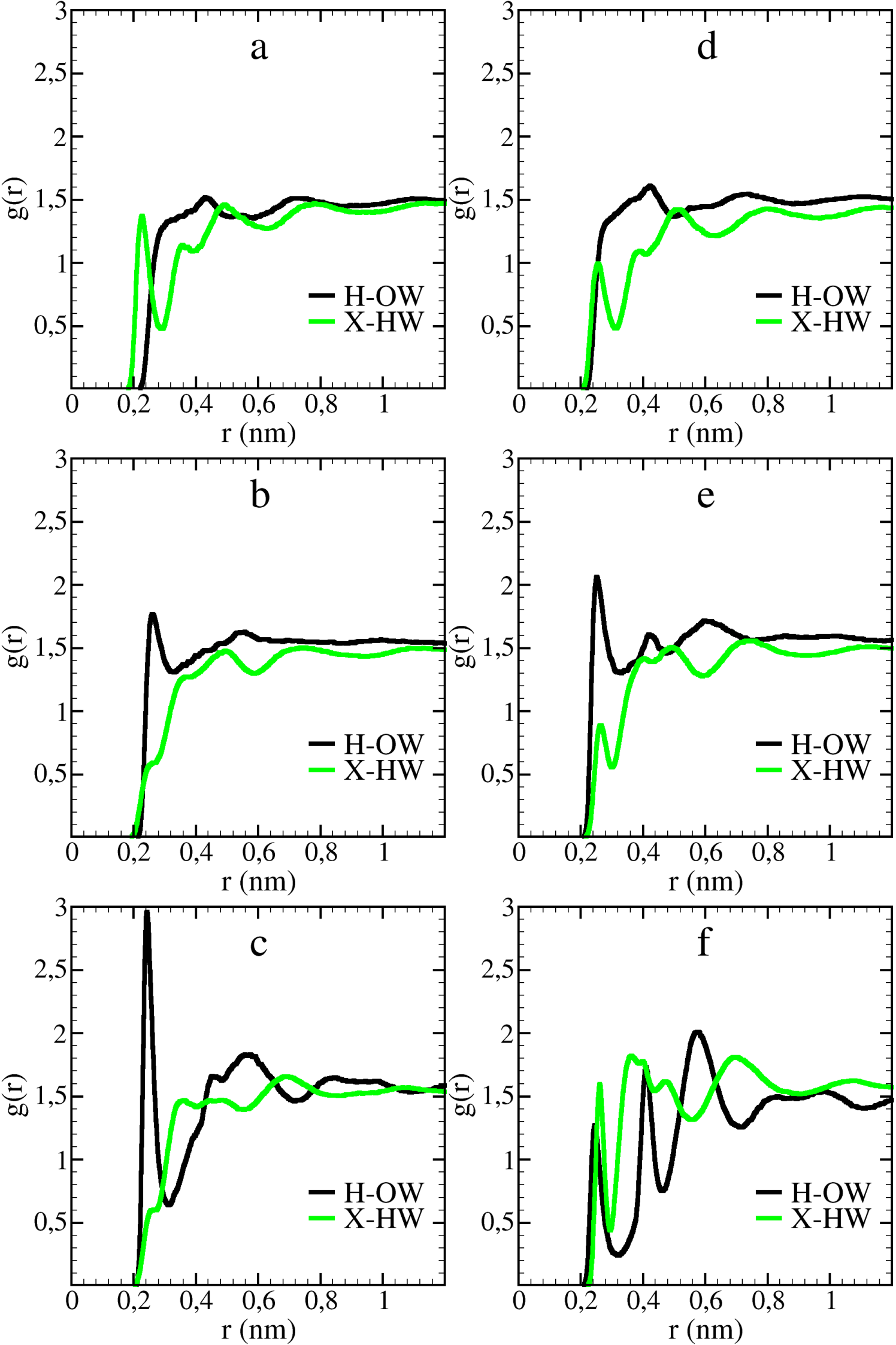
a
d
b
e
c
f
g(r)
r (nm)
H-OW
X-HW
0
0,2
0,4
0,6
0,8
1
0,5
1,5
2
2,5
3

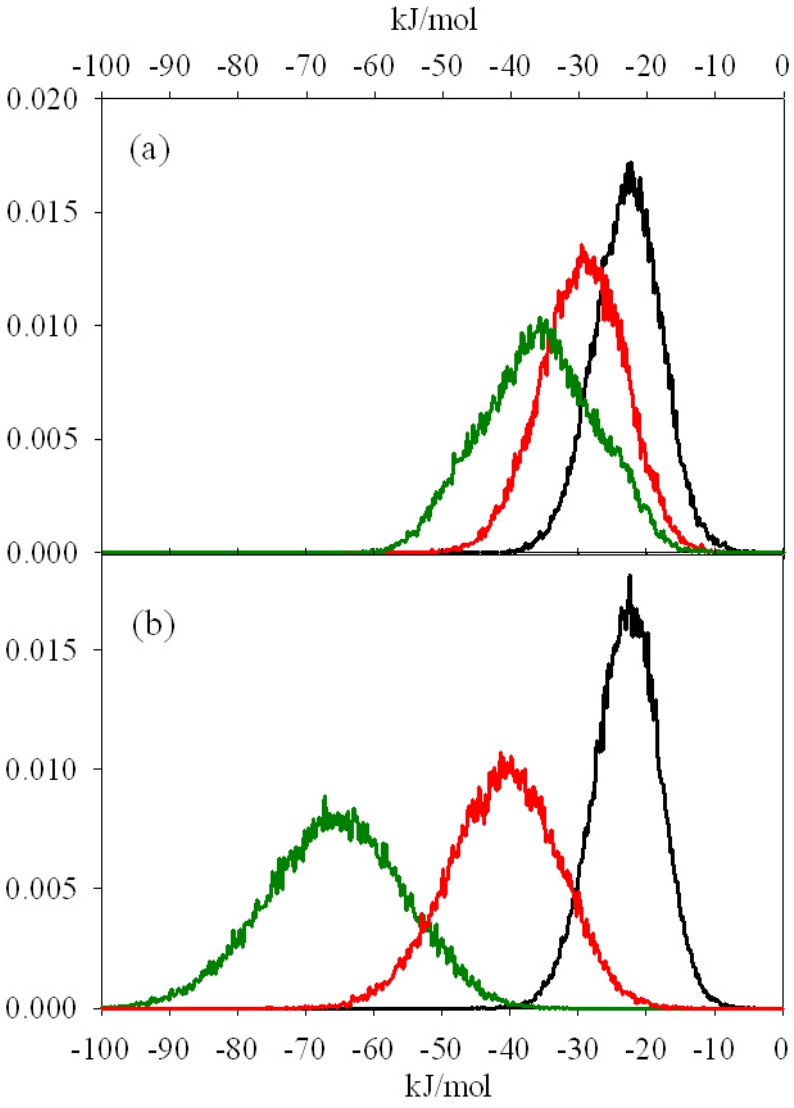
kJ/mol
-100 -90 -80 -70 -60 -50 -40 -30 -20 -10 0
0.020
0.015
0.010
0.005
0.000
(a)
(b)
kJ/mol